



MILLIMETRE-WAVE POWER SENSOR DESIGN

By

DUC DANG DINH

A thesis submitted to the University of Birmingham for the degree of

DOCTOR OF PHILOSOPHY

School of Electronic, Electrical and Systems Engineering
College of Engineering and Physical Sciences
University of Birmingham
June 2017

UNIVERSITY OF
BIRMINGHAM

University of Birmingham Research Archive

e-theses repository

This unpublished thesis/dissertation is copyright of the author and/or third parties. The intellectual property rights of the author or third parties in respect of this work are as defined by The Copyright Designs and Patents Act 1988 or as modified by any successor legislation.

Any use made of information contained in this thesis/dissertation must be in accordance with that legislation and must be properly acknowledged. Further distribution or reproduction in any format is prohibited without the permission of the copyright holder.

Abstract

This study is to maintain and extend the power standards at National Physical Laboratory (NPL) in the United Kingdom. The calibration service of microwave power sensors at high frequencies is endangered because a limited number of traceable waveguide power sensors is available at 50 GHz and above. In this thesis, the technologies of sensing microwave power in waveguides are reviewed, and the bolometric power sensor is investigated further, as its principle is suitable for the traceability requirement at NPL. The conventional design technique of bolometric sensor based on transmission line theory is generalised and two power sensor designs are introduced. The X-band sensor was fabricated, measured at the University of Birmingham and calibrated at NPL. Excellent linearity and high effective efficiency of the design was obtained. The high frequency power sensor designs based on the proposed technique can be scalable to 300 GHz and above, and a W-band sensor is introduced as an example. In order to add more flexibility in selecting frequency and bandwidth, a novel design of microwave power sensor with integrated filter function is described. An analytical power sensor synthesis technique using coupling matrix is presented for the first time. An X-band power sensor with integrated third order Chebyshev filter function was designed and manufactured. Experimental measurements in Birmingham and NPL are in good agreement with simulation and theoretical expectation.

Acknowledgements

This work is the outcome of a three years PhD programme in a collaboration between the University of Birmingham and National Physical Laboratory (NPL). In this context, the work has been carried out at the Department of Electronic, Electrical and Systems Engineering University of Birmingham, UK and Power Laboratory, National Physical Laboratory, UK.

The author wishes to thank Prof. Michael Lancaster at the University of Birmingham who introduced the author to the PhD project, and firmly and tirelessly provided support and guidance over the whole period of the study. A grateful thank is for Dr. John Howes, Mr. James Miall, Mr. Daniel Stokes and Mr. Sam Alvey-Taylor who gave support during the period spent at NPL, for their availability, helpful discussions and comments. Special thanks to Dr. Yuvaraj Dhaylan, Mr. Alan Yates, Mrs Donna Johnson and Mr. Warren Hay for their continuous supports and efforts in fabrication of the devices presented in the thesis. Also, a thank goes to the friends and people met during all these years: in particular to the Emerging Device Technology Research Group and to all other friends with whom was a pleasure to work with and to share time and experiences together.

A special thought and thank also goes to my parents and my wife for the care, support and encouragement.

Birmingham, UK, June 2017.

Contents

Abstract.....	i
Acknowledgements	ii
Contents.....	iii
List of Figures.....	vii
List of Tables.....	xiv
Chapter 1 Introduction	1
1.1. Thesis Motivation	1
1.2. Thesis Overview	5
Chapter 2 Review of Microwave Power Measurement	10
2.1. Microwave Power	10
2.2. Microwave Power Measurement	14
2.3. Techniques of Sensing Microwave Power.....	18
2.3.1. Diode sensors.....	19
2.3.2. Thermoelectric sensors	21
2.3.3. Bolometric sensors	22
2.3.4. Discussion on measurement techniques	23
2.4. Bolometric Sensors for Microwave Power Measurement	25
2.4.1. The sensing elements.....	25
2.4.2. The bolometer mount	28
2.4.3. Meter circuits.....	35
2.4.4. Bolometer Calibration	38
Chapter 3 Transmission Line Theory Based Power Sensor Design	46
3.1. Transmission Line for Rectangular Waveguides.....	46
3.2. Bolometer Mount Design.....	52
3.2.1. Transmission line presentation of the waveguide bolometer	52
3.2.2. Two-port impedance extraction of the mount	58

3.2.3. Process of design.....	63
Chapter 4 X-band Microwave Power Sensor Design	67
4.1. Modelling of the Sensing Element.....	67
4.2. Design of the Mount for the Matching Condition Using Full Wave Simulation ...	71
4.2.1. The structure of the thermistor mount.....	71
4.2.2. Determination of the mount dimensions.....	73
4.3. The Structure of the X-band Power Sensor.....	77
4.4. Thermal Consideration	81
4.5. Fabrication and Measurement	88
4.5.1. The fabrication of X-band power sensor.....	88
4.5.2. Measurement of the reflection coefficient.....	89
4.5.3. Measurement of the linearity with power	93
4.5.4. Measurement of effective efficiency and calibration factor	97
Chapter 5 High Frequency Microwave Power Sensor Design Using Temperature Dependent Resistive Films	102
5.1. The Material of Temperature Dependent Resistive Film.....	103
5.1.1. Positive temperature coefficient (PTC) materials.....	103
5.1.2. Negative temperature coefficient (NTC) materials.....	104
5.1.3. Discussion on the thin film bolometers	106
5.2. Modelling the Thin Film Element.....	107
5.2.1. Power transmission and power reflection coefficient in a rectangular waveguide blocked by a thin film	108
5.2.2. Reactance of narrow thin film in a rectangular waveguide	112
5.3. Design the Mount for Matching Condition	115
5.3.1. Structure of the thin film mount.....	115
5.3.2. Determination of the mount dimensions.....	116
5.4. The Structure of the W-band Power Sensor	120
5.4.1. The aluminium waveguide layers.....	122
5.4.2. The thin film layer and isolation layer	123
5.4.3. The design optimisation.....	126

5.4.4.	The effects of platinum side deposition on the SU-8 substrate	127
5.5.	Thermal properties of the sensor structure	128
5.6.	Fabrication of the W-band power sensor.....	134
5.7.	The microwave power sensor design up to 300 GHz.....	136
Chapter 6	Microwave Power Sensor with Integrated Band-pass Filter Functions	144
6.1.	General Coupling Matrix Theory of Band-pass Filters	145
6.2.	Realisation of Filter with Rectangular Waveguide Resonators	150
6.2.1.	Rectangular waveguide cavity resonators	150
6.2.2.	Extraction of external quality factor Q_e	153
6.2.3.	Extraction of coupling coefficient M	155
6.2.4.	Examples of a third order filter realisation.....	157
6.3.	Integration of Microwave Power Sensor with Filter	159
6.3.1.	Sensor-resonator	160
6.3.2.	Coupling matrix presentation of the integration of the sensor with filter	163
6.3.3.	Extraction of external quality factor Q_{er} of the sensor-resonator	164
6.4.	The Design of X-band Sensor with Integrated Third Order Filter Functions.....	166
6.4.1.	Extraction of the external quality factor Q_{er} of the X-band sensor-resonator using a bead thermistor as the sensing element.....	167
6.4.2.	Extraction of the external quality factor of the X-band rectangular waveguide resonator	169
6.4.3.	Extraction of the coupling coefficient between the X-band rectangular waveguide resonators	171
6.4.4.	Filter-sensor integration.....	173
6.4.5.	The structure of the third order filter-sensor	176
6.4.6.	Fabrication and measurement.....	180
Chapter 7	Conclusion and Future Work	187
7.1.	Conclusion	187
7.2.	Future Work.....	190

Appendix A- Field analysis of Transmission lines.....	192
Appendix B- Parasitic capacitance of bead thermistors	195
Appendix D- Thin film nickel manganese developed at the University of Birmingham	200
Appendix E- The detailed structure of the W-band power sensor	203
Appendix F - The structure of WR6 power sensor.....	209
Appendix G - The structure of WR-3 waveguide power sensor	217
Appendix H - The method of extracting the external quality factor Q_e for a lossless resonator	223
Appendix I – The method of extracting the quality factor Q_0 for a lossy resonator	226
Appendix J – The construction of the X-band filter-sensor.....	229
List of Publications.....	232

List of Figures

Figure 1.1:	The traceability path of power references [12].....	2
Figure 1.2:	Calibration and traceability of high frequency power (taken from [14])	4
Figure 2.1:	GSM pulse specification (taken from [6]).....	12
Figure 2.2:	A rectangular pulse response with the pulse width τ and the period T	13
Figure 2.3:	(a) The power measurement setup in which a power sensor is connected directly to the output of the generator; (b) the signal flow graph of the measurement setup [9].	15
Figure 2.4:	(a) The junction rectifying characteristic of a low barrier Schottky diode, showing the small signal, square law characteristic around the origin; (b) circuit diagram of a source and a diode detector with matching resistor [10].	20
Figure 2.5:	(a) the thermocouple consisting of two different metals [10]; (b) the simplified diagram of a thermocouple detector (taken from [5]).	21
Figure 2.6:	Functional diagram of a bolometric sensor and its power meter [5].....	22
Figure 2.7:	Diagram of a coaxial thermistor mounts[4].....	30
Figure 2.8:	The co-axial thermistors mount with line taper as transformer section (Taken from [4]).....	31
Figure 2.9:	A simplified diagram of coaxial gold film bolometer (taken from [23])	31
Figure 2.10:	Schematic diagram of two fixed-tuned designs of rectangular waveguide thermistor mounts, the capacitor symbols present the d-c open circuit and r-f short circuit [4].....	32
Figure 2.11:	Ridge waveguide type of thermistor mount (a) front view and (b) cut side view (taken from [23])	33
Figure 2.12:	Bar and post type of waveguide thermistor mount (a) front view and (b) cut side view (taken from [23])	34
Figure 2.13:	Transverse thin film bolometer mount in rectangular waveguide (a) front view and (b) cut side view (taken from [23]).....	34
Figure 2.14:	A simple Wheatstone bridge for bolometer operation, where R_1 and R_2 are the bridge resistance and often equal, R_g is the ammeter resistance, R_{ref} is the reference resistance to set the operating value of the bolometer element resistance R_T	35
Figure 2.15:	The close-loop measurement of bolometer with balancing circuit.....	36
Figure 2.16:	Functional diagram of a multistate reflectometer at National Physical Laboratory.....	39
Figure 3.1:	A rectangular waveguide structure	47

Figure 3.2: (a) The electric field and magnetic field of TE ₁₀ mode(taken from [9]); (b)The surface current in the TE ₁₀ mode(taken from [10]).....	50
Figure 3.3: Equivalent transmission line circuit of a waveguide bolometer.....	53
Figure 3.4: Matching condition of the mount resistance, reactance and the shorted electrical length.....	55
Figure 3.5: The reflection coefficient S_{11} for inductive matching condition at different resistance of the mount.....	57
Figure 3.6: The reflection coefficient S_{11} at capacitive matching condition.....	57
Figure 3.7: Equivalent transmission line circuit of the impedance extracting method.....	58
Figure 3.8: The equivalent of the circuit in Figure 3.7.....	59
Figure 3.9: The CST model of a circular post in the middle of X-band waveguide (the cut view is shown for the clarification of objects).....	60
Figure 3.10: Comparison of normalised reactance of circular post in X-band waveguide between the extractions from simulation and theoretical calculation.....	62
Figure 3.11: The power sensor design process based on transmission line theory.....	64
Figure 4.1: The bead thermistor from Sensor Scientific [3]......	68
Figure 4.2: An equivalent circuit of an RF thermistor [4]......	69
Figure 4.3: Equivalent capacitor C_{th} at different d-c biased thermistor's resistance.	70
Figure 4.4: (a) The section in the waveguide of the PCB accommodating the bead thermistor; (b) the cut view to show how the thermistor is soldered on the PCB.....	71
Figure 4.5: (a) The bead thermistor in the CST simulation; (b) the CST schematic diagram which includes the equivalent circuit of the thermistor bead.	72
Figure 4.6: The two port simulation of impedance extraction for the thermistor mount.....	73
Figure 4.7: The effective length l_R and l_X at different widths w	75
Figure 4.8: The simulation of the designed mount in a shorted waveguide.	75
Figure 4.9: The reflection coefficient of the sensor simulation in Figure 4.8.....	76
Figure 4.10: The power loss distribution inside the sensor at operating condition.....	77
Figure 4.11: The structure of the X-band power sensor (a) before and (b) after assembling.....	77
Figure 4.12: (a) The PCB clamped between two waveguide parts; (b) one side of the PCB.....	78
Figure 4.13: The simulation result of the power sensor in CST Microwave Studio.....	79

Figure 4.14: Comparison between the results from computer simulation and calculated model of the X-band sensor.....	80
Figure 4.15: The change in S_{11} in the full-wave simulation when adjusting the shorted length.....	81
Figure 4.16: (a) The direction of the heat flow in the power sensor; (b) the equivalent thermal circuit of the sensor.....	83
Figure 4.17: (a) The regions of the equivalent thermal resistances on the PCB; (b) the thermal circuit of the heat flow from the thermistor bead in the upper part.....	85
Figure 4.18: The temperature distribution in the sensor at operation condition.	87
Figure 4.19: The double-sided PCB with a thermistor soldered at the centre and (b) the assembled X-band sensor.	89
Figure 4.20: The measured reflection coefficient of the sensor at 200 Ω thermistor biasing.....	90
Figure 4.21: The simulated response of the sensor with the measured PCB dimensions ...	91
Figure 4.22: The tuned S_{11} parameter (in blue) by introducing a tuning screw at 200 Ω bias.....	91
Figure 4.23: The optimised response of the sensor at different biasing conditions.	92
Figure 4.24: The power measurement set up. The red box contains a power meter and a signal generator to monitor the input power of the X-band sensor. The auto-balancing circuit and the voltmeter in the black box are to monitor the thermistor resistance and record the biased voltage on the thermistor. The directional 3dB coupler in the green box is to divide the power from the input port to the power sensor and the sensor.....	93
Figure 4.25: The relationship between input power and substitutional power at 200 Ω thermistor operation.....	94
Figure 4.26: The relationship between input power and substitutional power at 400 Ω thermistor operation.....	96
Figure 5.1: (a) perspective view and (b) side view of a thin metal film in a rectangular waveguide in which the thin film thickness is exaggerated to show the field in the medium [17].....	109
Figure 5.2: The CST simulation model of an Ohmic sheet in a rectangular waveguide	110
Figure 5.3: Comparison between calculation and simulation results of the power transmission of thin platinum film at 94 GHz.	112
Figure 5.4: A narrow thin film in waveguide (a) crossed section, (b) top view and (c) Equivalent circuit [19]. a and b are the dimension of the waveguide, Z_0 is the characteristic impedance of the guide and X is the reactance of the thin film.....	112

Figure 5.5: Simulation model of a narrow thin platinum film in a W-band waveguide for the reactance extraction.....	113
Figure 5.6: Calculated and simulated reactance of thin film in W band waveguide at 94 GHz.....	114
Figure 5.7: The mount of the thin platinum film in the W-band waveguide, where $b = 1.27$ mm is the height of the W-band waveguide, t_{sub} is the substrate thickness of 50 μ m, the film and the substrate have the same width w	115
Figure 5.8: The thin film structure in a two-port W-band waveguide.....	117
Figure 5.9: Electrical length extraction results for the thin film mount at different widths.....	118
Figure 5.10: The simulation of the designed mount in a shorted waveguide.....	118
Figure 5.11: The reflection coefficient of the waveguide sensor in Figure 5.10.....	119
Figure 5.12: The W-band thin film power sensor (a) before and (b) after assembling.....	121
Figure 5.13: The initial reflection coefficient of the full W-band power sensor.....	122
Figure 5.14: Waveguide layer with four round edges of the waveguide window.....	122
Figure 5.15: The simulated reflection coefficient of the power sensor with round edge compensation.....	123
Figure 5.16: The thin film layer.....	124
Figure 5.17: (a) The simulation model to determine the microwave leakage between two W-band waveguides separated by isolation layer and thin film layer; (b) the zoomed-in view of the waveguides. The matched waveguide ports are shown in red.....	125
Figure 5.18: The microwave power loss versus the thickness of the isolation and thin film layer.....	126
Figure 5.19: The optimised reflection coefficient of the power sensor.....	127
Figure 5.20: (a) surface deposition; (b) surface and side deposition of platinum on the SU-8 substrate.....	128
Figure 5.21: Simulated result when the side deposition takes all the thickness of the substrate.....	128
Figure 5.22: The heat flow paths in the power sensor. The dimension of SU-8 layers are exaggerated for clarity.....	130
Figure 5.23: The equivalent thermal circuit of the power sensor structure.....	131
Figure 5.24: The temperature distribution in the power sensor at the operating condition (a) shows the whole thin film structure and (b) shows the distribution at the edge of the thin film.....	133

Figure 5.25:	The thin film layer with 10nm silver deposited.	135
Figure 5.26:	(a) Thin silver film on Su-8 in the W-band sensor; (b) The tabs were removed and two d-c terminals were attached to the structure ;(c) back view (d) a standard W-band waveguide attached to the front of the sensor, which can help the sensor to connect with the measurement system in NPL.	135
Figure 5.27:	WR6 and WR3 waveguide power sensor construction (a) before assembling (b) assembled.	137
Figure 5.28:	The structure of the layer carrying a circular choke with the parameters of the choke ring, note that the depth of the choke ring is equal to the thickness of the layer.	138
Figure 5.29:	Power leakage in WR-6 and WR-3 power sensor with and without the choke ring design.	139
Figure 6.1:	The topology of a two-port n coupled resonator filter.	147
Figure 6.2:	(a) Third order Chebyshev filter response generated form the matrix in equation 6.9; (b) the ripple of 0.0436 dB in the pass-band of the filter; (c) the topology of the filter.	149
Figure 6.3:	The geometry of a waveguide cavity, a and b are the standard dimensions of the waveguide cross section, the waveguide is shorted at $z = 0$ and $z = d$	150
Figure 6.4:	Some popular waveguide irises: (a) capacitive iris, (b) symmetrical capacitive iris, (c) rectangular iris, (d) inductive iris, (e) symmetrical inductive iris and (f) circular iris.	153
Figure 6.5:	(a) The equivalent circuit of the extraction of the external quality factor Q_e , port 2 is weakly coupled to the LC circuit (i.e. $G_2 \gg G_1, L$ and C); (b) the transmission coefficient of the resonator.	154
Figure 6.6:	(a) The equivalent circuit of the extraction of the coupling coefficient M , the output ports are weakly coupled to the resonant circuits; (b) the transmission coefficient of the coupling circuit.	156
Figure 6.7:	The structure of a 3 rd order Chebyshev filter, the specifications of the filter are in Table 6.1, only half of the filter is shown in the figure.	158
Figure 6.8:	The initial and optimised response of the designed third order Chebyshev filter.	159
Figure 6.9:	The topology of the power sensor with integrated band-pass filter function. ..	160
Figure 6.10:	The sensor-resonator structure realised by adding a capacitive iris to the conventional power sensor structure discussed in Chapter 3	160
Figure 6.11:	(a) Topology of the sensor-resonator; (b) equivalent topology of the resonator.	162

Figure 6.12: The equivalent topology of the power sensor integrated band-pass filter function in Figure 6.7.	162
Figure 6.13: (a) Equivalent circuit of the extraction of quality factor or a lossy resonator; (b) the typical the reflection coefficient of the one-port measurement of the resonator.	164
Figure 6.14: Equivalent topology of third order Chebyshev filter-sensor	166
Figure 6.15: The simulation structure of X-band sensor-resonator (a) waveguide body (b) PCB (c) schematic including the thermistor circuit.	167
Figure 6.16: Extraction of Q_{er} with the resistance of the bead thermistor.	168
Figure 6.17: Extraction of Q_{er} at $R=100 \Omega$ and different track width w of the PCB	169
Figure 6.18: Two port measurement to extract the quality factor (a) cut side view (b) cut perspective view	170
Figure 6.19: External quality factors and the cavity length of X-band waveguide resonator at different iris widths.....	170
Figure 6.20: Measurement to extract coupling coefficient (a) cut side view (b) cut perspective view	171
Figure 6.21: Coupling coefficient and the cavity length of X-band waveguide resonator at different iris widths.....	172
Figure 6.22: The filter-sensor integration (a) cut side view (b) cut perspective view (c) Schematic including the thermistor circuit.....	173
Figure 6.23: Initial response of the filter-sensor integration	174
Figure 6.24: Optimised result of the integration of sensor-resonator to filter.....	175
Figure 6.25: The structure of the X-band filter-sensor in 3D design environment.	176
Figure 6.26: The reflection coefficient of the filter-sensor	177
Figure 6.27: Comparison between simulated responses of the sensor in chapter 4 and the X band filter-sensor	178
Figure 6.28: The rms amplitude of the electric field inside the filter-sensor structure at (a) 9.6 GHz, (b) 10.05 GHz and (c) 10.4 GHz.	179
Figure 6.29: (a) The fabricated PCB for the X-band filter-sensor (b) the waveguide parts after assembling and (c) the fully assembled X-band filter-sensor.	181
Figure 6.30: The measured and simulated reflection coefficient of the X-band filter-sensor at 100Ω thermistor resistance.	182
Figure 6.31: The tuned S_{11} parameter of the X-band filter-sensor by tuning screws at 100Ω thermistor resistance.	183

Figure 6.32: The reflection coefficient of the X-band filter-sensor at 150 Ω thermistor resistance and the ideal third order Chebyshev filter response in comparison..... 183

Figure 6.33: The relationship between input power and substitutional power at 150 Ω thermistor operation of the X-band filter-sensor. 184

List of Tables

Table 4.1:	The initial and optimised parameters of the designed sensor.....	80
Table 4.2:	The values of the thermal resistances of the thermal circuit in Figure 4.17(b) ..	84
Table 4.3:	The calibration factor and effective efficiency from the measurement at the University of Birmingham.....	97
Table 4.4:	The calibration factor and effective efficiency form the measurement at National Physical Laboratory.....	98
Table 5.1:	PTC metallic materials used for microwave bolometric sensor.....	104
Table 5.2:	NTC materials for thin film bolometric element.....	105
Table 5.3:	Record of importance parameters of the power sensor.....	126
Table 5.4:	The thermal resistance of the equivalent thermal circuit in Figure 5.23.....	132
Table 6.1:	The design parameters of the 3 rd order Chebyshev filter with 10% FBW	149
Table 6.2:	The initial and optimised values of the dimensions of the filter in Figure 6.11.....	158
Table 6.3:	Specification of 3 rd order filter sensor with 10 % FBW	166
Table 6.4:	Initial dimensions of the filter sensor integration.....	174
Table 6.5:	The record of all parameters before and after optimisation process.....	176
Table 6.6:	Optimised parameter of the filter-sensor for the initial and optimised responses.....	177
Table 6.7:	The calibration factor and effective efficiency form the measurement at the University of Birmingham and National Physical Laboratory.....	185

Chapter 1

Introduction

1.1. Thesis Motivation

The utilisation of the millimetre wave range of the electromagnetic spectrum from 30 GHz to 300 GHz has been significantly increased in recent years. It has been reported in a wide range of applications such as climate and space research [1-3], remote sensing [4], spectroscopy [5], biology and medicine [6], security instruments [7], short range communication [8], etc. Advantages of higher frequency applications are: higher data transfer rates (due to increase absolute available bandwidth), miniaturisation (circuit, waveguide, antennas) and higher resolution in case of imaging and radar applications.

The approval of safety, quality and performance of the mentioned applications depends directly on the availability of measurement capabilities such as vector network analysis, spectrum analysis and signal power measurement. Research and development of millimetre wave system also require sufficient supporting measurements where power is one of the primary measurements. For low frequency operation, it is customary to measure voltage and current instead of power. In radio frequency region (30 MHz - 3 GHz), both power and voltage measurement are common. However, power is considered more meaningful, since the definition of power is independent of the characteristic impedance of the transmission line,

whereas voltage is meaningless without the specification of the line impedance, for example in waveguide transmission line the characteristic impedance can be defined in different ways. Additionally, voltage and current can vary with position along a lossless transmission line, whereas the average power maintains a constant value with position. In microwave region (3 GHz – 300 GHz), it is extremely difficult to make an accurate voltage determination. Therefore, the measurement of power is of primary concern [9].

It is critical for scientific and industrial research and development that power measurements can be duplicated at different times and places. As a result, the common agreement to the standard Watt (W) in the International System of Units (SI) has been established. National reference standards in the form of micro-calorimeters for different frequency bands have been developed. The national reference standards are available in a few National Measurement Institutes (MNIs) such as National Physical Laboratory (NPL) in the United Kingdom and National Institute of Standard and Technology (NIST) in the United States [10, 11]. Microwave power sensors should be referenced back to the national standards, the measurement by the instruments is said to be traceable.

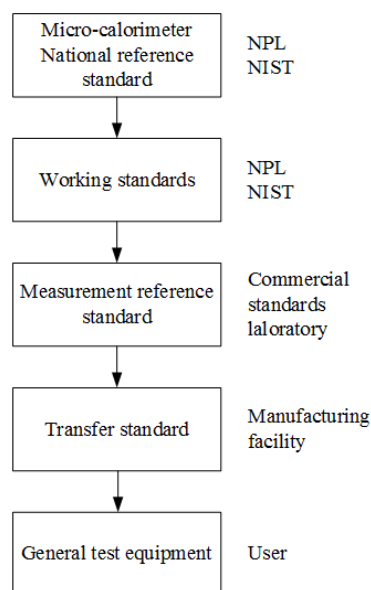


Figure 1.1: The traceability path of power references [12].

The traceability path for a power sensor is shown in Figure 1.1. At each echelon, several power standards are maintained for the frequency bands of interest. The power sensors are periodically recalibrated by the next higher standard. At a lower level than working standards, the calibration can be performed by accredited laboratories. The cost of calibration tends to be greatest at national level and reduces at each lower level. Each level along the traceability path adds some measurement uncertainty which is strictly regulated by NMIs and accredited laboratories [13].

High frequency (HF) power traceability needs to be maintained across the developed electromagnetic spectrum and also established at higher frequencies for future applications. Microwave power, in the range of 50 GHz to 300 GHz, is one of the millimetre wave quantities that cannot be measured with confidence due to lack of traceability to the SI unit. Furthermore, in order to verify HF radiation safety limits, there is a need for traceability of power-related quantities such as power flux density, electric and magnetic field strength. Technically, these quantities are directly traced to HF power. Therefore, lack of power measurement traceability will directly result in the inability to enforce importance safety legislation [14].

In order to provide traceability of high frequency power, two basic building blocks are needed, one is traceable microwave power transfer sensors and the second is calorimeters to calibrate the former [15]. This is shown in Figure 1.2. The calibration of commercial sensors directly results from the availability of calibrated transfer standard sensor and the technique to compare the standards to the commercial sensors. Standard power sensors have been developed for two transmission line systems: coaxial lines or rectangular waveguides.

The coaxial calorimeter and power standards of this type are available at NPL up to 50 GHz [16]. For the higher frequencies, direct comparison setups using waveguide transfer sensors as calibration standard are currently applied to calibrate commercial coaxial sensor [17]. The

traceable measurement capability in the coaxial line system is currently available in some European NMIs and a few accredited calibration laboratories for frequency up to 67 GHz [14].

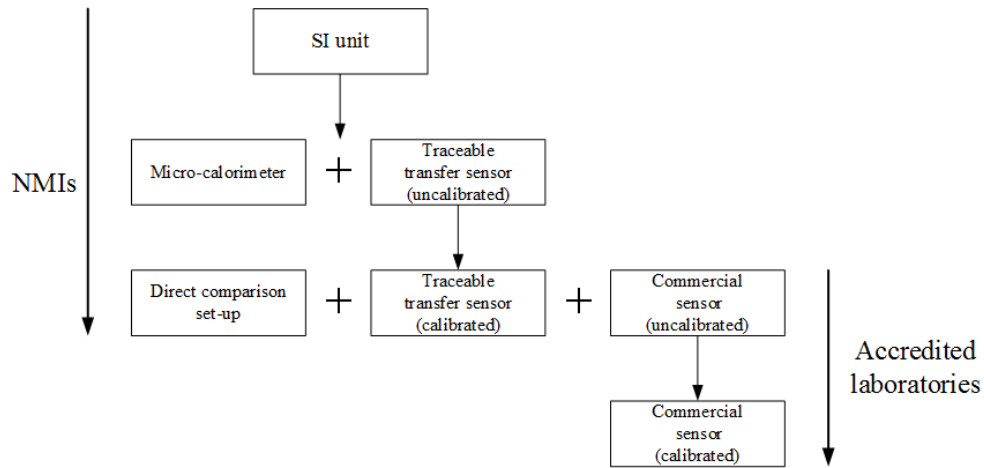


Figure 1.2: Calibration and traceability of high frequency power (taken from [14])

In waveguide, micro-calorimeters up to 110 GHz have been developed by NPL [18, 19]. It is also known that several national measurement institutes, such as in Japan [20-23] and in China [24-26], are actively developing their own micro-calorimeters up to and above 110 GHz to support domestic industrial and scientific measurement requirements. The transfer standards of micro-calorimeter calibration is based on waveguide thermistor power sensors manufactured by Hughes and subsequently by Millitech [24, 27]. The continuation of the calibration service in the United Kingdom beyond 50 GHz is endangered because the production of the thermistor sensors stopped in the 1990s and sensors above 110 GHz are extremely rare [19].

Modern commercial HF power sensors are currently available up to 110 GHz (coaxial) and 1.1 THz (waveguide), but they are not suitable as direct traceable transfer standards. Their detection principle, based on rectification or direct heating effect of a thermocouple, is incompatible with the existing calorimetric method. In the past, a millimetre wave power standard for WR-6 waveguide band has been developed [28, 29], but a detailed uncertainty

calculation towards traceability has not been published. A traceable power sensor at 94 GHz was developed at Queen Mary College, University of London in 1980s under a contract from NPL [30]. The sensor is commercially available but it is not suited to making measurements of power in waveguide [19].

This project is a collaboration between the University of Birmingham and National Physical Laboratory. The aim is to maintain and extend the existing traceable microwave power measurement capability by designing transfer power sensor not only at high frequencies (> 110 GHz) but also at lower frequencies, filling the gap left by the discontinued production of commercial thermistor sensors in waveguide frequency bands.

In the thesis, two design techniques of traceable microwave power sensors are presented. The first design is based on Transmission line theory, the mathematics and design process are fully described here for the first time. The second design technique is a novel design based on coupling matrix synthesis. The power sensor can be designed in the same manner as the microwave filter design. The techniques are validated by the design of power sensors in X-band waveguide. The sensors are fabricated and measured, the experimental results are in good agreement with simulation and theoretical expectation. The design and fabrication techniques for high frequency sensors up to 300 GHz are discussed in this work.

1.2. Thesis Overview

The following work is organised into 6 chapters.

Chapter 2 describes the basic knowledge and background of microwave power measurement.

Chapter 3 presents the conventional power sensor design based on Transmission line theory. The chapter introduces the derivation of rectangular waveguide transmission line, and its application to find the matching in waveguide sensor.

Two design examples of conventional waveguide power sensor are introduced in Chapter 4 and Chapter 5. The two designs utilise different sensing elements at different frequencies. The problems of modelling the sensing element in electromagnetic simulator such as CST are addressed and the solutions are then proposed. Chapter 4 describes the fabrication and measurements of an X-band power sensor. The W-band sensor design presented in Chapter 5 is a promising design as it can be scaled to work up to 300 GHz.

Chapter 6 presents a novel design approach in which the conventional power sensor is integrated with a microwave filter. In this chapter, the design of microwave filter-sensor based on coupling matrices is presented. The coupling matrix of narrow band filter is modified to integrate the power sensor. In order to provide experimental verification of the design approach, the design, fabrication and measurements of an X-band sensor with integrated third order Chebyshev filter function are described.

Conclusions and future work of the thesis are included in Chapter 7.

References

- [1] P. d. Maagt, "Terahertz technology for space and earth applications," in *2006 First European Conference on Antennas and Propagation*, 2006, pp. 1-4.
- [2] P. d. Maagt, "Terahertz applications and technology," in *2009 International Conference on Microwave Technology and Computational Electromagnetics (ICMTCE 2009)*, 2009, pp. 8-11.
- [3] G. Chattopadhyay, "Terahertz science, technology, and communication," in *2012 5th International Conference on Computers and Devices for Communication (CODEC)*, 2012, pp. 1-4.
- [4] I. Hosako, N. Sekine, M. Patrashin, S. Saito, K. Fukunaga, Y. Kasai, *et al.*, "At the Dawn of a New Era in Terahertz Technology," *Proceedings of the IEEE*, vol. 95, pp. 1611-1623, 2007.
- [5] T. Masayoshi, "Prospect of terahertz technology," in *2007 19th International Conference on Applied Electromagnetics and Communications*, 2007, pp. 1-4.
- [6] P. H. Siegel, "Terahertz technology in biology and medicine," *IEEE Transactions on Microwave Theory and Techniques*, vol. 52, pp. 2438-2447, 2004.
- [7] D. Adrian, O. Chiko, and K. Kodo, "Terahertz-wave sources and imaging applications," *Measurement Science and Technology*, vol. 17, p. R161, 2006.
- [8] H. J. Song and T. Nagatsuma, "Present and Future of Terahertz Communications," *IEEE Transactions on Terahertz Science and Technology*, vol. 1, pp. 256-263, 2011.
- [9] "Technique of microwave measurements / edited by Carol G. Montgomery. Vol.1," C. G. Montgomery, Ed., ed. New York: Dover : Constable, 1966.
- [10] F.R.Clague, "A calibration service for coaxial reference standards for microwave power," *NIST Technical Note 1374*, May 1995.
- [11] F. R. C. J. W. Allen, N T. Larsen, and M. P. Weidman, "The NIST Microwave Power Standards in Waveguide," *NIST Technical Note 1511*, Feb 1999.
- [12] "Fundamentals of RF and Microwave Power Measurements (Part 1) Introduction to Power, History, Definitions, International," *Agilent Technologies, Application Note 1449-1, 5988-9213N*, April 2003.
- [13] M.P.Weidman, "Direct Comparison Transfer of Microwave Power Sensor Calibrations," *NIST Technical Note 1379*, January, 1996.
- [14] R. Judaschke, "Traceable Metrology for high frequency power in the millimetre-wave range," in *Annex la-JRP-Protocol*, ed, Oct 2012.

- [15] R. A. Ginley, "Traceability for microwave power measurements: Past, present, and future," in *Wireless and Microwave Technology Conference (WAMICON), 2015 IEEE 16th Annual*, 2015, pp. 1-5.
- [16] J. T. Ascroft, "Developments in coaxial power standards at NPL," in *1998 Conference on Precision Electromagnetic Measurements Digest (Cat. No.98CH36254)*, 1998, pp. 619-620.
- [17] J.P.Ide, "The United Kingdom Power Standards Above 40 GHz," *NPL Report DES 105*, December, 1990.
- [18] D. Adamson, J. Miall, J. Howes, M. Harper, and R. Thompson, "A new 75-110 GHz primary power standard with reduced thermal mass," in *75th ARFTG Microwave Measurement Conference*, 2010, pp. 1-4.
- [19] D. B. Adamson, Howes, J, Ridler, N M, "Recent and future developments in millimetre and sub-millimetre wavelength measurement standards at NPL," *Proceedings of the Joint 5th ESA Workshop on Millimetre Wave Technology and Applications and 31st ESA Antenna Workshop*, pp. Noordwijk, The Netherlands, 463-467, 18-20 May 2009.
- [20] K. Shimaoka, M. Kinoshita, K. Fujii, and T. Tosaka, "Design of a broadband calorimeter for mm-wave power standard in the frequency range from 110 GHz to 170 GHz," in *2012 37th International Conference on Infrared, Millimeter, and Terahertz Waves*, 2012, pp. 1-2.
- [21] K. Shimaoka, M. Kinoshita, and T. Inoue, "A broadband waveguide calorimeter for mm-wave power meter calibration in the frequency range from 50 GHz to 110 GHz," in *2012 Conference on Precision electromagnetic Measurements*, 2012, pp. 88-89.
- [22] K. Shimaoka, M. Kinoshita, K. Fujii, and T. Tosaka, "Calibration of mm-wave power meters using a broadband calorimeter in the frequency range from 110 GHz to 170 GHz," in *2013 38th International Conference on Infrared, Millimeter, and Terahertz Waves (IRMMW-THz)*, 2013, pp. 1-2.
- [23] K. Shimaoka, M. Kinoshita, and T. Inoue, "A Broadband Waveguide Calorimeter in the Frequency Range From 50 to 110 GHz," *IEEE Transactions on Instrumentation and Measurement*, vol. 62, pp. 1828-1833, 2013.
- [24] X. Cui, Y. S. Meng, R. Judaschke, J. R uhaak, T. P. Crowley, and R. A. Ginley, "International comparison of WR15 (50 to 75 GHz) power measurements among NIST, NIM, PTB and NMC, A∗STAR," in *2016 Conference on Precision Electromagnetic Measurements (CPEM 2016)*, 2016, pp. 1-2.
- [25] X. Cui, W. Yuan, Y. Li, C. Jia, and Y. S. Meng, "Development of a national WR-10 (75 to 110 GHz) microcalorimeter," in *2016 URSI Asia-Pacific Radio Science Conference (URSI AP-RASC)*, 2016, pp. 478-480.
- [26] C. Ma, X. Cui, W. Yuan, and Y. Li, "Design of a WR-6 thermoelectric conversion power sensor," in *2015 40th International Conference on Infrared, Millimeter, and Terahertz waves (IRMMW-THz)*, 2015, pp. 1-2.

- [27] R. H. Judaschke and J. Rühaak, "Leakage effects in millimeter-wave power transfer standards," in *2016 Conference on Precision Electromagnetic Measurements (CPEM 2016)*, 2016, pp. 1-2.
- [28] J. A. Mallat, S. N. Dudorov, D. V. Lioubtchenko, and A. V. Raisanen, "110-170 GHz Millimetre Wave Power Standard," in *2006 European Microwave Conference*, 2006, pp. 482-485.
- [29] A. N. Akhiezer, A. P. Senko, and V. P. Seredniy, "Millimeter wave power standards," *IEEE Transactions on Instrumentation and Measurement*, vol. 46, pp. 495-498, 1997.
- [30] D. G. Moss, J. R. Birch, D. B. Adamson, B. Lunt, T. Hodgetts, and A. Wallace, "Comparison between free space and in-waveguide power measurement standards at 94 GHz," *Electronics Letters*, vol. 27, pp. 1134-1137, 1991.

Chapter 2

Review of Microwave Power Measurement

The chapter covers the fundamentals of microwave power measurement beginning with definitions, basic concepts and terminologies. It also addresses the main focus of the thesis in the vast field of microwave power measurement. Different techniques of detecting microwave power are discussed. The appropriate technology for a transfer power standard is described in further detail. The important components and operation of the bolometric sensor are reviewed.

2.1. Microwave Power

The term “microwave” is typically used for frequencies between 3 GHz and 300 GHz, with a corresponding electrical wavelength between $\lambda = c/f = 10$ cm and $\lambda = 1$ mm, respectively., where c is the speed of light in vacuum and f is the frequency. Signals with wavelengths on the order of millimetres are often referred to as millimetre waves [1].

Power is the rate at which energy is transferred, used or transformed [2]. The instantaneous microwave power of an electromagnetic field can be defined as [3].

$$P(t) = \frac{1}{2} \text{Re} \{ \mathbf{E} \cdot \mathbf{H}^* \} \quad (2.1)$$

where $\vec{E}(t)$ and $\vec{H}(t)$ are the electric and magnetic fields at a time t and S is the surface over which the power is being measured. In a transmission line, the power can be written by [1].

$$P(t) = V(t) \times I(t) \quad (2.2)$$

where V and I are the voltage and current on the line. In practice, the instantaneous voltage, current and the field distributions cannot be easily measured. Therefore, microwave power is often derived by substitution techniques or by rectification, which is discussed in more detail in the following section.

The SI unit of power is Watt (W) where $1\text{W} = 1\text{kgm}^2\text{s}^{-3}$. For the convenience in presentation and calculation, the power ratio is often expressed in decibels (dB).

$$\text{Power(dB)} = 10 \log \left(\frac{\text{Power level 1}}{\text{Power level 2}} \right) \quad (2.3)$$

Power in dBm is defined as the ratio with respect to 1 mW, that is

$$\text{Power(dBm)} = 10 \log \left(\frac{\text{Power}}{1 \text{ mW}} \right) \quad (2.4)$$

The range of microwave power can be categorised in to three groups: high power (greater than 1W), medium power (10 mW to 1W) and low level (less than 10 mW) [4]. The techniques and equipment of power measurement for different power levels vary significantly. This thesis mainly deals with low level microwave power.

In terms of the power measurement, there are many power quantities that can be defined when looking at sinusoidal or other complex periodic waveforms. Figure 2.1 shows an example of a pulsed waveform, in which there are a number of power measurement that can be performed

such as average power, peak power. The type of power must be determined prior to the measurement to avoid confusion and incompatible results [5]. The most common definitions of microwave power in measurement are average power, pulse power and peak or peak envelope power.

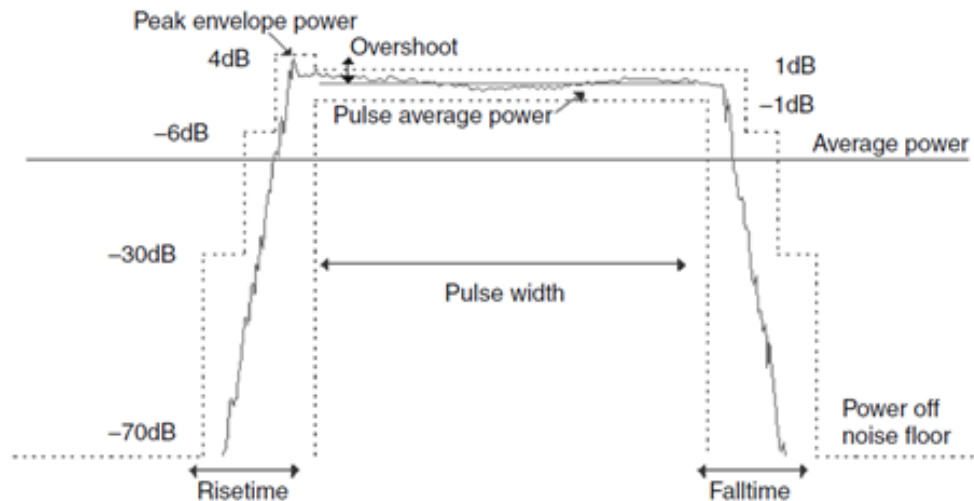


Figure 2.1: GSM pulse specification (taken from [6])

The average power and pulse power are both time-averaged values. The average power can be obtained by averaging the instantaneous power over a long period of time, which is very large compared to the duration of a single pulse and the time interval between successive pulses [4]. For example, the instantaneous power of continuous-waves (CW) are combined by a d-c component and a varying component at twice the frequency of the wave, the average power of the sinusoidal wave is the d-c component which does not vary with time.

The pulse power can be obtained by averaging the power measured over the duration of a single pulse or pulse width τ . The pulse power has been widely used in radar applications [7]. The pulse width is generally considered to be the time between the half-amplitude points on the

rising and falling side of the pulse. Figure 2.2 shows a rectangular pulse with the pulse width τ and the period T , the pulse power P_{pulse} indicates the power averaged within the pulse duration and therefore has a greater amplitude than the average power. A power measurement often determines the average power, but the pulse power can be calculated from the average power as [5].

$$P_{pulse} = \frac{T}{\tau} P_{average} \quad (2.5)$$

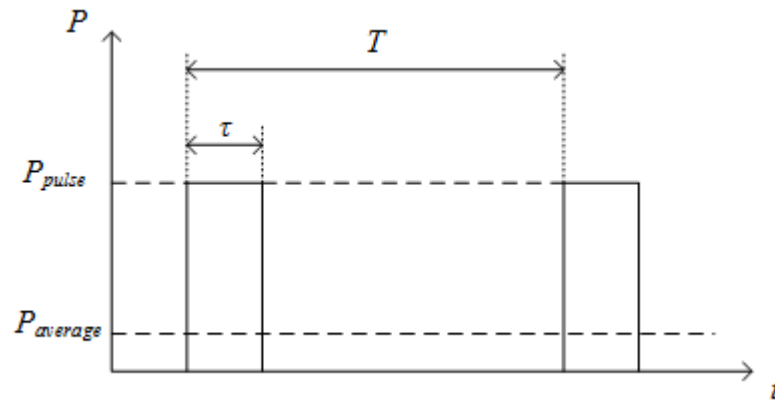


Figure 2.2: A rectangular pulse response with the pulse width τ and the period T .

The last category of microwave power is peak or peak envelope power, which is mainly seen in the measurement of modulated signals. Peak power is referred to the highest power point in the pulse such as the rise time overshoot as shown in Figure 2.1. Certainly more sophisticated measurement is required to determine the peak power [5].

In general, if the pulse shape or the power distribution is known, the pulse and peak envelope power can often be obtained from the average power [8]. This thesis concentrates on determining the average power of CW signals.

2.2. Microwave Power Measurement

This section discusses microwave power measurement in general. Important components and terminologies in the measurement are introduced. The requirements of the measurement equipment are discussed.

The name ‘power detector’ and ‘power sensor’ are usually used interchangeability. For clarity in this thesis, a power detector is referred as a combination of a power sensor and a power meter.

The goal of a power measurement is to characterise the unknown power from some source, for example a generator or an oscillator. The source is often separated from the point of measurement by such components as transmission lines, couplers, amplifiers, etc. It is convenient to consider the equivalent generator output to be the port that is connected to the power sensor. Figure 2.3(a) presents a general power measurement setup, in which the power sensor is attached directly to the output of the generator. The incident power from the output to the power sensor P_i is different from the power generated at the source P_g due to the non-zero reflection coefficient Γ_g of the generator. Also, the total of the dissipated power in the sensor (or load) P_d and the reflected power P_r from the sensor, due to the reflection coefficient Γ_l of the load, should be equal to the incident power P_i , that is

$$P_i = P_d + P_r \quad (2.6)$$

The power meter is the auxiliary circuit to measure the dissipated power P_d , giving the measured power P_{meas} . The measured power P_{meas} is then corrected in order to provide the power reading P_{rdg} which should be equal to the incident power P_i to the sensor. It should be noted that the

measured power P_{meas} is not often equal to the dissipated power P_d in the sensor; this will be discussed later in the chapter. The discussion on power meters can be found in section 2.4.3.

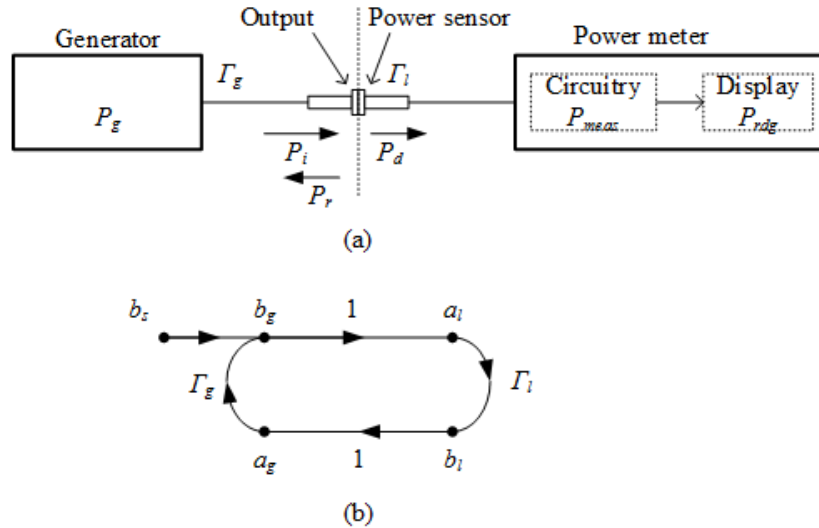


Figure 2.3: (a) The power measurement setup in which a power sensor is connected directly to the output of the generator; (b) the signal flow graph of the measurement setup [9].

It is convenient to analyse the power flow between the generator and the sensor in Figure 2.3(a) by an equivalent signal flow-graph in Figure 2.3(b). The variables a and b are proportional to the voltage of the incident wave and the reflected wave, respectively. The subscript l is for the sensor variables, and the generator variable is denoted by subscript g . The variable b_s presents the wave which is internally generated by the generator. The quantities of the variables are normalised so that the relationship between them and the powers can be expressed by the following equations

$$P_i = |a_i|^2 \quad (2.7a)$$

$$P_r = |b_i|^2 \quad (2.7b)$$

$$P_g = |b_s|^2 \quad (2.7c)$$

The signal flow graph shows the effect of mismatch at both the generator and the sensor. The incident wave to the sensor is reflected back to the generator. The reflected wave is then re-reflected and combines with the power created by the source to generate a new incident wave. The process continues until the convergence happens. The incident wave to the sensor can be written as

$$a_l = b_g = b_s + \Gamma_g a_g \quad (2.8)$$

The reflected wave from the sensor is

$$b_l = \Gamma_l a_l = a_g \quad (2.9)$$

Solving the equation 2.8 and 2.9 for the powers in equation 2.7, we have

$$P_i = P_g \frac{1}{|1 - \Gamma_g \Gamma_l|^2} \quad (2.10a)$$

$$P_r = P_g \frac{|\Gamma_l|^2}{|1 - \Gamma_g \Gamma_l|^2} \quad (2.10b)$$

Hence, the dissipated power in the sensor is

$$P_d = P_i - P_r = P_g \frac{1 - |\Gamma_l|^2}{|1 - \Gamma_g \Gamma_l|^2} \quad (2.11)$$

If the sensor reflection coefficient Γ_l is zero or is impedance matched, the power dissipated in the sensor will be equal to the power generated by the source which is also equal to the incident power P_i to the sensor.

$$P_{Z_0} = P_d \Big|_{\Gamma_l=0} = P_g = P_i \quad (2.12)$$

There also is a second case of interest when $\Gamma_l = \Gamma_g^*$, meaning the reflection coefficient looking toward the sensor is the complex conjugate of the reflection coefficient looking toward the generator. The dissipated power in this case is

$$P_{av} = P_d \Big|_{\Gamma_l=\Gamma_g^*} = \frac{P_g}{1-|\Gamma_g|^2} \quad (2.13)$$

The second case is called conjugate matching. It can be easily seen that the dissipated power in the case of conjugate matching is greater than the power created by the generator, the power is defined as the maximum available power P_{av} [9].

It should be noted that although the magnitudes of the reflection coefficient of the sensor and the generator can be measured or specified, whereas the determination of the phases is often omitted [10]. In practice, the impedance matching condition is mostly used because it can provide the true generated power of the source and the measurement does not depend on the corrections of Γ_l and Γ_g . As a result, zero reflection coefficient sensor is the main challenge in the power sensor design.

When a non-matching condition happens, the generated power can be calculated from the incident power by equation 2.10a as

$$P_g = P_i |1 - \Gamma_g \Gamma_l|^2 \quad (2.14)$$

The reading P_{rdg} from the power meter should be always equal to the incident power P_i , hence the source power can be obtained from the reading as

$$P_g = P_{rdg} |1 - \Gamma_g \Gamma_l|^2 \quad (2.15)$$

Equation 2.15 shows the determination of the source power from the output of the power meter. However, the equation cannot be exactly calculated because of the lack of phase information of Γ_l and Γ_g [9]. On the other hand, its maximum and minimum values can be obtained by the magnitudes of the reflection coefficient as follows

$$P_g = P_{rdg} \left(1 \pm |\Gamma_g| |\Gamma_l|\right)^2 \quad (2.16)$$

For small mismatch such as $|\Gamma_g| |\Gamma_l|$ less than 2%, equation 2.16 can be approximated as

$$P_g = P_{rdg} \pm 2P_{rdg} |\Gamma_g| |\Gamma_l| \quad (2.17)$$

The second term of equation 2.17 indicates the mismatch uncertainty of $200|\Gamma_g| |\Gamma_l|%$ when making a power measurement [6]. Note that the mismatch uncertainty contributes for 50% of the total error in power measurements that also explains why zero reflection coefficient is desired. In the next section, the techniques of realising the microwave power sensors are discussed.

2.3. Techniques of Sensing Microwave Power

There are a variety of power sensor technologies for detecting and characterizing microwave power. As discussed in section 2.1, the determination of microwave power from the fundamental definitions is not feasible. The measurement, therefore, can be done by transforming the microwave power to such quantities as d-c voltage (or current) and temperature [11], electro-mechanical force [12, 13], and Hall effect [14, 15] which can be easily

quantified. The first technique based on rectification or heating effect are suitable for scaling to millimetre wavelengths and are widely used in microwave power measurement [16]. In general, there are three popular types of power sensors, using the techniques namely, diode sensors, thermoelectric sensors and bolometric sensors [10]. The diode sensors are based on the rectification characteristic and the last two sensors are thermal sensors. The following sections provide detail of the principle and the application of each power sensor type.

2.3.1. Diode sensors

The principle of diode detectors is based on the rectification properties of the p-n junction which can convert a-c signals to d-c signals. The low barrier Schottky diode is widely used as they are very rugged and consistent from diode to diode at microwave frequencies [10]. The i - v characteristic of the Schottky diode can be written by the diode law [17]

$$i = I_s (e^{\alpha v} - 1) \quad (2.18)$$

where i is the diode current, v is the voltage across the diode, I_s is the saturation current and $\alpha = q/nKT$. K is the Boltzmann's constant, T is the absolute temperature, q is the charge of an electron and n is a correction constant (n is usually equal to 1.1 for the devices in the power sensing application) [10]. The nonlinear current-voltage curve of a Schottky diode is shown in Figure 2.4(a). For low level of voltage, equation 2.18 can be mathematically expanded.

$$i = I_s \left(\alpha v + \frac{(\alpha v)^2}{2!} + \frac{(\alpha v)^3}{3!} + \dots \right) \quad (2.19)$$

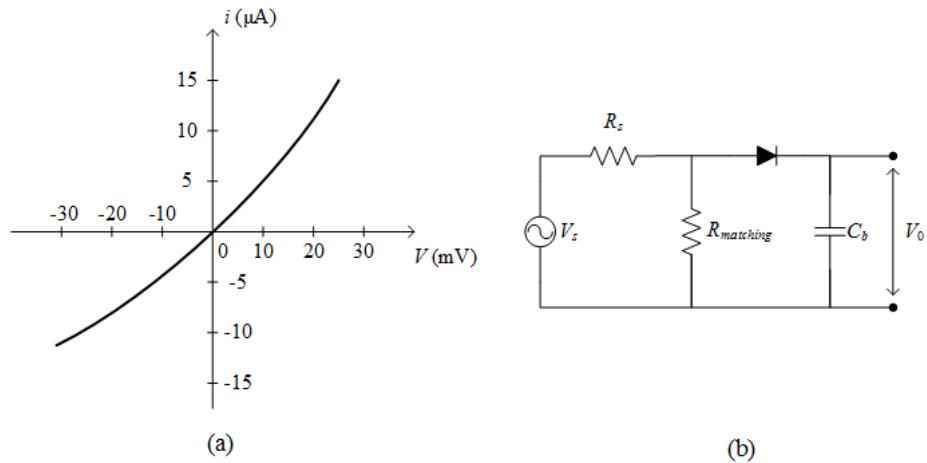


Figure 2.4: (a) The junction rectifying characteristic of a low barrier Schottky diode, showing the small signal, square law characteristic around the origin; (b) circuit diagram of a source and a diode detector with matching resistor [10].

The second and other even order terms of the series provide the rectification. For small signals, the second term is significant so that the diode is operating in the square-law region. In that region, the output i is proportional to microwave input voltage squared. A typical low barrier Schottky diode requires a microwave signal of -20 dBm to overcome the 0.3 V junction voltage [5]. Therefore, the square law operation is suitable for signals with the maximum power of -20 dBm.

Figure 2.4(b) shows a simplified circuit diagram of an unbiased diode device for detecting low level r-f and microwave signal. The matching resistor $R_{matching}$ acts as the termination for the microwave source. The diode rectifies microwave voltage to d-c voltage, and the bypass capacitor C_b is used to remove any microwave signal that leaks through the diode. The design would detect the signal from the noise level of -70 dBm to about -20 dBm [5]. Diode detectors can offer sensitivity and a large dynamic range, they can substitute the thermal sensors within their square-law regions. However, if the incident signal power has spikes which exceed the square-law range, data errors will occur.

The diode technology can also be used to measure peak or peak envelop power due to the fast response characteristic. Modern peak and average diode sensors can operate in a wider dynamic range compared to the previous diode technology. In general, diode sensor technologies are the ideal solution for characterizing pulse waveform envelopes or complex time-dependent signals [10].

2.3.2. Thermoelectric sensors

Thermoelectric sensors are based on the principle of the thermocouples. A metal rod with different temperatures at the two ends can generate a voltage called Thomson electromotive force due to the diffusion of electrons from their parent atoms [18]. The same principle applies at a junction of dissimilar metals where different free electron densities in the two metals give rise to diffusion and an electromotive force. The output voltage of thermocouple is the total of several thermoelectric voltages generated along the two-metal circuit as shown in Figure 2.5(a).

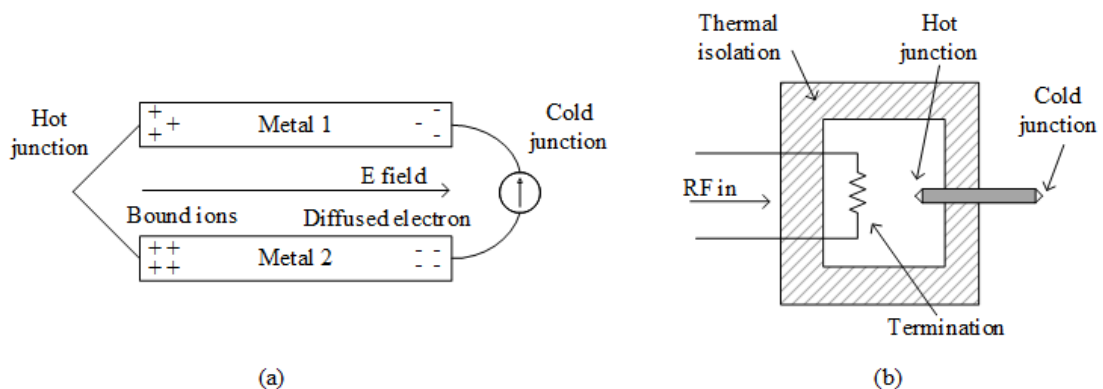


Figure 2.5: (a) the thermocouple consisting of two different metals [10]; (b) the simplified diagram of a thermocouple detector (taken from [5]).

Figure 2.5(b) show a basic circuit of a thermoelectric detector. The termination is heated up by the incident microwave power. The heat energy is transferred to the thermal couple, a hot junction is then created. The voltage, generated by the thermocouple, can be used to determine the amount of microwave power applied.

The determination of power by thermocouples exhibits high sensitivity with a square-law detection characteristic. The dynamic range of the thermoelectric sensors is from -35 dBm to +20 dBm [10]. Since the thermocouples are heat-based, they are used to measure the average power.

2.3.3. Bolometric sensors

The last category discussed here is bolometric sensor which has a historically important position in r-f and microwave power measurements as it is a true average power sensor. This type of sensors is linear, sensitive, accurate and very robust. The functional diagram of a typical bolometer and its auxiliary circuit is shown in Figure 2.6.

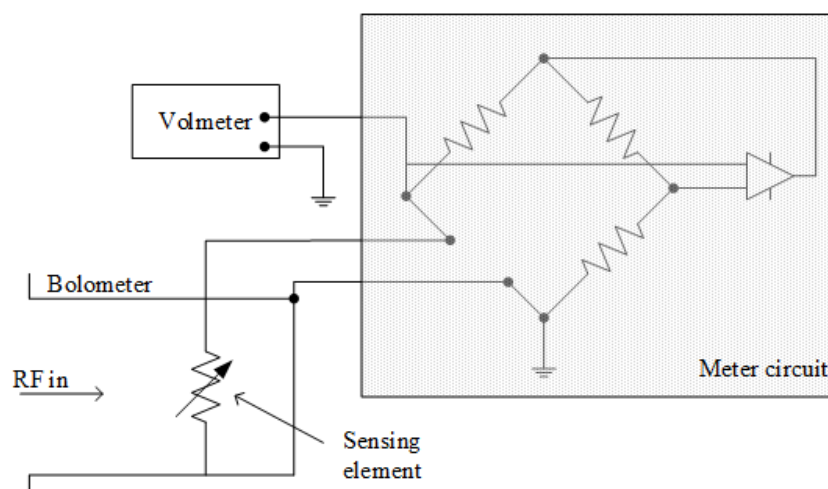


Figure 2.6: Functional diagram of a bolometric sensor and its power meter [5]

Bolometers were first developed to measure the infrared power and are now widely used in microwave power measurements [19]. The sensing element of the bolometer is capable of dissipating the incident microwave power and then turning the heat into a change in resistance [4, 20, 21]. By measuring the change in resistance, the amount of applied microwave power can be determined. In other words, the determination of microwave power is replaced by a d-c measurement. The substitution of the microwave power to the d-c power is performed by the meter circuit which is discussed in more details in section 2.4.3.

Historically, there are two popular types of bolometer, namely, barretters and thermistors. A barretter is an appropriately mounted short length of a very fine thin wire, usually platinum, with its length and diameter giving suitable resistance. As the resistance increases when the barretter experiences the rise in temperature, the barretter is said to have positive temperature coefficient (PTC). A thermistor, as the name suggests, is an electronic component in which the resistance changes with its body's temperature. A thermistor can have either positive temperature coefficient (PTC) or negative temperature coefficient (NTC), both types are ideal for sensor applications. In microwave measurement, NTC thermistors are preferred over barretters, because they can offer smaller sizes and better power handling [22].

Bolometric sensors are the most common type of detectors in the range of -10 dBm to +10 dBm. Their sensitivity, in Ohm per milliwatt, is independent of frequency [4].

2.3.4. Discussion on measurement techniques

Each type of the above sensors has its strengths and weaknesses. The diode technology can offer a widest dynamic range of 1 nW to 100 mW, and diode coaxial sensors are available up

to 50 GHz [6] and up to 1.1 THz for wave guide sensor as reported by Erickson power sensor. The thermoelectric sensors have slightly higher accuracy over a smaller power range from 1 μ W to 100 mW, the coaxial type of this sensor is available up to 110 GHz and the commercial waveguide thermoelectric sensor can work up to 260 GHz [23]. The bolometric power sensor has the smallest range from 10 μ W to 10 mW, this type of sensor has been reported in the coaxial and waveguide design up to 140 GHz [24].

Power measurements with thermocouples and Schottky diodes are called open-loop, since there is no feedback to correct for different sensitivities due to aging or temperature, or the differences between sensors [10]. As a result, the output voltages of the sensors could be different for the same r-f or microwave power. The problem can be solved by incorporating power reference oscillator whose output power is controlled very accurately. However, the reference power requires a special injection configuration i.e. waveguide to coax adapter, which can increase the overall reflection coefficient of the sensor and increase the uncertainty in the measurement [8].

On the other hand, the measurement with bolometric sensor and its meter circuit is closed-loop, as the change in resistance of the sensing element in Figure 2.6 triggers the feedback signal to the r-f to d-c power substitution so that the resistance is kept constant. The close-loop measurement is discussed in more detail in section 2.4.3 The power detection principle, rather than rectifying diode or direct heating of thermocouple, is compatible with existing calorimetric methods [25]. In the next section, the bolometric sensors are discussed in greater detail as they are the sensor of choice for the power transfer standards and the work in this thesis.

2.4. Bolometric Sensors for Microwave Power Measurement

The structure of the bolometric sensor can be seen in Figure 2.6. The important components of the sensor type including the sensing element and the accommodating structure of the bolometer element are discussed further in this section. The meter circuits are presented and the operation of the sensor is described. Finally, the calibration of the bolometric sensor is also introduced.

2.4.1. The sensing elements

As briefly discussed in section 2.3.3, the bolometer element is a temperature sensitive resistor. There are two major categories of the resistor, namely Negative Temperature Coefficient (NTC) and Positive Temperature Coefficient (PTC). Traditionally, thermistor is referred to the first group and the second group is often known by the name of barretter.

Negative Temperature Coefficient (NTC) thermistor

The NTC thermistors consist of a polycrystalline sintered ceramic made from the mixture of metal oxides such as manganese, nickel, cobalt, iron, copper and titanium [22, 23, 26-29]. In term of construction, commercial NTC thermistor can be categorized into two groups, namely, bead type thermistor (i.e. bare beads, glass coated beads, ruggedized bead, miniature glass bead, glass probes, glass rods, bead-in-glass enclosure) and metallized surface contacts for surface mounting (i.e. disks, chips, surface mount, flakes, rods, washers) [30]. In microwave power measurement, the bead type thermistors are commonly used.

In general, the resistance of NTC thermistor can be expressed by Steinhart-Hart equation [31].

$$R_T = R_0 \exp\left(B\left(\frac{1}{T} - \frac{1}{T_0}\right)\right) \quad (2.20)$$

where R_T is the resistance of the thermistor at the body temperature T (K), R_0 is the resistance at the nominal operating temperature T_0 (K), B constant of a commercial thermistor is often about 2000-5000 K [29, 32, 33].

The temperature sensitivity coefficient α can be obtained by differentiating equation 2.20 [29]

$$\alpha = \frac{1}{R} \frac{dR}{dT} = -\frac{B}{T^2} \quad (2.21)$$

The negative sensitivity coefficient indicates the decrease in the thermistor resistance with the rise in temperature.

Another characteristic of thermistor can be described by the thermal dissipation constant δ . When the dissipated power P is spent to rise the thermistor's temperature from ambient temperature T_0 to temperature T , the dissipation constant is given by [34].

$$\delta = \frac{P}{T - T_0} \quad (2.22)$$

Equation 2.20 can be re-written by substituting T from equation 2.22 to present the relationship between the thermistor resistance R_P and the dissipated power P as [4]

$$R_P = J \exp\left(\frac{B}{T_0 + \delta P}\right) \quad (2.23)$$

where $J = R_0 \exp(-B/T_0)$.

The sensitivity of the devices, expressed in Ohm per milliwatt, is of interest. The sensitivity of a thermistor sensor is defined as the rate of change in resistance with respect to the change in the applied power. Mathematically, it can be written as

$$\frac{\delta R}{\delta P} = \frac{\delta R}{\delta T} \div \frac{\delta P}{\delta T} \quad (2.24)$$

The first term of the equation can be obtained by differentiating equation 2.20, and the second term is approximately equal to the dissipation constant in equation 2.22. Sensor sensitivity is indicated from the curve of d-c resistance plotted against power for the detector. In practice, NTC thermistors process a very high sensitivity of about 10 to 50 Ω/mW [23, 35].

Positive Temperature Coefficient (PTC) barretter

The wire barretter discussed in section 2.3.3 is the first PTC element which was used in the power detection before the arrival of NTC thermistor [4, 23, 36]. Compared to the thermistor the wire barretter is very fragile and can be burnt out easily. The production and development of this sensing element was therefore limited.

The recent development in thin film technology has enabled the use of barretter in the form of metallic thin films. The thin film can be mounted easily to coaxial or waveguide structure, and the performance of the thin film is also more robust than its predecessor. Coaxial film bolometers were developed for the application up to 18 GHz [37-39]. Waveguide film bolometers can work up to 94 GHz [40-46].

The material of the resistive film can be platinum, nickel or nichrome. In general, the resistance of the thin films can be expressed with respect to the temperature by Callender Van-Dusen equation [47, 48].

$$R_T = R_0(1 + AT + BT^2 - 100CT^3 + CT^4) \quad (2.25)$$

where R_T is the resistance at temperature $T(^{\circ}\text{C})$, R_0 is the resistance at nominal temperature of zero degree Celsius, A, B and C are thermal material constants. For a platinum thin film, the constants are as follows [48],

$$A = 3.908 \times 10^{-3}$$

$$B = -5.775 \times 10^{-7}$$

$$C = -4.183 \times 10^{-12}$$

In this case the, value of C is negligible, equation 2.25 is often presented in the second order of temperature T .

The dissipation constant δ and the sensor sensitivity can be defined for the thin film element in the same manner as in equation 2.22 and equation 2.24. The sensitivity of a thin film bolometer is considerably smaller than that of the NTC thermistor sensor and is in the order of 1 to 3 Ω/mW [45, 46].

2.4.2. The bolometer mount

The bolometer mount, or microwave transmission line housing, is probably the most difficult problem in utilizing bolometric equipment for microwave power measurement. Most of the

information in the literature is devoted for thermistor mount, but the general specification of bolometer mount should be the same regardless of the sensing element type. The essential requirement of the mount is that its impedance should be closely matched to the characteristic impedance of the transmission line as discussed in section 2.2. It is obvious that when the mount is matched exactly to the transmission line at a specified frequency, the most accurate and sensitive possible power determination can be performed. However, accuracy and sensitivity are more often sacrificed for convenience in the operation over a broad frequency band and compensated by the development of the power meter discussed in the next section. In other words, it demands a detector mount having a broadband impedance match. It also requires that the minimum microwave leakage from or into the mount. In particular, for absolute microwave power measurement, the mount should not have any sources of power dissipation other than the thermistor [4].

Thermistor mounts can be classified as un-tuned mounts, fixed-tuned mounts and tuneable mounts. An un-tuned thermistor mount is designed so that the mount is satisfactorily impedance matched over a specific frequency band with no adjustable tuning element needed. A fixed-tuned mount is one which incorporates tuning adjustment. The mount can offer a nearly perfect matching at mid-band frequency by tuning, a degree of mismatch at the band edge can also be provided. Fixed-tuned mounts are commonly used at the frequency of 10 GHz and 30 GHz, while un-tuned mounts are more common at 3 GHz and lower frequency band where the variations in the impedances of thermistors are relatively small. Tuneable thermistor mounts are very similar to the fixed mount, except that the tuning is specified for optimum impedance match at each frequency. Tables of calibration data are provided to facilitate mount settings at each measurement [4].

Both coaxial-line and waveguide mounts have been used. While the former is used for centimetre wave range of frequency, the latter is more common at millimetre wave range. The following section reviews some designs for each type of transmission line.

Co-axial cable mounts

There are many techniques available for creating broadband impedance matching in co-axial transmission line. The design principle is particularly applicable at long wavelengths where the reactive component of the thermistor impedance is small and relatively frequency insensitive. Figure 2.7 shows a simple diagram of the construction of a coaxial thermistor mount.

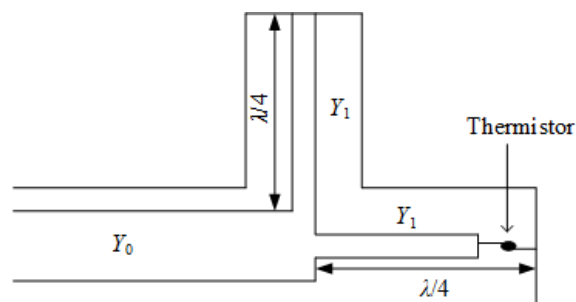


Figure 2.7: Diagram of a coaxial thermistor mounts[4]

A stub and a series transformer section, each $\lambda/4$ in length, are used to match the thermistor to the transmission line. The impedance matching between the thermistor conductance and the characteristic admittance Y_0 at the centre frequency is achieved by the series transformer. The quarter wavelength stub has no effect on the input impedance of the mount at the centre frequency. For broadband use, the admittance Y_1 of both the stub and the transformer can be slightly adjusted from the mid-band matching value, in order to cancel reflections at frequencies other than the mid-band frequency. The detailed calculation is given in [4]. A number of variations on the stub-transformer matching technique have been developed. For instance, the

distance from thermistor to the short circuit can be adjusted by using an end-plunger adjustment as an additional variable in finding impedance matching. In addition, using a line taper as transformer section, as shown in Figure 2.8, could be expected to obtain a broadband impedance match.

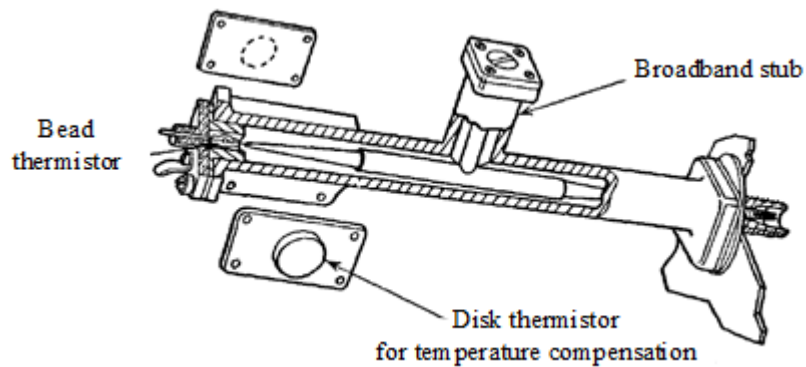


Figure 2.8: The co-axial thermistors mount with line taper as transformer section (Taken from [4]).

This design was adopted for housing thin film element in coaxial transmission line and Figure 2.9 shows the structure of a coaxial film bolometer developed by Harris [39]. Here a gold film is used in conjunction with a conical sheath to achieve a uniform power absorption along the length of the resistor.

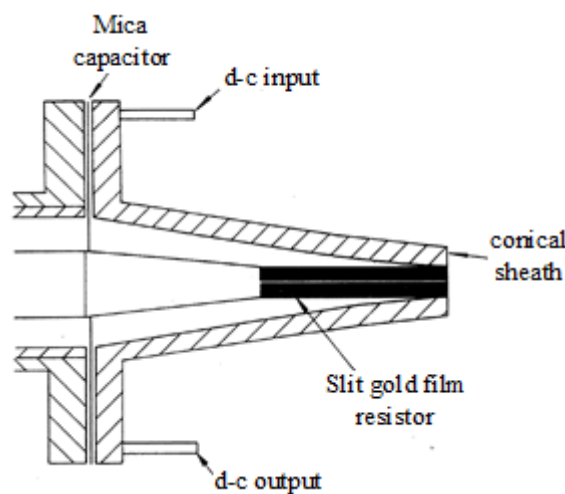


Figure 2.9: A simplified diagram of coaxial gold film bolometer (taken from [23])

Waveguide mounts

In general, a thermistor mount is installed in parallel with the electric fields in the waveguide. The position is usually in the middle of the guide where it can experience the maximum electric field. Figure 2.10 represents the schematic drawings of two designs of waveguide thermistor mounts. The lead wires from the thermistor are usually brought out through co-axial stubs. In other words, there is transition from waveguide to co-axial cable constructed on the waveguide body. One lead from the thermistor wire is grounded to the waveguide, and the other is isolated from the waveguide and used for the d-c or low frequency signal. The waveguide is terminated by a short circuit placed at an appropriate distance from the thermistor [4].

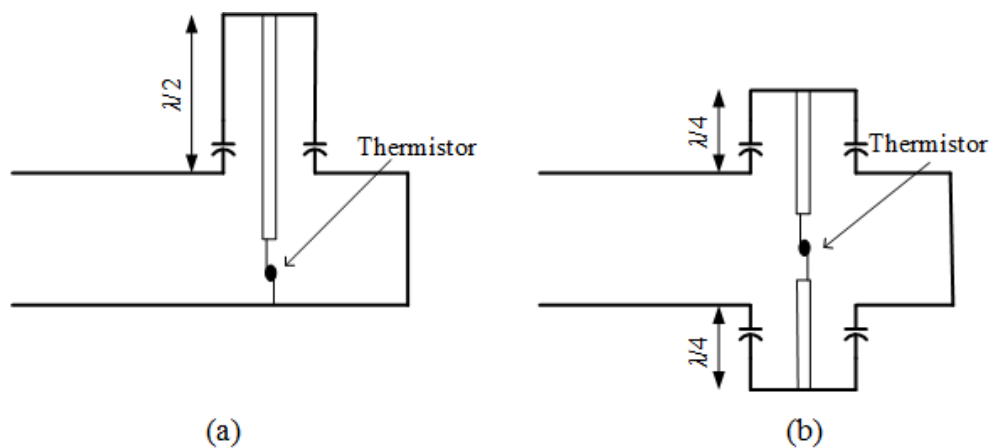


Figure 2.10: Schematic diagram of two fixed-tuned designs of rectangular waveguide thermistor mounts, the capacitor symbols present the d-c open circuit and r-f short circuit [4].

The mount in Figure 2.10(a), developed by the MIT Radiation Laboratory [49], uses an adjustable stub and an adjustable end-plunger for the waveguide short circuit. The $\lambda/2$ stub represents a short circuit to the thermistor. In the other design in Figure 2.10(b), a single stub is replaced by two $\lambda/4$ stubs which provide an open circuit to the thermistor. The latter design, developed by Bell Telephone Laboratories [50], uses one adjustable stub and an adjustable

waveguide shorting plunger [4]. In both mount designs, the objective is to compensate the change in reactance of the short circuit of the waveguide over a broadband of frequency in order to maintain matched mount impedance. By using the combination of the stub characteristic impedance, the stub length and the short circuit length, a solution for narrow-band and/or broadband matching could exist. Practical designs can be found in [4], the devices operate up to 24 GHz with reflection coefficient of about -15 dB for the bandwidth of 4% centre frequency.

Other techniques in matching the mount of both thermistors and barretters to the waveguide have been developed. Aslan's work [51] is one example, he presented a mount design which uses a ridge to match the waveguide impedance to the thermistor impedance, rather than trying to match the mount impedance to the waveguide impedance, as presented in Figure 2.11.

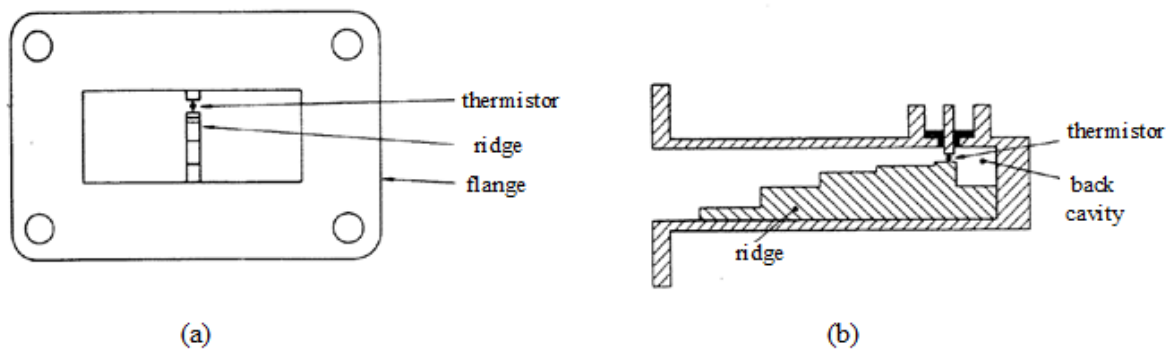


Figure 2.11: Ridge waveguide type of thermistor mount (a) front view and (b) cut side view (taken from [23])

Another design employing the waveguide thermistor mount in the form of bar and post in the centre of, and parallel to, the electric field is shown in figure 2.12. The location and the size of the post and bar are designed to present impedance match to the shorted waveguide section. This arrangement provides broadband impedance matching of the mount [35]. The structure

should follow the same principle discussed later in this thesis. Although it is not considered here, the design process still can be applied.

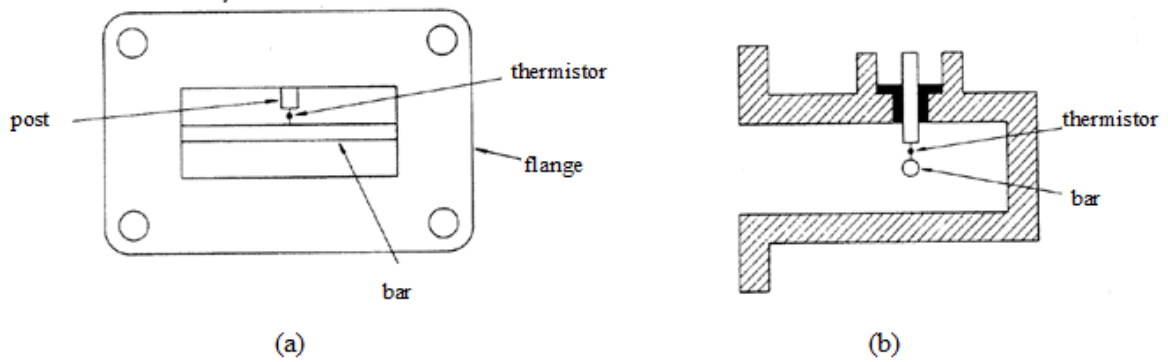


Figure 2.12: Bar and post type of waveguide thermistor mount (a) front view and (b) cut side view (taken from [23])

The mount of a thin film barretter can be applied in the same manner as the thermistor mount. A waveguide transverse film bolometer mount was developed by Lane [40, 41, 43] in which both platinum and nickel films have been positioned on the transverse plane at the appropriate distance to the shorted end of the waveguide. This is shown in Figure 2.13.

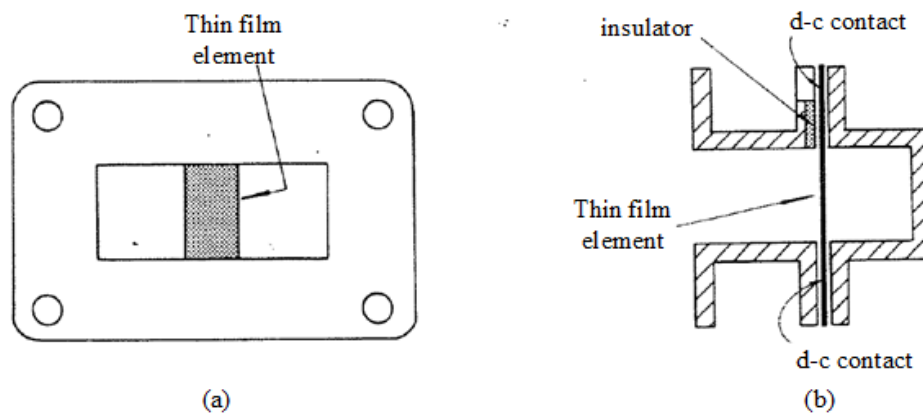


Figure 2.13: Transverse thin film bolometer mount in rectangular waveguide (a) front view and (b) cut side view (taken from [23])

This type of bolometer has been used to measure absolute microwave power up to 94 GHz [46]. The mount provides a narrow band response, for example, the reflection coefficient of better than -20 dB can be obtained from 8.8 GHz to 9.8 GHz in one of the Lane's X-band waveguide designs [43].

2.4.3. Meter circuits

In microwave power measurements, bolometer operation is monitored and regulated by a power meter circuit as shown in Figure 2.6. The circuit not only maintains the sensing element in the sensible resistance range of the mount operation, but also extracts the changes, providing meaningful reading of absorbed microwave power. Conventionally, the sensing element (barrettes or thermistors) is operated as one arm of Wheatstone bridge as shown in Figure 2.14.

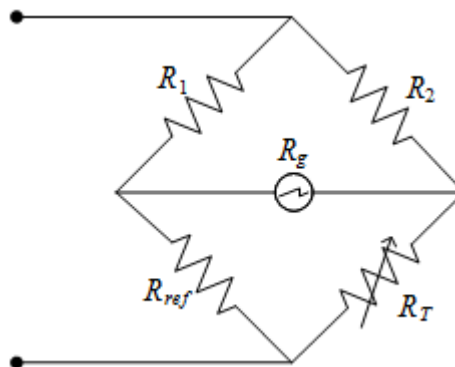


Figure 2.14: A simple Wheatstone bridge for bolometer operation, where R_1 and R_2 are the bridge resistance and often equal, R_g is the ammeter resistance, R_{ref} is the reference resistance to set the operating value of the bolometer element resistance R_T .

The development of the bias and measurement circuit has gone through a major evolution from the early bridge such as a simple Wheatstone bridge, to automatically balanced circuit with increasing dynamic ranges. The Wheatstone bridge is a fundamental circuit used to operate the bolometer elements, and most of the modern circuits still work based on its principle.

The bridge can function either as un-balanced (direct-reading) or balancing bridges. The direct reading bridge [4, 52] is more convenient to use, but the balancing bridges have an advantage of greater accuracy. The close-loop measurement can be described by the diagram in Fig 2.15. The operation of the balancing bridge and the bolometer element is straightforward. Initially, in the absence of microwave power, d-c power is supplied so that the resistance of the bolometer element is biased to the operating value R_0 . Once the d-c equilibrium is established, microwave power is applied. The sensing element is heated up by the absorbed power, and the resistance reduces in the case of thermistor (or increases in the case of barretter). As a result, the bridge is un-balanced. The balance is then restored by removing enough d-c power so that the element resistance returns to the original value R_0 .

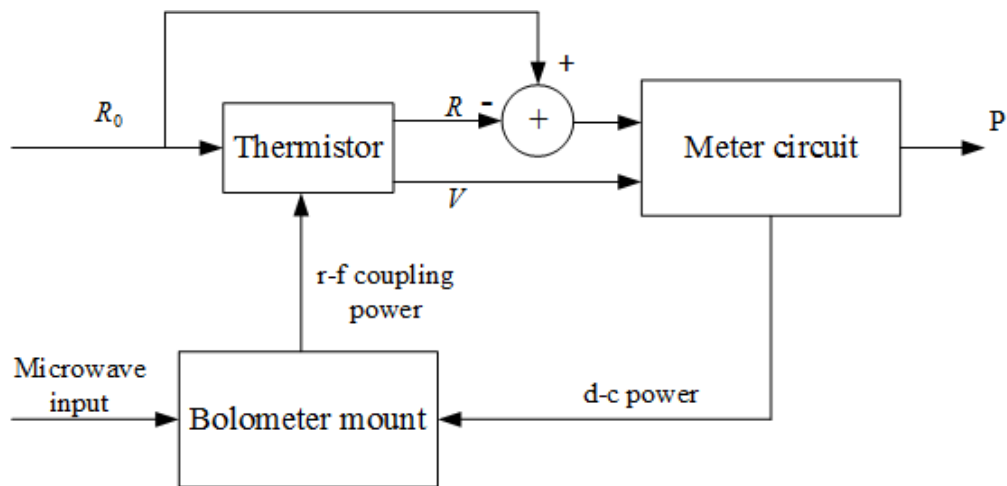


Figure 2.15: The close-loop measurement of bolometer with balancing circuit.

The amount of incident microwave power can be determined by measuring the change in d-c power. The measurement is called closed-loop. For the setup in Figure 2.6, the d-c substitution power can be calculated as

$$P_{sub} = \frac{V_{off}^2 - V_{on}^2}{R_0} \quad (2.26)$$

where V_{on} and V_{off} is the d-c bias voltage across the sensing element with and without microwave power applied, R_0 is the operating resistance of the bolometer.

Studies of the d-c bridge have been conducted investigating the effect of external factors in the measurement such as ambient temperature, and have been presented by Aslan in [51, 53]. The bridge circuits have been developed for both types of the microwave power sensor including coaxial type and waveguide type [54-57]. Historically, the auto-balanced bridge circuits were designed for the dual thermistor coaxial mount, in which the two 100 Ω thermistors appear in parallel to the r-f signal (to be matched with 50 Ω transmission line) but in series to d-c signal [23], the 200 Ω operating resistance of the bridge became popular. The operating resistance of waveguide bolometer mount was then conveniently chosen at the same value. The modern bridge circuits and commercial meters are designed to operate at different resistance such as 50 Ω , 100 Ω , 150 Ω , 300 Ω and 400 Ω [58, 59].

Another design of the auto-balancing circuit was introduced by Larsen and also known as NIST Type IV power meter [60]. Unlike its predecessors, the balancing circuit is not a self-balancing Wheatstone bridge. Instead, it passes a current through the bolometer mount while sensing the voltage across it in such a way that the resistance of the bolometer is defined at the d-c terminals of the bolometer. The resistance is maintained at a reference resistance which can be switched between 100 Ω and 200 Ω . The Type IV Power Meter is a standards laboratory quality instrument used to measure accurately high-frequency or microwave power in terms of substitution d-c power [61].

Later in the thesis, the microwave power measurement is conducted with the use of the auto-balancing circuit based on Larsen's design.. The circuit is available at National Physical Laboratory and easy to re-configure to operate at arbitrary operating resistance. Moreover, the

bridge can work equally well with both NTC and PTC elements by simply interchanging the bolometer element and the reference resistor [60].

2.4.4. Bolometer Calibration

As discussed in section 2.2, the measured power P_{mea} is the result of the measurement of the dissipated power P_d by the meter circuit (in section 2.4.3). For a bolometric sensor, the measured power P_{mea} is the d-c substitution power P_{sub} in equation 2.26. In an ideal power detector, the incident power P_i , dissipated power P_d and the substitution power P_{sub} would be equal. However, no detector is perfect. In order to accurately find the incident power to the sensor, it is necessary to calibrate the detector. The calibration also ensures the traceability of the detector to the power standards [62]. In general, there are two terms which are determined in a calibration process, namely, effective efficiency and calibration factor.

The effective efficiency η_e of a detector is defined as the ratio of the power determined by the electronics of the power meter P_{sub} to the power dissipated in the sensing element P_d [9]

$$\eta_e = \frac{P_{sub}}{P_d} \quad (2.27)$$

The calibration factor k_b is defined as the ratio of the substituted power P_{sub} to the incident power P_i [9]

$$k_b = \frac{P_{sub}}{P_i} \quad (2.28)$$

From equation 2.10a and equation 2.11, the relationship between the calibration factor and the effective efficiency can be written as

$$k_b = \eta_e (1 - |\Gamma_l|^2) \quad (2.29)$$

The calibration factor is considered more general than the effective efficiency as it accounts for both imperfection in the detection of dissipated power and the mismatch loss of the bolometer mount. It should be noted that the definitions are applicable for diode and thermoelectric detectors with the substitution power P_{sub} being replaced by P_{mes} .

The determination of the two factors can be performed by using a micro-calorimeter, which is ultimately traceable to the primary standard of microwave power. More details of the technique can be found in [5, 23, 63, 64]. For lower level of traceability i.e. commercial standards or laboratory uses (see Figure 1.1), multi-state reflectometers can be used to calibrate waveguide sensors [65] as shown in Figure 2.16.

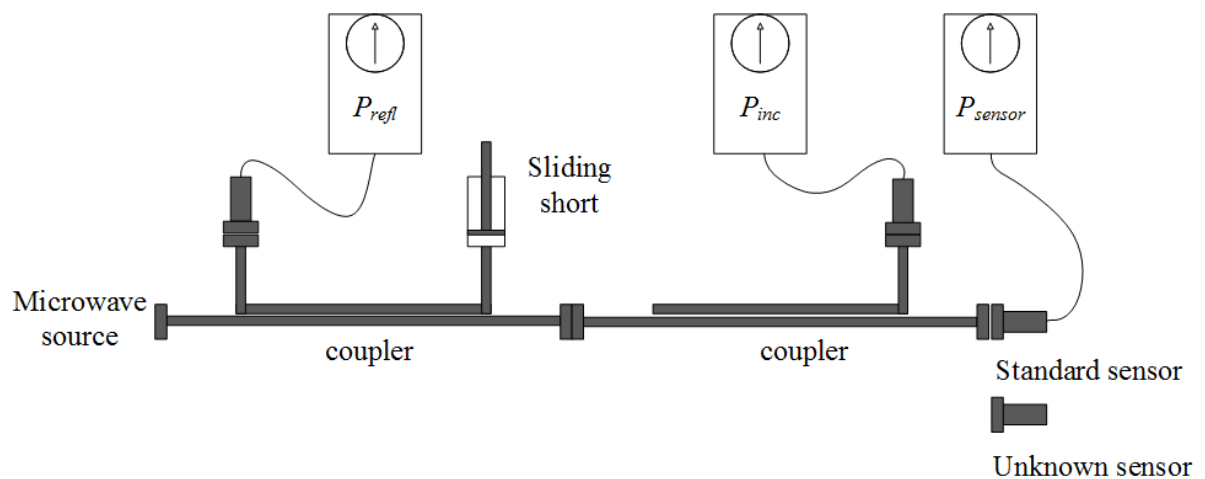


Figure 2.16: Functional diagram of a multistate reflectometer at National Physical Laboratory

In this case, the complex reflection coefficient of the unknown sensor can be determined at the same time as taking necessary power ratios to calibrate the device allowing mismatch correction to be made. The multistate reflectometer is also suitable for comparing the efficiencies of power sensors. The effective efficiency of a standard sensor is determined by a micro-calorimeter. The effective efficiency of the unknown sensor can be obtained by the relative efficiency with respect to the standard sensor. The calibration factor k_b can then be calculated from the reflection coefficient and the effective efficiency by equation 2.29. In practice, a number of standard sensors are used, therefore, the more accurate values of k_b and η_e are averaged from the comparisons. The technique is applicable at any frequency band for which suitable standards are available.

At National Physical Laboratory, multistate reflectometers using three states and four known standard sensors are used for the commercial service of waveguide bolometric sensor calibrations between 8.2 GHz and 110 GHz [66]

References

- [1] D. M. Pozar, "Microwave engineering / by David M. Pozar," 4th ed. ed. Hoboken, N.J.: Wiley, 2012.
- [2] D. Halliday, "Fundamentals of physics / David Halliday, Robert Resnick, Jearl Walker. Vol.2," R. Resnick and J. Walker, Eds., 6th ed., extended. ed. New York: Wiley, 2001.
- [3] S. Ramo, "Fields and waves in communication electronics / Simon Ramo, John R. Whinnery, Theodore Van Duzer," T. Van Duzer and J. R. Whinnery, Eds., 3rd ed. ed. Hoboken, N.J.: Wiley, 1994.
- [4] "Technique of microwave measurements / edited by Carol G. Montgomery. Vol.1," C. G. Montgomery, Ed., ed. New York: Dover : Constable, 1966.
- [5] "Modern RF and microwave measurement techniques / edited by Valeria Teppati, Andrea Ferrero, Mohamed Sayed," A. Ferrero, M. Sayed, and V. Teppati, Eds., ed. Cambridge: Cambridge University Press, 2013.
- [6] R. Collier and D. Skinner, *Microwave Measurements, third edition*, 2007.
- [7] C. A. Balanis, "Antenna theory : analysis and design / Constantine A. Balanis," 3rd ed. ed. Hoboken, NJ: Wiley-Interscience, 2005.
- [8] B. Shaw, "Power Measurement Basics," ed. USA: Microwave Instruments Division-Hewlett-Packard Company, 1997.
- [9] "Fundamentals of RF and Microwave Power Measurements (Part3) Power Measurement Uncertainty per International Guides," *Agilent Technologies, Application note 64-32, 5988-9215EN*, April 2011.
- [10] "Fundamentals of RF and Microwave Power Measurements (Part 2) Power Sensors and Instrumentation," *Agilent Technologies, Application note 14449-1, 5988-9214EN*, July 2006.
- [11] G. F. Engen, "A survey of microwave power-measurement techniques employed at the National Bureau of Standards," *Proceedings of the IEE - Part B: Electronic and Communication Engineering*, vol. 109, pp. 734-739, 1962.
- [12] N. Carrara and P. Lombardini, "Radiation pressure of centimetre waves," *Nature*, vol. 163, 1949.
- [13] A. L. Cullen, "A general method for the absolute measurement of microwave power," *Proceedings of the IEE - Part IV: Institution Monographs*, vol. 99, pp. 112-120, 1952.
- [14] H. M. Barlow, "The Hall Effect and Its Application to Microwave Power Measurement," *Proceedings of the IRE*, vol. 46, pp. 1411-1413, 1958.

- [15] L. M. Stephenson and H. E. M. Barlow, "Power measurement at 4 Gc/s by the application of the Hall effect in a semiconductor," *Proceedings of the IEE - Part B: Radio and Electronic Engineering*, vol. 106, pp. 27-30, 1959.
- [16] A. L. Cullen, "Microwave power measurement (introductory lecture)," *Proceedings of the IEE - Part B: Electronic and Communication Engineering*, vol. 109, pp. 724-733, 1962.
- [17] A. Grebennikov, *RF and Microwave Transmitter Design*: Wiley, 2011.
- [18] R..A. Shankar, "Fundamentals of physics : mechanics, relativity, and thermodynamics / R. Shankar," ed. New Haven: Yale University Press, 2014.
- [19] P. L. Richards, "Bolometers for infrared and millimeter waves," *Journal of Applied Physics*, vol. 76, pp. 1-24, 1994.
- [20] E. L. Ginzton, *Microwave measurements*: McGraw-Hill, 1957.
- [21] S. F. Adam, *Microwave Theory and Applications*: Adam Microwave Consulting, 1992.
- [22] J. A. Becker, C. B. Green, and G. L. Pearson, "Properties and Uses of Thermistors---Thermally Sensitive Resistors," *American Institute of Electrical Engineers, Transactions of the*, vol. 65, pp. 711-725, 1946.
- [23] A. Fantom, *Radio Frequency & Microwave Power Measurement*: P. Peregrinus, 1990.
- [24] R. Roy, A. K. Kush, and R. P. Dixit, "Design and Development of Thermistor based Power Meter at 140 GHz Frequency Band," *Journal of Infrared, Millimeter, and Terahertz Waves*, vol. 32, pp. 1407-1414, 2011.
- [25] R. Judaschke, "Traceable Metrology for high frequency power in the millimetre-wave range," in *Annex la-JRP-Protocol*, ed, Oct 2012.
- [26] R. Scarr and R. Settingington, "Thermistors, Their Theory, Manufacture and Application," *IRE Transactions on Component Parts*, vol. 8, pp. 6-22, 1961.
- [27] F. J. Hyde, "Mersey and North Wales Centre: Chairman's address. Thermistors," *Electrical Engineers, Proceedings of the Institution of*, vol. 115, pp. 100-102, 1968.
- [28] G. T. Anderson, J. W. Valvano, and R. R. Santos, "Self-heated thermistor measurements of perfusion," *Biomedical Engineering, IEEE Transactions on*, vol. 39, pp. 877-885, 1992.
- [29] A. Feteira, "Negative Temperature Coefficient Resistance (NTCR) Ceramic Thermistors: An Industrial Perspective," *Journal of the American Ceramic Society*, vol. 92, pp. 967-983, 2009.
- [30] "NTC Thermistors," *Application notes, edited by BOWTHORPE THERMOMETRICS, THERMOMETRICS, INC. KEYSTONE THERMOMETRICS CORPORATION*.

- [31] C. Chen, "Evaluation of resistance-temperature calibration equations for NTC thermistors," *Measurement*, vol. 42, pp. 1103-1111, 8// 2009.
- [32] SensorScientific. *Small Bead thermistor*. Available: http://www.sensorsci.com/literature/122766/Glass_Bead_Thermistors
- [33] muRata. (Oct 6, 2016). *NTC Thermistors*. Available: <http://www.murata.com/media/webrenewal/support/library/catalog/products/thermistor/ntc/r44e.ashx>
- [34] "NTC thermistors," *Application notes, edited by BOWTHORPE THERMOMETRICS, THERMOMETRICS, INC. KEYSTONE THERMOMETRICS CORPORATION*.
- [35] J. A. Lane, *Microwave power measurement / (by) J.A. Lane*. London: London : Peter Peregrinus Ltd (for) the Institution of Electrical Engineers, 1972.
- [36] L. D. Hill, "New method for producing and mounting barretter elements for power measurement in waveguides," *Electronics Letters*, vol. 19, pp. 352-354, 1983.
- [37] M. C. Selby, "The Bolovac and Its Applications," *IEEE Transactions on Instrumentation and Measurement*, vol. 19, pp. 324-331, 1970.
- [38] M. C. Selby, "Microwave Two-Port Coaxial Power and Voltage Mounts," *IEEE Transactions on Instrumentation and Measurement*, vol. 22, pp. 166-173, 1973.
- [39] I. A. Harris, "A coaxial film bolometer for the measurement of power in the u.h.f. band," *Proceedings of the IEE - Part B: Electronic and Communication Engineering*, vol. 107, pp. 67-72, 1960.
- [40] J. A. Lane, "The measurement of power at a wavelength of 3 cm by thermistors and bolometers," *Proceedings of the IEE - Part B: Radio and Electronic Engineering*, vol. 102, pp. 819-824, 1955.
- [41] J. A. Lane, "Transverse film bolometers for the measurement of power in rectangular waveguides," *Proceedings of the IEE - Part B: Radio and Electronic Engineering*, vol. 105, pp. 77-80, 1958.
- [42] I. Lemco and B. Rogal, "Resistive-film milliwattmeters for the frequency bands: 8·2-12·4 Gc/s, 12·4-18 Gc/s and 26·5-40 Gc/s," *Proceedings of the IEE - Part B: Electronic and Communication Engineering*, vol. 107, pp. 427-430, 1960.
- [43] J. A. Lane and D. M. Evans, "The design and performance of transverse-film bolometers in rectangular waveguides," *Proceedings of the IEE - Part B: Electronic and Communication Engineering*, vol. 108, pp. 133-135, 1961.
- [44] B. M. Schiffman, L. Young, and R. B. Larrick, "Thin-Film Waveguide Bolometers for Multimode Power Measurement," *Microwave Theory and Techniques, IEEE Transactions on*, vol. 12, pp. 155-163, 1964.

- [45] K. Sakurai and T. Nemoto, "A Thin-Film Bolometer Unit," *Instrumentation and Measurement, IEEE Transactions on*, vol. 16, pp. 206-211, 1967.
- [46] T. Inoue, I. Yokoshima, and M. Sasaki, "High-performance thin-film barretter mount for power measurement in W-band," *Electronics Letters*, vol. 21, pp. 170-172, 1985.
- [47] Z. Hocenski, L. Cvitas, and Z. Lasinger, "Comparison of methods for nonlinearity correction of platinum resistance thermometer," in *SICE Annual Conference, 2008*, 2008, pp. 3151-3154.
- [48] E. Fiedler, M. F. Porto Cruz, O. F. Cota Monjaras, and T. Stieglitz, "Evaluation of thin-film temperature sensors for integration in neural probes," in *Neural Engineering (NER), 2015 7th International IEEE/EMBS Conference on*, 2015, pp. 549-552.
- [49] T. A. Saad, "The story of the MIT Radiation Laboratory," *IEEE Aerospace and Electronic Systems Magazine*, vol. 5, pp. 46-51, 1990.
- [50] *Nokia Bell Labs*. Available: <http://www.bell-labs.com/>
- [51] E. E. Aslan, "Temperature-Compensated Microwatt Power Meter," *Instrumentation, IRE Transactions on*, vol. I-9, pp. 291-297, 1960.
- [52] H. J. Carlin and J. Blass, "A Direct Reading D-C Bridge for Microwave Power Measurements," *American Institute of Electrical Engineers, Transactions of the*, vol. 67, pp. 311-315, 1948.
- [53] E. E. Aslan, "Accuracy of a Temperature-Compensated Precision RF Power Bridge," *Instrumentation and Measurement, IEEE Transactions on*, vol. 18, pp. 232-236, 1969.
- [54] L. A. Rosenthal and J. L. Potter, "A Self-Balancing Microwave Power Measuring Bridge," *Proceedings of the IRE*, vol. 39, pp. 927-931, 1951.
- [55] G. F. Engen, "A self-balancing direct-current bridge for accurate bolometric power measurements," *Journal of Research of the National Bureau of Standards*, vol. 59, p. 101, 1957.
- [56] G. F. Engen, "A DC-RF Substitution Error in Dual-Element Bolometer Mounts," *Instrumentation and Measurement, IEEE Transactions on*, vol. 13, pp. 58-64, 1964.
- [57] E. E. Aslan, "A Single Bead Broadband Coaxial Thermistor Mount," *Instrumentation and Measurement, IEEE Transactions on*, vol. 14, pp. 102-106, 1965.
- [58] D. Allal, D. Bélières, and M. Charles, "Development of a new DC-substitution RF power meter at LNE," in *29th Conference on Precision Electromagnetic Measurements (CPEM 2014)*, 2014, pp. 754-755.
- [59] K. Technologies. (November 21, 2014). *N432A Thermistor Power Meter*. Available: <http://literature.cdn.keysight.com/litweb/pdf/5990-5740EN.pdf?id=1891411>

- [60] N. T. Larsen, "A new self-balancing DC-substitution RF power meter," *Instrumentation and Measurement, IEEE Transactions on*, vol. IM-25, pp. 343-347, 1976.
- [61] N. T. Larsen, "NBS type IV RF power meter operation and maintenance," N. B. o. Standards, Ed., ed, Oct 1977.
- [62] R. A. Ginley, "Traceability for microwave power measurements: Past, present, and future," in *Wireless and Microwave Technology Conference (WAMICON), 2015 IEEE 16th Annual*, 2015, pp. 1-5.
- [63] F.R. Clague, "A calibration service for coaxial reference standards for microwave power," *NIST Technical Note 1374*, May 1995.
- [64] F. R. C. J. W. Allen, N T. Larsen, and M. P. Weidman, "The NIST Microwave Power Standards in Waveguide," *NIST Technical Note 1511*, Feb 1999.
- [65] L. C. Oldfield, J. P. Ide, and E. J. Griffin, "A Multistate Reflectometer," *IEEE Transactions on Instrumentation and Measurement*, vol. IM-34, pp. 198-201, 1985.
- [66] N. P. Laboratory. *Waveguide Power Transfer Standards - Multi-State Reflectometers*. Available: <http://www.npl.co.uk/instruments/products/rf-microwave/waveguide-power-transfer-standards-multi-state-reflectometers/>

Chapter 3

Transmission Line Theory Based Power Sensor Design

This chapter outlines the basic of transmission line theory used in this thesis to design the power sensors, this includes investigating the case of rectangular waveguides based transmission line. Important equivalent transmission line parameters of the waveguides are discussed. The second part of the chapter is devoted to the design procedure of the waveguide power sensors based on the transmission line theory.

3.1. Transmission Line for Rectangular Waveguides

There are many types of transmission lines used in microwave applications [1]. In terms of structure, the simplest transmission line is free space [2]. Parallel wire lines are one of the oldest types of transmission line for radio applications [3], the lines are inexpensive but lack shielding [4]. Coaxial lines provide shielding but come with the difficulty of fabricating complex microwave components and integrating with circuit devices [5]. An alternative is planar transmission lines including: strip-lines, micro-strip lines and coplanar waveguides [6]. They are versatile, compact, low cost and highly integrated with circuit devices such as, resistors, diodes and transistors. Hollow waveguides i.e. circular and rectangular waveguides [7] are more expensive but have low loss, high operating frequency and high power handling. In this section,

the property of rectangular waveguide is presented as they form the basis for the power sensors. The field analysis of the rectangular waveguide are well covered in [1, 4]. We will use the results to derive the transmission line parameters which are frequency, propagation constant, attenuation constant and characteristic impedance.

Unlike most of transmission lines supporting transverse electromagnetic (TEM) waves, the rectangular waveguide in Figure 3.1 have a single conductor. Therefore, it only supports transverse electric (TE) and/or transverse magnetic (TM) waves. The waveguide is sometimes not strictly considered as a transmission line. However, the concept of transmission line theory is still applicable at a single frequency.

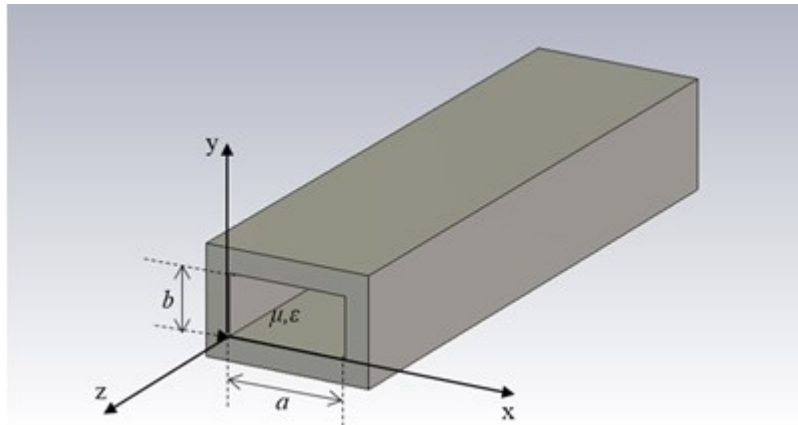


Figure 3.1: A rectangular waveguide structure

The propagating waves are characterised by different modes such as TE_{mn} for transverse electric waves and TM_{mn} for transverse magnetic waves, where m and n are wave numbers i.e. $0,1,2,\dots$

The cut-off frequency of each mode can be found as [4]

$$f_{c_{mn}} = \frac{1}{2\pi\sqrt{\mu\epsilon}} \sqrt{\left(\frac{m\pi}{a}\right)^2 + \left(\frac{n\pi}{b}\right)^2} \quad (3.1)$$

Where μ and ε are the permeability and the permittivity of the material filling the hollow volume of the waveguide, a and b are the waveguide dimension as shown in Figure 3.3. Conventionally, rectangular waveguides have $a \geq 2b$ [8].

From the expressions of the electric field \vec{E} and the magnetic field \vec{H} in [4], the lowest cut-off frequency of the transverse electric waves occurs for the TE₁₀ ($m=1, n=0$) mode as there is no TE₀₀ mode. This frequency is

$$f_{c10} = \frac{1}{2a\sqrt{\mu\varepsilon}} \quad (3.2)$$

The second lowest cut-off frequency in this category f_{c20} at TE₂₀ mode is

$$f_{c20} = \frac{1}{a\sqrt{\mu\varepsilon}} \quad (3.3)$$

In transverse magnetic modes, the first propagating mode is TM₁₁ since neither m nor n should be zero for the TM wave to exist, the cut-off frequency is

$$f_{c11} = \frac{1}{2\sqrt{\mu\varepsilon}} \sqrt{\left(\frac{1}{a}\right)^2 + \left(\frac{1}{b}\right)^2} \quad (3.4)$$

It easily can be seen that $f_{c10} < f_{c20} \leq f_{c11}$ and the cut-off frequency get higher as the mode numbers increase. Conventionally, the operating frequency band of standard waveguides is between the cut-off frequency of TE₁₀ mode and that of TE₂₀ mode, so that only one mode is propagating. As a result, TE₁₀ is the dominant mode of the waveguide.

It is worth presenting here the field expression of the TE₁₀ mode for future use [9]

$$H_z = H_1 \cos \frac{\pi x}{a} e^{j\omega t - \gamma z} \quad (3.5a)$$

$$H_y = 0 \quad (3.5b)$$

$$H_x = jH_1 \frac{2a}{\lambda} \sqrt{1 - \left(\frac{\lambda}{2a}\right)^2} \sin \frac{\pi x}{a} e^{j\omega t - \gamma z} \quad (3.5c)$$

$$E_z = 0 \quad (3.5d)$$

$$E_y = -H_1 \frac{2a}{\lambda} \sqrt{\frac{\mu}{\varepsilon}} \sin \frac{\pi x}{a} e^{j\omega t - \gamma z} \quad (3.5e)$$

$$E_x = 0 \quad (3.5f)$$

where λ is the wavelength of a plane wave in the medium filling the guide.

The fields are visualised in Figure 3.2(a) and the surface current is presented in Figure 3.2(b). A useful result from the field analysis is that there is no current traveling along the central line of the broad waveguide wall. Therefore, in rectangular waveguide sensor construction, the cut in central E-plane will have minimum effect on the device's performance.

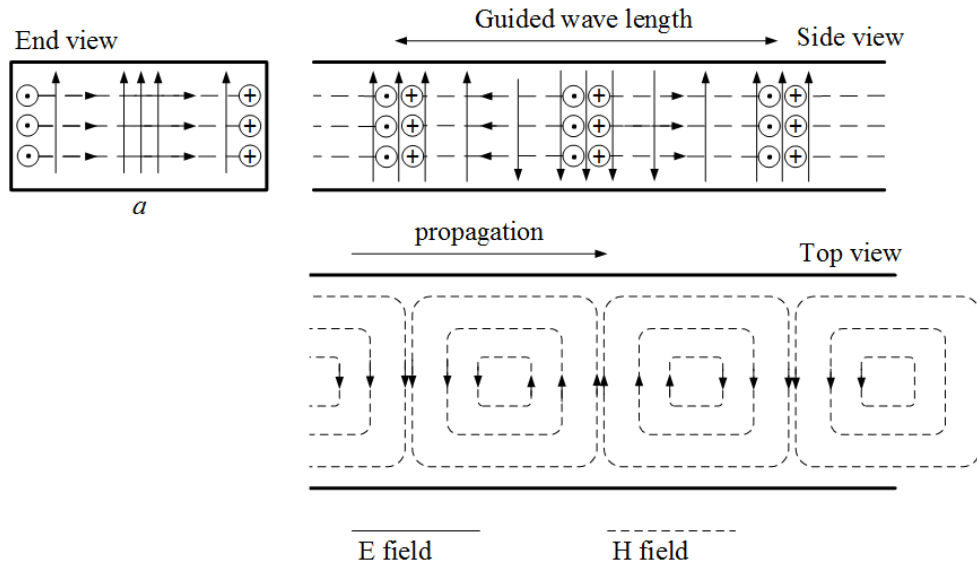
For a lossless rectangular waveguide, the complex propagation constant is pure imaginary $\gamma = j\beta$, the propagation constant β for TE₁₀ mode is as follow [4].

$$\beta = \sqrt{\mu\varepsilon\omega^2 - \left(\frac{\pi}{a}\right)^2} \quad (3.6)$$

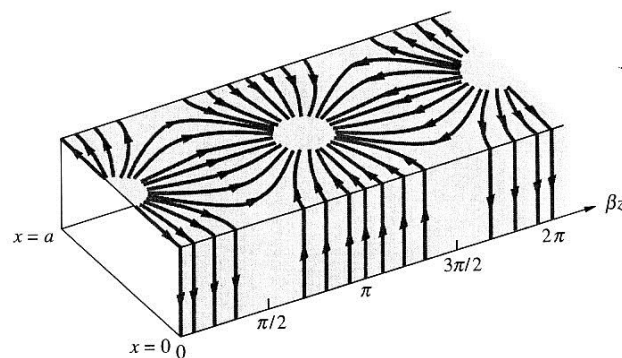
The guided wavelength in the waveguide is then equal to

$$\lambda_g = \frac{2\pi}{\beta} = \frac{2\pi}{\sqrt{\mu\varepsilon\omega^2 - \left(\frac{\pi}{a}\right)^2}} \quad (3.7)$$

The expression suggests that guided wavelength of the traveling wave in a rectangular waveguide is greater than the wavelength λ .



(a)



(b)

Figure 3.2: (a) The electric field and magnetic field of TE_{10} mode (taken from [9]); (b) The surface current in the TE_{10} mode (taken from [10])

The attenuation in waveguide can be caused by conductor loss α_c and/or dielectric loss α_d , the total attenuation constant is $\alpha = \alpha_c + \alpha_d$. The conductor loss results from finite conductivity of the waveguide wall material, the attenuation constant due to conductor loss for the TE_{10} mode is given as [4]

$$\alpha_c = \sqrt{\frac{2}{\omega\mu\sigma}} \frac{\pi}{a^3 b \beta} \left(b + \frac{a}{2} + \frac{\beta^2 a^3}{2\pi^2} \right) \quad (3.8)$$

Where σ is the conductivity of the material of the waveguide wall.

The dielectric loss is due to lossy dielectric material filling the guide. The dielectric attenuation constant of TE or TM waves in a guide with homogeneous dielectric filling can be calculated as follows [4]

$$\alpha_d = \frac{\mu\epsilon\omega^2 \tan \delta}{2\beta} \quad (3.9)$$

where $\tan \delta$ is the loss tangent of the dielectric filling the guide, normally $\tan \delta \ll 1$.

Finally, the characteristic impedance of rectangular waveguides is considered here. In case of TEM transmission lines which have at least two conductors, the characteristic impedances of the lines can be defined. On the other hand, the single conductor transmission line does not have unique characteristic impedance definition. The discussion of equivalent impedance for non-TEM lines is presented in [4]. In this work, we will use the definition of the transmission line impedance which is derived from the power transmitted in to the guide and the traveling current, as it is most appropriate and comprehensive for the particular power sensing application.

The power transmitted can be calculated by [4]

$$P = \frac{1}{2} \operatorname{Re} \int_{x=0}^a \int_{y=0}^b E_y H_x^* dy dx \quad (3.10)$$

The total current traveling down the guide is obtained from Ampere's law as

$$I = -\int_0^a H_x dx \quad (3.11)$$

Using the field expressions in equations 3.22 c and 3.22e, the characteristic impedance of the rectangular waveguide for TE₁₀ mode is [9]

$$Z_0 = \frac{P}{II^*/2} = \frac{2b}{a} \sqrt{\frac{\mu}{\varepsilon}} \frac{1}{\sqrt{1-(\lambda/2a)^2}} \quad (3.12)$$

It is worth noticing that the above impedance is a real number and depends on frequency of the traveling wave.

3.2. Bolometer Mount Design

In this section, the transmission line theory is applied to rectangular waveguides to design waveguide bolometers. It believed that the technique was applied in previously published designs up to 94 GHz [11-15], but it has not been explicitly documented in the literature. The mathematics of the design principle is presented, and the full design procedure for waveguide bolometric sensor is then introduced with the aid of CST Microwave Studio Simulation [16].

3.2.1. Transmission line presentation of the waveguide bolometer

As described in Chapter 2, a waveguide bolometer usually consists of a sensing element mount which is placed at an appropriate distance from the shorted end of the waveguide. The waveguide bolometer can be presented in terms of the transmission line model shown in Figure 3.3. The characteristic impedance of the line is Z_0 at the operating frequency f_0 . The shorted end of the waveguide is represented by the zero load impedance $Z_L = 0$. The impedance

of the mount is $R + jX$. It is important to note that the mount impedance is the total impedance of the sensing element and the structure that accommodates the element. The transmission line length l relates to the distance between the mount and the shorted end of the waveguide.

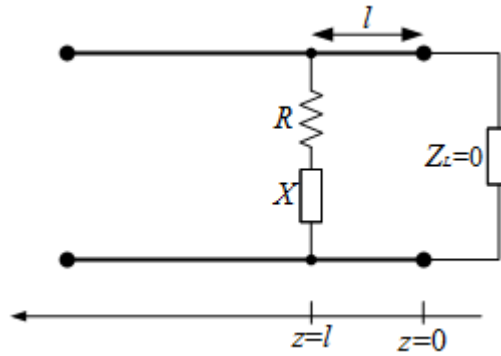


Figure 3.3: Equivalent transmission line circuit of a waveguide bolometer.

As the waveguide with no dielectric fill has very low loss, the analysis can assume to deal with a lossless transmission line. The bolometer is designed to absorb all the incident microwave power as discussed in Chapter 2, the reflection coefficient at the open end of the transmission line model should be zero i.e. $\Gamma_{out} = 0$. The reflection coefficient Γ_l at the mount can be derived from Γ_{out} , equation 3.14 gives $\Gamma_l = 0$. The reflection coefficient Γ_l can be calculated as

$$\Gamma_l = \frac{Z_l - Z_0}{Z_l + Z_0} = 0 \quad (3.13)$$

where Z_l is the total impedance at $z = l$ looking toward the load. The admittance is obtained from the parallel circuit.

$$Y_l = \frac{1}{Z_l} = \frac{1}{R + jX} + \frac{1}{Z_1} \quad (3.14)$$

where Z_l is the impedance of the shorted transmission line, which can be calculated by equation 3.17 when Z_L is zero.

$$Z_1 = jZ_0 \tan(\beta l) \quad (3.15)$$

The admittance Y_l can be rewritten as

$$Y_l = \frac{1}{Z_l} = \frac{R}{R^2 + X^2} - j \frac{X}{R^2 + X^2} - j \frac{1}{Z_0 \tan(\beta l)} \quad (3.16)$$

Equations 3.30 and 3.33 give

$$\frac{1}{Z_0} = \frac{R}{R^2 + X^2} - j \frac{X}{R^2 + X^2} - j \frac{1}{Z_0 \tan(\beta l)} \quad (3.17)$$

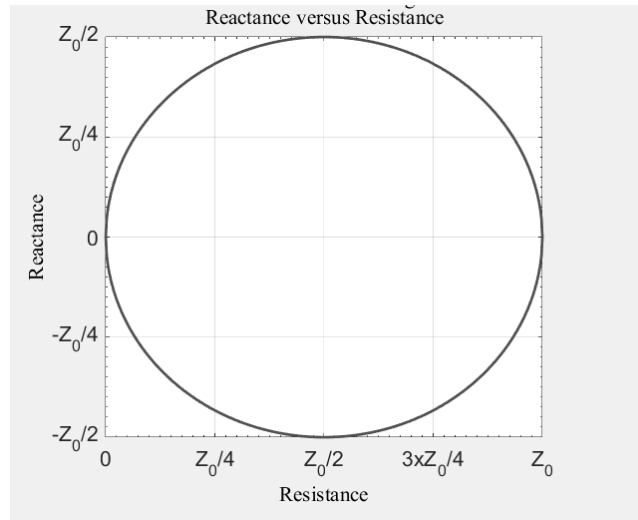
Solving the equation for the mount resistance R and the mount reactance X assuming R and X cannot be zero. The expressions for the resistance and reactance are

$$X^2 + \left(R - \frac{Z_0}{2}\right)^2 = \left(\frac{Z_0}{2}\right)^2 \quad (0.18a)$$

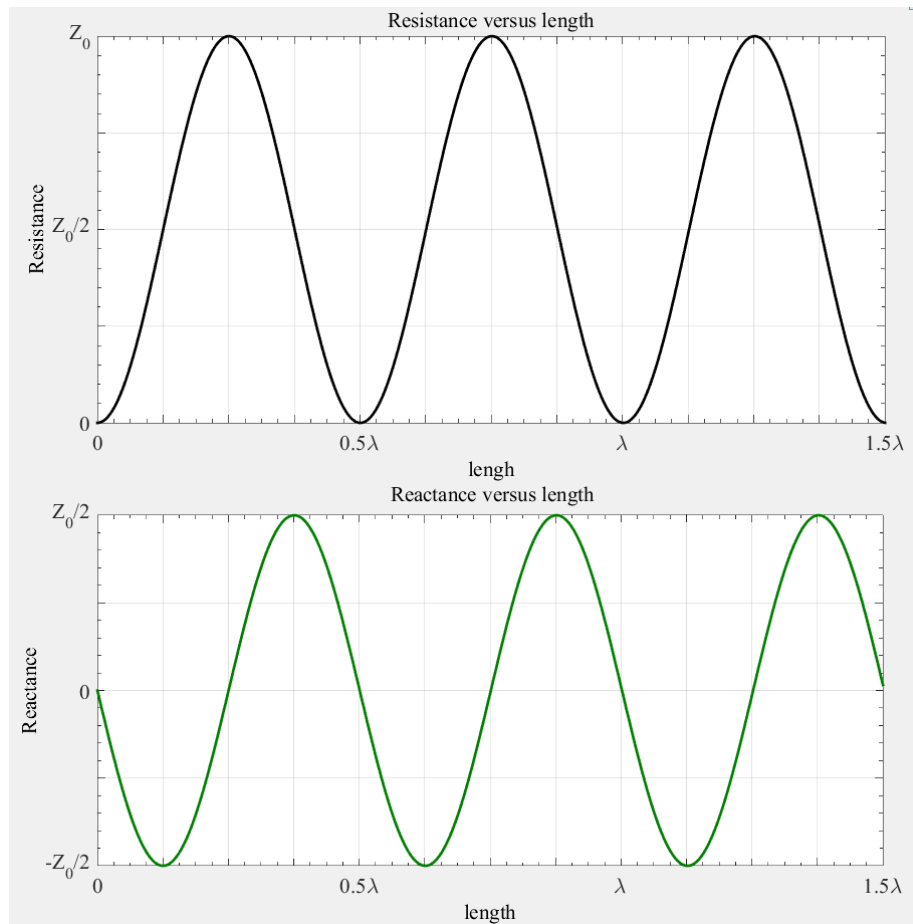
$$\frac{R}{Z_0} = \frac{1}{2}(1 - \cos(2\beta l)) \quad (3.18b)$$

$$\frac{X}{Z_0} = -\frac{1}{2}\sin(2\beta l) \quad (3.18c)$$

The expressions present the relationship of the mount resistance R and the mount reactance X to the electrical length l at matching condition i.e. no power being reflected. The relationship can be plotted in Figure 3.4. The graph in Figure 3.4(a) shows that the matching resistance R and the reactance X are on a circle with the diameter equal Z_0 . The circle is the reciprocal circle of $r = 1.0$ on Smith Chart [4], a similar matching technique using Smith Chart was utilised in [14, 17, 18].



(a)



(b)

Figure 3.4: Matching condition of the mount resistance, reactance and the shorted electrical length

There are two cases of matching which are inductive matching and capacitive matching. When $\lambda_g/4 + n\lambda_g/2 \leq l \leq \lambda_g/2 + n\lambda_g/2$ ($n = 0, 1, 2, \dots$), the reactance X is greater than zero, inductive matching happens. Otherwise, it is capacitive matching. In practice, the bolometer mount is often placed at the transverse plane of the waveguide and parallel to the narrow side wall where the electric field is maximum [17]. As a result, the mount should normally have positive reactance. In fact, to the best of the author's knowledge, all the published microwave power sensor designs are in the category of inductive matching.

A mathematic model of bolometer mount in a rectangular waveguide was created in Matlab [19] using equation 3.14 to 3.18. The reflection coefficient S_{11} in dB of the sensor can be calculated as

$$S_{11} = -20 \log \left| \frac{Z_l - Z_0}{Z_l + Z_0} \right| \text{ (dB)} \quad (3.19)$$

The reflection coefficient S_{11} for the inductive matching condition was investigated for different resistances such as: $Z_0/4$, $Z_0/2$, $3Z_0/4$ and Z_0 . The corresponding electrical short length l_s at matching condition can be calculated by equation 3.35b, it gives the length of $\lambda_g/3$, $\lambda_g/8$, $\lambda_g/6$ and $\lambda_g/4$, respectively. It should be noted that the characteristic impedance Z_0 of the waveguide is for the frequency f_0 . At other frequencies, the characteristic impedance can be calculated by equation 3.29. As can be seen in Figure 3.5, the matching occurs at the centre frequency f_0 . The maximum -20 dB bandwidth of $15\%f_0$ can be archived at $R = Z_0$. The bandwidths are narrow and reduce with the decrease of the matching resistance.

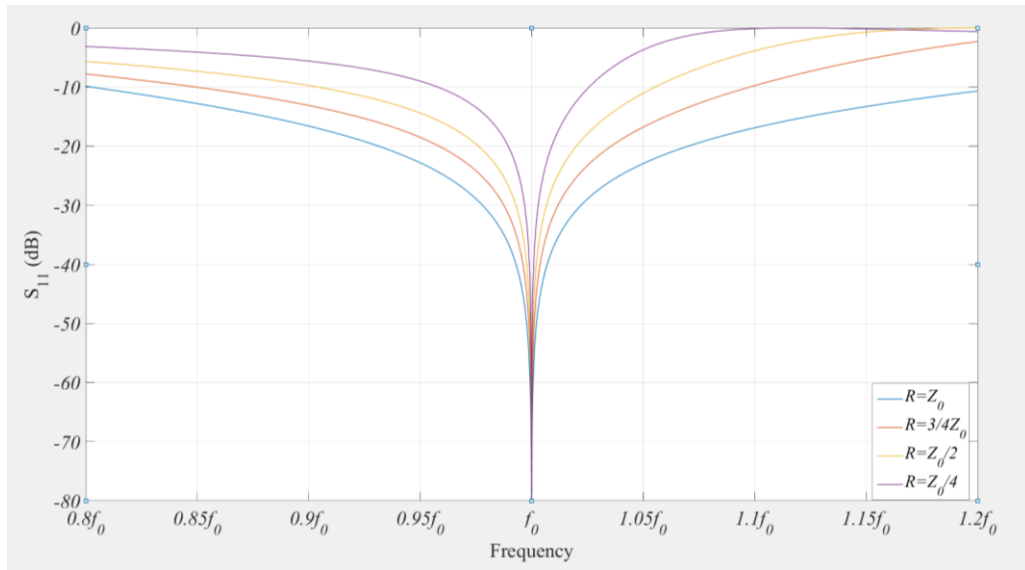


Figure 3.5: The reflection coefficient S_{11} for inductive matching condition at different resistance of the mount

The interesting case of capacitive matching is also investigated by the mathematic model as shown in Figure 3.6. The bandwidth of this matching type is slightly better at $Z_0/2$ and $3Z_0/4$ matching resistances, but it is also narrow band at -20 dB level.

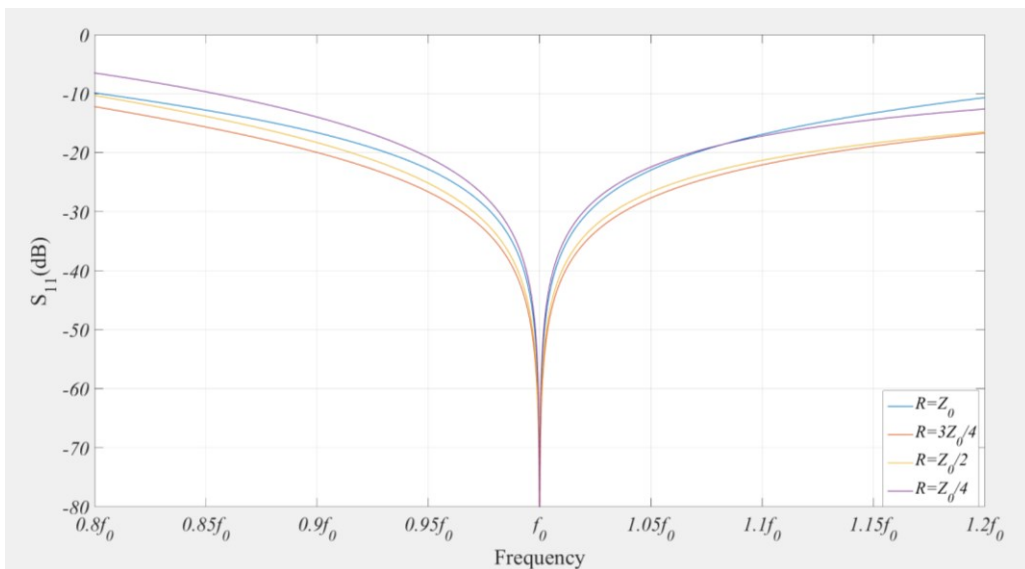


Figure 3.6: The reflection coefficient S_{11} at capacitive matching condition

In the following chapters, the simulated bolometer results will be compared to the mathematical model to demonstrate the agreement between transmission line theory in waveguide and the simulated field analysis solution.

3.2.2. Two-port impedance extraction of the mount

The theory discussed suggests that if the complex impedance of the bolometer mount is known, we can easily determine whether the impedance is suitable for a matching condition and then find the appropriate shorted length l_s . The main problem is that Z is unknown for the waveguide bolometer. This section introduces a method to calculate the impedance Z of a waveguide bolometer mount by using CST Microwave Studio Simulation [16].

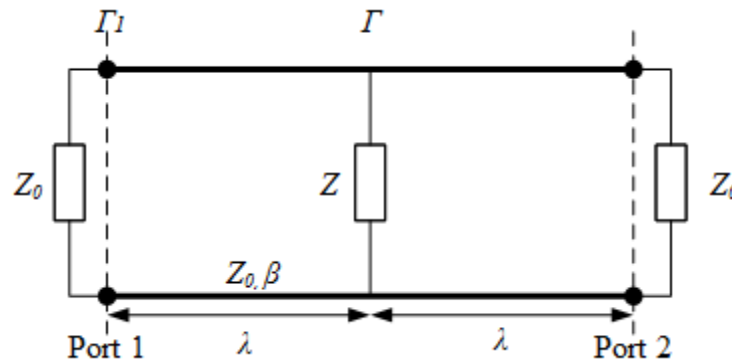


Figure 3.7: Equivalent transmission line circuit of the impedance extracting method

Consider the circuit in Figure 3.7, there is an arbitrary load Z placed in the middle of a transmission line. The length of the line is two wavelengths (2λ), the characteristic impedance is Z_0 . At each end of the transmission line, there is a matched port to measure the complex reflection coefficient Γ_1 . The reflection coefficient at the load can be calculated as

$$\Gamma = \Gamma_1 e^{-j2\beta\lambda} = \Gamma_1 \quad (3.20)$$

The equivalent impedance of the right side of the circuit in Figure 3.7 can be obtained as

$$Z_1 = Z_0 \frac{Z_L + jZ_0 \tan \beta\lambda}{Z_0 + jZ_L \tan \beta\lambda} = Z_0 \quad (3.21)$$

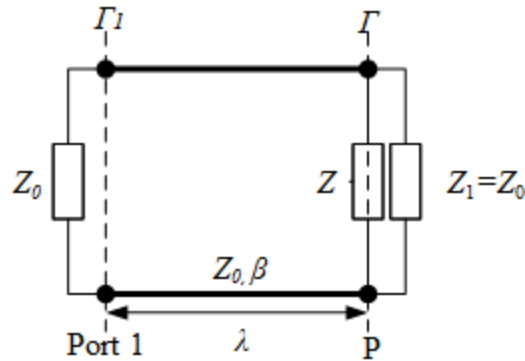


Figure 3.8: The equivalent of the circuit in Figure 3.7

The circuit in Figure 3.7 can be redrawn as shown in Figure 3.8. The reflection coefficient at the load is

$$\Gamma = \frac{Z_P - Z_0}{Z_P + Z_0} \quad (3.22)$$

where Z_P is the total impedance of the parallel circuit of Z and Z_1 .

$$Z_P = \frac{ZZ_0}{Z + Z_0} \quad (3.23)$$

Solving the equation 3.22 and 3.23 for Z gives

$$\frac{Z}{Z_0} = -\frac{1 + \Gamma}{2\Gamma} \quad (3.24)$$

Equation 3.24 shows that the normalised impedance of an arbitrary load on a transmission line can be calculated from the measure reflection coefficient. In a waveguide structure, the bolometer mount is placed at the middle of the waveguide with the length equal to two guided

wavelength λ_g . The opened ends of the waveguide are connected to matched waveguide ports. The complex reflection coefficient at each port can be obtained by the two-port simulation. The coefficients at the two ports should be equal as the structure is symmetrical.

In order to demonstrate the impedance extraction method, an example of reactance extraction for a cylindrical metal post in X-band waveguide is presented. Such a post has an analytical solution for comparison with the simulations.

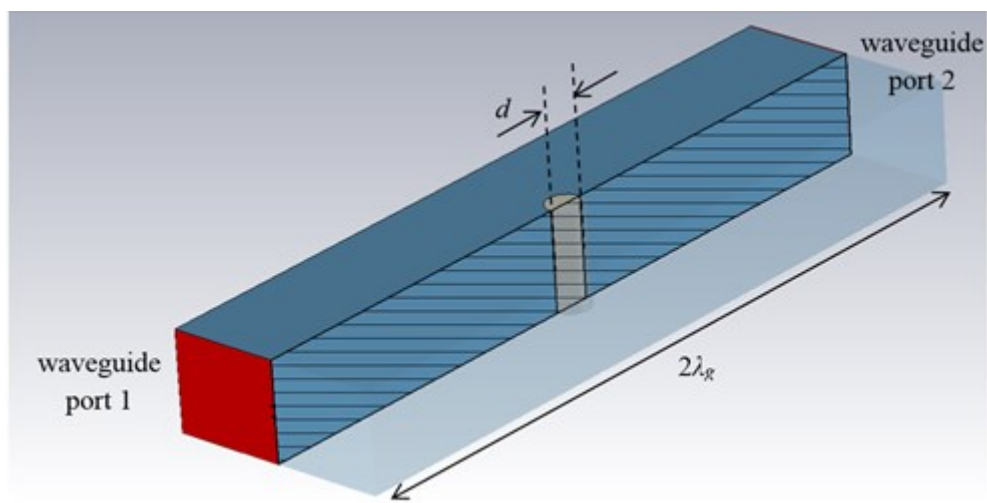


Figure 3.9: The CST model of a circular post in the middle of X-band waveguide (the cut view is shown for the clarification of objects)

The 3D model of the structure in Figure 3.9 was built in CST. Only the vacuum filling in blue colour of the waveguide is shown. In the simulation, the filling material of the waveguide is vacuum, and the material of the post is Perfect Electric Conductor (PEC). The diameter of the cylinder is d . The post is situated in the middle of the $22.86 \text{ mm} \times 10.16 \text{ mm}$ rectangular waveguide with the length of two times of the guided wavelength λ_g . At the frequency of 10 GHz, the guided wavelength is 39.75 mm (calculated by equation 3.7). The simulation was run for the post diameter d changing from 0.1 mm to 1.4 mm at 0.1 mm interval and the complex

reflection coefficients for each case was obtained. The reactance of the post was then calculated by equation 3.24.

The results from the simulations can be compared to the theoretical calculation of the reactance of the symmetrically located post aligned parallel to the electric field in a rectangular waveguide. The normalised reactance X_a/Z_0 can be calculated as [20]

$$\frac{X_a}{Z_0} - \frac{X_b}{2Z_0} = \frac{a}{2\lambda_g} \left[S_0 - \left(\frac{\pi d}{2\lambda} \right)^2 - \frac{5}{8} \left(\frac{\pi d}{2\lambda} \right)^4 - 2 \left(\frac{\pi d}{2\lambda} \right)^4 \left(S_2 - 2S_0 \frac{\lambda^2}{\lambda_g^2} \right)^2 \right] \quad (3.25a)$$

where

$$\frac{X_b}{Z_0} = \frac{a}{\lambda_g} \frac{\left(\frac{\pi d}{a} \right)^2}{1 + \frac{1}{2} \left(\frac{\pi d}{\lambda} \right)^2 \left(S_2 + \frac{3}{4} \right)} \quad (3.25b)$$

$$S_0 = \ln \frac{4a}{\pi d} - 2 + 2 \sum_{n=3,5,\dots}^{\infty} \left[\frac{1}{\sqrt{n^2 - \left(\frac{2a}{\lambda} \right)^2}} - \frac{1}{n} \right] \quad (3.25c)$$

$$S_2 = \ln \frac{4a}{\pi d} - \frac{5}{2} + \frac{11}{3} \left(\frac{\lambda}{2a} \right)^2 - \left(\frac{\lambda}{a} \right)^2 \sum_{n=3,5,\dots}^{\infty} \left[\sqrt{n^2 - \left(\frac{2a}{\lambda} \right)^2} - n + \frac{2}{n} \left(\frac{a}{\lambda} \right)^2 \right] \quad (3.25d)$$

The equations are valid for the wavelength $a < \lambda < 2a$ and the post diameter $d < 2a$. The theoretical values are accurate to within a few percent, compared to experimental results in X-band waveguide [20].

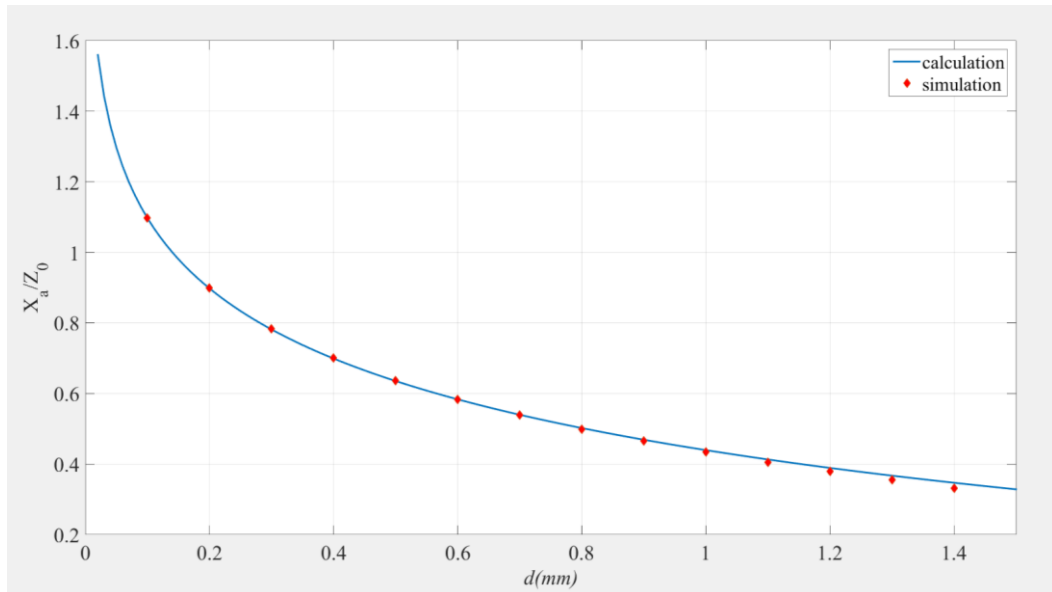


Figure 3.10: Comparison of normalised reactance of circular post in X-band waveguide between the extractions from simulation and theoretical calculation

The normalised reactances at different values of the diameter d , obtained from CST simulation and theoretical calculations are plotted in Figure 3.10. It can be seen the excellent agreement between two approaches. The deviation between the results increases as the post diameter gets larger i.e. at $d = 1$ mm, the deviation is 1.3%, and it reaches to 4.4% at $d = 1.4$ mm. In theory, the calculated values from equation 3.25 have the accuracy of a few percent for $d < 3.4$ mm [20]. Therefore, the differences of more than 4% is caused by the limitation of extraction method. A possible explanation is that in transmission line analysis, the load is assumed to have negligible longitude dimension compared to the wavelength. As the post expands in diameter, the accuracy of the method declines.

In conclusion, the impedance extraction could give valid results within a few percent as long as the longitude dimension of the structure is kept small. In design practice, the dimension of the mount should be less than 1/20 of the broad side wall of the waveguide.

3.2.3. Process of design

The bolometer design process is presented in form of a flowchart as shown in the Figure 3.11 below. The design starts with the choice of the sensing element for the application such as Negative Temperature Coefficient (NTC) thermistors or Positive Temperature Coefficient (PTC) barretters discussed in Chapter 2. The mount structure to accommodate the sensing element is then determined, for instance PCBs for soldering thermistors or substrates for thin film and electrical deposition. The mount impedance can be calculated by using the impedance extraction method discussed in the previous section. With the initial dimensions, the extracted impedance may be not satisfied the matching condition in equations 3.18. In that case, the dimensions of the mount need to be adjusted until the matching condition is satisfied. The equations 3.18b and 3.18c can be used to calculate the shorted length l_s . At this stage, the structure of the mount with suitable dimensions can be put in a shorted waveguide at the determined distance l_s from the shorted end, the model can be built in 3D design environment of CST Studio. The simulation computes the electromagnetic field equations for the bolometers structure and returns the reflection coefficient S_{11} . The initial simulation result should be in the form of the responses in Figure 3.5 or 3.6, there may be a small shift in the centre frequency or the reflection coefficient response at this stage. However, the deviations can be eliminated by running the built-in optimisation of the simulator program. The optimum dimensions of the microwave power sensor are then used to fabricate the real device. Several devices using this techniques are discussed in future chapters.

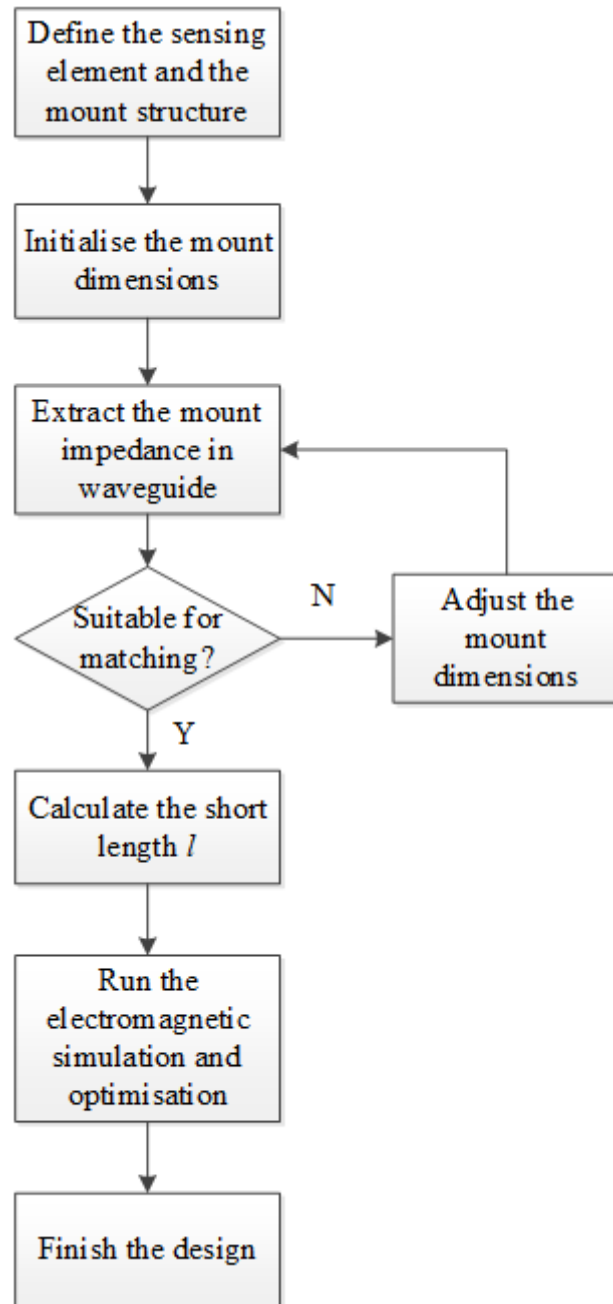


Figure 3.11: The power sensor design process based on transmission line theory

References

- [1] R. E. Collin, "Foundations for microwave engineering / Robert E. Collin," E. Institute of and E. Electronics, Eds., 2nd ed. ed. New York: IEEE Press, 2001.
- [2] C. A. Balanis, "Antenna theory : analysis and design / Constantine A. Balanis," 3rd ed. ed. Hoboken, NJ: Wiley-Interscience, 2005.
- [3] E. Lecher, "Eine Studie über electrische Resonanzerscheinungen," *Annalen der Physik*, vol. 277, pp. 850-870, 1890.
- [4] D. M. Pozar, "Microwave engineering / by David M. Pozar," 4th ed. ed. Hoboken, N.J.: Wiley, 2012.
- [5] S. A. Schelkunoff, "The electromagnetic theory of coaxial transmission lines and cylindrical shields," *The Bell System Technical Journal*, vol. 13, pp. 532-579, 1934.
- [6] T. H. Lee, "Planar microwave engineering : a practical guide to theory, measurement, and circuits / Thomas H. Lee," ed. Cambridge: Cambridge University Press, 2004.
- [7] K. S. Packard, "The Origin of Waveguides: A Case of Multiple Rediscovery," *IEEE Transactions on Microwave Theory and Techniques*, vol. 32, pp. 961-969, 1984.
- [8] R. Sorrentino, "Microwave and RF engineering / R. Sorrentino, G. Bianchi," G. Bianchi, Ed., ed. Oxford: Wiley-Blackwell, 2010.
- [9] T. K. Ishii, *Microwave engineering*. San Diego: Harcourt Brace, 1989.
- [10] D. K. Cheng, "Field and wave electromagnetics / David K. Cheng," ed. Reading, Mass.Wokingham: Addison-Wesley, 1983.
- [11] J. A. Lane, "Transverse film bolometers for the measurement of power in rectangular waveguides," *Proceedings of the IEE - Part B: Radio and Electronic Engineering*, vol. 105, pp. 77-80, 1958.
- [12] I. Lemco and B. Rogal, "Resistive-film milliwattmeters for the frequency bands: 8·2-12·4 Gc/s, 12·4-18 Gc/s and 26·5-40 Gc/s," *Proceedings of the IEE - Part B: Electronic and Communication Engineering*, vol. 107, pp. 427-430, 1960.
- [13] J. A. Lane and D. M. Evans, "The design and performance of transverse-film bolometers in rectangular waveguides," *Proceedings of the IEE - Part B: Electronic and Communication Engineering*, vol. 108, pp. 133-135, 1961.
- [14] K. Sakurai and T. Nemoto, "A Thin-Film Bolometer Unit," *Instrumentation and Measurement, IEEE Transactions on*, vol. 16, pp. 206-211, 1967.
- [15] T. Inoue, I. Yokoshima, and M. Sasaki, "High-performance thin-film barretter mount for power measurement in W-band," *Electronics Letters*, vol. 21, pp. 170-172, 1985.

- [16] *CST-Computer Simulation Technology- Microwave Studio* Available: <https://www.cst.com/>
- [17] "Technique of microwave measurements / edited by Carol G. Montgomery. Vol.1," C. G. Montgomery, Ed., ed. New York: Dover : Constable, 1966.
- [18] T. Inoue and T. Nemoto, "High-Efficiency Millimeter-Wave Bolometer Mount," *Microwave Theory and Techniques, IEEE Transactions on*, vol. 25, pp. 694-697, 1977.
- [19] T. M. MATLAB and Statistics Toolbox Release 2015b, Inc., Natick, Massachusetts, United States.
- [20] N. Marcuvitz, "Waveguide handbook / N. Marcuvitz," E. Institution of Electrical, Ed., ed. London: Peregrinus on behalf of The Institution of Electrical Engineers, 1986.

Chapter 4

X-band Microwave Power Sensor Design

The chapter presents the design of a microwave power sensor in X-band waveguide, which is based on Transmission line theory discussed in Chapter 3. Microwave power sensors traditionally use NTC thermistors for frequencies up to 50 GHz [1, 2]. As the first example of the design, an X-band waveguide thermistor power sensor at 10 GHz is designed using the design process. The chapter starts with solving the problem of modelling the sensing element in CST Microwave 3D design environment, which is followed by the determination of the mount dimensions. In this chapter, the complete structure of the sensor is introduced and the operating condition including temperature of the thermistor, heat dissipation is discussed in the thermal consideration section. The X-band sensor was fabricated and measured both at the University of Birmingham and at the National Physical Laboratory (NPL).

4.1. Modelling of the Sensing Element

The small bead thermistor from Sensor Scientific [3] was used in the design of the 10 GHz sensor. The bead has the body diameter of 0.36 mm and the nominal length of 0.5 mm, the lead wire diameter is 0.028 mm as shown in Figure 4.1. Due to the small size, the thermistor can be easily fitted in the 22.86 mm × 10.16 mm rectangular waveguide. The room temperature

(at 25 °C) resistance of the thermistor is 1000 Ω. At operating condition, the thermistor should be biased by d-c power down to a selected operating resistance, the resistance could be an arbitrary value but traditionally chosen at 100 Ω, 200 Ω or 400 Ω. In this application, the operating resistance is 200 Ω. The high negative temperature coefficient of -3.33% is desirable for the substitution power application as discussed further in Chapter 2.



Figure 4.1: The bead thermistor from Sensor Scientific [3].

In order to determine the impedance of the thermistor mount, the presentation of thermistor in EM simulation is required. There are two options of modelling electrical components. The first option is to build the physical component with all parameters from its datasheet in a full wave electromagnetic simulator such as CST. This method can obtain the closest representation of the component in simulation. Unfortunately, this approach encounters difficulties in obtaining the bead materials i.e. the permittivity; this information on bead thermistors is not available. The alternative way is to represent the component by its equivalent circuit. The latter approach is utilised in this design.

The bead behaviour was modelled over a broadband frequency range by the equivalent circuit in Figure 4.2. R_{th} is the d-c resistance of the thermistor. L_{wire} and r_{wire} are parasitic elements of

the thermistor wires. The capacitance C_{th} represents the non-linear semiconductor-type behaviour of the inner structure of the bead thermistor.

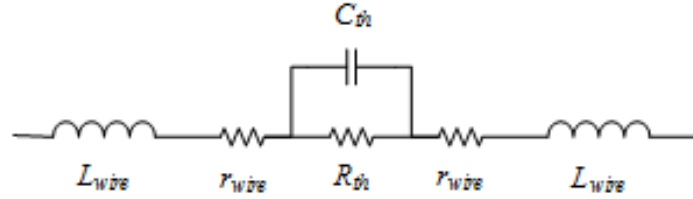


Figure 4.2: An equivalent circuit of an RF thermistor [4].

Unlike the values of the parasitic inductance and resistance of the wires which can be easily derived from the dimensions and the wire's material, the value of C_{th} depends on the thermistor body condition such as: temperature and the d-c resistance of the bead. In the work of Kazemipour [4], the self-capacitance was estimated at different resistance values from the measured scattering parameters of his bead thermistor. Note that the thermistor used by Kazemipour and the thermistor used in this design are different in size, 0.228 mm and 0.5 mm long, respectively. However, the electrical characteristic of the thermistors should be similar. Therefore, the capacitance C_{th} of the Sensor Scientific thermistor can be derived from the values of the capacitance recorded in [4].

The self-capacitance of the bead body can be calculated by equation 4.1, the derivation of the equation is presented in Appendix B.

$$C_{th} \approx \frac{\pi \epsilon_r \epsilon_0 l}{\ln(d - d_{wire}/2) - \ln(d_{wire}/2)} \quad (4.1)$$

where ϵ_r is the relative permittivity of the inner body material of the bead thermistor, the permittivity is assumed to have a non-linear relationship with the bead temperature. l and d are

the length and the width of the bead, respectively. d_{wire} is the diameter of the connecting wire. d_{wire} is very small compared to d , hence the capacitance is proportional to $\epsilon_r l / \ln(d)$.

The scaling formulas for the capacitances can be written as:

$$C_2 = \frac{\epsilon_{r2}}{\epsilon_{r1}} \frac{l_2}{l_1} \frac{\ln(d_1)}{\ln(d_2)} C_1 \quad (4.2)$$

where the capacitance values from [4] is denoted by 1 and the thermistor from Sensor Scientific is denoted by 2. With the assumption that the relative permittivities are equal at the same resistance of the thermistor, the equivalent capacitance C_{th} of the thermistor in this application can be estimated at different d-c resistance R_{th} , the result is shown in Figure 4.3.

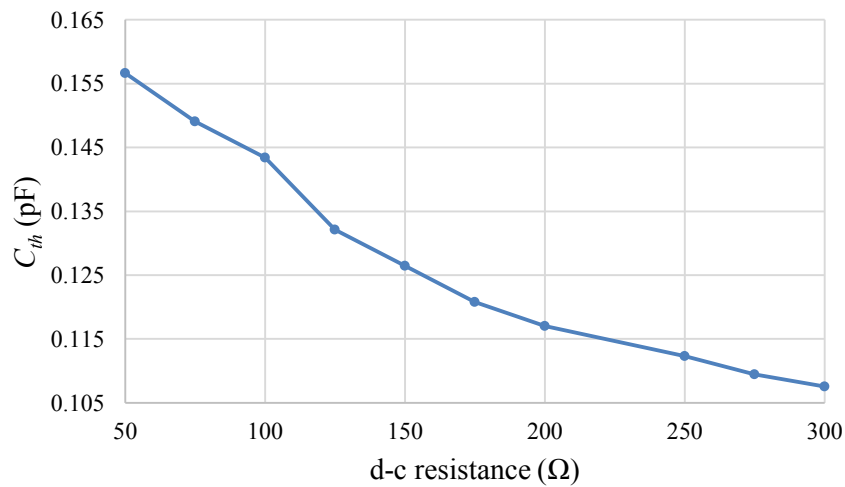


Figure 4.3: Equivalent capacitor C_{th} at different d-c biased thermistor's resistance.

At the chosen operating resistance of 200 Ω , the self-capacitance of the thermistor is about 0.117 pF. Note that if we use equation 4.1 to calculate the capacitance of the thermistor from Sensor Scientific, it gives 0.112 pF with the relative permittivity of ceramic of 25. Both approaches give very close values of the thermistor capacitance. In the following design, the

thermistor bead is presented by the resistor R_{th} of 200Ω in parallel with the capacitor C_{th} of 0.112 pF . Note that the simulation results in the following sections show no difference when using either of the capacitance values.

4.2. Design of the Mount for the Matching Condition Using Full Wave Simulation

This section presents the design of the thermistor mount in X-band power sensor. The structure of the mount is first introduced. The determination of the mount dimensions for matching condition is discussed.

4.2.1. The structure of the thermistor mount

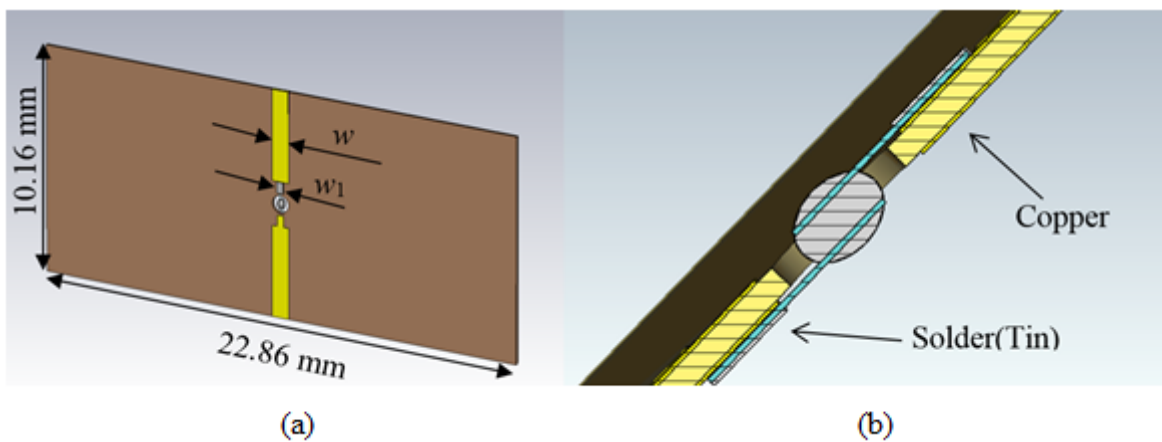


Figure 4.4: (a) The section in the waveguide of the PCB accommodating the bead thermistor; (b) the cut view to show how the thermistor is soldered on the PCB.

The bead thermistor is mounted on a double-sided PCB as can be seen in Figure 4.4(a). The PCB is made from RT/duroid 6010.2LM from Roger corporation [5]. The substrate thickness is $127 \mu\text{m}$, the substrate permittivity is 10.2 , and both sides are clapped with $17.5 \mu\text{m}$ copper. Figure 4.4(a) shows only the section of the PCB which is inside an X-band rectangular

waveguide, the width w of the copper track is an important parameters in finding matching condition. The width w_1 of the soldering area is 0.5 mm. In the centre of the PCB, a hole is drilled with 0.8 mm diameter for the thermistor to be accommodated. Additionally, the two connecting wires of the bead thermistor are soldered on the upper and lower sides of the PCB as shown in Figure 4.4(b).

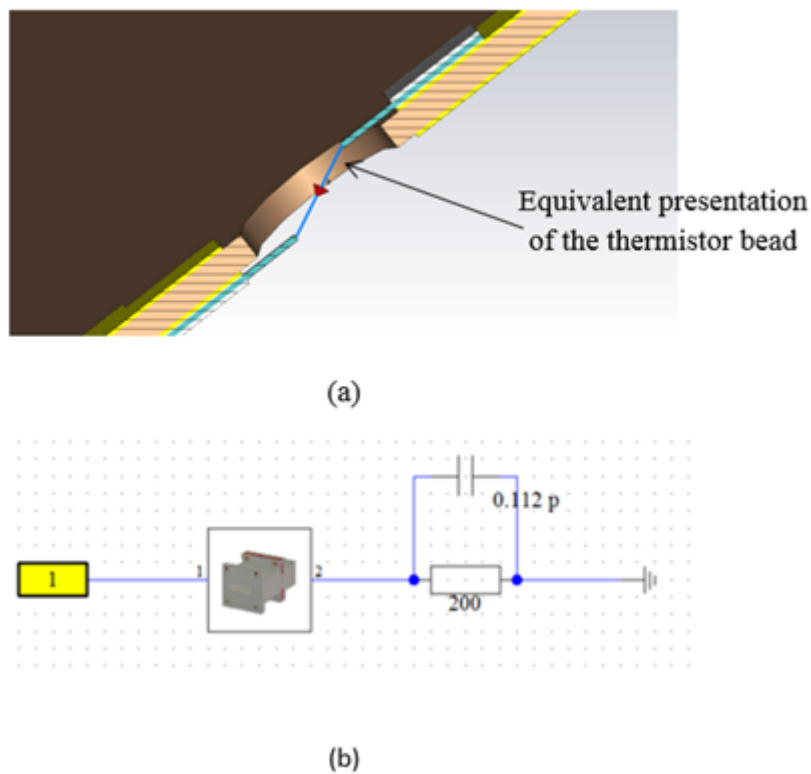


Figure 4.5: (a) The bead thermistor in the CST simulation; (b) the CST schematic diagram which includes the equivalent circuit of the thermistor bead.

As discussed in the previous section, the thermistor bead has an equivalent circuit of 200Ω resistor in parallel with a 0.112 pF capacitor. In simulation, the bead is modelled by the parallel circuit, the connecting wires of the thermistor are modelled by their physical constructions as the dimensions and the material of the wire are known. Figure 4.5(a) shows the model of the thermistor in CST design environment. The bead is replaced by a discrete port which is then

assigned as the equivalent circuit in Schematic design of the simulation as shown in Figure 4.5(b).

4.2.2. Determination of the mount dimensions

The dimensions of the mount consisting of the PCB and the bead thermistor are determined by the process of finding the matching condition as described in Chapter 3. The mount is first placed in the middle of an X-band waveguide with a length of two guided wavelengths ($2\lambda_g$) as illustrated in Figure 4.6. At the frequency of 10 GHz, the guided wavelength can be calculated by equation 3.24, it gives $\lambda_g = 39.75$ mm. Only the vacuum filling of the waveguide is presented in the figure, the surrounding material is set as PEC, and the two ends of the waveguide are connected to matched waveguide ports.

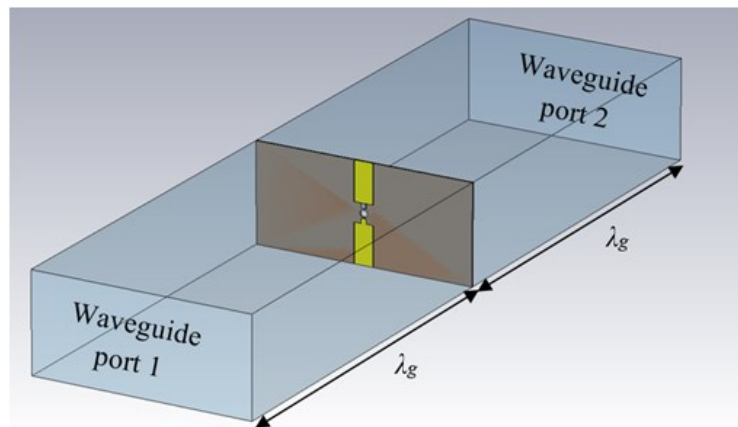


Figure 4.6: The two port simulation of impedance extraction for the thermistor mount.

The width of the PCB track, w (see Figure 4.4(a)) is treated as the parameter to adjust the impedance of the thermistor mount. The initial value for the PCB track width w is 2 mm. The reflection coefficient at the mount obtained from the simulation is $\Gamma = -0.511 + j0.327$. The normalised impedance of the mount can be calculated by equation 3.40, as follows.

$$\frac{Z}{Z_0} = \frac{R}{Z_0} + j \frac{X}{Z_0} = 0.1995 + j0.4416 \quad (4.3)$$

Where the characteristic impedance of the X-band waveguide at 10 GHz, Z_0 , is 444 Ω (calculated by equation 3.29), the resistance of the mount is then 88.58 Ω , which is smaller than the d-c operating resistance of the bead thermistor. This is an expected result because of the effect of the equivalent self-capacitance of the thermistor bead at high frequency.

Equations 3.18b and 3.18c can be used to determine the length l_R and l_X , respectively as follows

$$l_R = \frac{1}{2\beta} \arccos\left(1 - 2\frac{R}{Z_0}\right) = 16.927 \text{ mm} \quad (4.4)$$

$$l_X = \frac{1}{2\beta} \arcsin\left(-2\frac{X}{Z_0}\right) = 16.432 \text{ mm} \quad (4.5)$$

Where the propagation constant $\beta = 158.24 \text{ m}^{-1}$ is calculated from equation 3.23. Note that the electrical length l_R and l_X do not have physical meaning, these mathematical terms are used to find the matching point.

In order to obtain the matching at the centre frequency of 10 GHz, the effective electrical length l_R and l_X have to be equal. Therefore, the matching condition does not happen with the PCB width w of 2 mm. The values of the resistance length l_R and the reactance length l_X can be obtained at different track width w , these values can be plotted in Figure 4.7.

The figure shows how the effective lengths behave with the increase in the mount dimension. The change in the width of the PCB track mostly affects the reactance of the mount. As a result, there is a noticeable rise in the reactance effective length l_X while the resistance length l_R stays

almost unchanged. The interception between the two lines is where the matching condition is satisfied. The matching is suggested at the width $w = 2.325$ mm and the shorted electrical length $l_s = 16.92$ mm.

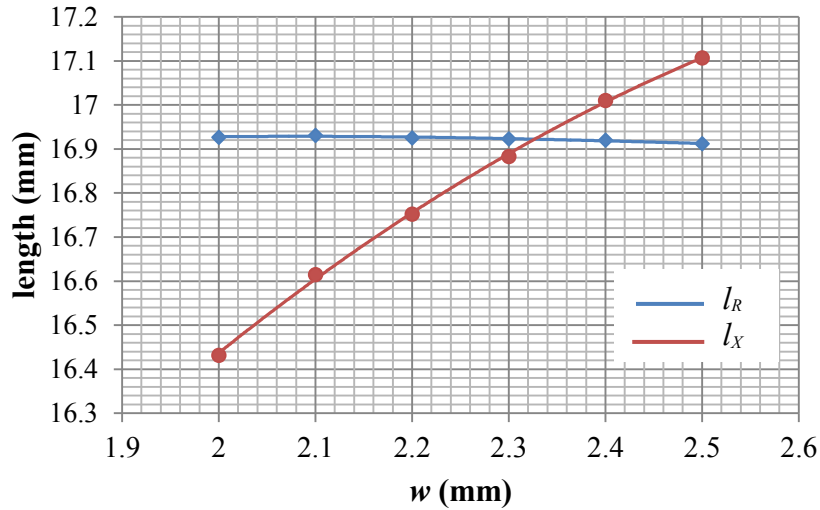


Figure 4.7: The effective length l_R and l_X at different widths w .

The above design process is validated by electromagnetic simulation. The designed mount is placed in a shorted X-band waveguide as shown in Figure 4.8, in which the distance from the mount to the shorted end is the determined length l_s and the length from the mount to the waveguide port 1 is equal to the guided wavelength λ_g .

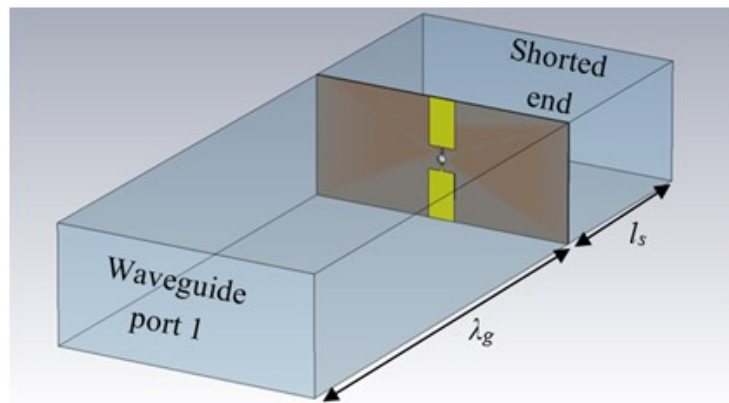


Figure 4.8: The simulation of the designed mount in a shorted waveguide.

The CST simulation gives the initial reflection coefficient of the waveguide sensor structure at the waveguide port 1, the result is depicted on Figure 4.9.

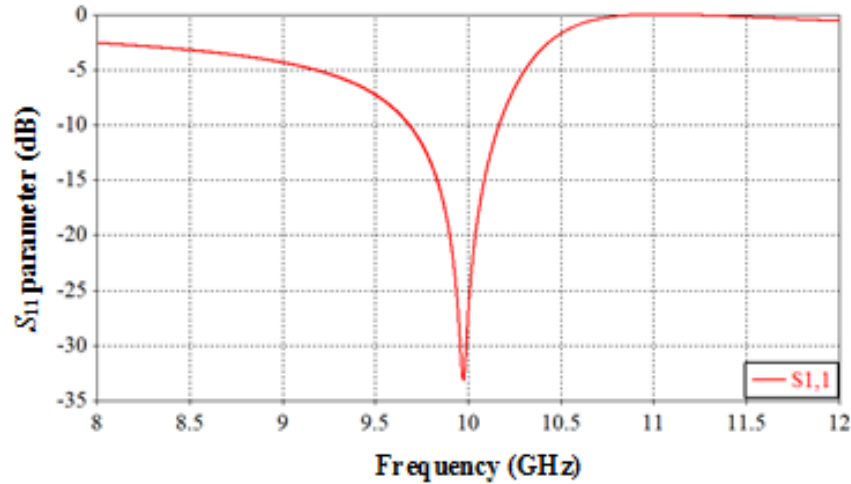


Figure 4.9: The reflection coefficient of the sensor simulation in Figure 4.8.

The reflection coefficient shows that the matching condition was obtained at 9.98 GHz which is very close to the targeted frequency of 10 GHz. The result proves the validity of the proposed design procedure. At 9.98 GHz, there is almost no reflected power. The incident power is dissipated at the lossy components inside the sensor structure including the PCB and the thermistor. The power loss simulation was conducted at 9.8 GHz, the result is shown in Figure 4.10. It can be seen that almost all the microwave power is dissipated at the region near the thermistor including four edges of the PCB and the thermistor itself. The contour is not displayed at the thermistor because it is a virtual port presenting the equivalent circuit of the thermistor bead (discussed in section 4.1). The power dissipated at the thermistor can be obtained by deducting the dissipated power on the PCB from the total input power.

The dissipated power on the PCB can be estimated by computing the amount of power dissipated in 0.5 mm radius around the edges. Note that at the distance of 0.5mm from the peak amplitude, the power loss distribution reduces from the maximum of 0.0263 W/m³ to

$0.001\text{W}/\text{m}^3$ by the radius. Thus, the power dissipated on the PCB is approximately 10^{-11} W. While In the simulation, the input signal of an excited waveguide port is normalised to 1 W peak power [6]. Therefore, the thermistor plays a dominant role in absorbing the incident microwave power.

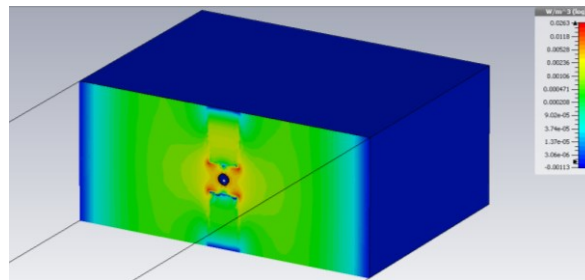


Figure 4.10: The power loss distribution inside the sensor at operating condition
The shift in the frequency can be eliminated by adjusting the shorted length l_s and the width w . A full wave optimisation will be run after the design of the complete power sensor structure discussed in the next section, because only the structure inside the hollow guide of the sensor is considered at this stage.

4.3. The Structure of the X-band Power Sensor

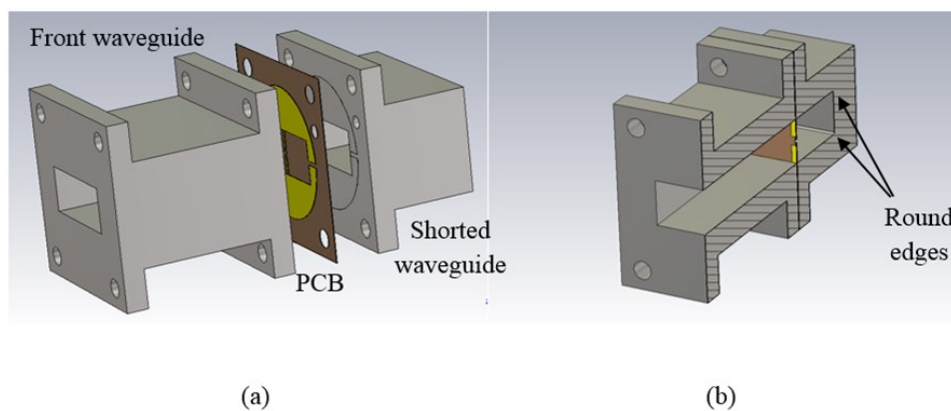


Figure 4.11: The structure of the X-band power sensor (a) before and (b) after assembling.

The structure of the power sensor is presented in Figure 4.11. There are two separate parts of the waveguide. The front part is a conventional X-band waveguide with the length of λ_g , and the second part is a shorted waveguide with the determined short length l_s . Due to the fabrication limitation of the milling tool, there are round edges of 0.5 mm in radius at the shorted end as shown in Figure 4.11 (b).

The double sided PCB, shown in Figure 4.11 (a), is positioned between the two waveguide parts. In addition to the PCB inside the waveguide in Figure 4.8, circular electrodes is added. The separation of 1 mm between the upper and lower electrodes is to create electrical isolation as shown in Figure 4.12(b). The circular electrodes is inspired by the circular waveguide flange [7] which is designed to stop leakages at waveguide flanges interfaces. Here it is to eliminate the microwave leakage through air gap at the contact between the PCB and the waveguide flanges. The distance from the broad waveguide wall to the top of the circular electrode is a quarter of the guided wavelength, so that it transforms the open circuit at the top of the electrode to the short circuit on the broad wall of the waveguide.

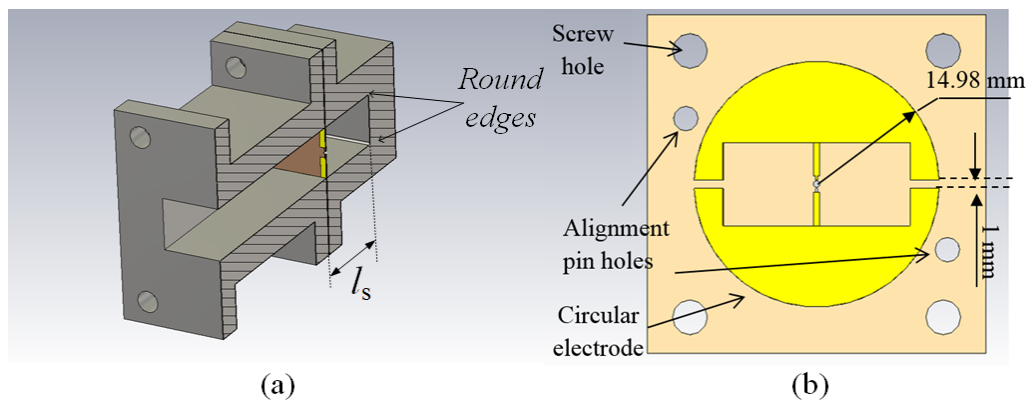


Figure 4.12: (a) The PCB clamped between two waveguide parts; (b) one side of the PCB.

When assembling, the PCB is clamped between the two waveguide parts by nuts and bolts through four holes. There are two additional holes for alignment pins on the PCB.

The simulation result, in CST Microwave Studio, of this whole structure is shown in red in Figure 4.13. This simulation uses the same dimensions w and l_s determined in the design progress in section 4.2.2. The presence of the PCB between the two waveguide parts causes the discontinuity in the waveguide. As a result, it can be seen that the reflection coefficient S_{11} is slightly shifted more to the lower frequency compared to the previous simulation result in Figure 4.9. The centre frequency is now at 9.932 GHz.

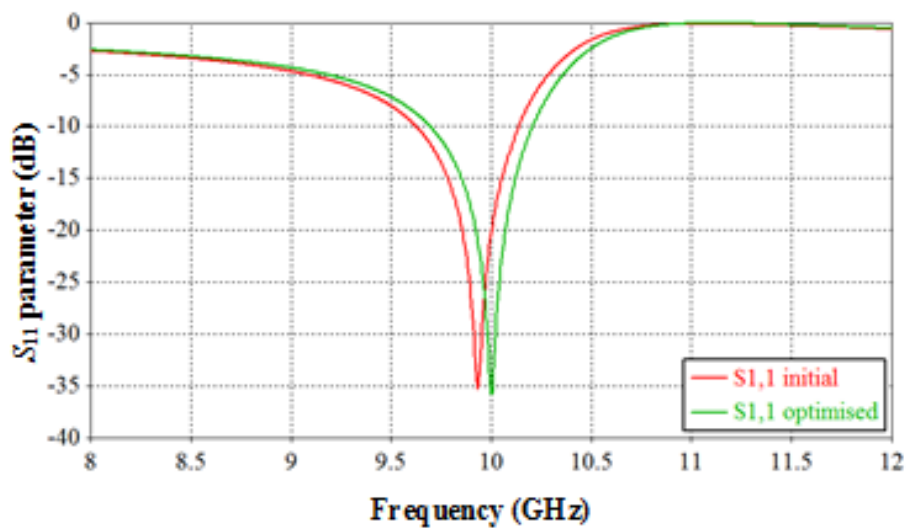


Figure 4.13: The simulation result of the power sensor in CST Microwave Studio.

As the targeted frequency of the power sensor is 10 GHz, the optimisation on the sensor dimensions can be run to achieve that goal. By adjusting the PCB track width w and the shorted length l_s , the optimised result, presented in Figure 4.13, was obtained with the minimum value of S_{11} of -35.8 dB at 10 GHz. The optimum parameters are included in Table 4.1. The construction of the sensor with detailed dimension of all the parts is presented in Appendix C.

Parameter	Initial	Optimised
The PCB width w	2.325 mm	2.330 mm
The shorted length l_s	16.920 mm	16.756 mm

Table 4.1: The initial and optimised parameters of the designed sensor.

It is worth comparing the optimum reflection coefficient obtained from the CST simulation to the transmission line model of the sensor described in Chapter 3 at the same electrical shorted length l_s of 16.756 mm. The comparison is shown in Figure 4.14. It can be easily seen that the calculated reflection coefficient from Transmission line theory agrees well with the simulated result. The bandwidths from the two approaches are very close. Both approaches have the minimum of S_{11} at less than -30 dB that means more than 99.9% of incident power is absorbed.

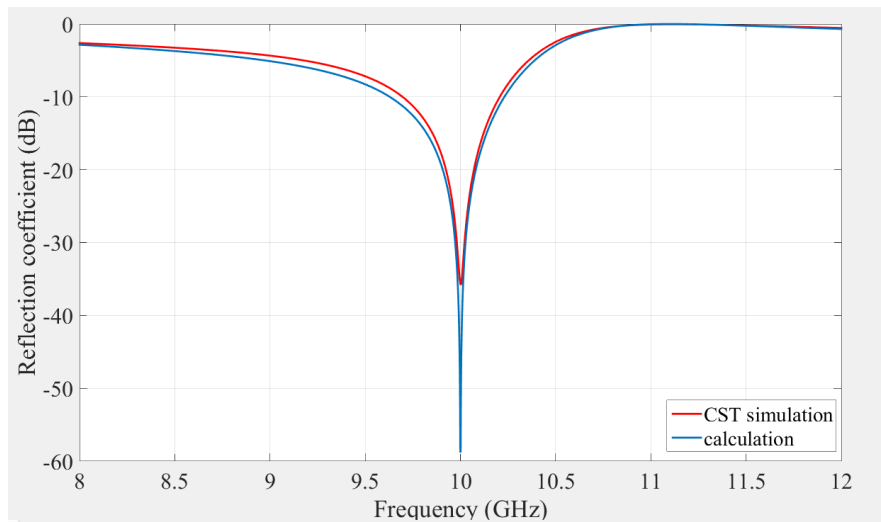


Figure 4.14: Comparison between the results from computer simulation and calculated model of the X-band sensor.

An important factor of the sensor is the bandwidth. As discussed in Chapter 3, the design approach results in narrow band sensors. The optimum S_{11} gives the -20 dB bandwidth of 145 MHz and the -15 dB bandwidth of 200 MHz. In practice, the reflection coefficient of -

15 dB is widely accepted for microwave power sensors [8], the -15 dB bandwidth of the X-band sensor can be improved by introducing a movable shorted end. The practice was reported in [1, 2, 9]. Figure 4.15 illustrates the simulated reflection coefficient of the sensor at different shorted lengths. By adjusting the shorted length l_s from 14.258 mm to 20.140 mm, the -15 dB band width can be enlarged to 1.5 GHz at the expense of the minimum value of S_{11} .

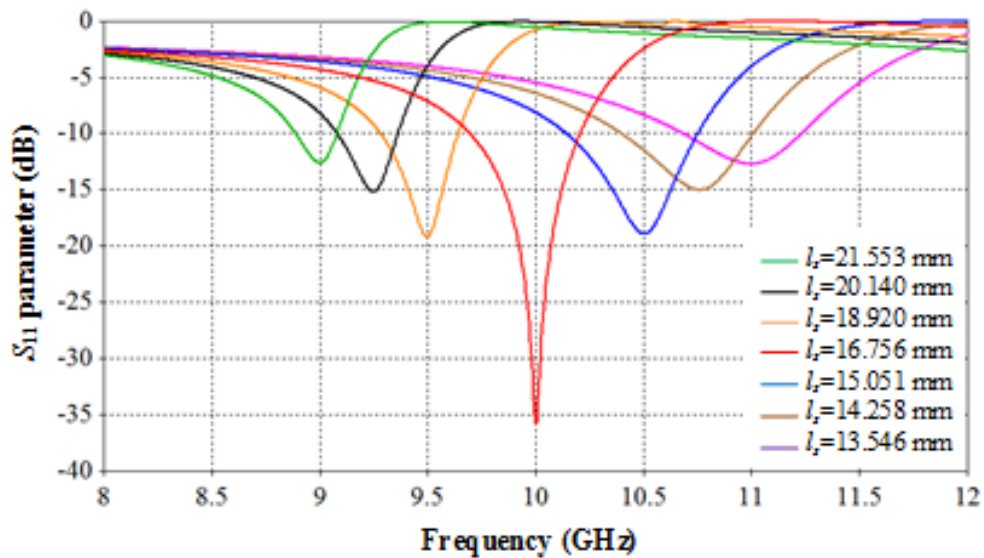


Figure 4.15: The change in S_{11} in the full-wave simulation when adjusting the shorted length.

4.4. Thermal Consideration

At the operating condition, the bead thermistor is heated by both d-c power and the absorbed microwave power as discussed in more detail in Chapter 2. The resistance of the bead is remained at the desired resistance of 200 Ω by the auto-balancing circuit. The bead itself is a heat source in the sensor, and there is a heat flow from the thermistor body and through the electrical contacts of the mount and the waveguide to the surrounding environment. At equilibrium, the heat flow should be equal to the total of d-c bias power and the absorbed

incident microwave power. In this work, the heat flow is estimated by both mathematical analysis and computer thermal simulation.

The thermistor is biased from $R_0=1000 \Omega$ ($T_0 =25 \text{ }^\circ\text{C}$) to $R=200 \Omega$. The temperature T of the bead thermistor can be obtained by Steinhart-Hart equation [10]

$$\frac{1}{T} = \frac{1}{T_0} + \frac{1}{B} \ln\left(\frac{R}{R_0}\right) \quad (4.6)$$

where B constant of the bead thermistor is 3000 [3], it gives $T = 354.7 \text{ K}$ or $81.7 \text{ }^\circ\text{C}$.

The heat not only dissipates through the surface of the bead by convection, but also flows in vertical and horizontal directions as demonstrated in red in Figure 4.16(a). The heat flow in the upper part is identical to the heat flow in the lower part of the power sensor. The equivalent thermal circuit of the sensor is shown in Figure 4.16(b), in which R_{conv} is the convection resistance of the bead body, R_{upper} and R_{lower} represent the thermal resistance of the upper and lower part. The temperature of the bead thermistor is T and the ambient temperature T_∞ is $20 \text{ }^\circ\text{C}$. When the heat flows in vertical direction, it follows the copper track of the PCB. The heat transfer in this direction mainly consists of conduction. In the horizontal direction, the heat goes through layers of the copper and the substrate of the PCB before transferring to the air on both sides of the PCB by convection.

In order to investigate the amount of heat flow, an equivalent thermal circuit representing the heat traveling in the upper part from the bead is used as shown in Figure 4.17, the heat flow in the lower part is identical. The heat source is the bead with temperature T , the ambient temperature T_∞ is $20 \text{ }^\circ\text{C}$. The thermal resistance R_{wire} represents the section of the thermistor

wire that connects the bead to the PCB. The resistance R_1 , R_2 and R_3 represent the thermal properties of the copper regions of the PCB as can be seen in Figure 4.17 (a).

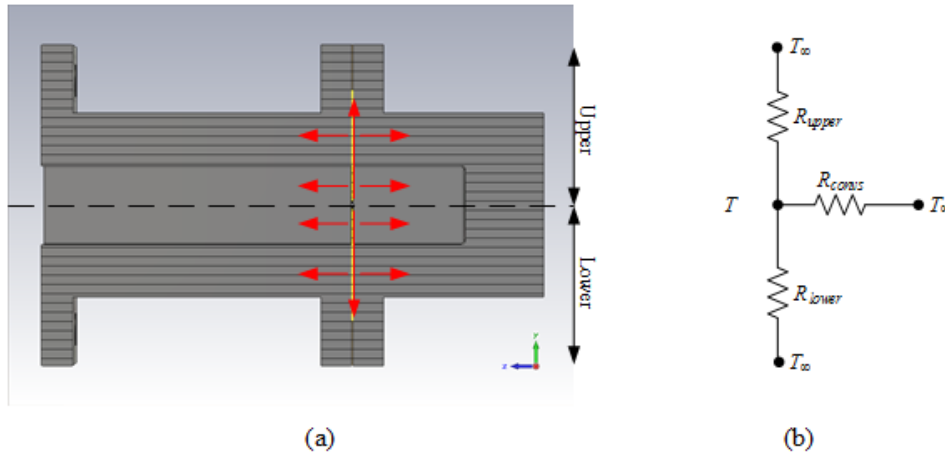


Figure 4.16: (a) The direction of the heat flow in the power sensor; (b) the equivalent thermal circuit of the sensor.

The resistance R_{d1} , R_{d2} , R_{d3} , $R_{copper1}$, $R_{copper2}$ and $R_{copper3}$ are the thermal resistances of the dielectric and the copper on the PCB corresponding to the position of the resistance R_1 , R_2 and R_3 . The convection resistances are R_{conv} , R_{conv1} , R_{conv2} and R_{conv3} . The heat transfer in the horizontal direction can be approximated to happen at the average temperature of each region. As a result, in the equivalent thermal circuit, the horizontal branches start in the middle of the thermal resistances R_1 , R_2 and R_3 as shown in Figure 4.17(b).

The calculation of the thermal resistance for conduction and convection is reviewed in [11] and all thermal calculations below are explained in this reference. The detailed dimensions of the sensor, especially the PCB, can be found in Appendix C. The calculation of the thermal resistance R_3 is based on the assumption that the heat transfer from R_2 in to R_3 region is in a fan-like fashion. The resistance R_3 can be estimated as

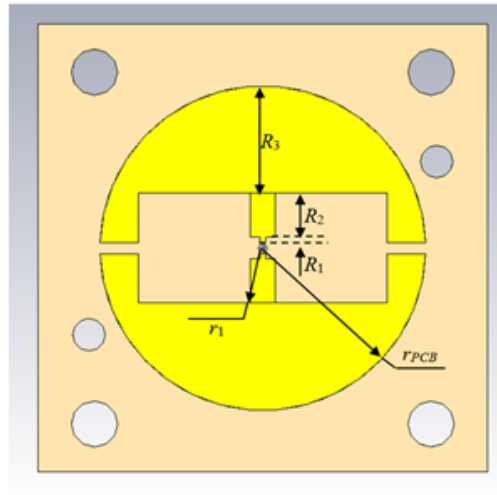
$$R_3 = \frac{1}{k_C t_{copper}} \int_{r_1}^{r_{PCB}} \frac{dr}{2r \times \arccos \frac{b}{2r}} \quad (4.7)$$

where k_C is the thermal conductivity of copper and equal to 401 W/(mK), t_{copper} is the thickness of the copper track on the PCB which is 17.5 μm . b is equal to 10.16 mm corresponding to the waveguide height. The integration radius r_1 and r_{PCB} are 5.199 mm and 14.98 mm, respectively. The equation gives $R_3 = 96.17 \text{ KW}^{-1}$. The calculation of the other equivalent resistors by equation 4.8 are straight forward as they have uniform cross sections. The values of the thermal resistances are included in Table 4.3.

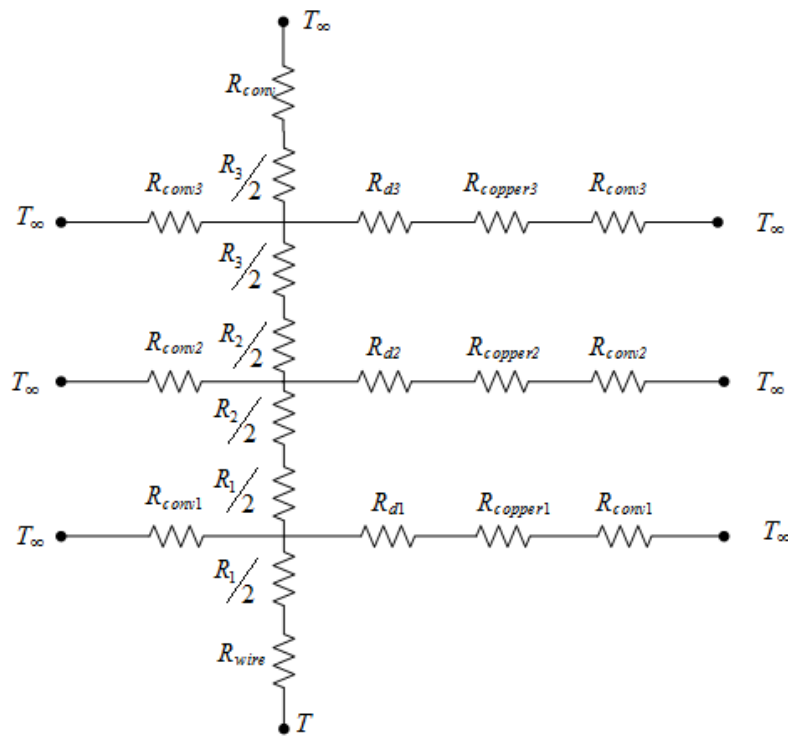
$$R_{thermal} = \frac{1}{k} \frac{l}{S} \quad (4.8)$$

Thermal resistance	Value (KW ⁻¹)
R_{wire}	7904
R_1	142.5
R_2	249.5
R_3	96.17
R_{d1}	2540
R_{d2}	66.8
R_{d3}	3.13
$R_{copper1}$	0.175
$R_{copper2}$	4.59×10^{-3}
$R_{copper3}$	2.15×10^{-4}
R_{conv}	288309
R_{conv1}	800000
R_{conv2}	21038
R_{conv3}	984

Table 4.2: The values of the thermal resistances of the thermal circuit in Figure 4.17(b).



(a)



(b)

Figure 4.17: (a) The regions of the equivalent thermal resistances on the PCB; (b) the thermal circuit of the heat flow from the thermistor bead in the upper part.

The total resistance of the circuit in Figure 4.16(b) can be obtained by the circuit analysis, and gives $R_{upper} = 8794 \text{ KW}^{-1}$

The convection resistance of the body of the bead can be calculated as

$$R_{convs} = \frac{1}{k_{air} S_{ellipsoid}} \quad (4.9)$$

where the convection coefficient of still air k_{air} is $5 \text{ W}/(\text{Km}^2)$, the surface area of the bead $S_{ellipsoid}$ is $5.16 \times 10^{-7} \text{ m}^2$. Thus, the resistance R_{convs} is $387.6 \times 10^3 \text{ KW}^{-1}$ and is considerably larger than the conduction resistance showing convection has only a small effect.

The total heat flow from the bead thermistor can be calculated by the equivalent circuit in Figure 4.15(b) as

$$Q_{total} = (T - T_{\infty}) \left(\frac{1}{R_{upper}} + \frac{1}{R_{lower}} + \frac{1}{R_{convs}} \right) = 14.19 \text{ mW} \quad (4.10)$$

The result can be validated by using CST MPhysics simulation [6]. The whole structure of the sensor in Figure 4.10 is input into the simulator. The thermistor bead presented by a physical bead in Figure 4.17 is set as a temperature source of 354.7 K. The physical properties of the surrounding space is inputted as those of the dry air with the convection constant of $5 \text{ W}/(\text{km}^2)$ and the thermal boundary is isothermal ($T=293.15 \text{ K}$). The temperature distribution of the sensor in Figure 4.17 shows that the hottest region in the sensor is at the bead and the connecting wires, the temperature of the copper on the PCB is equal to the ambient temperature. The thermal simulation also gives the total heat flow of 14.44 mW from the temperature source. The result is very close to the calculated value of 14.19 mW. As discussed in Chapter 2, the heat flow from the thermistor at operating condition suggests that the maximum measuring power is about 14 mW.

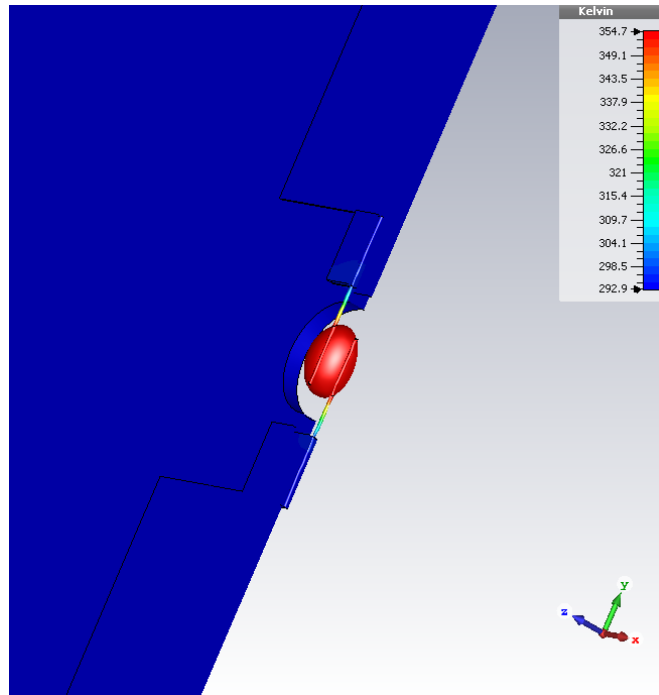


Figure 4.18: The temperature distribution in the sensor at operation condition.

At the thermal equilibrium without the presentation of r-f power, the d-c dissipated power on the thermistor is equal to the heat flow out of it, an equation can be generated as follows.

$$P = I^2 R = \delta(T - T_{\infty}) \quad (4.11)$$

Where δ , the dissipation constant of the bead thermistor, defines the amount of electrical power which will raise the body temperature by one degree Celsius above ambient temperature. The dissipation constant at the ambient temperature of 20 °C can be calculated as [10]

$$\delta = \frac{P}{T - T_{\infty}} = 0.246 \text{ mW}/^{\circ}\text{C} \quad (4.12)$$

The power sensitivity of the sensor at operating condition can be derived from equation 4.6 and equation 4.11 as follows

$$\frac{\delta R}{\delta P} = \frac{\delta R}{\delta T} \times \frac{\delta T}{\delta P} = 19.386 \text{ } \Omega/\text{mW} \quad (4.13)$$

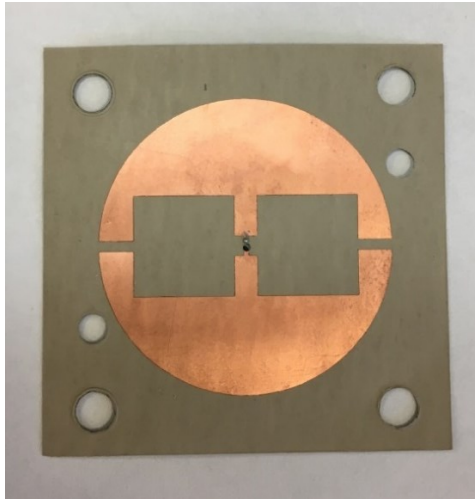
The result suggests that the resistance of the bead thermistor should change about 19 Ω if there is 1 mW of microwave power absorbed by the sensor. The value is sufficient for the power application and similar to the sensitivity of published thermistor sensors [12, 13]

4.5. Fabrication and Measurement

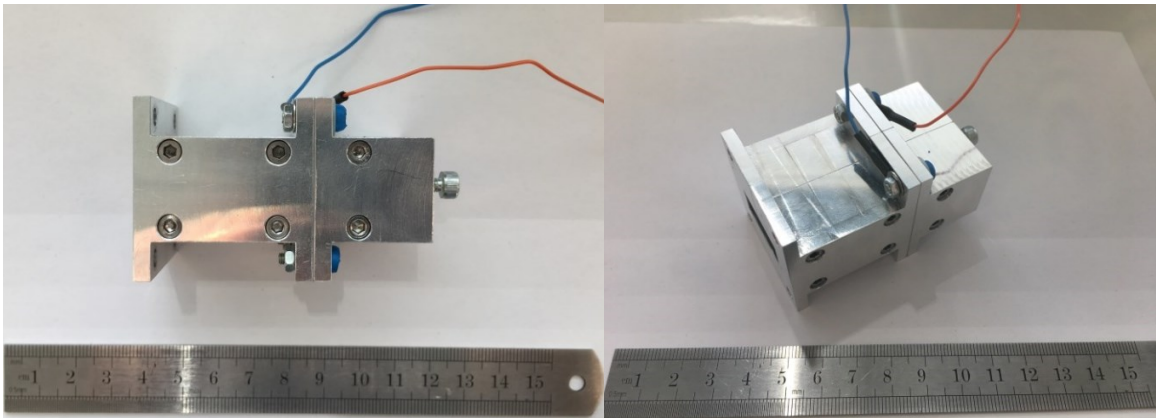
This section introduces the fabricated X-band power sensor. The measurement of the reflection coefficient of the sensor is discussed. The measurement of the power linearity at the University of Birmingham is introduced. Finally, the result of the sensor calibration at NPL is presented.

4.5.1. The fabrication of X-band power sensor

The fabricated PCB and sensor are shown in Figure 4.19; all the dimensions are the same as described in the simulations above. The PCB is made of Roger RT/duroid 6010.2 LM [5]. The thermistor from Sensor Scientific [3] was soldered on two sides on the PCB as shown in Figure 4.4. The waveguide parts are made from two halves with the cut on E-plane as discussed in Chapter 3. The PCB is clamped in the middle of the two aluminium waveguide parts by four isolation screws. At the back of the shorted waveguide part, there is an M4 screw for tuning which can be seen in Figure 4.19(b). The red wire is connected to the short waveguide part and the blue wire is connected to the front waveguide of the sensor, then the d-c bias is applied to the thermistor through the wires.



(a)



(b)

Figure 4.19: The double-sided PCB with a thermistor soldered at the centre and (b) the assembled X-band sensor.

By using the NPL auto-balancing circuit reviewed in Chapter 2, the thermistor can be biased to any resistances for testing. The assembled sensor was taken in to measurements of the reflection coefficient, the sensor linearity, the effective efficiency and the calibration factor.

4.5.2. Measurement of the reflection coefficient

The sensor is connected to one port of the Vector Network Analyser (VNA). The result of the measurement, when the thermistor is at 200Ω , is presented in Figure 4.20. The measured

reflection coefficient has the minimum of -21.53 dB at 9.88 GHz. The measured response has the similar shape to the simulated response, but the centre frequency was shifted away from 10 GHz. The difference between simulation and measurement may be attributed to a number of factors such as the dimensions of the fabricated PCB and waveguide and the modelling of the bead thermistor in the simulation.

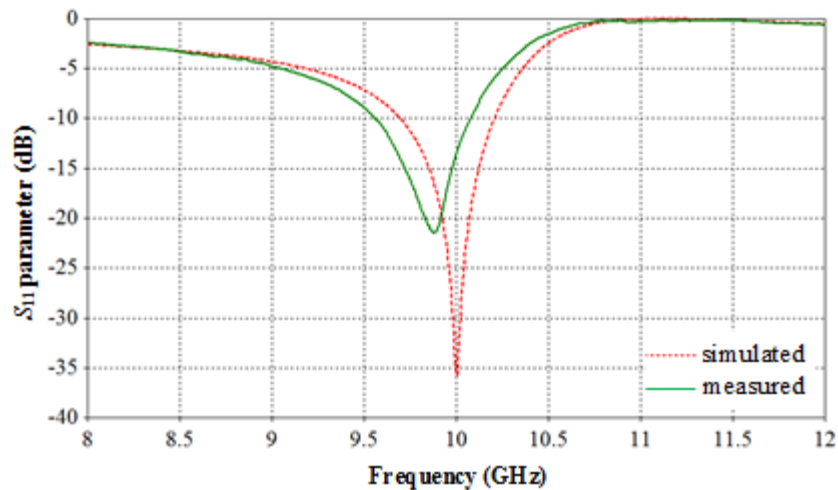


Figure 4.20: The measured reflection coefficient of the sensor at 200 Ω thermistor biasing.

In fact, the waveguide parts of the sensor were made by CNC milling technique with the accuracy of $\pm 10 \mu\text{m}$. The measured dimensions of the fabricated waveguide was used to simulate the sensor response, and no deviation from the simulated response in Figure 4.20 was observed.

The dimensions of the PCB were measured by microscope. The measured PCB track width w and soldering area width w_1 (see Figure 4.4) are 2.247 mm and 435 μm , instead of the designed values of 2.33 mm and 500 μm , respectively. The other dimensions of the PCB are very close to the simulated values. The simulation is run for the measured values of the PCB, the result is shown in black in Figure 4.21.

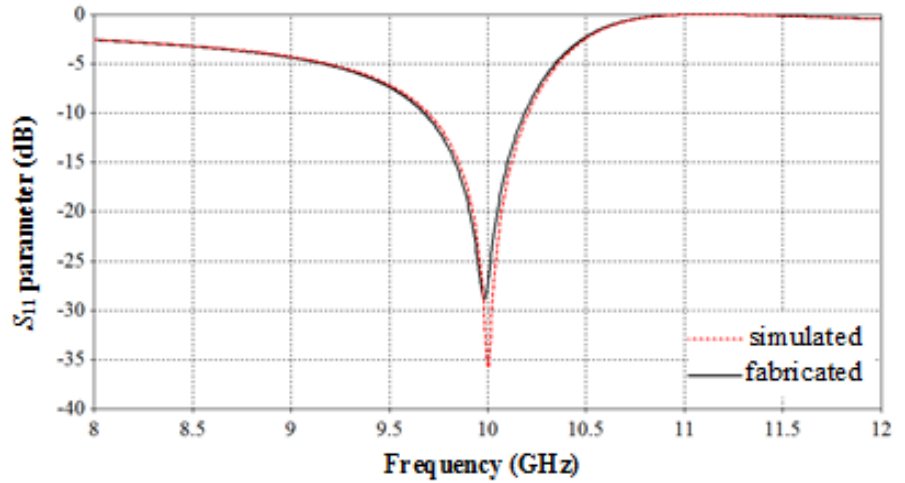


Figure 4.21: The simulated response of the sensor with the measured PCB dimensions

The figure shows a small deviation compared to the expected simulated response. Therefore, the main cause of the deviation between the simulated and measured response in Figure 4.20 is believed to be at the bead thermistor equivalent circuit in section 4.1. The CST simulation was used to simulate the response of the sensor at different equivalent self-capacitance C_{th} of the bead thermistor other than the estimated value of 0.112 pF, the large deterioration in the reflection coefficient was observed and the simulated response in Figure 4.20 could not be achieved. Therefore, the equivalent circuit of the thermistor should be much more complex at high frequency than the equivalent circuit in Figure 4.2.

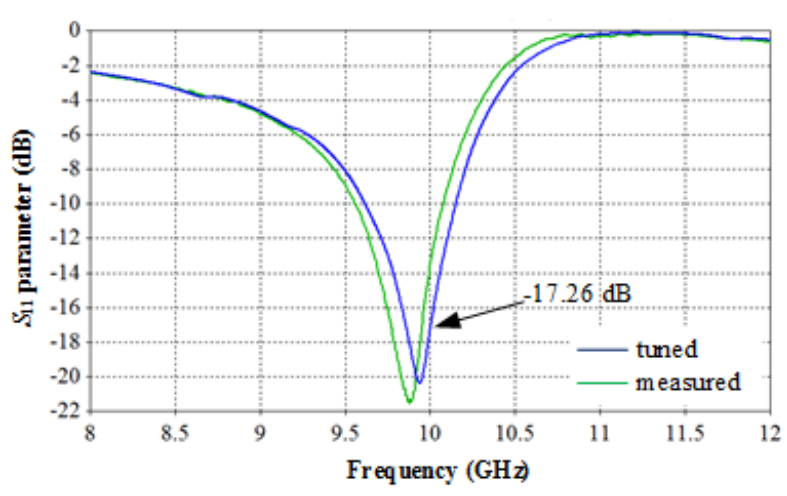


Figure 4.22: The tuned S_{11} parameter (in blue) by introducing a tuning screw at 200 Ω bias.

In order to minimise the shift in frequency, a M4 tuning screw was introduced at the shorted end as shown in Figure 4.19(b). The extrusion of the screw from the shorted wall changes the effective shorted length l_s of the sensor. By applying the method, the centre frequency can be moved to 9.94 GHz as shown in blue in Figure 4.22. The reflection coefficient at 10 GHz is -17.26 dB.

The second method of tuning the response of the sensor is by adjusting the thermistor resistance. The thermistor can be biased to and maintained at different resistances other than 200 Ω by the auto-balancing circuit. The change of the d-c bias on the thermistor varies the impedance of the mount, thus changing the reflection coefficient of the sensor. By adjusting the operating resistance of the thermistor to 400 Ω , the centre frequency of S_{11} can be moved to 10 GHz without additional deterioration in S_{11} , this is shown in Figure 4.23. The reflection coefficient at 10 GHz is -23.41 dB in this case.

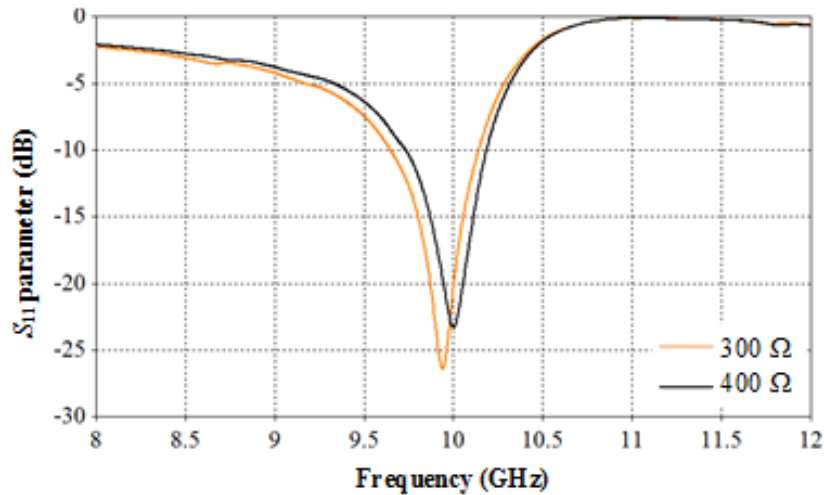


Figure 4.23: The optimised response of the sensor at different biasing conditions.

It is worth mentioning that the best absorption of incident power can be found at 300 Ω thermistor resistance as shown in orange in the above figure, here S_{11} is -26.41 dB at 9.94 GHz.

4.5.3. Measurement of the linearity with power

The measurement is to observe the d-c substitution power on the bead thermistor at different microwave input powers to the X-band sensor. The sensor was measured in two operation modes at the centre frequency of 10 GHz including: (1) 200 Ω thermistor resistance and (2) 400 Ω thermistor resistance. The measurement set up is presented in Figure 4.24.

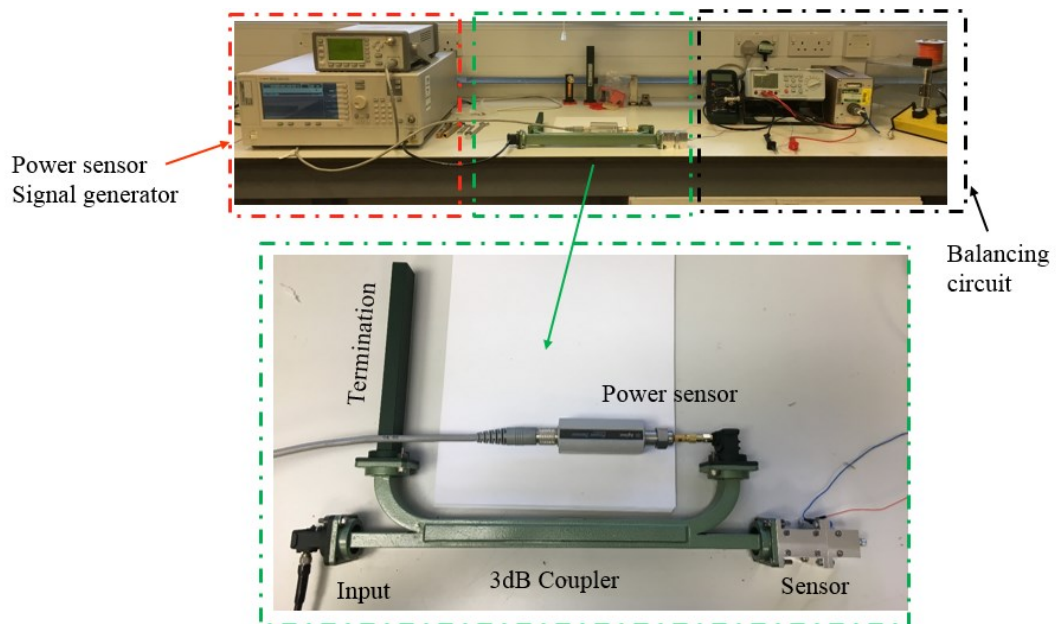


Figure 4.24: The power measurement set up. The red box contains a power meter and a signal generator to monitor the input power of the X-band sensor. The auto-balancing circuit and the voltmeter in the black box are to monitor the thermistor resistance and record the biased voltage on the thermistor. The directional 3dB coupler in the green box is to divide the power from the input port to the power sensor and the sensor.

A 3 dB coupler is used to split the input power from a signal generator at 10 GHz to both its through port and coupled port. The coupled port is connected to a coaxial power meter by a coax to waveguide adapter from Flann Microwave [14]. The sensor is connected to the through port of the coupler. The ratio of the power available at the through port to that at the coupled

port is 1.168 which is close to the specification of equally splitting power at the two ports of the 3 dB directional coupler. The coax to waveguide adapter itself has the measured insertion loss of -0.275 dB. By monitoring the power meter at the coupled port, the incident power to the sensor at the through port is known.

At 200 Ω thermistor resistance, the sensor has the reflection coefficient as in blue in Figure 4.21. The resistance of the thermistor is maintained at 200 Ω during the measurement by the NPL auto-balancing circuit, the voltage on the bead is recorded by a voltmeter. Without microwave power, the voltage on the thermistor is 1.615 V. The d-c dissipated power is 13 mW that is close to the expected value discussed in Section 4.4. When the microwave power is applied, the d-c power should be reduced in order to maintain the thermistor resistance. The reduction in power is indicated by the decrease in the thermistor voltage reading. The d-c substitution power P_{sub} was recorded at different r-f input powers P_{in} . The relationship between P_{sub} and P_{in} at 200 Ω operation is plotted in Figure 4.25.

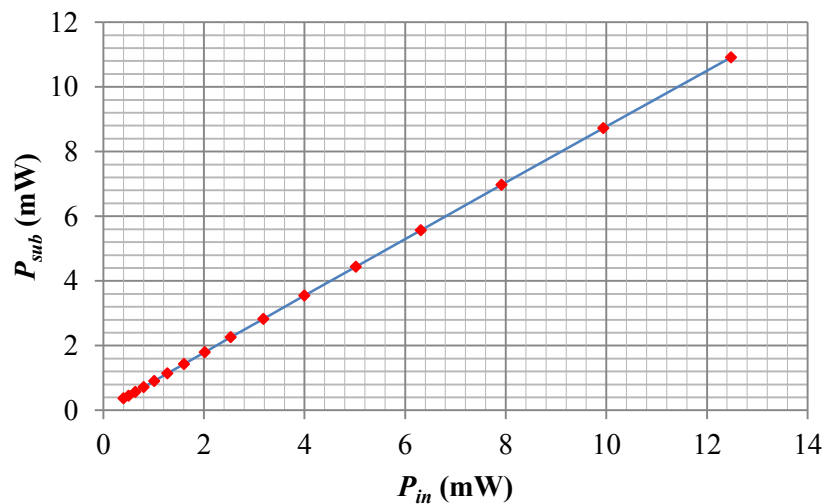


Figure 4.25: The relationship between input power and substitutional power at 200 Ω thermistor operation.

In the above figure, the red dots are the measured points at different input powers up to 12.5 mW and the blue fitted line shows that the d-c substitution power is linear to the microwave input power. The mathematical relationship can be obtained by using linear regression algorithm, which gives

$$P_{sub} = 0.8815P_{in} + 0.0269 \text{ (mW)} \quad (4.14)$$

The correlation coefficient r of the regression is 0.9999, which suggests an excellent positive linear relationship. The small common error variance σ of 17×10^{-3} validates the small errors obtained. The non-zero second term in equation 4.14 of 0.0269 can be due to the factors such as the temperature drift and noise which are common for this kind of power sensor. The phenomenon was reported in [15] as power meter zero offset.

There are deviation between P_{sub} and P_{in} can be caused by other uncertainties associated with the electronics. The non-zero offset is likely attributed by improper zero-setting, zero carryover, drift and noise[15]. The noise in power measurement can come from the electronic circuit of the meter and the thermistor itself. At the operating condition of 200 Ω , the thermistor is heated to 354.7 K as discussed in section 4.4, the mean power of thermal noise of the thermistor can be estimated by the total thermal noise on a 200 Ω resistor and 0.112 pF capacitor. Thermal noise on capacitor is dominant and can be calculated as [16]

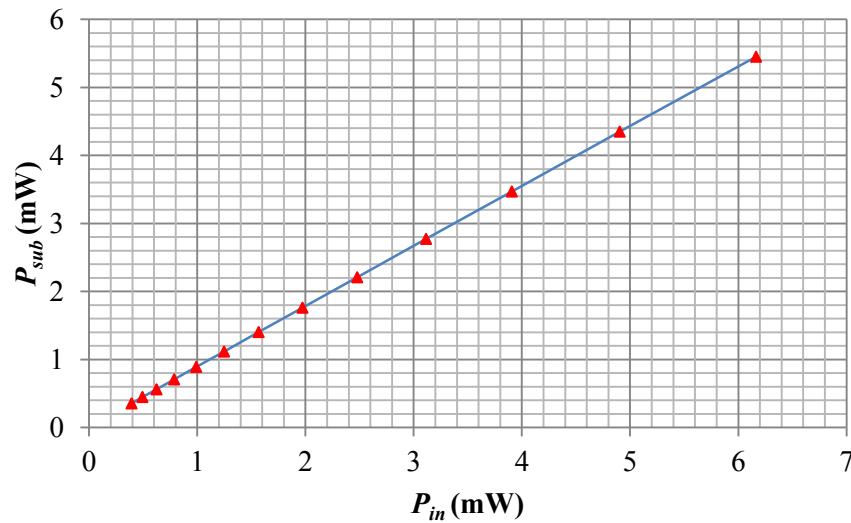
$$P_{ther} = \frac{kT}{C} = 4.37 \times 10^{-5} \text{ (mW)} \quad (4.15)$$

where k is the Boltzmann constant, T is the temperature of the bead thermistor and C is the equivalent capacitance.

It can be seen that the thermal noise of the thermistor is very small compare to the non-zero offset of 0.0269. In fact, for a typical absolute power measurement, the total noise contributes

the uncertainty of $\pm 0.025 \mu\text{W}$ [15], which is negligible in the measurement range of bolometer (10 μW to 10 mW). Therefore, at low power level, the non-zero offset is caused by the electronics of the power meter and can be eliminated in the calibration and offsetting the power meter.

Another interesting case is when the thermistor is at 400 Ω was also investigated, the sensor response is in black in Figure 4.22. The measured reflection coefficient of the sensor in this case is the lowest value obtained from the sensor tuning described in section 4.5.2. The same set-up can be used, the balancing circuit was modified so that the circuit maintains the thermistor resistance at 400 Ω . The results of the substitution power P_{sub} and input power P_{in} up to about 6 mW are shown in Figure 4.26.



The correlation coefficient r and the error variance σ of the linear regression are 0.9999 and 4.85×10^{-3} , respectively. They confirm the excellent linearity with low error.

The measurement of the sensor with microwave powers showed that the sensor has a linear response with r-f input power at 10 GHz when the thermistor is operating at either 200 Ω or 400 Ω . The importance result indicates the usability of the sensor, and it should be compatible with commercial thermistor meter i.e. N432A power meter from Keysight [17].

4.5.4. Measurement of effective efficiency and calibration factor

The definition of the factor and efficiency was reviewed in Chapter 2. The calibration factor k_b of the sensor can be obtained from the previous power measurement as the ratio of the d-c substitution power to the r-f input power. The effective efficiency η_e is defined as the ratio of substitution power to absorption power and it can be calculated as [15].

$$\eta_e = \frac{k_b}{1 - |I|^2} \quad (4.17)$$

where I is the Voltage Reflection Coefficient (VRC) at the operating frequency. The calibration factor and effective efficiency at 200 Ω and 400 Ω sensor operation are determined from equation 4.16 and given in Table 4.3.

Thermistor resistance (Ω)	VRC	Calibration factor	Effective efficiency
200	$0.137 \angle -29.564^\circ$	0.8815	89.73%
400	$0.068 \angle -6.145^\circ$	0.8836	89.95%

Table 4.3: The calibration factor and effective efficiency from the measurement at the University of Birmingham.

The sensor was taken to National Physical Laboratory (NPL) and measured by the X-band multi-state reflectometer [18]. The setup measures the sensor under different microwave input powers, the relationship between substitution power and input power of the sensor is obtained and then compared to the data of three standard sensors, which are preserved by NPL for commercial calibration services. The effective efficiency and calibration factor are subsequently deduced by averaging the results of the three comparison. The results are given in Table 4.4.

Thermistor resistance (Ω)	VRC	Calibration factor	Effective efficiency
200	$0.133 \angle 328.531^\circ$	0.8450	86.06%
400	$0.073 \angle 24.145^\circ$	0.8494	85.4%

Table 4.4: The calibration factor and effective efficiency from the measurement at National Physical Laboratory.

The measured VRCs of the sensor at both places are similar, but the calibration factors and efficiencies are slightly different. It is clear that the measurement at Birmingham suffers from improper zeroing and the accumulated errors in the equipment such as the coax to waveguide adapter and the power meter. Therefore, the measurement at Birmingham can be used to prove the linearity of the sensor and estimate the calibration factor, while the more accurate measurements of the calibration factor and effective efficiency can be the values obtained from the measurement at NPL.

The imperfect effective efficiency (less than 100 %) is caused by (i) microwave leakage and/or (ii) a fraction of absorbed power dissipating outside of the thermistor bead. The potential microwave leakage is at the substrate of the PCB and the contacts between the PCB and waveguide flanges. In this particular case, the leakage is negligible because the air gap (about

20 μm) and the PCB thickness (127 μm) are very small as compared to the waveguide size of 22.86 mm \times 10.16 mm, the leakage of less than 0.2 % incident power was evaluated by EM simulation. Therefore, the main reason here is believed to be at the thermistor. The phenomenon was discussed in Collard 's work [19]. The thermistor resistance consists of the contact resistance and the semiconductor resistance which is sensitive to temperature. At d-c and low frequency operation, the semiconductor resistance is dominant. At high frequency, the effective capacitance C_{th} (see figure 4.2) tends to shunt the semiconductor resistance, so that the effective resistance of the bead gets smaller and the contact resistance becomes comparable to it. Thus, the absorbed microwave power is not entirely dissipated in the semiconductor part of the thermistor. A high frequency bead thermistor is designed to minimise the effect, and is used in the standard power sensors with the effective efficiency of about 98%. The thermistor used in this thesis is, in fact, intended for much lower frequency applications. As a result, the parasitic elements can affect the performance of the thermistor as indicated by the measured effective efficiency.

References

- [1] "Technique of microwave measurements / edited by Carol G. Montgomery. Vol.1," C. G. Montgomery, Ed., ed. New York: Dover : Constable, 1966.
- [2] K. Sakurai and T. Nemoto, "A Thin-Film Bolometer Unit," *Instrumentation and Measurement, IEEE Transactions on*, vol. 16, pp. 206-211, 1967.
- [3] SensorScientific. *Small Bead hermistor*. Available: http://www.sensorsci.com/literature/122766/Glass_Bead_Thermistors
- [4] A. Kazemipour, F. Ziade, D. Allal, M. Z. M. Jenu, and E. Bergeault, "Nonlinear Modeling of RF Thermistor: Application to Bolometer Mount Calibration," *Instrumentation and Measurement, IEEE Transactions on*, vol. 60, pp. 2445-2448, 2011.
- [5] Rogercorp. (2015). *RT/duroid® 6006/6010LM High Frequency Laminates*. Available: <https://www.rogerscorp.com/documents/612/acs/RT-duroid-6006-6010LM-Laminate-Data-Sheet.pdf>
- [6] *CST-Computer Simulation Technology- Microwave Studio* Available: <https://www.cst.com/>
- [7] D. M. Pozar, "Microwave engineering / by David M. Pozar," 4th ed. ed. Hoboken, N.J.: Wiley, 2012.
- [8] G. H. Bryant, "Principles of microwave measurements / by G.H. Bryant," E. Institution of Electrical, Ed., ed. London: Peregrinus on behalf of the Institution of Electrical Engineers, 1988.
- [9] I. Lemco and B. Rogal, "Resistive-film milliwattmeters for the frequency bands: 8·2-12·4 Gc/s, 12·4-18 Gc/s and 26·5-40 Gc/s," *Proceedings of the IEE - Part B: Electronic and Communication Engineering*, vol. 107, pp. 427-430, 1960.
- [10] "NTC Thermistors," *Application notes, edited by BOWTHORPE THERMOMETRICS, THERMOMETRICS, INC. KEYSTONE THERMOMETRICS CORPORATION*.
- [11] *Principles of heat and mass transfer / Frank P. Incropera ... [et al.]*, 7th ed. ed. Hoboken, N.J.: Hoboken, N.J. : Wiley, 2013.
- [12] A. Fantom, *Radio Frequency & Microwave Power Measurement*: P. Peregrinus, 1990.
- [13] J. A. Lane, *Microwave power measurement / (by) J.A. Lane*. London: London : Peter Peregrinus Ltd (for) the Institution of Electrical Engineers, 1972.
- [14] FlannMicrowave. *Waveguide to SMA Coax Adaptors Series 094-SF40*. Available: <https://www.flann.com/wp-content/uploads/2015/09/Series-094-SF40.pdf>

- [15] "Fundamentals of RF and Microwave Power Measurements (Part3) Power Measurement Uncertainty per International Guides," *Agilent Technologies, Application note 64-32, 5988-9215EN*, April 2011.
- [16] T. D. a. C. A. M. R. Sarpeshkar, "White noise in MOS transistors and resistors," *IEEE Circuits and Devices Magazine*, vol. 9, pp. 23-29, Nov. 1993.
- [17] K. Technologies. (November 21, 2014). *N432A Thermistor Power Meter*. Available: <http://literature.cdn.keysight.com/litweb/pdf/5990-5740EN.pdf?id=1891411>
- [18] N. P. Laboratory. *Waveguide Power Transfer Standards - Multi-State Reflectometers*. Available: <http://www.npl.co.uk/instruments/products/rf-microwave/waveguide-power-transfer-standards-multi-state-reflectometers/>
- [19] J. Collard, G. R. Nicoll, and A. W. Lines, "Discrepancies in the Measurement of Microwave Power at Wavelengths below 3 cm," *Proceedings of the Physical Society. Section B*, vol. 63, p. 215, 1950.

Chapter 5

High Frequency Microwave Power Sensor Design Using Temperature Dependent Resistive Films

The validity of the microwave power design process based on Transmission line theory was proven in Chapter 4. This chapter introduces the design of W-band waveguide sensor using the same principle. The waveguide size reduces as the operating frequency increases. Consequently, commercial thermistors are no longer suitable for the sensor design. For instance, the bead thermistor with 0.5 mm long is half of the size of the WR3 waveguide (0.864 mm × 0.432 mm). Therefore, the temperature dependent resistive (TDR) films need to be used as the sensing element for the high frequency application. This approach is believed to be the way forward in high frequency power sensor designs, in which the sensing element is made for specific sensor designs. The chapter first reviews the material choices for the resistive films. The proposed solution to modelling problems in the electromagnetic wave simulation is then presented. The design procedure based on the Transmission line theory is implemented for 94 GHz power sensor, and the complete structure of the W-band sensor is introduced. Finally, the designs of WR-6 and WR-3 power sensors are presented to show the feasibility of high frequency designs up to 300 GHz and beyond.

5.1. The Material of Temperature Dependent Resistive Film

The sensing element can be fabricated by the thin film deposition. As the power sensors is based on the substitution principle between r-f and d-c power, the resistance of the thin film element should be sensitive to the temperature. The materials for the temperature dependent resistive films can be classified into two major groups: Positive Temperature Coefficient (PTC) and Negative Temperature Coefficient (NTC). The materials are reviewed in the following sections.

5.1.1. Positive temperature coefficient (PTC) materials

Most thin metallic films have positive temperate coefficients. One of most famous materials for barrater applications is platinum which was used to make very fine fuse wire (about 0.089 to 0.19 μm in diameter)[1]. Platinum thin films were also utilised in microwave power measurement as transverse thin films in rectangular waveguides. For instance, Lane's design has a 10 nm platinum deposited on the 100 μm thick mica strip [2]. This design for X-band rectangular waveguide power sensor had an inaccuracy of less than 3% at any power level from 1 mW to 120 mW at 10 GHz.

In the later experiment, Lane also investigated thin film of nichrome deposited on glass strips, 120 μm wide and 4 mm long [3]. Lane's the thin film resistance at room temperature was 509 Ω , which results in a thickness of between 5 nm and 7.5 nm. Nichrome can be used as substitution for platinum as it is slightly less sensitive to temperature than platinum. The bolometer application of nichrome thin film was extended up to 40 GHz [4].

In another design at 35 GHz, the evaporated bolometer element was nickel, about 10 nm in thickness, 1 mm in length and 0.06 mm in width. The nikel film is deposited on a 30 μm mica

substrate [5]. The unit was proved to have a good performance over the frequency range between 30 GHz and 40 GHz. In the 94 GHz design by Inoue, the nickel thin film on a 12.5 μm polyimide sheet was utilised. The thin resistive film is 1.27 mm long and 0.2 mm wide. The resistance is 143 Ω from d-c measurement at room temperature [6]. Table 5.1 summarises all the mentioned PTC materials, the sheet resistivity and the temperature coefficient α (discussed in section 2.4.1) are included.

Material	Substrate	Sheet Resistivity (at 20⁰C)	Temperature coefficient (x10⁻³ /⁰C) (at 20⁰C)
Platinum [1, 2, 7]	Mica	105 n Ωm	3.927
Nichrome [3, 4, 8]	Glass	1000-1500 n Ωm	0.4
	Mica		
Nickel [5, 6, 9]	Mica	69.3 n Ωm	6.41
	Polyimide		

Table 5.1: PTC metallic materials used for microwave bolometric sensor.

5.1.2. Negative temperature coefficient (NTC) materials

Prior to the application of PTC thin metallic films, NTC thermistors were widely used in microwave power measurement, due to small sizes, sensitivity, accuracy and robustness. Bead thermistors were developed extensively in materials, and most power meters were developed for NTC thermistors. The NTC thermistors are composed of metal oxides, such as oxides of manganese, nickel, cobalt, iron, copper and titanium. Operation frequency of bead thermistor power sensors were reported up to 50 GHz on [5] and recently at 140 GHz [10].

The commercial NTC bead thermistor will be no longer fit into the small waveguide at high frequency. The practical approach is to fabricate NTC thin film thermistors and apply them in the same way as the thin metallic films discussed above. A study of thin films of nickel manganese oxides showed the NTC characteristics and that it was possible to achieve the resistivity of 3300 Ωcm [11]. Thin film nickel manganite (NiMn_2O_4) was also investigated at the University of Birmingham. The material was deposited on 10 mm x 10mm Alumina substrates, the thin films have NTC characteristics and the resistivity was reported at 470-745 Ωcm . For further information, a detailed investigation of thin film nickel manganite on SU-8 substrate can be found in Appendix D.

Thin film vanadium oxides deposited by pulsed d-c reactive magnetron sputtering has a promising resistance to make the sensing elements in the power application, although the sensitivity is lower than that of bulk NTC thermistor [12]. Another popular material of NTC thermistor is manganese vanadium oxides. Material deposited on polished quartz and pyrex glass also has very high resistivity [13].

Material	Substrate	Sheet resistance (at 300K)	B constant
Nickel manganese oxides [11]	Microscope glass	33 Ωm	4000
Nickel manganite	Alumina Su-8	4.70-7.45 Ωm	3000
Manganese vanadium oxides [13]	Polished quartz Pyrex glass	7.99-92.5 $\text{k}\Omega\text{m}$	3180-4150
Vanadium oxides [12]	Cleared glass	0.05-35.73 $\text{m}\Omega\text{m}$	188-2182
Ge [14]	GaAs(100)	0.1-1 $\text{m}\Omega\text{m}$	3945

Table 5.2: NTC materials for thin film bolometric element.

Ge/GaAs is another candidate for NTC thin film thermistors. It was reported that thermal evaporation of Germanium in the vacuum onto semi-insulating Gallium-Arsenide (100) substrates can obtain the thickness from 1 nm to 250nm and low resistance of 0.01 - 0.1 Ωcm [14]. Table 5.2 summarises the thin film materials that have been discussed, the sheet resistivity and B constant of the materials (discussed in section 2.4.1) are included.

5.1.3. Discussion on the thin film bolometers

The PTC films have been used in microwave power measurement as listed with frequencies of operation in section 5.1.1. At room temperature (i.e. 20⁰C), the thin film resistance should be smaller than the operating resistance as discussed in section 2.3.4, for instance the room temperature resistance of 150 Ω for the operating resistance of 200 Ω . Because of the low resistivity listed in Table 5.1, the thickness of PTC thin film is usually in the order of 10 nm.

The use of NTC films in the waveguide power sensing application, on the other hand, has not been seen in the literature. In Son's work [15], the thin film vanadium oxide of the size 1 μm \times 52 μm was integrated to spiral antennas structure to detect microwave power. The example shows the feasibility of integrating NTC thin films to waveguide power sensor. The discussed materials and substrates can be suitable candidates for thin film bolometers. Unlike the PTC film, the NTC film can be few micrometres thick, the resistance at room temperature can be in the order of 1 k Ω as the thermistor used in Chapter 4.

In this work, the platinum thin film on SU-8 substrate is utilised, because of the promising temperature sensitivity and the feasibility of the thin film fabrication. The SU-8 substrate has

similar thermal conductivity to other substrate, the lossy substrate will be considered in the design simulation.

5.2. Modelling the Thin Film Element.

A problem arises when running microwave simulation of a thin metal film inside a rectangular waveguide. The thin film structure can be created by the real dimensions and is very small compared to the waveguide dimension. The full wave solvers such as CST cannot produce the adequate mesh density and the simulations consume a lot of memory and time. Consequently, the results are unrealisable. For example, the simulation of 10 nm thick platinum thin film in W-band waveguide in Figure 5.2, requires 40,425 tetrahedrons meshes and takes nearly 4 hours of computing, the simulated S_{21} is less than -1280 dB and spikes and discontinuities can be seen in the S-parameter responses. In more complex cases, the convergence criterion cannot be met. To solve the problem, the thin film is modelled as an Ohmic sheet, the concept of which is described below.

In Ramey's work [16], the microwave transmission through thin metal and semiconducting films depends on the product of σd , in which σ is the bulk conductivity of the film and d is the film thickness. The proposed solution to using thin films in full wave models is to model the thin films as Ohmic sheets which are infinitely thin and are characterised by the sheet resistance.

$$R_s = \frac{1}{\sigma d} \quad (5.1)$$

The resistance of a thin film can be calculated from the sheet resistance as

$$R = \frac{l}{\sigma} \frac{l}{wd} = R_s \frac{l}{w} \quad (5.2)$$

where l and w are the length and the width of the film, respectively.

The proposed model of thin films in the electromagnetic simulation is valid if it can present the same the resistance and reactance of the thin film in a rectangular waveguide. The following sections demonstrate the comparison of the simulated model and the theoretical analysis of the thin film under similar conditions. First, the power transmission coefficient and the power reflection coefficient of the TE₁₀ wave in a waveguide through and reflected from a thin film medium is investigated. Secondly, the analytical solution of the reactance of the thin film in a rectangular waveguide is also compared to the simulated values.

5.2.1. Power transmission and power reflection coefficient in a rectangular waveguide blocked by a thin film

This section investigates the electromagnetic waves traveling in a waveguide which is blocked by a thin film medium as shown in Figure 5.1(a). The waveguide transmission is separated by the thin film region in the two mediums including vacuum and metallic medium as medium 1 and 2 in Figure 5.1(b). The zero conductivity σ_0 , the permittivity ϵ_0 and the permeability μ_0 are of vacuum. The conductivity σ , the permittivity ϵ and the permeability μ are of the thin film medium. The film has the same dimension as the waveguide $a \times b$, the thickness of the film is d in the figure.

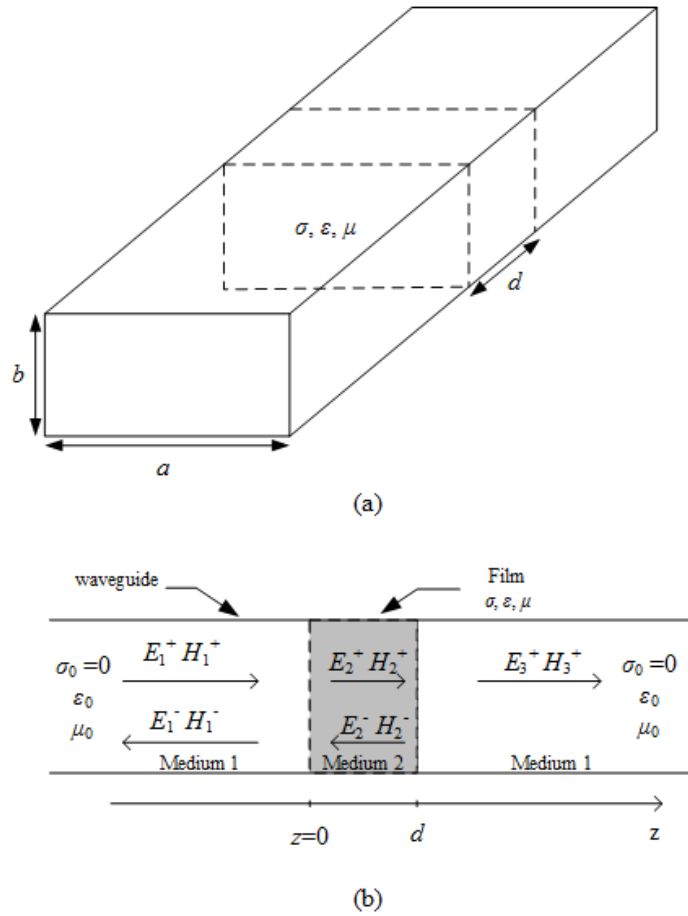


Figure 5.1: (a) perspective view and (b) side view of a thin metal film in a rectangular waveguide in which the thin film thickness is exaggerated to show the field in the medium [17].

The equivalent model in CST simulation of the structure in Figure 5.1 is shown in Figure 5.2. The thin film is replaced by the Ohmic sheet in yellow colour with the same dimensions except the thickness of the Ohmic sheet is zero. The sheet resistance can be calculated from the conductivity and the thickness of the film by equation 5.1. Only the vacuum filling of the waveguide in blue colour is shown in the simulation. The two ends of the waveguide are attached to matched waveguide ports.

The simulation is run for a platinum thin film (the electrical conductivity at 20 °C σ is 9.524×10^6 Sm) in W-band waveguide (size 1.27 mm \times 2.54 mm) at 94 GHz. At different film thicknesses d changing from 5 nm to 100 nm at 5 nm interval, the two-port simulation gives the

transmission and reflection coefficients. The power transmission coefficient T and the power reflection coefficients R can be derived from transmission and reflection coefficients as follows:

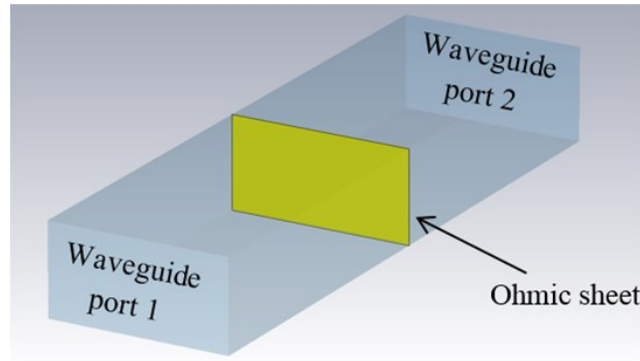


Figure 5.2: The CST simulation model of an Ohmic sheet in a rectangular waveguide

$$T = |S_{21}|^2 \quad (5.3)$$

$$R = |S_{11}|^2 \quad (5.4)$$

An analytical solution of the structure in Figure 5.1 was presented by Ramey [16, 17]. The expressions for the power transmission coefficient T , the power reflection coefficient R can be derived from the analysis of the dominant mode TE_{10} of the electromagnetic wave. The continuity condition of tangential components of E fields and H fields through the mediums was used to solve the amplitude of transmitted and reflected waves. The power transmission coefficient T and power reflection coefficient R are [17].

$$T = \left| \frac{E_3}{E_0} \right|^2 = \left| \frac{4 \exp(\gamma d)}{\left(I - \frac{\mu_0 \gamma_2}{\mu \gamma} \right) \left(I - \frac{\mu \gamma}{\mu_0 \gamma_2} \right) \exp(-\gamma_2 d) + \left(I + \frac{\mu_0 \gamma_2}{\mu \gamma} \right) \left(I + \frac{\mu \gamma}{\mu_0 \gamma_2} \right) \exp(\gamma_2 d)} \right|^2 \quad (5.5)$$

$$R = \left| \frac{E_1}{E_0} \right|^2 = \left| \frac{\left(I - \frac{\mu_0 \gamma_2}{\mu \gamma} \right) \left(I + \frac{\mu \gamma}{\mu_0 \gamma_2} \right) + \left(I + \frac{\mu_0 \gamma_2}{\mu \gamma} \right) \left(I - \frac{\mu \gamma}{\mu_0 \gamma_2} \right) \exp(-2\gamma_2 d)}{\left(I + \frac{\mu_0 \gamma_2}{\mu \gamma} \right) \left(I + \frac{\mu \gamma}{\mu_0 \gamma_2} \right) + \left(I - \frac{\mu_0 \gamma_2}{\mu \gamma} \right) \left(I + \frac{\mu \gamma}{\mu_0 \gamma_2} \right) \exp(-2\gamma_2 d)} \right|^2 \quad (5.6)$$

where the propagation constant γ for TE₁₀ wave in an vacuum-filled rectangular waveguide is

$$\gamma = \sqrt{\left(\frac{\pi}{a}\right)^2 - \omega^2 \mu_0 \epsilon_0} \quad (5.7)$$

The propagation constant in the metal film medium inside the waveguide is [17]

$$\gamma_2 = \sqrt{\left(\frac{\pi}{a}\right)^2 - \omega^2 \mu \epsilon + j \omega \mu \sigma} \quad (5.8)$$

where $\omega = 2\pi f$ is the angular frequency

According to Harrington [18], the relative permittivity of the metal film is around unity since it is a highly conductive medium, therefore $\epsilon = \epsilon_0$. The permeability μ of non-magnetic material is equal to the permeability μ_0 of vacuum.

The power absorption coefficient A can be calculated for the power transmission coefficient T and power reflection coefficient R as

$$A = 1 - T - R \quad (5.9)$$

As stated above the calculation is applied for thin film in W-band waveguide ($a = 2.54$ mm) at the frequency $f = 94$ GHz. The thin film thickness d varies from 5 nm to 100 nm. The simulated and the calculated values of the power absorption coefficient A are compared as shown in Figure 5.3.

The figures indicate excellent agreement between simulation and calculation. The absorption of the thin film medium decreases as the thin film thickness increases. The thin film presents higher resistance at thinner thickness, when the film gets thicker, the film resistance declines and becomes saturated when the thickness is greater than the skin depth.

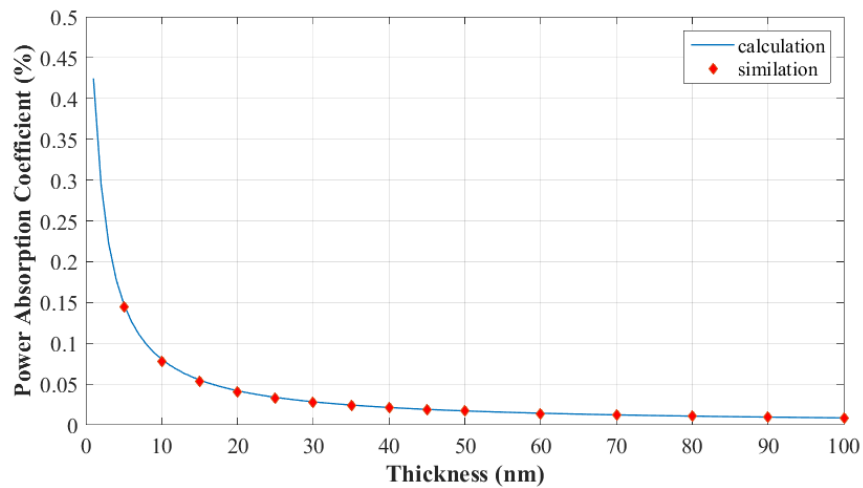


Figure 5.3: Comparison between calculation and simulation results of the power transmission of thin platinum film at 94 GHz.

5.2.2. Reactance of narrow thin film in a rectangular waveguide

This section investigates the reactance of a thin film in a rectangular waveguide when it is placed at the middle of the guide as illustrated in Figure 5.5. The width w of the film is smaller than the broad wall dimension. The equivalent circuit of the thin film is a series circuit of the film resistance R and the film reactance X as shown in Figure 5.5(c).

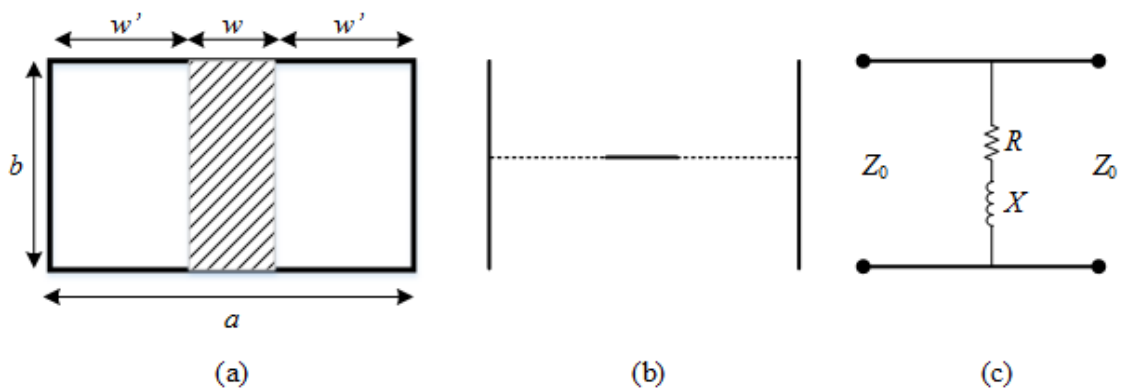


Figure 5.4: A narrow thin film in waveguide (a) crossed section, (b) top view and (c) Equivalent circuit [19]. a and b are the dimension of the waveguide, Z_0 is the characteristic impedance of the guide and X is the reactance of the thin film.

The simulation model of the film is built in CST as shown in Figure 5.5. The thin film is presented by the Ohmic sheet with the width w . The sheet resistance of the Ohmic sheet is $10.5 \Omega/\text{sq}$, corresponding to 10 nm thick platinum film (calculated by equation 5.1). The waveguide in the simulation has standard W-band waveguide size of $2.54 \text{ mm} \times 1.27 \text{ mm}$. The length of the waveguide is two guided wavelength λ_g . The guided wavelength at 94 GHz can be calculated by equation 3.7 and is 4.1 mm. The vacuum filling of the guide is shown in the figure. The two ends are connected to matched waveguide ports.

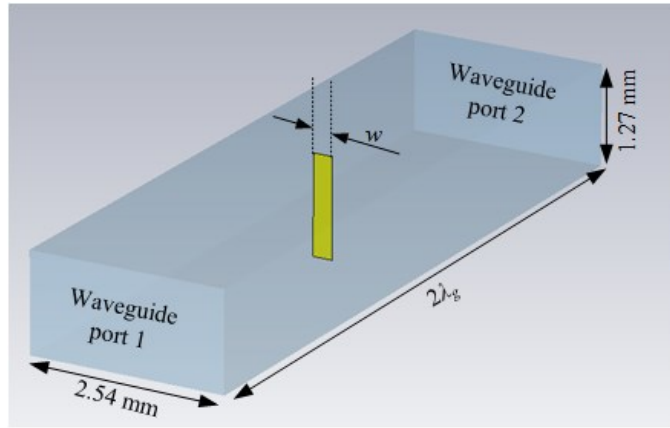


Figure 5.5: Simulation model of a narrow thin platinum film in a W-band waveguide for the reactance extraction.

The simulation is run for different width w changing from $50 \mu\text{m}$ to $300 \mu\text{m}$ at $50 \mu\text{m}$ interval. The normalised impedance of the film can be derived from the simulated reflection coefficient as discussed in section 3.2.2. The normalised reactance of the sheet is obtained from the imaginary part of the extracted normalised impedance.

The theoretical solution for the reactance of the infinitely thin films in Figure 5.5 is also available. The normalised reactance is given by the equation [19]

$$\frac{X}{Z_0} = \frac{a}{2\lambda_g} \left[\ln \left(\frac{8}{\pi e^2} \frac{a}{w} \right) + \frac{4}{27} \frac{a}{\lambda} \right] \quad (5.10)$$

where the wavelength λ of the electromagnetic wave is associated with the frequency f of the calculated reactance as $\lambda = c/f$ (c is the speed of light in vacuum). The calculation is applied for the case of infinitely thin film in a W-band waveguide ($a = 2.54$ mm). Equation 5.10 is valid in the wavelength range $2a/3 < \lambda < 2a$ and $w/a \leq 0.15$. For W-band application at 94 GHz, the first condition is satisfied. The second condition is valid when the width w is smaller than $380\mu\text{m}$. The guided wavelength λ_g is 4.1 mm as mentioned previously. The normalised reactances obtained from equation 5.10 are compared to the simulated values, and the comparison is displayed in Figure 5.6.

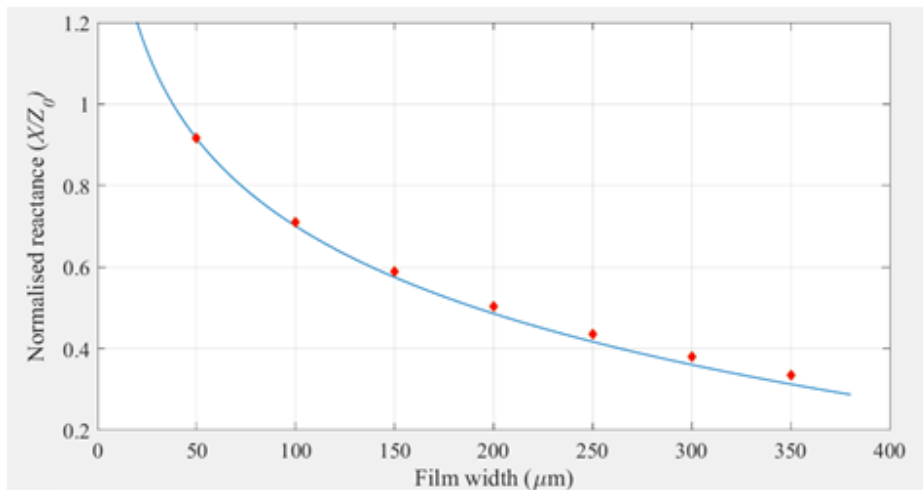


Figure 5.6: Calculated and simulated reactance of thin film in W band waveguide at 94 GHz.

The simulated normalised reactances agree well with the calculated values. At large values of the film width, equation 5.10 becomes less accurate as w reaches its maximum valid value, which explains the deviation in the reactances from the two approaches.

The two verifications of the thin film representation in the computer simulation was successfully conducted. Excellent agreement between the simulation and theoretical calculation were obtained. The Ohmic sheets can be used confidently to represent thin films in the future design process.

5.3. Design the Mount for Matching Condition

This chapter presents the design of the thin film mount in W-band power sensor. The structure of the mount is first introduced. The determination of the mount dimensions for matching condition is discussed.

5.3.1. Structure of the thin film mount

Platinum thin film was chosen as the sensing element. The substrate of the thin film is made of SU-8 photoresist [20]. Compared to the traditional substrate such as mica or polyimide discussed in section 5.1, SU-8 photoresist has suitable thermal conductivity and it can be made in to complex shapes with various thickness at the University of Birmingham. Figure 5.7 shows the structure of the mount in W-band waveguide, in which the thin film as an Ohmic sheet on a 50 μm thick SU-8 substrate is positioned in the transverse plane of the waveguide. The length of the thin film is equal to the narrow side wall dimension of the W-band waveguide $b = 1.27\text{mm}$.

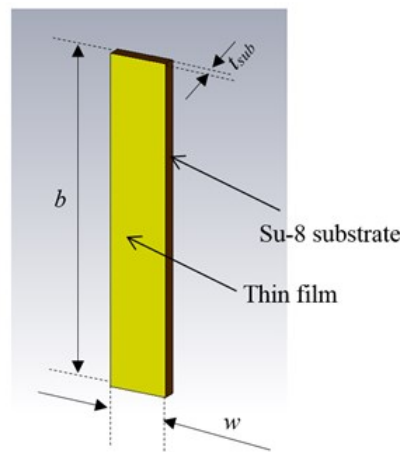


Figure 5.7: The mount of the thin platinum film in the W-band waveguide, where $b = 1.27\text{ mm}$ is the height of the W-band waveguide, t_{sub} is the substrate thickness of 50 μm , the film and the substrate have the same width w .

The operating resistance of the thin film element is 200Ω , because it is compatible with the auto-balancing circuit used in measurement discussed in Chapter 2. The sheet resistance of the Ohmic sheet in the simulation can be calculated by equation 5.2 with $R = 200 \Omega$ and $l = b = 1.27 \text{ mm}$.

$$R_s = 157.48 \times 10^3 w \text{ } (\Omega/\text{sq}) \quad (5.11)$$

5.3.2. Determination of the mount dimensions

This section presents the determination of the film width w , in order to satisfy the matching condition discussed in Chapter 3. The technique is similar to the technique used in the thermistor mount design in Chapter 4.

The normalised reactance of the thin film can be related to the film width w by equation 5.9. The substrate contributes a negligible capacitance to the impedance of the thin film in the waveguide. The detailed analysis of the impedance of the thin film structure was investigated in [21]. Therefore, the reactance of the mount is approximated to that of the thin film. The matching condition in equation 3.35c suggests that the normalised reactance has to be smaller than 0.5. As can be seen in Figure 5.7, the width w of the thin film needs to be larger than $200 \mu\text{m}$.

The mount structure in Figure 5.8 is placed in the middle of the two-port W-band waveguide as can be seen in Figure 5.9, in order to extract the impedance at 94 GHz. At the initial width w of $220 \mu\text{m}$, the sheet resistance is $34.65 \Omega/\text{sq}$ (obtained by equation 5.10). The simulated reflection coefficient is given as $\Gamma = -0.4246 + j0.2216$. By applying equation 3.40, the normalised impedance of the mount is $Z/Z_0 = 0.4255 + j0.483$. The characteristic impedance of the W-band waveguide at 94 GHz is calculated by equation 3.29, which gives the impedance

Z_0 of 484.1 Ω . The resistance of the mount consequently is 205.5 Ω , which is slightly higher than the thin film's resistance. It can be explained by an equivalent circuit of the mount consisting of a series network of the thin film resistor and thin film inductor in parallel with the substrate capacitor. The small deviation between the effective resistance of the mount and the resistance of the thin film indicates a small effect of the capacitance caused by the substrate. More detail on the substrate capacitance is given in [21].

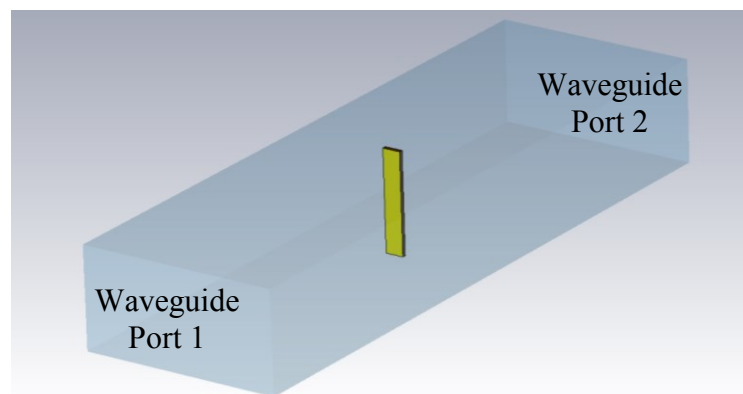


Figure 5.8: The thin film structure in a two-port W-band waveguide.

The impedance of the thin film structure was extracted at different thin film widths w , while the resistance of the film remains unchanged at 200 Ω . Note that the corresponding sheet resistance of the Ohmic sheet in the simulation is determined by equation 5.10. The corresponding resistance length l_R and the reactance length l_X were calculated by equations 4.4 and 4.5. Figure 5.9 depicts the calculated results of l_R and l_X . The interception is the potential matching point at the width w of 221.8 μm and the shorted length l_s of 1.586 mm.

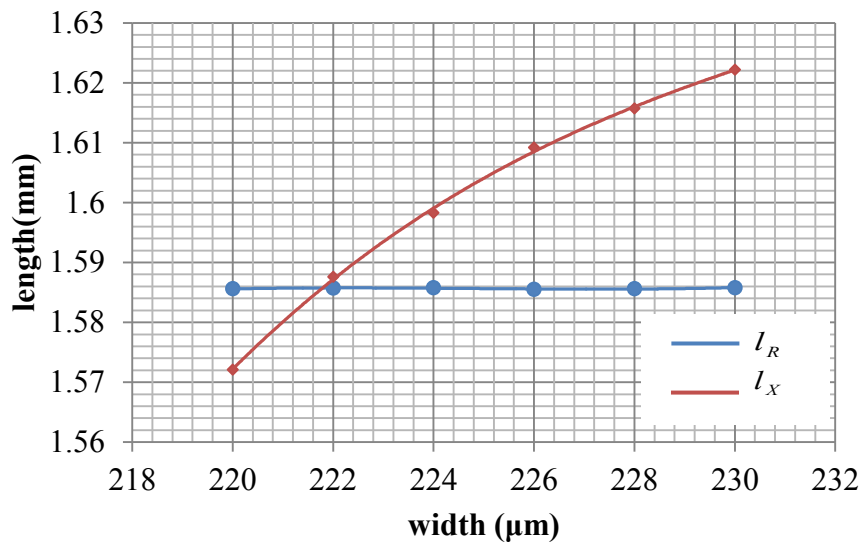


Figure 5.9: Electrical length extraction results for the thin film mount at different widths.

The width is round to 220 μm and equation 5.10 gives the sheet resistance of the platinum thin film at 34.65 Ω/sq, corresponding to 200 Ω operating resistance. The structure of the mount is simulated in a shorted W-band waveguide as illustrated in Figure 5.10.

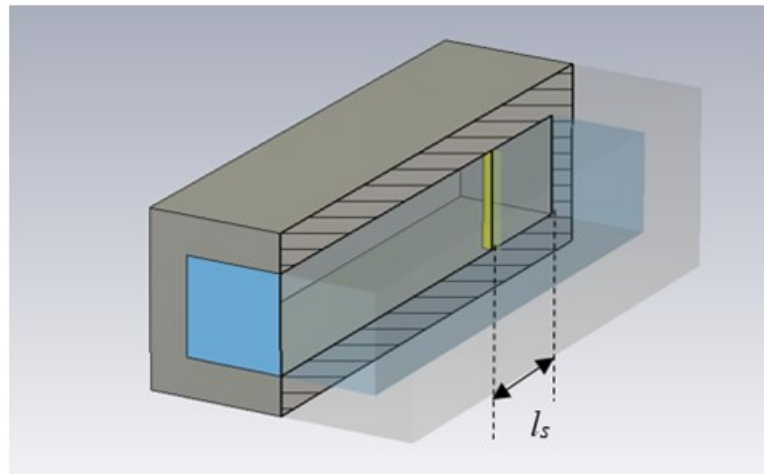


Figure 5.10: The simulation of the designed mount in a shorted waveguide.

The thin film structure is placed in a shorted W-band waveguide terminated at the determined distance l_s of 1.586 mm from the thin film. The reflection coefficient is shown in Figure 5.11.

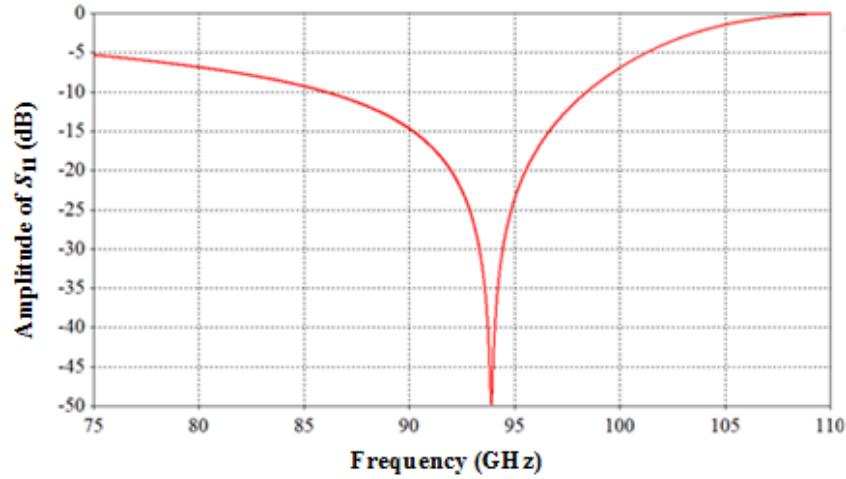


Figure 5.11: The reflection coefficient of the waveguide sensor in Figure 5.10.

The response indicates that the matching condition was obtained at 93.9 GHz. The simulation only takes in account of the inner structure of the power sensor. The complete structure is presented in the next section.

The power dissipated on the mount structure can be determined as the total of the power dissipated on the thin film and the SU-8 substrate. As the substrate is quite lossy compared to the traditional substrates such as polyimide and glass, it is critical that the microwave power is dissipated on the thin film rather than the substrate. The power dissipated on the thin film can be calculated as:

$$P_c = \sigma t |E_c|^2 \quad (5.12)$$

where $|E_c|$ is the magnitude of the electric field at the thin film, σ is the conductivity of the platinum $\sigma = 9.53 \times 10^6 \text{ Sm}$, t is the thickness of the film, here $t \approx 10 \text{ nm}$.

The power dissipated in the dielectric medium of the SU-8 substrate can be calculated as

$$P_d = \omega \epsilon_0 \epsilon_r d \tan \delta |E_d|^2 \quad (5.13)$$

where ω is the angular frequency at 94 GHz, the relative permittivity of SU-8 ϵ_r is 4.2, and the thickness of the substrate is $d = 50 \mu\text{m}$. the loss tangent of the SU-8 is $\tan\delta = 0.08$. $|E_d|$ is the magnitude of the electric field at the substrate, which should be equal to $|E_c|$.

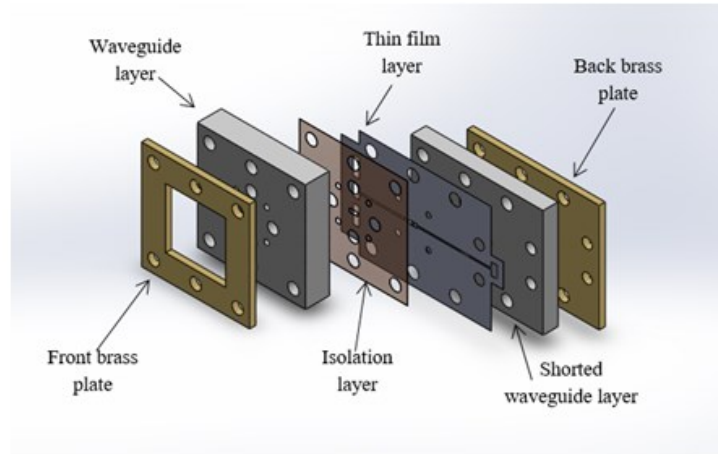
The ratio of the magnitude of the dissipated power on the thin film to that on the substrate can be written as

$$\frac{P_c}{P_d} = \frac{\sigma t}{\omega \epsilon_0 \epsilon_r \tan \delta d} = 1084 \quad (5.14)$$

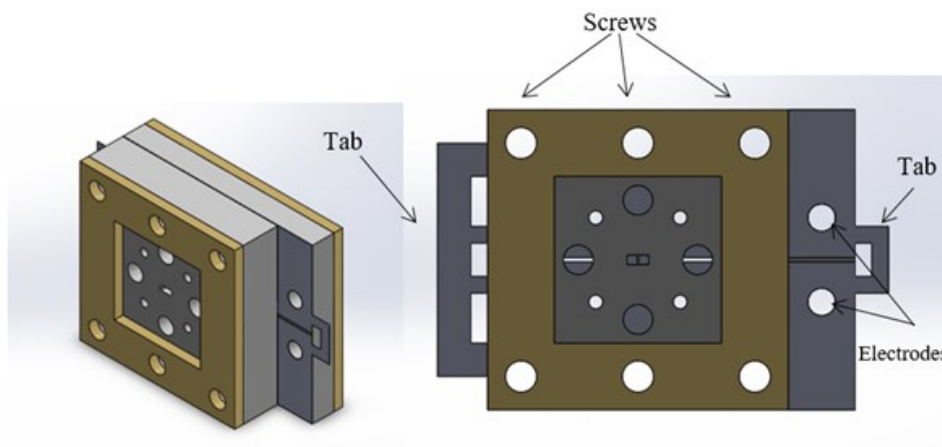
Equation 5.14 shows that the dissipated power on the substrate is negligible and the microwave power is absorbed by the thin film.

5.4. The Structure of the W-band Power Sensor

The power sensor is constructed using six layers as shown in Figure 5.12(a). The brass plates are used to hold the structure together with screws. The main four layers including waveguide layer, shorted waveguide layer, isolation layer and thin film layer will be discussed in more detail. The waveguide layer and the shorted waveguide layer are made of aluminium to realise the waveguide structure in Figure 5.10. The thin film layer is made of SU-8 and platinum is uniformly deposited on one side. The isolation layer has the same material and the thickness as the thin film layer, it provides the electrical isolation between the thin film and the waveguide layers. The assembled power sensor is presented in Figure 5.12(b). When the power sensor is fully assembled, the tabs of the thin film layer will be removed so that the d-c electrodes are not shorted. The isolation screws are used to fasten the layers together.



(a)



(b)

Figure 5.12: The W-band thin film power sensor (a) before and (b) after assembling

The initial simulation result of the power sensor is shown in Figure 5.13. The reflection coefficient minimum moves to 93.44 GHz at -27.7 dB. The difference between this response and the reflection coefficient in Figure 5.11 results from the discontinuity in the guide caused by the thin film layer and the isolation layer.

In fact, the realisation of the power sensor suffers from several limitations of the fabrication processes. The following sections will discuss the effects of the limitations on the sensor's performance.

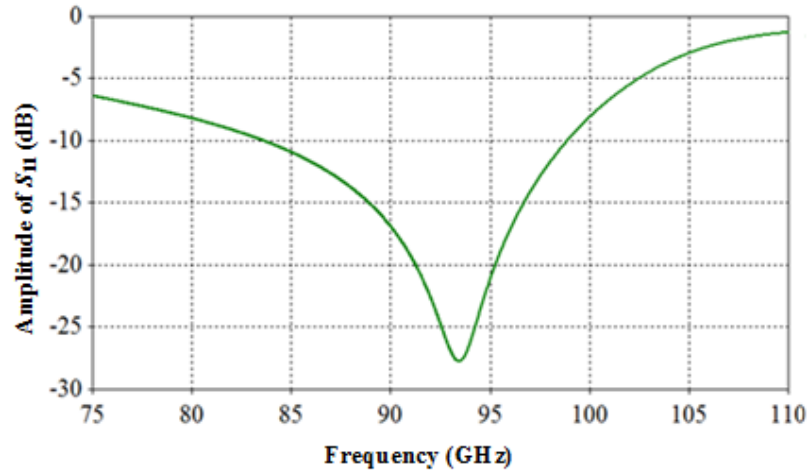


Figure 5.13: The initial reflection coefficient of the full W-band power sensor.

5.4.1. The aluminium waveguide layers

The actual waveguide in the waveguide layers is milled completely through the layer. While in the shorted waveguide layer, the waveguide is milled to a specific depth to create the short electrical length. Due to the milling process, there are round edges of 0.4 mm diameter in the waveguide rather than the right corners of the standard waveguide; this is shown in Figure 5.14.

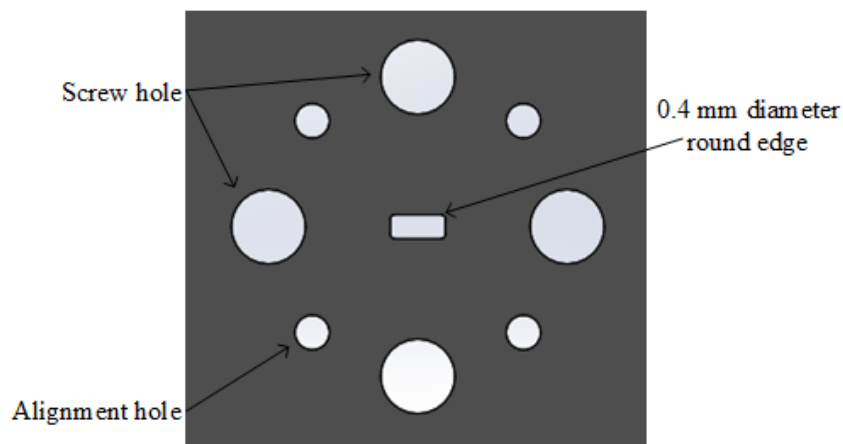


Figure 5.14: Waveguide layer with four round edges of the waveguide window.

The round edges will account for a further shift in the centre frequency as described in Figure 5.15. The short length l_s can be adjusted from 1.586 mm to 1.568 mm, to move the centre frequency back to 94 GHz. The minimum of the reflection coefficient is -33 dB.

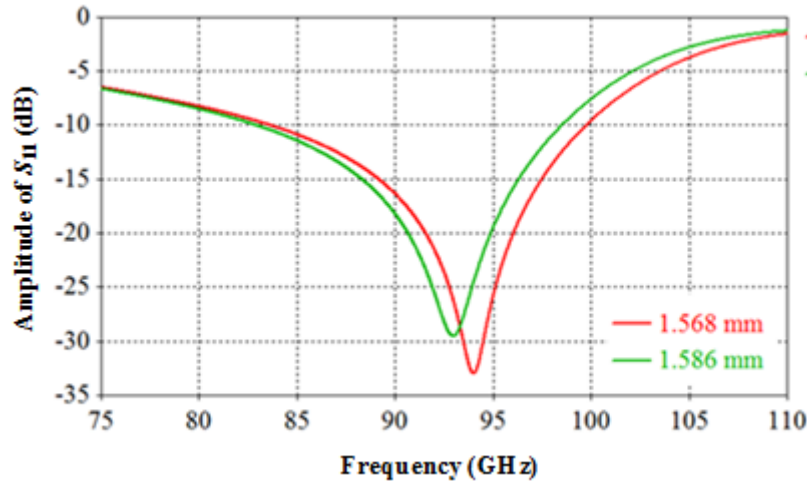


Figure 5.15: The simulated reflection coefficient of the power sensor with round edge compensation.

5.4.2. The thin film layer and isolation layer

The thin film layer whose construction is shown in Figure 5.16 is deposited with platinum on one side of the SU-8 substrate. There are two importance parameters of the layers: the thickness t_{sub} and the gap size g . The initial values of g in the previous simulations is 200 μm . The structure introduced in Figure 5.12(b) was re-simulated with varying gap sizes from 50 μm to 1000 μm . The results indicates that the gap has no effect on the reflection coefficient within the simulated range. The gap of 500 μm is used to ease the fabrication process of the layer but also maintain the mechanical strength of the piece.

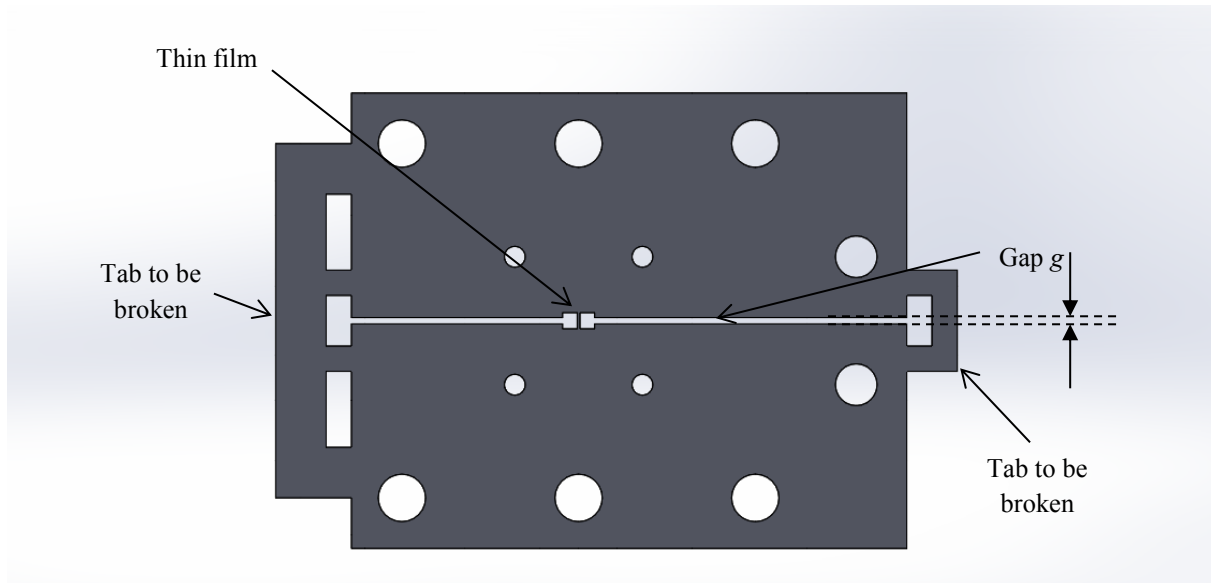


Figure 5.16: The thin film layer.

The isolation layer and the thin film layer introduce discontinuity between the waveguide layer and the shorted waveguide layer in terms of microwave transmission. The thicknesses t_{sub} of the layers is associated with the microwave leakage of the power sensor structure. The amount of power loss was studied by simulating two W-band waveguides separated by the isolation and thin film layer (without the mount in the waveguide) as shown in Figure 5.17.

The above structure was simulated with different thicknesses of the two SU-8 layers. The power loss coefficient can be derived from the transmission and reflection coefficient as follows.

$$L=1- |S_{11}|^2- |S_{21}|^2 \quad (5.15)$$

For a lossless transmission i.e. no microwave leakage, the loss coefficient L is zero. The loss was calculated for three different thicknesses of 12.5 μ m, 50 μ m and 100 μ m. The result is illustrated in Figure 5.18.

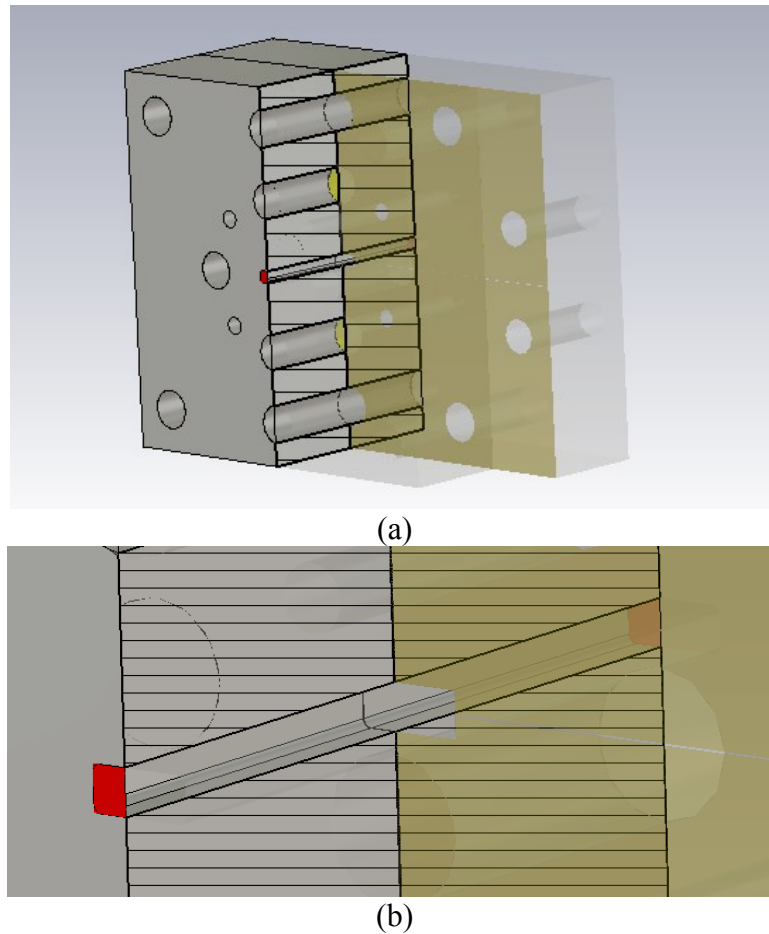


Figure 5.17: (a) The simulation model to determine the microwave leakage between two W-band waveguides separated by isolation layer and thin film layer; (b) the zoomed-in view of the waveguides. The matched waveguide ports are shown in red.

It can be easily seen that the thinner the layers are, the smaller the loss is. At $50\mu\text{m}$ thickness, the power sensor will experience about 7% loss in microwave power, and this amount is acceptable for the sensor operation. If thicker layers are used, the technique of using circular choke flange [22] or periodic structures on the waveguide flange including photonic band gap or bed of nails [23-25] could be used to minimise the microwave leakage.

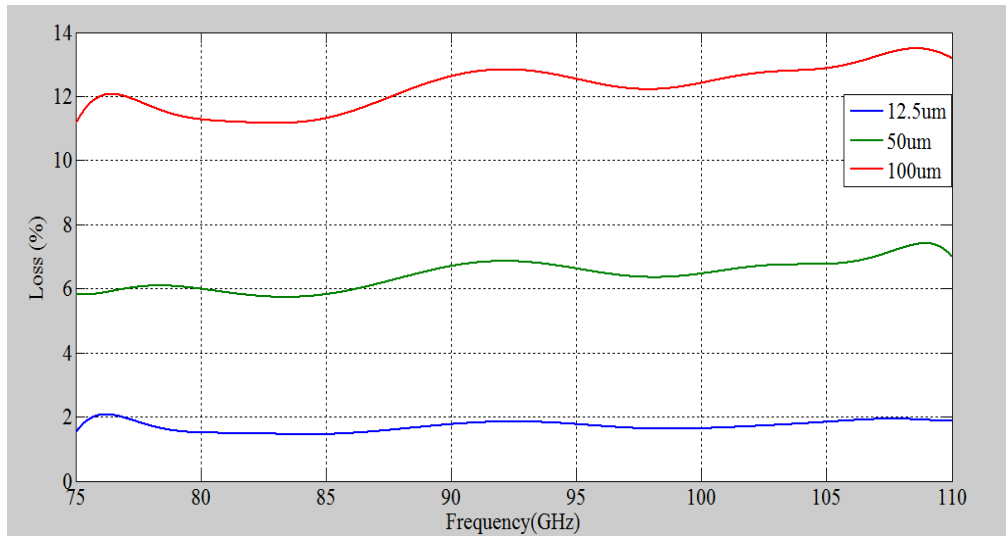


Figure 5.18: The microwave power loss versus the thickness of the isolation and thin film layer.

5.4.3. The design optimisation

At this stage, the designed power sensor has the reflection coefficient of nearly -35 dB at about 94 GHz as shown in Figure 5.15. The values of the parameters discussed are recorded in Table 5.3.

Parameter	Initial	Optimised
Waveguide width	2.54 mm	2.61 mm
Waveguide height	1.27 mm	1.14 mm
Diameter of waveguide s' round edges	0.4 mm	0.4 mm
Shorted length	1.568 mm	1.506 mm
Substrate thickness	50 μm	50 μm
Gap	500 μm	500 μm
Thin film width	220 μm	220 μm
Operating resistance	200 Ω	200 Ω

Table 5.3: Record of importance parameters of the power sensor.

The response of the power sensor can be further optimised by adjusting the waveguide dimensions and the shorted length to compensate for the imperfection of waveguide edges and the discontinuity in the waveguide transmission. A better sensor response is obtained by the computer based optimiser as shown in Figure 5.19.

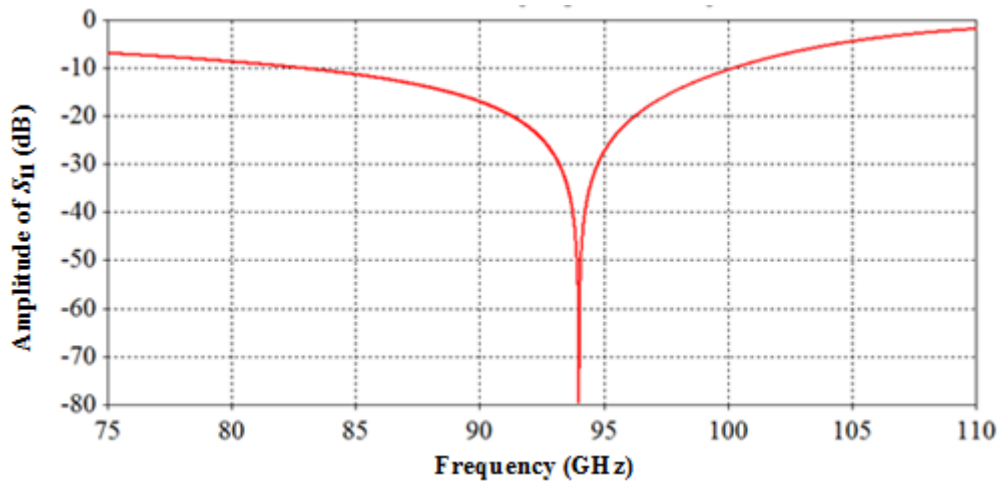


Figure 5.19: The optimised reflection coefficient of the power sensor

The optimised parameters are also recorded in Table 5.3. It can be seen from Figure 5.19 that the microwave power is fully absorbed at 94 GHz. The -20 dB band width is approximately 5 GHz. The detailed dimensions of the W-band power sensor can be found in Appendix E.

5.4.4. The effects of platinum side deposition on the SU-8 substrate

The discussed result is the best case scenario when platinum is deposited only on the surface of the substrate. In reality, platinum will unintentionally be deposited on the side of the substrate and it is very hard to control the side deposition. In the worst case scenario, platinum covers the edges of the substrate (see Figure 5.20(b)). In this case, a shift of about 4 GHz is predicted by

the full wave simulation as indicated in green in Figure 5.21. The -20 dB bandwidth reduces to about 3.5 GHz.



Figure 5.20: (a) surface deposition; (b) surface and side deposition of platinum on the SU-8 substrate

Therefore, with the optimum parameters in Table 5.3, the response of the realised power sensor is expected to be between the red and green responses in Figure 5.23.

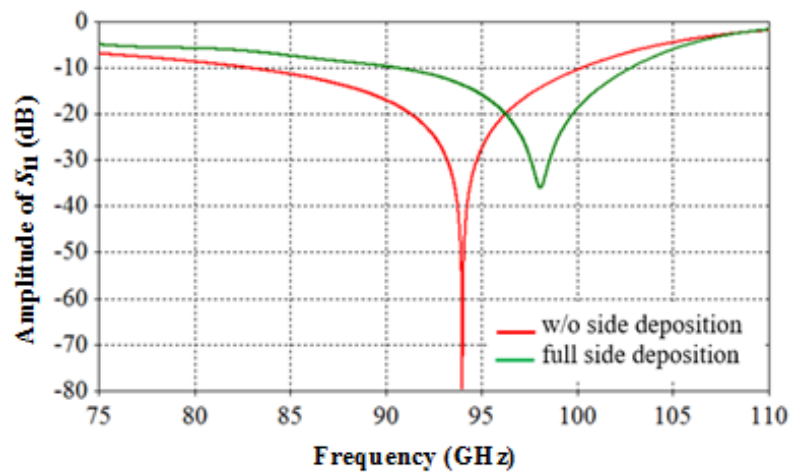


Figure 5.21: Simulated result when the side deposition takes all the thickness of the substrate.

5.5. Thermal properties of the sensor structure

In this section, the thermal properties of the power sensor structure is considered. The operating temperature and the corresponding dissipated power of the thin film element are investigated. The width w of the thin film is 220 μm , the length is equal to the height of the modified waveguide of 1.14 mm. At the room temperature $T = 20\text{ }^{\circ}\text{C}$, the resistance of 3 nm platinum thin film should be

$$R(20^{\circ}C) = \rho(20^{\circ}C) \frac{b}{d.w} = 182 \Omega \quad (5.16)$$

where the bulk resistivity $\rho(20^{\circ}C) = 105 \text{ n}\Omega\text{m}$. The effective resistivity of the platinum film reduces by more than three times as the thickness becomes less than 10 nm [26]. Therefore, the actual deposited film should be thicker than the predicted thickness from bulk resistivity. On the other hand, the film thickness should be smaller than the skin depth of platinum at 94 GHz, that is 532 nm [27], so that the d-c resistance is equal to the r-f resistance.

The relationship of platinum thin film resistance versus temperature is accurately described by Callender Van-Dusen equation [28].

$$R_T = R_0(1 + AT + BT^2 - 100CT^3 + CT^4) \quad (5.17)$$

where R_T is the resistance at temperature $T(^{\circ}C)$

R_0 is the resistance at the nominal temperature of $0^{\circ}C$

$$A = 3.908 \times 10^{-3}$$

$$B = -5.775 \times 10^{-7}$$

$$C = -4.183 \times 10^{-12}$$

The constant C is very small compared to A and B , the third and fourth order of T are often omitted. At the operating condition, the thin film needs to be heated to reach the operating resistance of 200Ω . The temperature T_r can be calculated by solving the equation 5.17 as follows.

$$T_R = \frac{-R_0 A + \sqrt{R_0^2 A^2 - 4R_0 B(R_0 - R_T)}}{2R_0 B} = 47.8^\circ\text{C} \quad (5.18)$$

Moreover, the temperature sensitivity of the thin film can also be derived from equation 5.17.

$$\frac{\delta R}{\delta T} = R_0 (A + 2BT) \quad (5.19)$$

The temperature sensitivity at the ambient temperature of 20 °C and the operating temperature of 47.8 °C is 0.655 Ω/°C and 0.65 Ω/°C, respectively. There is a negligible change in the sensitivity. Therefore, in the small range of temperature, the resistance is considered to be linear with its body temperature.

At operating condition, the platinum thin film is slightly hotter than the surrounding environment. As a result, there is a constant heat flow from the thin film which can be analysed in six main paths as shown in Figure 5.22.

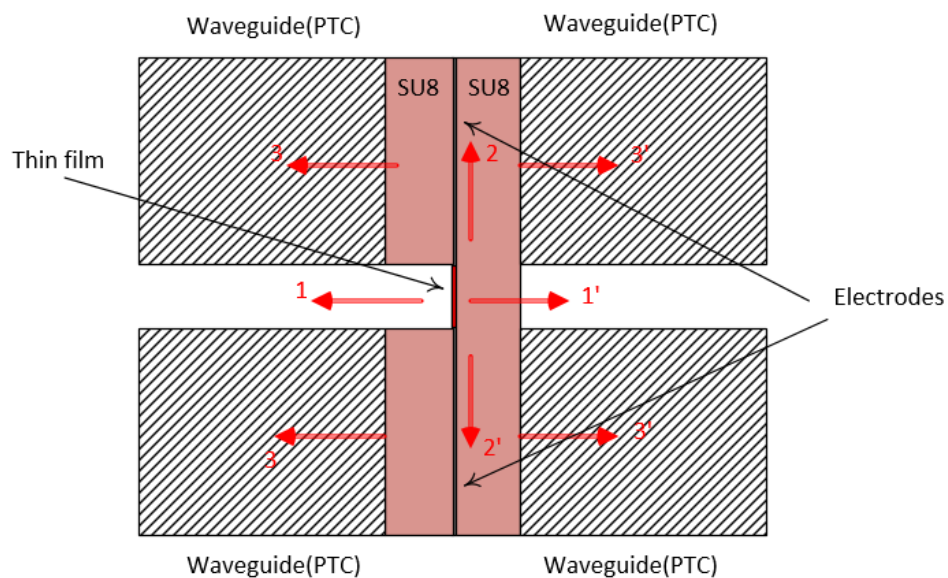


Figure 5.22: The heat flow paths in the power sensor. The dimension of SU-8 layers are exaggerated for clarity

On the first path, the heat goes directly from the surface of the thin film to the air by convection. In the opposite direction, the heat flows through the SU-8 substrate to the air. In direction 2 and 2', heat transfer follows the electrodes between the two SU-8 layers, and simultaneously flows through the SU-8 layers to the metal body of the power sensor in direction 3 and 3'. The heat transfer can be modelled in the thermal circuit in Figure 5.23.

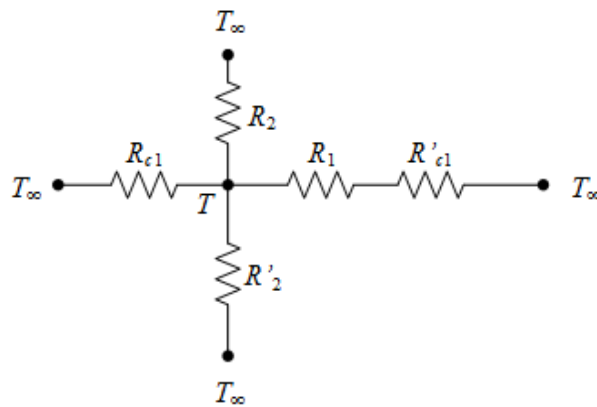


Figure 5.23: The equivalent thermal circuit of the power sensor structure.

The thin film is now presented by a temperature source $T = 47.8^{\circ}\text{C}$ while the ambient temperature $T_{\infty} = 20^{\circ}\text{C}$. R_{c1} and R'_{c1} represent the convection thermal resistance through the surface area which is equal to the thin film element area. R_1 is the conduction thermal resistance of SU-8 substrate in direction 1'. The heat transfer in direction 2 and 3 can be combined in the conduction thermal resistance R_2 . The isolation layer and the substrate of the thin film layer extend along the electrode and their thicknesses are much greater than the thin film thickness. The heat can have a sphere distribution with the centre being at the point of connection between the thin film and the electrode. The medium of the heat flow is SU-8. The heat transfer resistance R_2 can be approximated as [29].

$$R_2 = \int_{r_0}^{R_0} \frac{dr}{k_{SU8} \times 2\pi r^2} = 7190 \text{ K/W} \quad (5.20)$$

where r_0 is half of thin film width w and the height of the electrode R_0 is approximately 18 mm.

The other thermal resistances for conduction and convection modes can be easily calculated by the equations in [29] as discussed in Chapter 4. The values of the thermal resistances are presented in Table 5.4.

Thermal resistance	Value (KW ⁻¹)
R_1	0.997
R_2	7190
R_{c1}	797.5×10^3

Table 5.4: The thermal resistance of the equivalent thermal circuit in Figure 5.23.

The heat flow in direction 1 and 1' can be calculated as

$$Q_1 = T - T_\infty \left(\frac{1}{R_{c1}} + \frac{1}{R_1 + R_{c1}} \right) = 1.61 \times 10^{-4} \text{ W} \quad (5.21)$$

The heat flow in direction 2, 2', 3 and 3' is

$$Q_2 = 2 \frac{T - T_\infty}{R_2} = 7.73 \times 10^{-3} \text{ W} \quad (5.22)$$

Consequently, the total heat flow is $Q = Q_1 + Q_2 = 7.82 \text{ mW}$

The calculation of the heat transfer shows that most of the heat flows in direction 2, 2', 3 and 3'. The total heat flow from the thin film at the operating temperature is 7.82 mW.

Thermal simulation was also used to validate the thermal analysis. In the simulation, the assembled W-band power sensor is used, the dimensions of the sensor are determined in the previous section. The thin film is set as a temperature source of 47.8 °C. The surrounding area is set at the ambient temperature of 20 °C. The physical properties of the surrounding space is

input as those of the dry air with the convection constant of $5 \text{ W}/(\text{km}^2)$ and the thermal boundary is isothermal. The total heat flow from the thin film is given at 7.52 mW that is quite close to the calculated value of 7.82 mW .

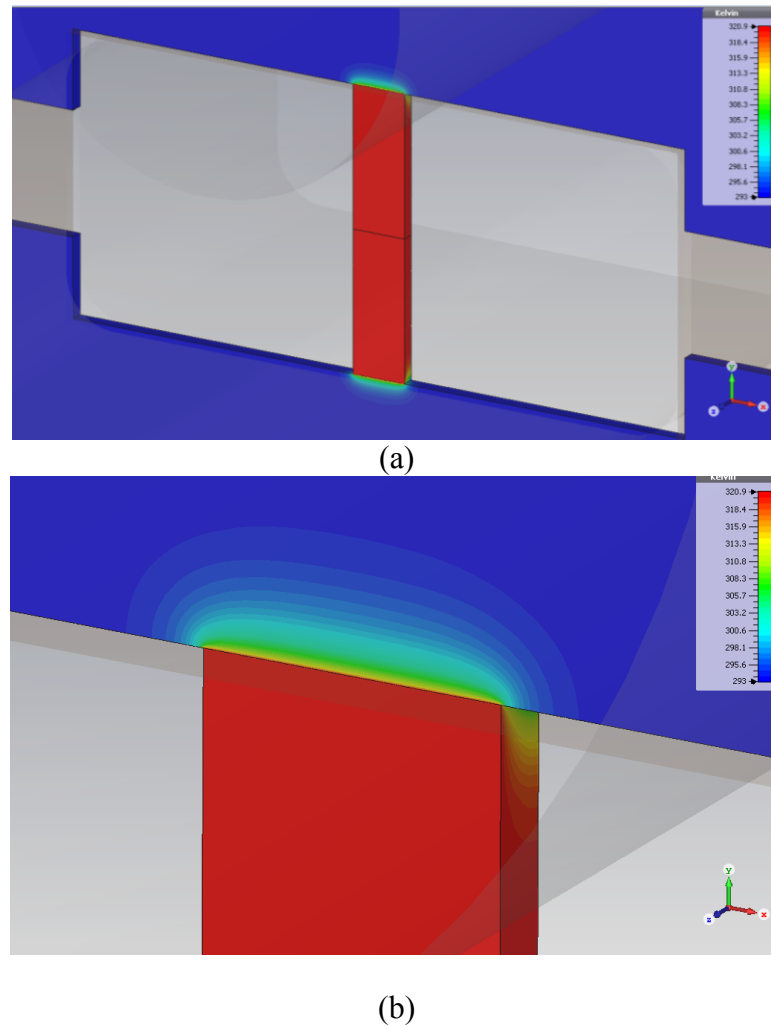


Figure 5.24: The temperature distribution in the power sensor at the operating condition (a) shows the whole thin film structure and (b) shows the distribution at the edge of the thin film.

At the thermal equilibrium, the dissipated power on the thin film is equal to the heat flow out of it. The dissipation constant δ of the platinum thin film can be calculated as

$$\delta = \frac{P}{T - T_{\infty}} = 0.27 \text{ mW}/^{\circ}\text{C} \quad (5.23)$$

Moreover, the power dissipated P indicates the limits in the microwave power range of the power sensor. Therefore, the designed power sensor can measure up to 7 mW.

The power sensitivity of the platinum thin film can be obtained from equations 5.19 and 5.23 as follows

$$\frac{\delta R}{\delta P} = \frac{\delta R}{\delta T} \times \frac{\delta T}{\delta P} = 2.42 \Omega / \text{mW} \quad (5.24)$$

The sensitivity is sufficient for a bolometer mount at the specified power range. It is also similar to the sensitivity reported for Nickel thin films of similar sizes [5, 6].

5.6. Fabrication of the W-band power sensor

The detailed dimensions of the power sensor layers are given in Appendix E. The waveguide layers and brass plates were made by Computer Numeric Control (CNC) Machining. The laboratory at the University of Birmingham was successfully made the SU-8 layers for isolation layer and thin film layer substrate. The fabrication process is well documented in [30]. However, the main problem in the fabrication is in the deposition of platinum on SU-8 substrate. At the temperature of the platinum evaporation process, the 50 μm SU-8 pieces tend to be deformed. On the other hand, the deformation can be avoided if the deposition takes place when the SU-8 layer has not been released from the Silicon wafer. However, the releasing process will damage the platinum, because the solvent used to separate SU-8 and Si wafer is harmful to the deposited platinum. The developed solution is to introduce a thin sacrificial layer of Polyacrylic acid (PAA) between the wafer and SU-8 layer, as the additional layer will be dissolved in water and the thin platinum film will take no damage during the lift-off process.

As an initial test the technique was used to produce thin film layers with 10 nm silver rather than platinum deposited on one side as shown in Figure 5.25. The test layer was assembled with the rest of the power sensor structure as shown in Figure 5.26.



Figure 5.25: The thin film layer with 10nm silver deposited.

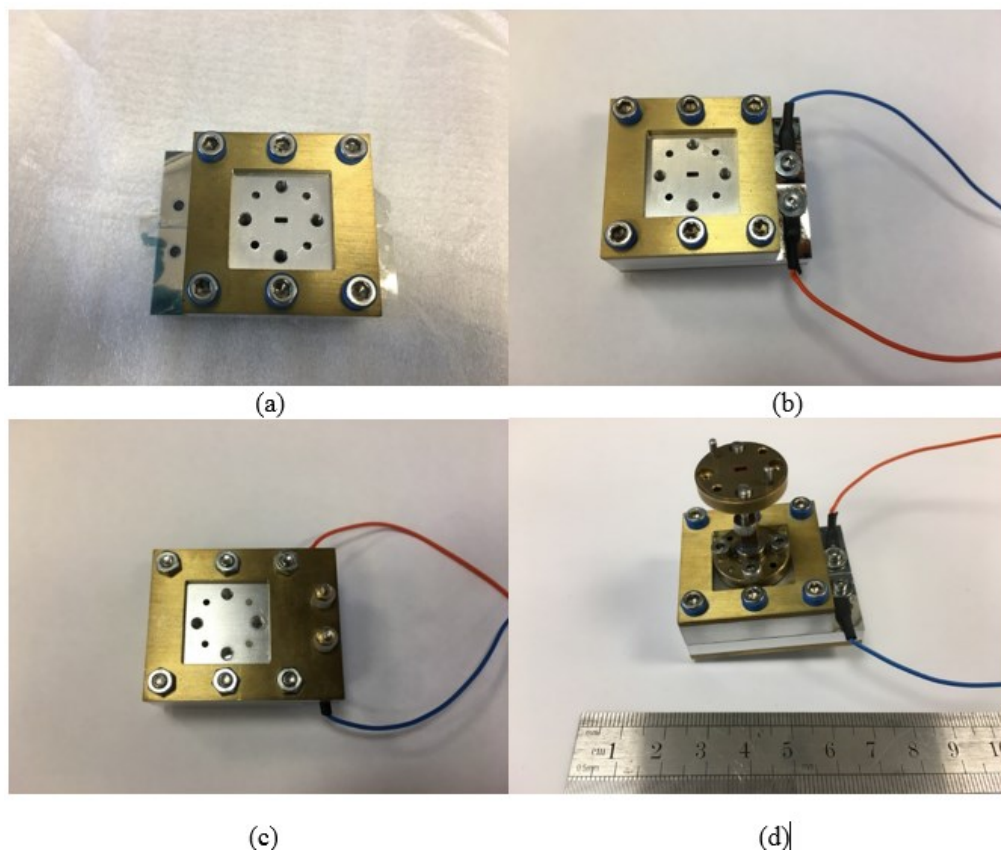


Figure 5.26: (a) Thin silver film on Su-8 in the W-band sensor; (b) The tabs were removed and two d-c terminals were attached to the structure ;(c) back view (d) a standard W-band

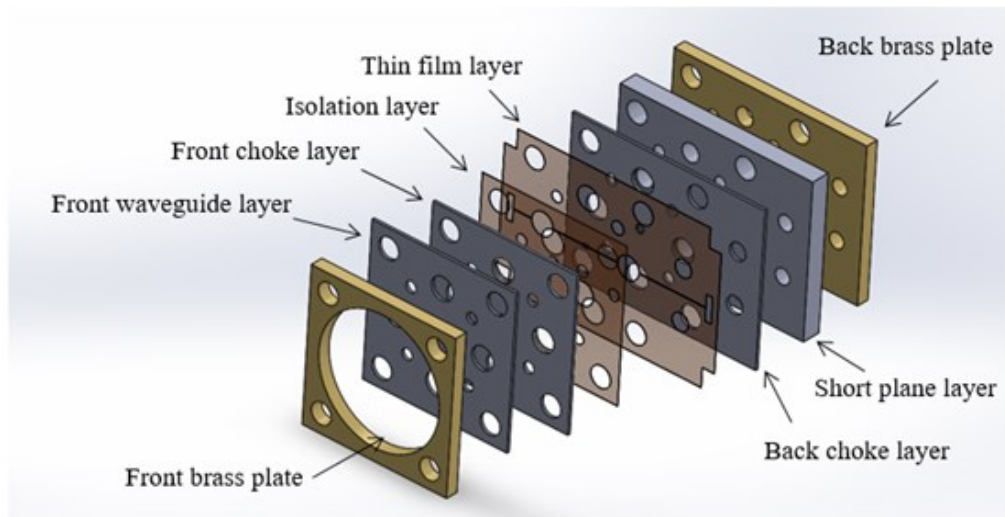
waveguide attached to the front of the sensor, which can help the sensor to connect with the measurement system in NPL.

The samples show good electrical connection between the two d-c terminals and good isolation to the waveguide body. The assembly shows that reliable silver samples can be produced for the W-band sensor. The Poly-acrylic acid (PAA) based process and the evaporator at the University of Birmingham are used to fabricate thin film platinum.

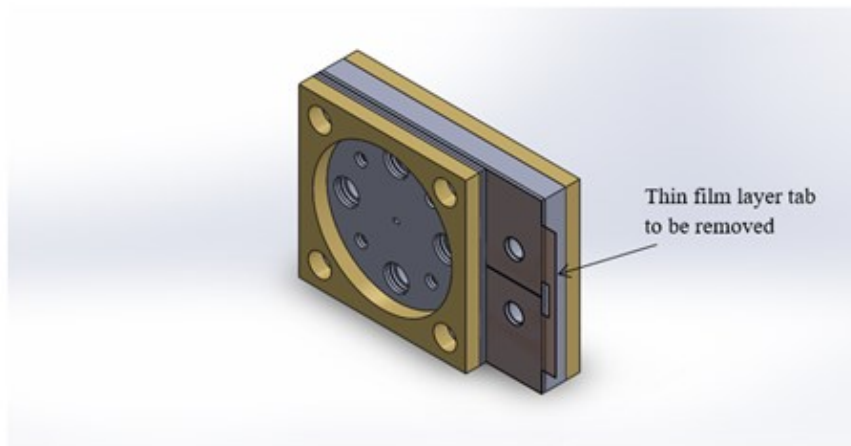
Due to the time constraint, the platinum deposition has not been performed and the results cannot be presented in this thesis. However, the fabrication progress proves that the W-band power sensor can be fabricated. The design approach is believed to be able to reach Terahertz frequency.

5.7. The microwave power sensor design up to 300 GHz

The designed structure of WR-6 and WR-3 waveguide thin film power sensors are introduced here. They are the scaled down version of W-band sensor as shown in Figure 5.27. All the layers of the power sensor will be fabricated by SU-8 micromachining technique except the brass plates. In both designs, the isolation layer and the thin film layer are 50 μm thick, the thin film layers are fabricated by the same technique disused in the W-band design. Other SU-8 layers are 640 μm and 432 μm for WR6 sensor and WR3 sensor, respectively.



(a)



(b)

Figure 5.27: WR6 and WR3 waveguide power sensor construction (a) before assembling (b) assembled.

An additional feature of the high frequency design is the two choke flange to minimise the microwave leakage as discussed in section 5.4.2. This is shown in Figure 5.28 below.

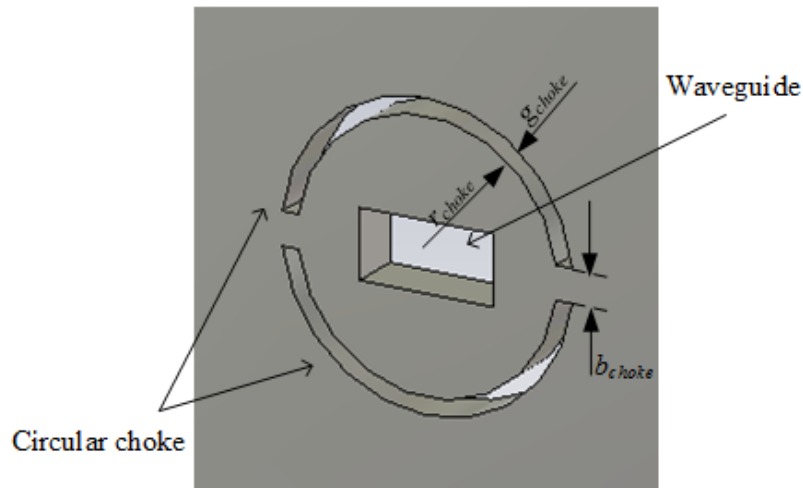
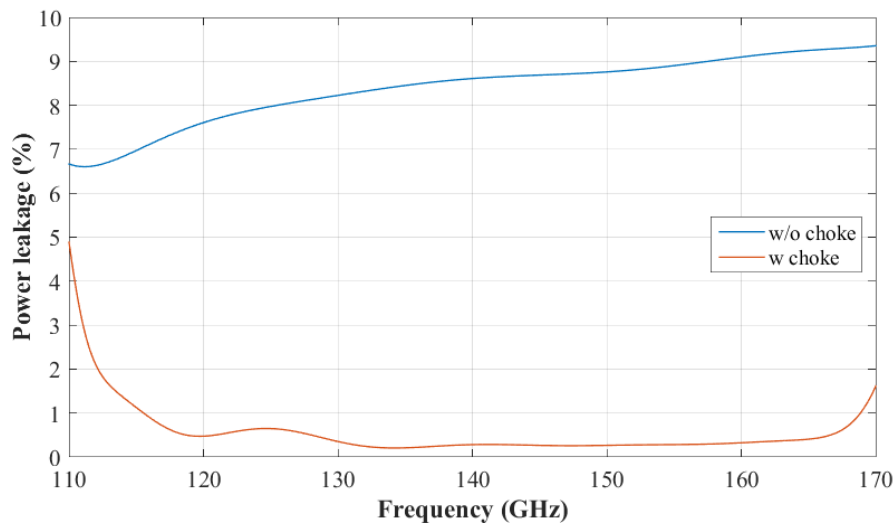


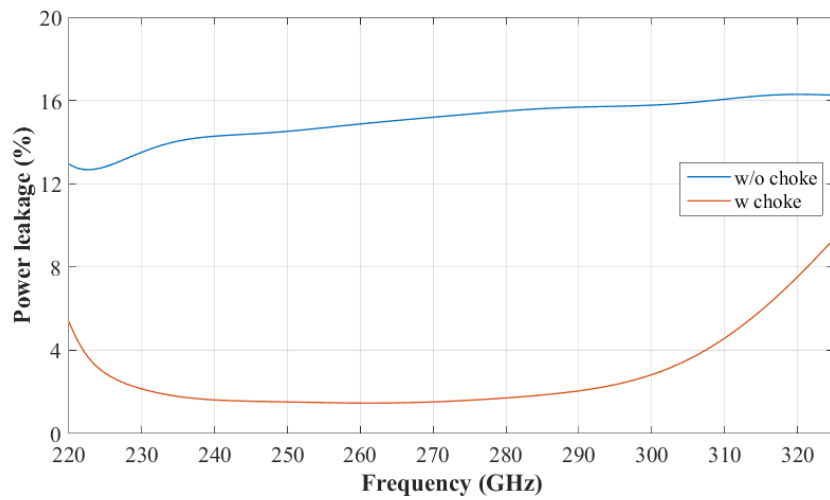
Figure 5.28: The structure of the layer carrying a circular choke with the parameters of the choke ring, note that the depth of the choke ring is equal to the thickness of the layer.

The effect of the choke ring design can be seen in Figure 29. The techniques discussed in section 5.4.2 is used to evaluate the amount of microwave leakage. For WR-6 or D-band waveguide design, the 50 μm thin film layer and isolation layer can result in about 8% of microwave leakage. The choke ring for WR-6 design has the following parameter $r_{choke} = 1.16$ mm, $b_{choke} = 0.4$ mm and $g_{choke} = 0.2$ mm, note the depth of the choke is equal to the SU-8 layer thickness of WR-6 design of 640 μm . The choke help to reduce the power leakage to below 0.5 % for most of the frequency band from 120 GHz to 160 GHz. This is shown in Figure 5.29(a).

Similarly, the choke design in WR-3 design help to reduce the leakage from greater than 14 % to less than 2% from 230 GHz to 300 GHz. The parameters of the WR-3 choke are as follows $r_{choke} = 0.6$ mm, $b_{choke} = 0.2$ mm and $g_{choke} = 0.15$ mm, the depth of the choke is 432 μm . the improvement if microwave leakage is presented in Figure 5.29(b).



(a)

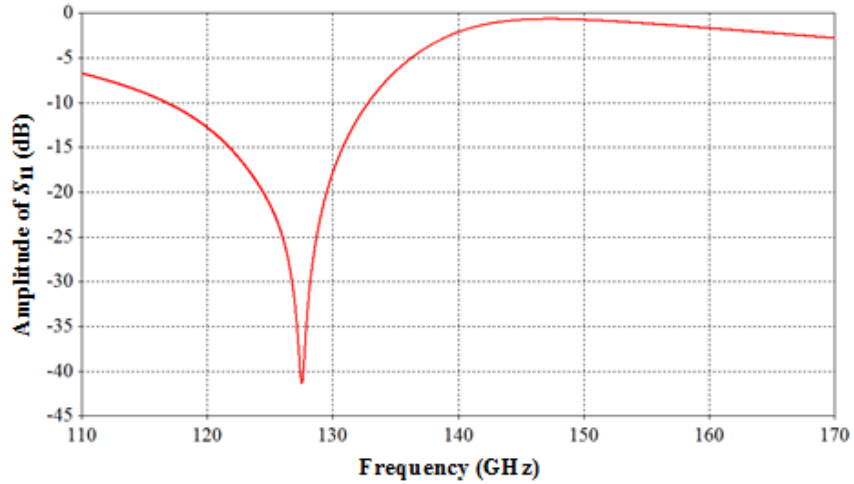


(b)

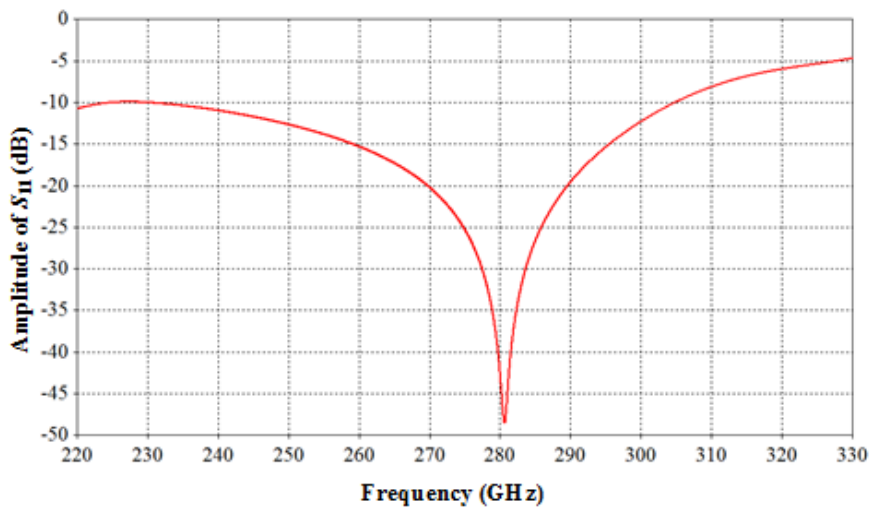
Figure 5.29: Power leakage in WR-6 and WR-3 power sensor with and without the choke ring design.

The detailed dimensions of the WR-6 and WR-3 designs are included in Appendix F and G, respectively. Both power sensor is design to operate with platinum thin film as in W-band design. The operating resistance is 200Ω . The simulated sensor response of the designs can be found in Figure 5.30. The WR-6 design has the matching at 128 GHz and the WR-3 design has

the matching at about 280 GHz. It is worth noticing that matching at different frequencies can be achieved by using various SU-8 waveguide layer thicknesses.



(a)



(b)

Figure 5.30: The response of (a) the WR-6 waveguide and (b) the WR-3 waveguide power sensor in Figure 5.28.

The introduced designs demonstrate the feasibility of the design techniques to high frequency power sensor design up to 300 GHz and beyond.

References

- [1] T. Moreno and O. C. Lundstrom, "Microwave Power Measurement," *Proceedings of the IRE*, vol. 35, pp. 514-518, 1947.
- [2] J. A. Lane, "Transverse film bolometers for the measurement of power in rectangular waveguides," *Proceedings of the IEE - Part B: Radio and Electronic Engineering*, vol. 105, pp. 77-80, 1958.
- [3] J. A. Lane and D. M. Evans, "The design and performance of transverse-film bolometers in rectangular waveguides," *Proceedings of the IEE - Part B: Electronic and Communication Engineering*, vol. 108, pp. 133-135, 1961.
- [4] I. Lemco and B. Rogal, "Resistive-film milliwattmeters for the frequency bands: 8·2-12·4 Gc/s, 12·4-18 Gc/s and 26·5-40 Gc/s," *Proceedings of the IEE - Part B: Electronic and Communication Engineering*, vol. 107, pp. 427-430, 1960.
- [5] K. Sakurai and T. Nemoto, "A Thin-Film Bolometer Unit," *Instrumentation and Measurement, IEEE Transactions on*, vol. 16, pp. 206-211, 1967.
- [6] T. Inoue, I. Yokoshima, and M. Sasaki, "High-performance thin-film barretter mount for power measurement in W-band," *Electronics Letters*, vol. 21, pp. 170-172, 1985.
- [7] "Technique of microwave measurements / edited by Carol G. Montgomery. Vol.1," C. G. Montgomery, Ed., ed. New York: Dover : Constable, 1966.
- [8] B. M. Schiffman, L. Young, and R. B. Larrick, "Thin-Film Waveguide Bolometers for Multimode Power Measurement," *Microwave Theory and Techniques, IEEE Transactions on*, vol. 12, pp. 155-163, 1964.
- [9] M. Regelsberger, R. Wernhardt, and M. Rosenberg, "Thin-film bolometer with fast response," *Review of Scientific Instruments*, vol. 58, pp. 276-278, 1987.
- [10] R. Roy, A. K. Kush, and R. P. Dixit, "Design and Development of Thermistor based Power Meter at 140 GHz Frequency Band," *Journal of Infrared, Millimeter, and Terahertz Waves*, vol. 32, pp. 1407-1414, 2011.
- [11] P. Fau, J. P. Bonino, J. J. Demai, and A. Rousset, "Thin films of nickel manganese oxide for NTC thermistor applications," *Applied Surface Science*, vol. 65, pp. 319-324, 1993/03/02 1993.
- [12] D. Xiang, W. Zhiming, X. Xiangdong, Y. He, G. Deen, W. Xiongbang, *et al.*, "Investigation of the influence of duty cycle on the vanadium oxide thin film thermistor deposited by pulsed dc reactive magnetron sputtering," in *Electron Devices and Solid-State Circuits (EDSSC), 2014 IEEE International Conference on*, 2014, pp. 1-2.

- [13] G. M. Gouda and C. L. Nagendra, "A new transition metal oxide sensor material for thermistor applications: Manganese-vanadium-oxide," in *Physics and Technology of Sensors (ISPTS), 2012 1st International Symposium on*, 2012, pp. 125-128.
- [14] V. F. Mitin, P. M. Lytvyn, V. V. Kholevchuk, V. V. Mitin, E. F. Venger, and O. A. Mironov, "Ge/GaAs thin films for thermometer and bolometer application," in *Electronics and Nanotechnology (ELNANO), 2013 IEEE XXXIII International Scientific Conference*, 2013, pp. 56-60.
- [15] L. N. Son, T. Tachiki, and T. Uchida, "Fabrication of VO_x microbolometer detector coupled with thin-film spiral antenna by metal-organic decomposition," in *2012 37th International Conference on Infrared, Millimeter, and Terahertz Waves*, 2012, pp. 1-2.
- [16] R. L. Ramey, W. J. Kitchen, J. M. Lloyd, and H. S. Landes, "Microwave Transmission through Thin Metal and Semiconducting Films," *Journal of Applied Physics*, vol. 39, pp. 3883-3884, 1968.
- [17] R. L. Ramey and T. S. Lewis, "Properties of Thin Metal Films at Microwave Frequencies," *Journal of Applied Physics*, vol. 39, pp. 1747-1752, 1968.
- [18] R. F. Harrington, "Time-harmonic electromagnetic fields / Roger F. Harrington," ed. London: McGraw-Hill, 1961.
- [19] N. Marcuvitz, "Waveguide handbook / N. Marcuvitz," E. Institution of Electrical, Ed., ed. London: Peregrinus on behalf of The Institution of Electrical Engineers, 1986.
- [20] X. Shang, M. Ke, Y. Wang, and M. J. Lancaster, "WR-3 Band Waveguides and Filters Fabricated Using SU8 Photoresist Micromachining Technology," *IEEE Transactions on Terahertz Science and Technology*, vol. 2, pp. 629-637, 2012.
- [21] J. Brown, "Reactive effects in transverse-film bolometers in rectangular waveguides," *Electrical Engineers, Proceedings of the Institution of*, vol. 110, pp. 77-78, 1963.
- [22] X. Shang, M. J. Lancaster, M. Ke, and Y. Wang, "Measurements of micromachined submillimeter waveguide circuits," in *Microwave Measurement Symposium (ARFTG), 2010 76th ARFTG*, 2010, pp. 1-4.
- [23] J. Hesler, "A photonic crystal joint (PCJ) for metal waveguides," in *Microwave Symposium Digest, 2001 IEEE MTT-S International*, 2001, pp. 783-786 vol.2.
- [24] A. R. K. J. L. Hesler, N. Horner, "A Broadband Waveguide Thermal Isolation," *ISSTT Proceedings*, vol. 6, pp. 148-154, 2003.
- [25] E. Pucci and P. S. Kildal, "Contactless non-leaking waveguide flange realized by bed of nails for millimeter wave applications," in *6th European Conference on Antennas and Propagation (EUCAP)*, 2012, pp. 3533-3536.
- [26] H. Hoffmann and J. Vancea, "Critical assessment of thickness-dependent conductivity of thin metal films," *Thin Solid Films*, vol. 85, pp. 147-167, 1981/11/06 1981.

- [27] D. M. Pozar, "Microwave engineering / by David M. Pozar," 4th ed. ed. Hoboken, N.J.: Wiley, 2012.
- [28] Z. Hocenski, L. Cvitas, and Z. Lasinger, "Comparison of methods for nonlinearity correction of platinum resistance thermometer," in *SICE Annual Conference, 2008*, 2008, pp. 3151-3154.
- [29] *Principles of heat and mass transfer / Frank P. Incropera ... [et al.]*, 7th ed. ed. Hoboken, N.J.: Hoboken, N.J. : Wiley, 2013.
- [30] X. Shang, "SU-8 micromachined terahertz waveguide circuits and coupling matrix design of multiple passband filters / Xiaobang Shang," Birmingham, 2011.

Chapter 6

Microwave Power Sensor with Integrated Band-pass Filter Functions

The chapter introduces a novel approach in microwave power sensor design that can control and improve the bandwidth of the design technique discussed in Chapter 4. The coupling matrix method of distributed resonance two port network is described. The filter realisation with rectangular waveguide resonators is then presented, in which the coupling matrix entries are mapped to the physical dimensions of the resonators. Later, the work introduces the sensor-resonator construction, and the method of integration of the sensor-resonator with filters. The design approach utilises the advantages of filter design into power sensor design. In particular, the specification of centre frequency and bandwidth can be easily implemented. The design of X-band sensor with integrated third order Chebyshev band-pass filter function is introduced. The fabrication and measurement are also presented.

6.1. General Coupling Matrix Theory of Band-pass Filters

The coupling matrix method was first introduced by Atia and Williams for designing narrow band-pass cavity filters [1, 2]. It is adventurous to use the matrix form to characterise a coupled resonator filter network, because the synthesis can be performed on the coupling matrix with normal algebraic operations and the topology of the filter can be reconfigured by such matrix operations regardless which type of resonator is used [3]. The physical dimension of the resonators in the filter circuit is then determined by the matrix elements. The coupling matrix method is particularly suitable for narrow band-pass filter design because the derivation is based on the narrow band width assumption.

In general, there are two ways to represent a two-port network by coupling matrix including:

(i) $n \times n$ coupling matrix [4] and (ii) $n+2$ coupling matrix [3], where n is the order of the circuit.

The latter method is considered to be more general than $n \times n$ coupling matrix, the $n+2$ matrix includes the source and load couplings in its entries. In this work, the $n \times n$ coupling matrix is reviewed as it is the milestone in understanding the coupling matrix presentation of a filter circuit.

The general matrix A for a n coupled resonator network can be written as [4]

$$[A] = [q] + p[U] - j[m] \quad (6.1)$$

where $[q]$ is $n \times n$ matrix containing the scaled external quality factor q_{e1} and q_{en}

$$[q] = \begin{bmatrix} 1/q_{e1} & 0 & \dots & 0 \\ 0 & 0 & \dots & 0 \\ \vdots & \vdots & \ddots & \vdots \\ 0 & 0 & \dots & 1/q_{en} \end{bmatrix} \quad (6.2)$$

$[U]$ is $n \times n$ identity matrix and p is the complex low-pass frequency variable

$$p = j \frac{1}{FBW} \left(\frac{\omega}{\omega_0} - \frac{\omega_0}{\omega} \right) \quad (6.3)$$

The general coupling matrix $[m]$ denotes the normalised coupling coefficient between resonators.

$$[m] = \begin{bmatrix} m_{11} & m_{12} & \cdots & \cdots & \cdots & \cdots \\ m_{21} & m_{22} & \cdots & \cdots & \cdots & \cdots \\ \vdots & \vdots & \ddots & \cdots & \cdots & \vdots \\ \vdots & \vdots & \vdots & \ddots & \cdots & \vdots \\ \vdots & \vdots & \vdots & \vdots & \ddots & \vdots \\ \vdots & \vdots & \vdots & \vdots & \vdots & \ddots \\ m_{n1} & m_{n2} & \cdots & \cdots & \cdots & \cdots \end{bmatrix} \quad (6.4)$$

$[m]$ is a reciprocal matrix ($m_{ij}=m_{ji}$) and the diagonal entries m_{ii} represent the self-coupling coefficients which are zero for synchronous tuned filters.

The scattering parameter of the network can be calculated from the A matrix and the scaled external quality factor as follows

$$S_{21} = 2 \frac{1}{\sqrt{q_{e1} \times q_{en}}} [A]_{n1}^{-1} \quad (6.5a)$$

$$S_{11} = \pm \left(1 - \frac{2}{q_{e1}} [A]_{11}^{-1} \right) \quad (6.5b)$$

For all-pole Chebyshev band-pass filters, the scaled external quality factors and the normalised coupling coefficients can be derived from low-pass prototype elements g_0, g_1, \dots, g_{n+1} as follows [4].

$$\begin{aligned}
q_{e1} &= g_0 g_1 \\
q_{en} &= g_n g_{n+1} \\
m_{i,i+1} &= m_{i+1,i} = \frac{1}{\sqrt{g_i g_{i+1}}} \quad \text{for } i = 1 \text{ to } n-1 \\
m_{ij} &= 0 \quad \text{for } i \neq j+1 \text{ and } j \neq i+1
\end{aligned} \tag{6.6}$$

For arbitrary filter responses, complex solutions are available to determine the A matrix components [3].

It is worth describing the topology of a two-port n coupled resonator filter in Figure 6.1. Q_{e1} and Q_{e2} are the external quality factors of the input and output resonators, respectively. M_{ij} is the coupling coefficient between resonator i and j . The parameters will be discussed in more detail in section 6.2. If the coupling coefficients between non-adjacent resonator are zero (i.e. $M_{ij} = 0$ with $i \neq j+1$ and $j \neq i+1$), the filter is called a direct-coupled filter. Otherwise, it is a cross-coupled filter.

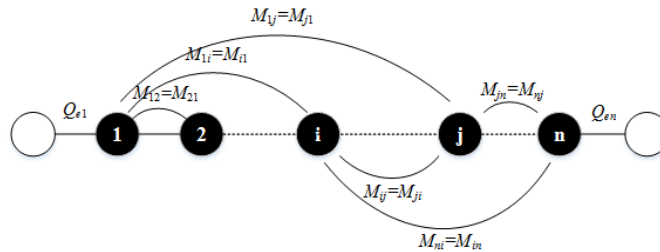


Figure 6.1: The topology of a two-port n coupled resonator filter.

The quality factors and coupling coefficients are related to the normalised quantities in the matrix A as follows

$$Q_{ei} = \frac{q_{ei}}{FBW} \tag{6.7a}$$

$$M_{ij} = m_{ij} \cdot FBW \tag{6.7b}$$

where FBW is defined as the fractional bandwidth of the band-pass filter with the centre frequency f_0 and the passband-edge frequency f_1 and f_2 ($f_2 > f_1$).

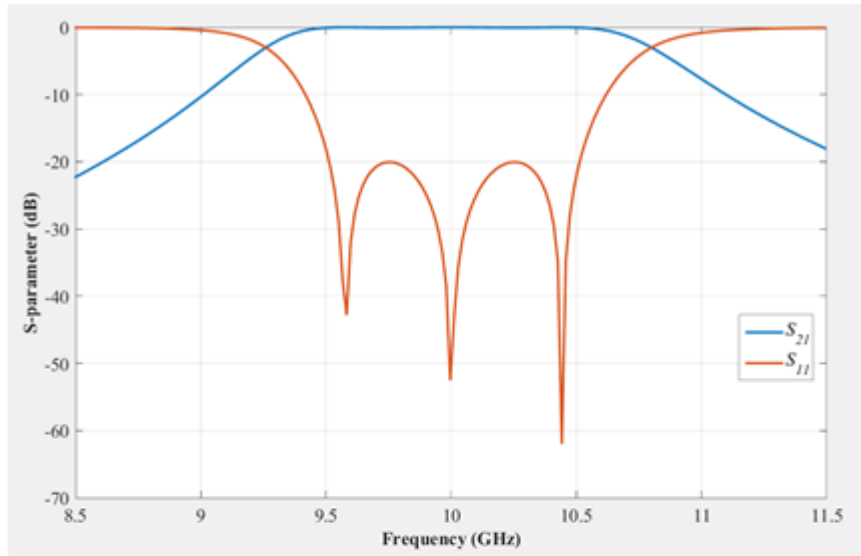
$$FBW = \frac{f_2 - f_1}{f_0} \quad (6.8)$$

As an example of the coupling matrix, a third order Chebyshev band-pass filter with 10% fractional bandwidth FBW and 0.0436 dB pass-band ripple at the centre frequency of 10 GHz can be designed. First, the g value of the low-pass prototype can be determined by equations or tabular values in [4], note that the order $n = 3$ and $L_{Ar} = 0.0436$ dB. The scaled external quality factors and normalised coupling coefficients are calculated by equation 6.6. The A matrix of the specified filter can be written as.

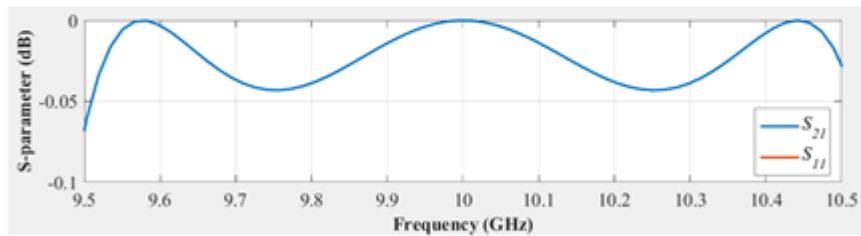
$$[A] = \begin{bmatrix} 0.117 & 0 & 0 \\ 0 & 0 & 0 \\ 0 & 0 & 0.117 \end{bmatrix} + j \frac{1}{FBW} \left(\frac{\omega}{\omega_0} - \frac{\omega_0}{\omega} \right) \begin{bmatrix} 1 & 0 & 0 \\ 0 & 1 & 0 \\ 0 & 0 & 1 \end{bmatrix} - j \begin{bmatrix} 0 & 0.103 & 0 \\ 0.103 & 0 & 0.103 \\ 0 & 0.103 & 0 \end{bmatrix} \quad (6.9)$$

where $\omega_0 = 2\pi f_0 = 20\pi \times 10^9$ rad.

The reflection coefficient S_{11} and the transmission coefficient S_{21} of the filter can be computed by equation 6.5. The S parameters are plotted in Figure 6.2. Filter has the centre frequency at 10 GHz, the minimum return loss of 20 dB can be seen in the pass-band from 9.5 GHz to 10.5 GHz. The pass-band ripple of 0.0436 dB is shown in Figure 6.2(b). The topology of the filter is presented in Figure 6.2(c), note that the filter is direct-coupled meaning only coupling between adjacent resonators i.e. 1 and 2 or 2 and 3 exists. The design parameters such as external quality factors and coupling coefficients of the band-pass filter can be calculated by equation 6.7 and are recorded in Table 6.1.



(a)



(b)



(c)

Figure 6.2: (a) Third order Chebyshev filter response generated from the matrix in equation 6.9; (b) the ripple of 0.0436 dB in the pass-band of the filter; (c) the topology of the filter.

Pass-band ripple L_{Ar}	Pass-band reflection coefficient	Quality factor Q_{e1}	Quality factor Q_{e3}	Coupling coefficient M_{12}	Coupling coefficient M_{23}
0.0436 dB	-20 dB	8.516	80516	1.031	1.031

Table 6.1: The design parameters of the 3rd order Chebyshev filter with 10% FBW

The design parameters are related to the physical dimension of the resonators forming the band-pass filter. The next section shows the realisation of filter by using rectangular waveguide resonators.

6.2. Realisation of Filter with Rectangular Waveguide Resonators

There are many types of microwave resonators in the filtering application, ranging from the parallel or series *RLC* resonant circuits to distributed elements such as microstrip lines, circular and rectangular waveguides. In this section, the rectangular waveguide resonator is reviewed and used for a demonstration of a simple filter. The resonant frequency and the quality factor of the resonator are discussed. The methods of extracting external quality factor and coupling coefficient between two resonators are introduced.

6.2.1. Rectangular waveguide cavity resonators

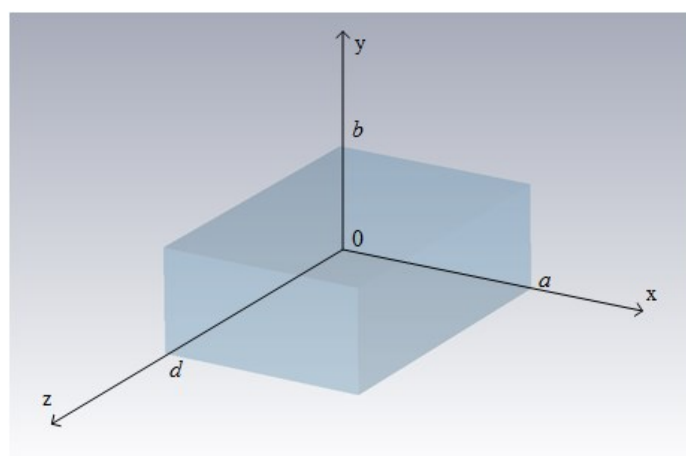


Figure 6.3: The geometry of a waveguide cavity, a and b are the standard dimensions of the waveguide cross section, the waveguide is shorted at $z = 0$ and $z = d$.

A waveguide resonator is constructed from a waveguide section with both ends being shorted, thus a cavity is created as shown in Figure 6.3. The standing electromagnetic waves are formed within the cavity of the resonator. The wave solution of the electric fields and the magnetic fields are reviewed in Chapter 3.

The short circuits at $z = 0$ and $z = d$ results in the boundary condition of zero electric field at both ends. As a result, the length d of the cavity should be an integer multiple of a half guided wavelength regardless the mode of the standing wave in the cavity.

$$d = l \frac{\lambda_g}{2} \quad \text{for } l = 1, 2, 3, \dots \quad (6.10)$$

The resonant mode in the cavity can be referred as TE_{mnl} or TM_{mnl} , where m , n and l are the wave number of the standing wave in the x , y and z direction, respectively. In general, the resonant frequency is given by [5]

$$f_{mnl} = \frac{c}{2\pi\sqrt{\mu_r\epsilon_r}} \sqrt{\left(\frac{m\pi}{a}\right)^2 + \left(\frac{n\pi}{b}\right)^2 + \left(\frac{l\pi}{d}\right)^2} \quad (6.11)$$

Where c is the speed of light in vacuum, μ_r and ϵ_r are the relative permeability and relative permittivity of the waveguide medium. In most cases, $b < a < d$, hence the TE_{101} mode has the lowest resonant frequency and is the dominant resonant mode.

Another important parameter of a resonator is quality factor Q , which is defined as the ratio of the average energy stored to the average energy loss. In other words, Q indicates the loss of the resonator. The loaded quality factor Q_l , is the combination of the internal loss, or unloaded quality factor Q_0 , and the external loss, so-called external quality factor Q_e , the relationship can be written as [5]

$$\frac{1}{Q_l} = \frac{1}{Q_0} + \frac{1}{Q_e} \quad (6.12)$$

Q_e indicates the amount of power coupled to the output of the resonator. When the resonator is not connected to or coupled by external ports i.e. shorted circuit at both ends of the cavity, the external quality factor Q_e is infinite and the loaded Q is equal to the unloaded Q .

The resonator loss can be due to conductor loss, dielectric loss or radiation loss, the unloaded quality factor Q_0 is the combination of all the losses of the resonator itself and given by [4]

$$\frac{1}{Q_0} = \frac{1}{Q_c} + \frac{1}{Q_d} + \frac{1}{Q_r} \quad (6.13)$$

where Q_c , Q_d and Q_r are the unloaded Q corresponding to lossy conductor, lossy dielectric and radiation, respectively.

For the case of enclosed waveguide cavity in Figure 6.3, there is no radiation to the environment, thus $Q_r = \infty$. The unloaded quality factor due to lossy conducting wall of the guide Q_c , and the lossy dielectric filling Q_d can be found as [5]

$$Q_c = \sqrt{\frac{\sigma}{\pi f \epsilon_0}} \frac{4\pi b}{\lambda^3} \frac{1}{2l^2 a^3 b + 2bd^3 + l^2 a^3 d + ad^3} \quad (6.14)$$

$$Q_d = \frac{1}{\tan \delta} \quad (6.15)$$

where σ is the conductivity of the waveguide wall material and $\tan \delta$ is the loss tangent of the dielectric material filling the waveguide.

6.2.2. Extraction of external quality factor Q_e

The coupling of the rectangular waveguide resonator with output ports or other resonators can be realised in the form of coupling irises. Some common iris types are shown in Figure 6.4. The coupling can be adjusted by controlling the area of the iris aperture. In general, the larger the aperture is, the lower the external quality factor is.

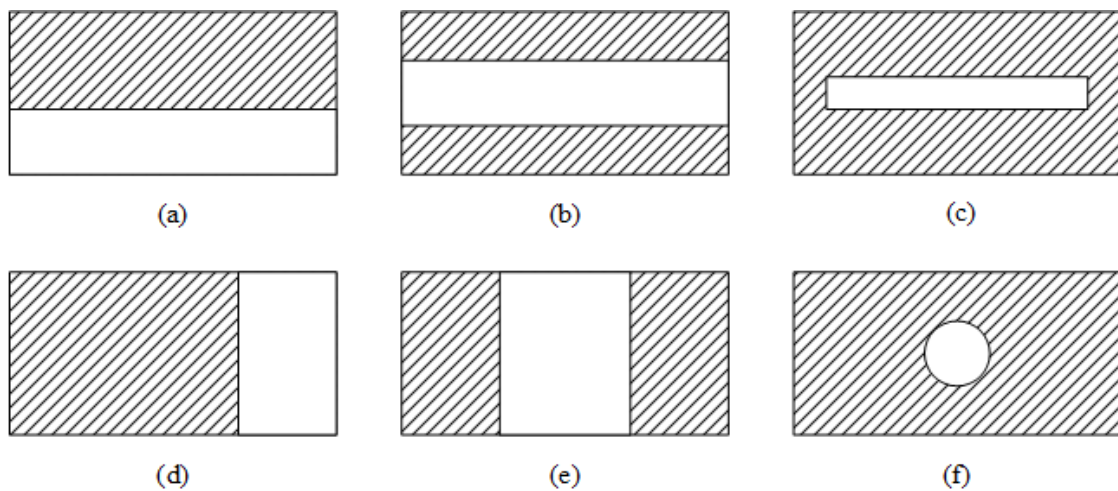


Figure 6.4: Some popular waveguide irises: (a) capacitive iris, (b) symmetrical capacitive iris, (c) rectangular iris, (d) inductive iris, (e) symmetrical inductive iris and (f) circular iris.

Regardless type of waveguide iris, the coupling of a resonator with two external ports can be presented by the lumped element model as shown in Figure 6.5 (a). The rectangular resonator is presented by a parallel LC circuit, the resonant frequency of the resonator is $\omega_0 = 1/\sqrt{LC}$. The external ports coupled with the resonator are presented by the conductance G_1 and G_2 . In order to have a very weak coupling at the second port, the conductance G_2 should be very large compared the conductance G_1 , the inductance and capacitance of the circuit.

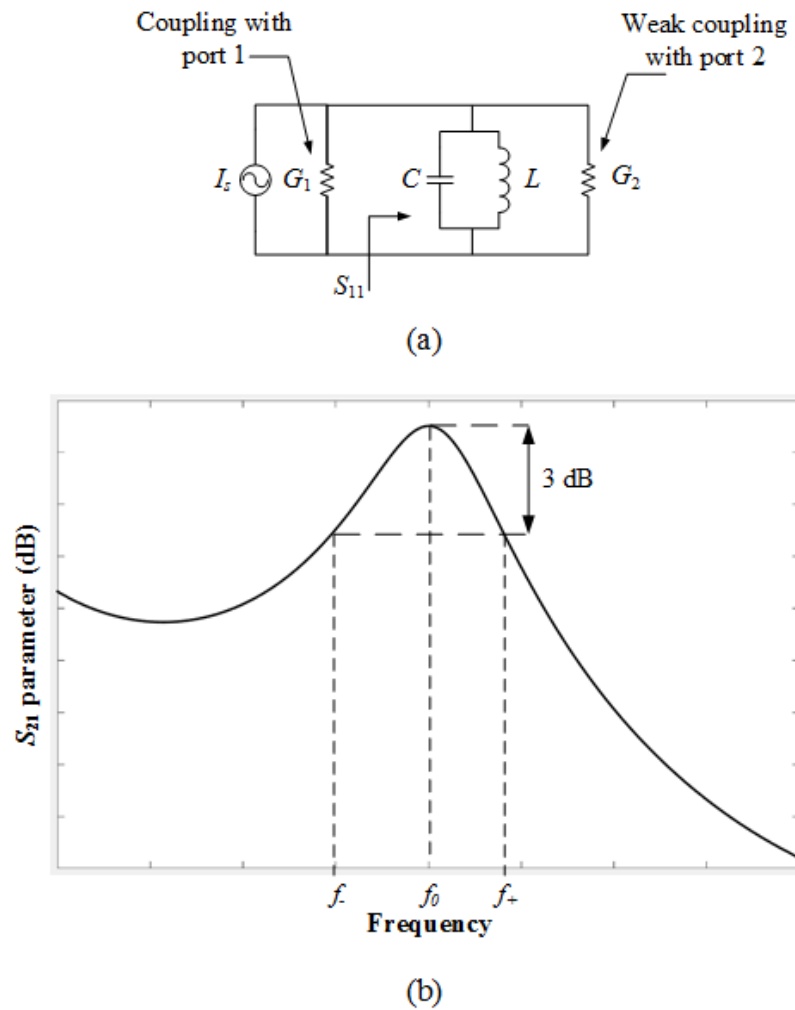


Figure 6.5: (a) The equivalent circuit of the extraction of the external quality factor Q_e , port 2 is weakly coupled to the LC circuit (i.e. $G_2 \gg G_1, L$ and C); (b) the transmission coefficient of the resonator.

The following method of extracting Q_e is useful for both symmetrical and asymmetrical resonator, and can be applied for resonators other than the waveguide resonator. The detailed derivation of the extracting Q_e used in this thesis is included in Appendix H. This method can be considered as an alternative formulations for extracting the external quality factor Q_e such as singly loaded resonator and symmetrically doubly loaded resonator discussed in [4].

The external quality factor can be calculated from the display of the transmission coefficient S_{21} in Figure 6.5(b) as follows.

$$Q_e = \frac{f_0}{f_+ - f_-} \quad (6.16)$$

where f_+ and f_- is the frequency at which S_{21} is reduced by 3 dB from its maximum value at the resonant frequency f_0 .

Note that the realisation of the coupling by using irises alters the resonant frequency because the condition of an enclosed cavity i.e. shorted at both ends in Figure 6.3 is not satisfied. Thus, the length of the resonator needs to be adjusted, in order to move the central frequency back to the designed value before the calculation of Q_e by equation 6.16.

6.2.3. Extraction of coupling coefficient M

The coupling coefficient between two resonators can also be obtained by evaluating the S parameter response. The equivalent lumped element circuit of the extracting method is shown in Figure 6.6(a), in which the two resonators in the form of parallel circuit L_1C_1 and L_2C_2 have the coupling coefficient M between them and weak couplings with the external ports. The general formula to calculate the coefficient M is given by [4].

$$M = \pm \frac{1}{2} \left(\frac{f_{02}}{f_{01}} + \frac{f_{01}}{f_{02}} \right) \sqrt{\left(\frac{f_{p2}^2 - f_{p1}^2}{f_{p2}^2 + f_{p1}^2} \right)^2 - \left(\frac{f_{02}^2 - f_{01}^2}{f_{02}^2 + f_{01}^2} \right)^2} \quad (6.17)$$

where f_{01} and f_{02} are the resonant frequencies of the resonators, the frequency f_{p1} and f_{p2} are the peak frequencies obtained from the S_{21} response of the coupling circuit. The plus and minus

signs differentiate coupling types such as magnetic, electric or mixed. Nevertheless, the positive or negative coupling have relative meaning. If one particular coupling is referred as positive then the negative coupling has the opposite phase response of S_{21} to that of the positive coupling. Equation 6.17 can be used to calculate the coupling coefficient between any two asynchronously tuned coupled resonators regardless of the coupling natures. More detailed of the derivation of the equation can be found in [4].

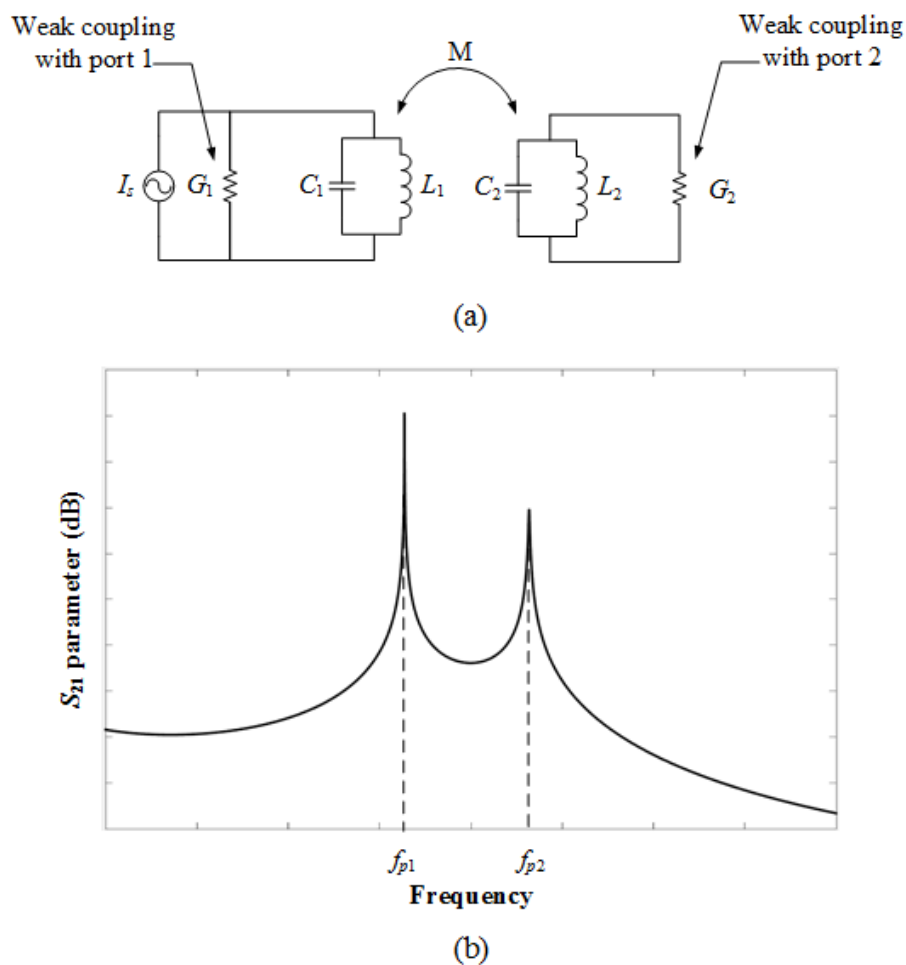


Figure 6.6: (a) The equivalent circuit of the extraction of the coupling coefficient M , the output ports are weakly coupled to the resonant circuits; (b) the transmission coefficient of the coupling circuit.

For synchronously tuned coupled resonator (i.e. $f_{01} = f_{02}$), the coupling coefficient can be calculated as.

$$M = \pm \frac{f_{p2}^2 - f_{p1}^2}{f_{p2}^2 + f_{p1}^2} \quad (6.18)$$

Note that the S_{21} parameter of the extraction in Figure 6.6(b) indicates the peak frequencies.

For narrow-band application, the centre frequency can be approximated as [4]

$$f_0 = \sqrt{f_{p1}f_{p2}} \quad (6.19)$$

The coupling between two rectangular waveguide resonators can be realised by one of the irises in Figure 6.4. In order to make the two resonator synchronously tuned, the lengths of the resonators should be equal. Like the extraction of quality factor, the enclosed cavity condition is also no longer satisfied due to the opened aperture between the two resonators. Thus, the length of the resonators should be adjusted from the initial value in equation 6.10 to tune the centre frequency by equation 6.19 before applying the calculation of M by equation 6.18.

6.2.4. Examples of a third order filter realisation

This section presents a third order Chebyshev filter realised by rectangular waveguide resonators at the centre frequency of 10 GHz. The topology and filter response calculated from the corresponding coupling matrix are in Figure 6.2. The design parameters including the coupling coefficient and the external quality factor of the filter can be found in Table 6.1.

The filter is realised by using capacitive irises. The extraction of the external quality factor and coupling coefficient of the X-band rectangular resonator at 10 GHz are discussed in section 6.4.2 and 6.4.3. Here, the results are used to integrate the filter as shown in Figure 6.7.

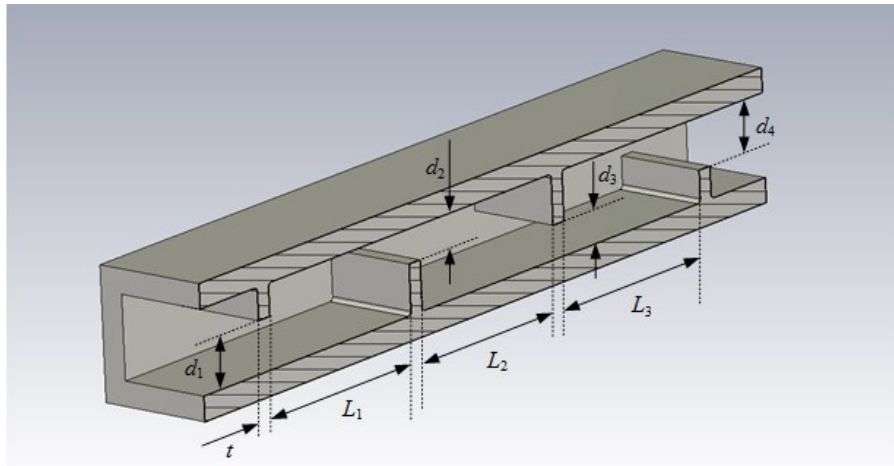


Figure 6.7: The structure of a 3rd order Chebyshev filter, the specifications of the filter are in Table 6.1, only half of the filter is shown in the figure.

The iris thickness t is 2 mm. The iris gap d and the length L of the resonators are selected from the extraction of the external quality factor and the coupling efficient in order to satisfy the design parameters in Table 6.1. The initial values of the filter dimensions are included in Table 6.2. Note that the dimensions of the first and the third resonator are identical. The initial simulated response of the filter is produced by full wave simulation, it is shown in Figure 6.8.

Parameter	Initial values	Optimised values
d_1	5.42 mm	6.25 mm
d_2	3.5 mm	4.09 mm
d_3	3.5 mm	4.09 mm
d_4	5.42 mm	6.25 mm
L_1	22.57 mm	25.04 mm
L_2	21.79 mm	24.15 mm
L_3	22.57 mm	25.04 mm

Table 6.2: The initial and optimised values of the dimensions of the filter in Figure 6.11.

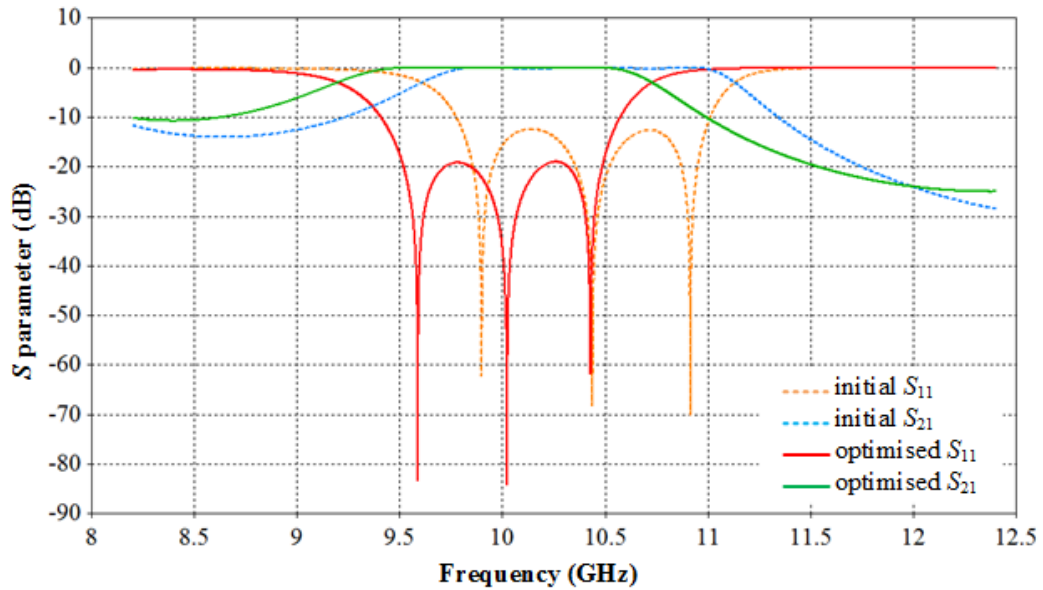


Figure 6.8: The initial and optimised response of the designed third order Chebyshev filter.

It can be seen that the initial simulated response of the filter has the characteristic of a third order filter as the reflection coefficient S_{11} has three transmission zeros. However, the centre frequency is shifted from the designed frequency of 10 GHz, and the return loss in the pass-band is about -14 dB. The optimisation is performed by the full wave simulation. The optimised response of the filter is also shown in Figure 6.8 for comparison. The deviations in the centre frequency and return loss are eliminated by adjusting the dimensions of the filter. The updated dimensions are included in Table 6.2. It is worth mentioning that the optimised response is identical to the filter response computed by the coupling matrix synthesis in Figure 6.2.

6.3. Integration of Microwave Power Sensor with Filter

This section discusses the integration the power sensor designed in Chapter 3 into the filter structure, in order to control and consequently improve the bandwidth of the integrated sensor. The conventional sensor is modified to turn into a resonator. The sensor-resonator, denoted as

R, will replace the last resonator and the output port in the filter topology in Figure 6.1; the new topology of the integration is shown in Figure 6.9. The coupling matrix of the integration is presented.

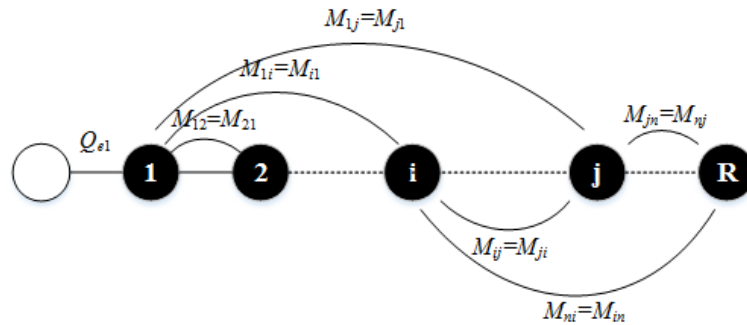


Figure 6.9: The topology of the power sensor with integrated band-pass filter function.

6.3.1. Sensor-resonator

The sensor structure discussed in Chapter 3 is indeed a resonator at the designed frequency f_0 . In order to be coupled with other waveguide resonator, an iris should be added to the structure while preserving the existing resonance. Figure 6.10 shows an example of the realisation of the sensor-resonator by adding a capacitive iris. Note that other types of irises in Figure 6.4 are applicable.

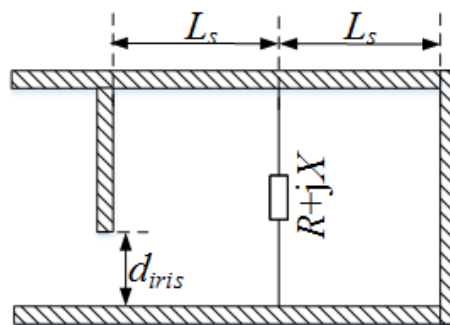


Figure 6.10: The sensor-resonator structure realised by adding a capacitive iris to the conventional power sensor structure discussed in Chapter 3

As discussed in Chapter 2, the mount of the sensing element, presented by $R + jX$ impedance, is placed at the position where the transverse electric field E_y is maximum. When the cavity is enclosed (i.e. $d_{iris} = 0$), the position of the iris should be where the electric field is zero, so that the resonant frequency is maintained and the boundary condition (i.e. $|E_y(z = 0)| = |E_y(z = 2L_s)| = 0$) is satisfied. For symmetrical structure, the length of the cavity is double that of the short length L_s .

When the sensor-resonator is coupled with an output port i.e. $d_{iris} > 0$, the loaded quality factor Q_l of the resonator can be written as follows

$$\frac{1}{Q_l} = \frac{1}{Q_e} + \frac{1}{Q_0} \quad (6.20)$$

Where Q_e is the external quality factor which is related to the width d_{iris} of the iris, Q_0 is the unloaded quality factor which can be further elaborated as

$$\frac{1}{Q_0} = \frac{1}{Q_c} + \frac{1}{Q_d} + \frac{1}{Q_r} + \frac{1}{Q_{er}} \quad (6.21)$$

Where Q_c , Q_d and Q_r are the quality factor corresponding to the conductance loss, dielectric loss and radiation loss, respectively. Since there is no loss in dielectric and radiation as well as the cavity wall, Q_d , Q_r and Q_c are infinitive. Therefore, Q_0 is equal to Q_{er} which is accounted for the power loss due to the absorption of the resistive sensing element in the cavity.

The topology of the sensor-resonator excited by one output port is shown in Figure 6.11(a). The power absorbed by the sensing element can be considered as an output with the power going to the element rather than an output port. This is shown in Figure 6.11(b).

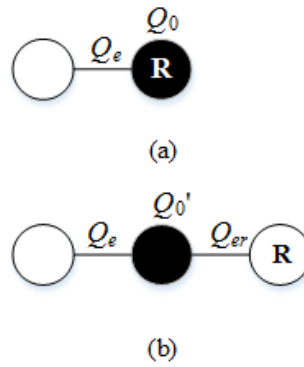


Figure 6.11: (a) Topology of the sensor-resonator; (b) equivalent topology of the resonator.

In this topology, the quality factor Q_{er} has the role of the external quality factor of the equivalent resonator, the unloaded quality factor Q_0' can be taken as infinity. As a result, the topology in Figure 6.9 can be transformed to an equivalent topology as shown in Figure 6.12.

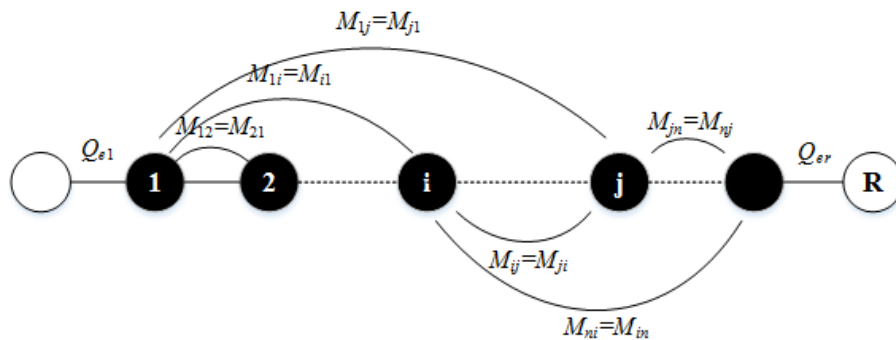


Figure 6.12: The equivalent topology of the power sensor integrated band-pass filter function in Figure 6.7.

The device described by the above topology is called filler-sensor in this thesis, the mathematical presentation of the device is covered in the following section.

6.3.2. Coupling matrix presentation of the integration of the sensor with filter

The topology in Figure 6.12 is similar to the n coupled resonator filter circuit discussed in the previous section, thus, it can be described by the A matrix as follows

$$[A] = \begin{bmatrix} \frac{1}{q_{er}} & 0 & \cdots & \vdots \\ 0 & 0 & \cdots & \vdots \\ \vdots & \vdots & \ddots & \vdots \\ 0 & 0 & \cdots & \vdots \end{bmatrix} \begin{bmatrix} 1 & 0 & \cdots & \vdots \\ 0 & 0 & \cdots & \vdots \\ 0 & 0 & \cdots & \vdots \end{bmatrix} \begin{bmatrix} m_{11} & m_{12} & \cdots & \vdots \\ m_{22} & \cdots & \vdots \\ m_{n1} & m_{n2} & \cdots & \vdots \end{bmatrix} \quad (6.22)$$

where q_{er} is the scaled quality factor of the sensor-resonator, m_{ni} and m_{in} ($i = 1$ to $n - 1$) are the normalised coupling coefficient between the sensor-resonator with other resonators and m_{nn} is the normalised self-coupling coefficient of the sensor-resonator.

The reflection coefficient S_{11} of the integration can be calculated by equation 6.5b as

$$S_{11} = \pm \left(1 - \frac{2}{q_{er}} [A]_{11}^{-1} \right) \quad (6.23)$$

It is worth mentioning that the filter-sensor is in fact a one port device, hence the calculation of S_{21} by equation 6.12a, although possible, does not have physical meaning.

It can be seen that the synthesis of filter-sensor can be applied in the same manner as the filter design. Each entry in the A matrix in equation 6.22 can be related to a physical dimension of the realised filter-sensor structure. The coupling coefficient between resonators can be extracted by the method discussed in section 6.2.3, the extraction of the external quality factor of the conventional resonator is introduced in section 6.2.2. Finally, the extraction of the quality factor Q_{er} is presented in the next section.

6.3.3. Extraction of external quality factor Q_{er} of the sensor-resonator

Unlike the resonator in section 6.2.2, the sensor-resonator is a lossy resonator. As discussed in section 6.31, the measurement of the quality factor Q_{er} is in fact the measurement of the unloaded Q_0 when there is no other loss than the power absorbed by the sensing element. The equivalent lumped element model of the extraction is shown in Figure 6.15(a), in which the resonator is presented by the parallel circuit GLC . The conductance G_e presents the external port coupled with the resonator. The detailed derivation of the method of the extraction can be found in Appendix I.

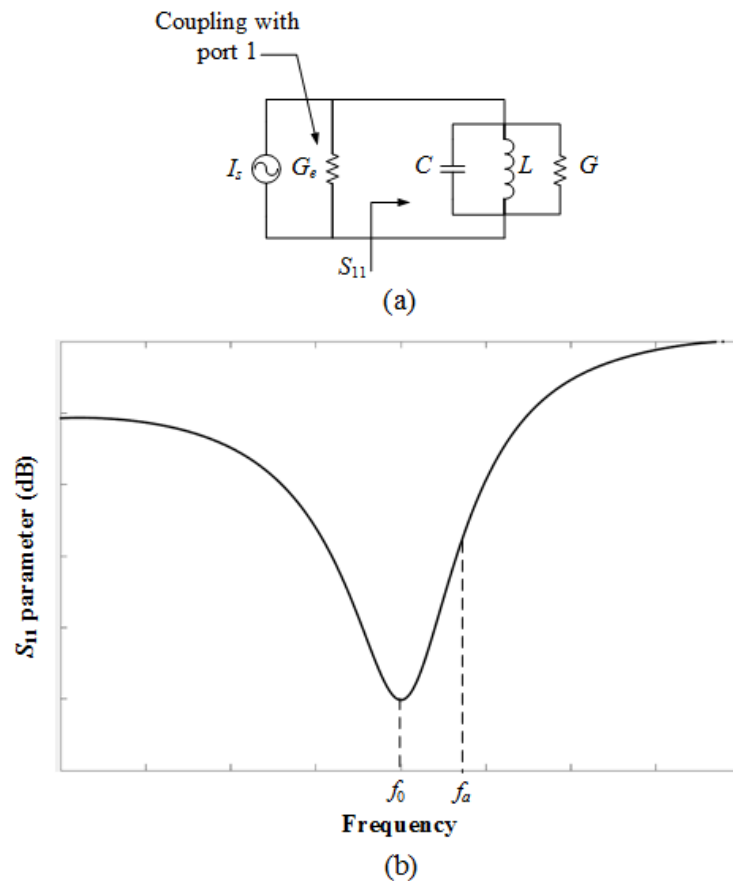


Figure 6.13: (a) Equivalent circuit of the extraction of quality factor of a lossy resonator; (b) typical the reflection coefficient of the one-port measurement of the resonator.

The external quality factor Q_{er} of the sensor resonator can be calculated by evaluating the reflection coefficient of the resonator and given by

$$Q_{er} = \frac{|1 + \beta|}{|\Delta(f_a)|} \sqrt{\frac{|S_{11}(f_a)|^2 - |S_{11}(f_0)|^2}{1 - |S_{11}(f_a)|^2}} \quad (6.24)$$

where f_0 is the centre frequency, f_a is some frequency other than the resonant frequency f_0 . $\Delta(f_a)$ is defined as

$$\Delta(f_a) = 1 - \frac{f_0^2}{f_a^2} \quad (6.25)$$

The coupling coefficient β can also be determined from the magnitude of S_{11} at the resonant frequency as follows.

$$\beta = \frac{1 \pm |S_{11}(f_0)|}{1 \mp |S_{11}(f_0)|} \quad (6.26)$$

The value of the coupling coefficient can be greater or smaller than unity, which corresponds to the case in which the resonator is over-coupled or under-coupled, respectively. A critically coupled condition is obtained when β is equal to unity. How the cavity is coupled can be determined from the gradient of the phase at the resonant frequency [6].

$$\left. \frac{d\phi}{df} \right|_{f=f_0} = \frac{2Q_0}{f_0} \frac{2\beta}{1 - \beta^2} \quad (6.27)$$

It can be easily seen that the gradient is positive, if β is smaller than unity and vice versa.

The quality factor Q_{er} can be calculated from equation 6.24 at a number of frequencies f_a near the resonant frequency, the values are then averaged to obtain a more accurate value of Q_{er} [6].

6.4. The Design of X-band Sensor with Integrated Third Order Filter Functions

In this section, the design of an X-band power sensor integrated with third order Chebyshev filter function is presented. The equivalent topology of a third order filter sensor is shown in Figure 6.14, in which the third resonator is the sensor –resonator with the equivalent external quality factor Q_{er} as discussed previously.

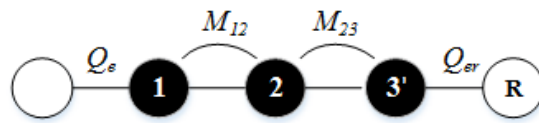


Figure 6.14: Equivalent topology of third order Chebyshev filter-sensor

The topology is realised by rectangular waveguide resonators and a bead thermistor sensor-resonator, which is similar to the sensor design in Chapter 4, at the centre frequency of 10 GHz. In order to have the similar reflection coefficient to the third order Chebyshev filter in Figure 6.6, the external quality factor and the coupling coefficient of the topology in Figure 6.18 should be identical to the design parameters in Table 6.1. The design parameter of the third order filter-sensor are summarised in Table 6.3 below.

Fractional Bandwidth	Pass-band ripple	Pass-band return loss	Quality factor Q_e	Quality factor Q_{er}	Coupling coefficient M_{12}	Coupling coefficient M_{23}
10%	0.0436 dB	-20 dB	8.516	8.516	1.031	1.031

Table 6.3: Specification of 3rd order filter sensor with 10 % FBW

In the following section, each design parameter is realised for the waveguide resonator using capacitive irises. The structure of the filter-sensor is introduced. The fabrication and measurement of the device are also presented.

6.4.1. Extraction of the external quality factor Q_{er} of the X-band sensor-resonator using a bead thermistor as the sensing element

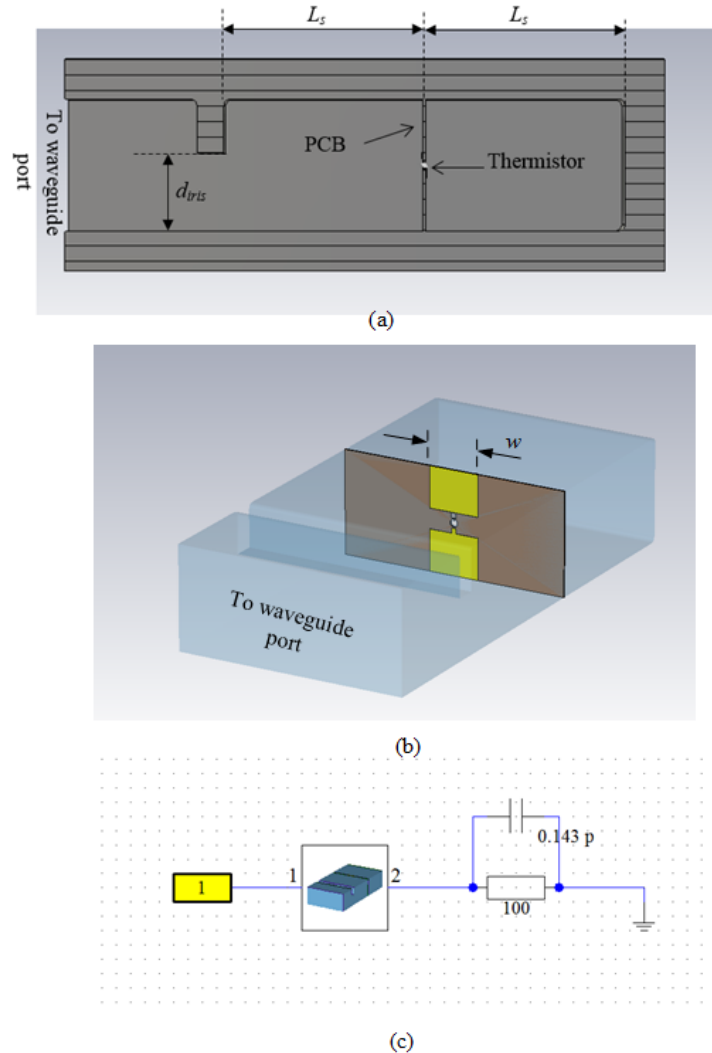


Figure 6.15: The simulation structure of X-band sensor-resonator (a) waveguide body (b) PCB (c) schematic including the thermistor circuit.

The extraction of the external quality factor Q_{er} of the sensor-resonator by evaluating the scattering response was presented in section 6.3.3, the electromagnetic simulation such as CST can be used to obtain the reflection coefficient of the X-band sensor-resonator. The sensor-resonator structure is shown in Figure 6.15(a) for one-port simulation, the thermistor mount

(see Chapter 4) is placed in the middle of the cavity. Figure 6.15(b) shows the inner structure of the resonator and the equivalent circuit of the bead thermistor is presented in Figure 6.15(c).

The external quality factor at different resistances of the bead thermistor was first extracted. It should be noted that the equivalent capacitance of the thermistor is dependent on the d-c resistance of the bead (see section 4.1), the estimated capacitance values in Figure 4.3 is used for the bead resistance up to 300 Ω . For larger d-c resistances, the capacitance of 0.1 pF was used. At different resistances, the cavity short length L_s also needs to be adjusted to maintain the resonant frequency of $f_0 = 10$ GHz. In this extraction the track width w of the PCB is remained at 3 mm. The result of the extraction is shown in Figure 6.16.

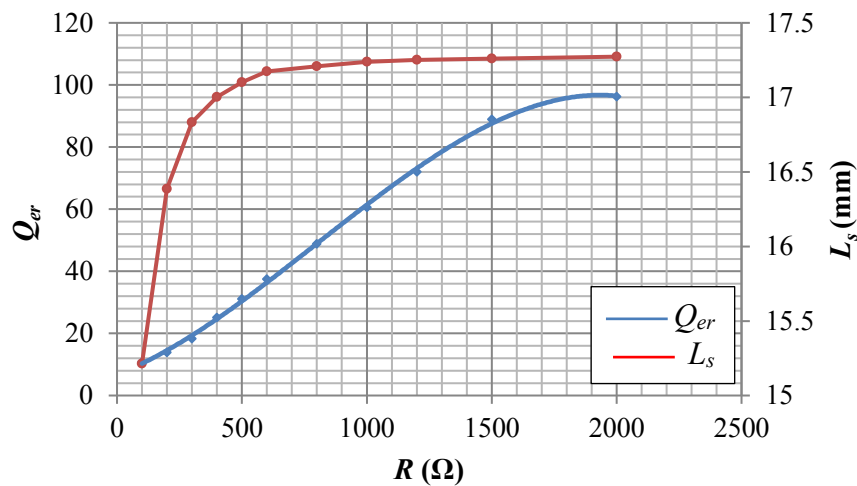


Figure 6.16: Extraction of Q_{er} with the resistance of the bead thermistor.

It can be seen that the quality factor Q_{er} of the sensor-resonator increase with the rise in the bead resistance. At 100 Ω resistances, Q_{er} is still greater than the target external quality factor of 8.516 in Table 6.3. The extraction was performed at the bead resistance of 100 Ω and with different copper track width w of the PCB as shown in Figure 6.15(b). Note that the equivalent circuit of the thermistor bead at 100 Ω operating resistance consists of a 100 Ω resistance in

parallel with 0.143 pF capacitor. The relationship between the external quality factor Q_{er} and the copper track width w is presented on Figure 6.17. The larger the width is, the lower the quality factor can be obtained. When w is 4.65 mm and L_s is 15.166 mm, the extracted quality factor is about 8.5 which is very close to the design parameter value in Table 6.3.

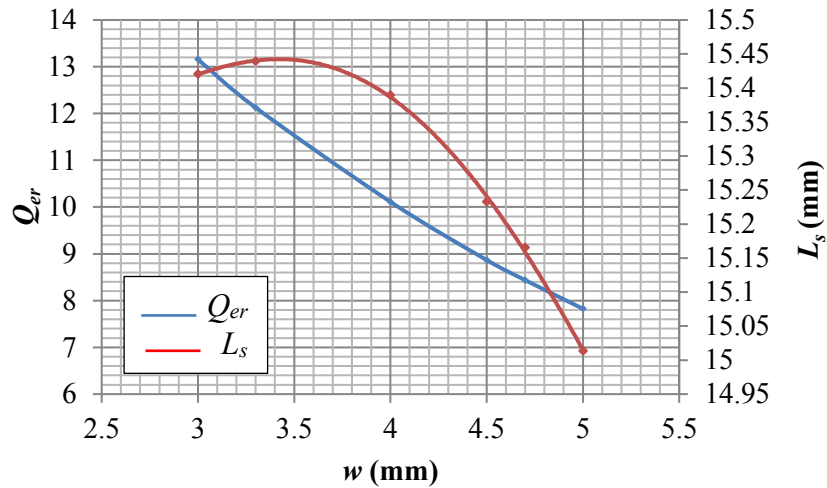


Figure 6.17: Extraction of Q_{er} at $R=100 \Omega$ and different track width w of the PCB

6.4.2. Extraction of the external quality factor of the X-band rectangular waveguide resonator

In order to extract the external quality factor of a rectangular waveguide cavity for the input to the filter-sensor, the two port measurement technique is used. The simulation model is shown in Figure 6.18. The cavity length is L_1 . The coupling between the resonator and the waveguide port is controlled by the first iris width d_1 . The iris width d is kept very small at 0.01 mm for very weak coupling at the right waveguide port.

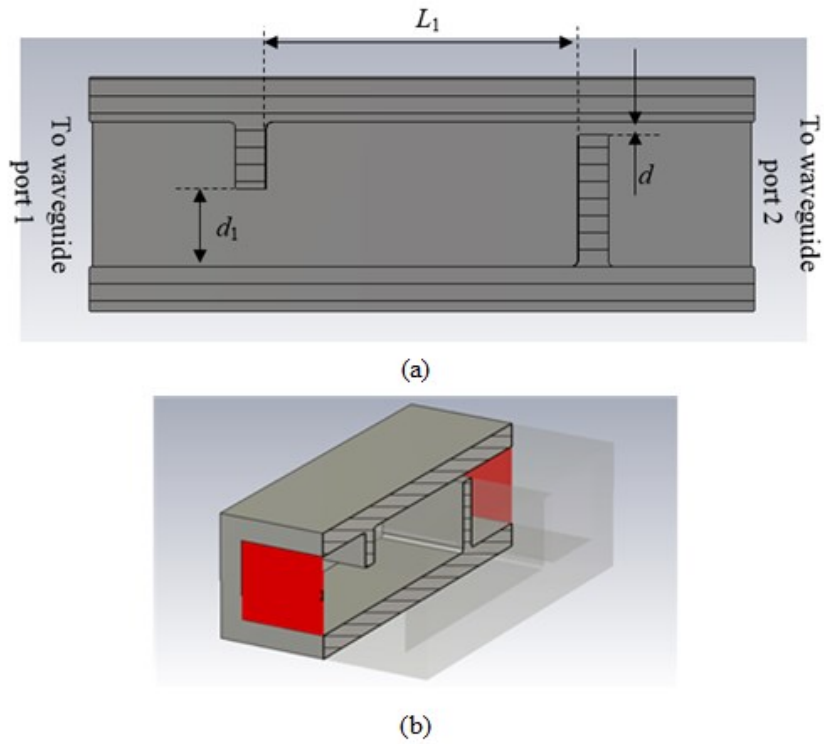


Figure 6.18: Two port measurement to extract the quality factor (a) cut side view (b) cut perspective view

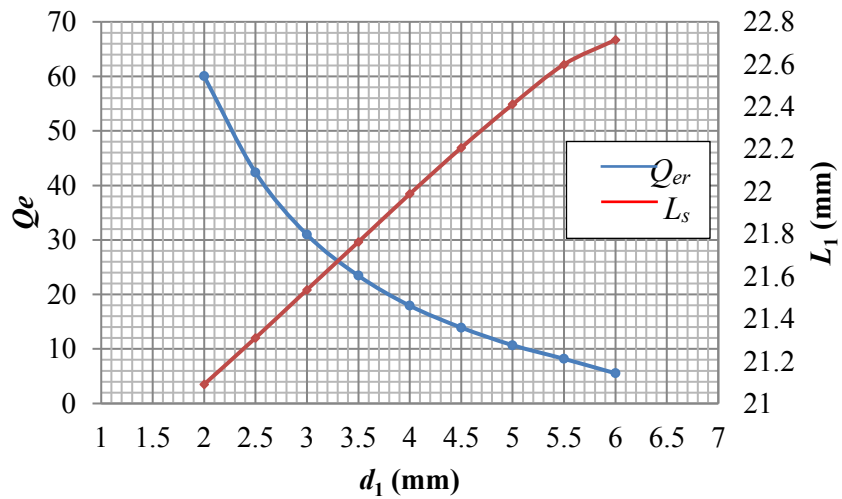


Figure 6.19: External quality factors and the cavity length of X-band waveguide resonator at different iris widths

The full wave simulation gives the transmission coefficient S_{21} of the two port simulation, the method of extracting the external quality factor introduced in section 6.2.2 is applied. The external quality factor was extracted at different the iris gap d_1 . The cavity length L_1 needs to be adjusted at different values of d_1 to keep the resonant frequency at 10 GHz. The result of the extraction is presented in Figure 6.19.

The results shows that the external quality factor Q_e reduces as the iris aperture increases as discussed in section 6.2.2. As the required external quality factor is 8.516, the iris gap d_1 is about 5.42 mm and L_1 is approximately 22.57 mm.

6.4.3. Extraction of the coupling coefficient between the X-band rectangular waveguide resonators

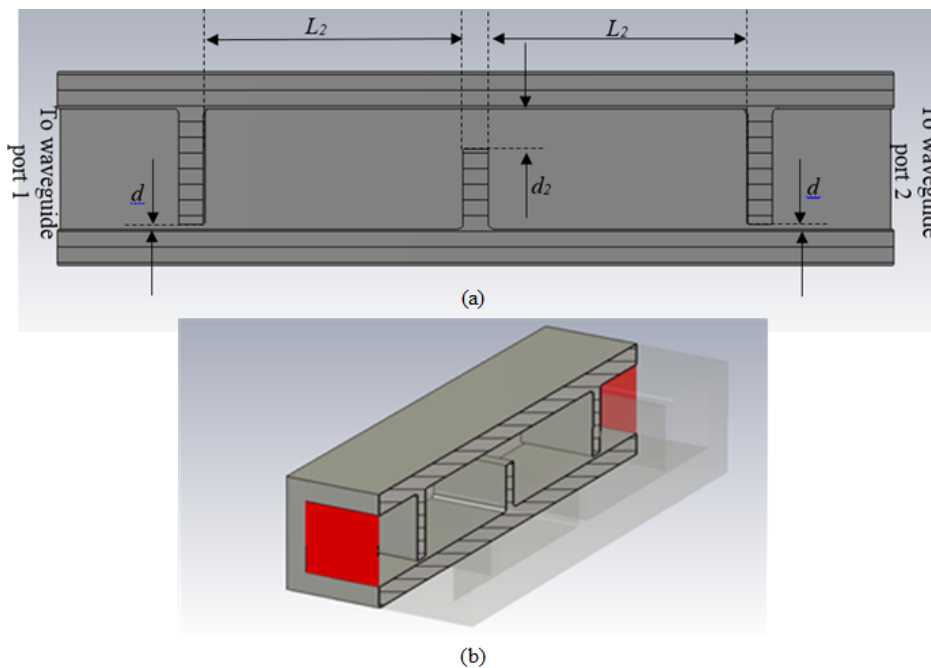


Figure 6.20: Measurement to extract coupling coefficient (a) cut side view (b) cut perspective view

In order to extract the coupling coefficient between two synchronous tuned coupled-rectangular waveguide resonators, the set-up in Figure 6.20 is used. The iris gap d was kept very small for weak coupling from the resonators to the output ports. The coupling between the two resonators is related to the iris width d_2 between them. The cavity lengths are equal at L_2 for both cavities in order to keep them resonating at the same frequency.

The electromagnetic simulation provides the transmission coefficient S_{21} . By using the extraction method introduced in section 6.2.3, the coupling coefficient between the two resonators can be calculated. The coupling coefficient was extracted at different the iris gap d_2 . The cavity length L_2 needs to be adjusted at each value of d_2 to keep the centre frequency at 10 GHz. The result of the extraction is presented in Figure 6.21. The result suggests that the coupling coefficient between the two resonators increase when the iris aperture gets larger. The required coupling coefficient is 1.031, hence the iris gap d_2 is about 3.5 mm and L_2 is approximately 21.79 mm.

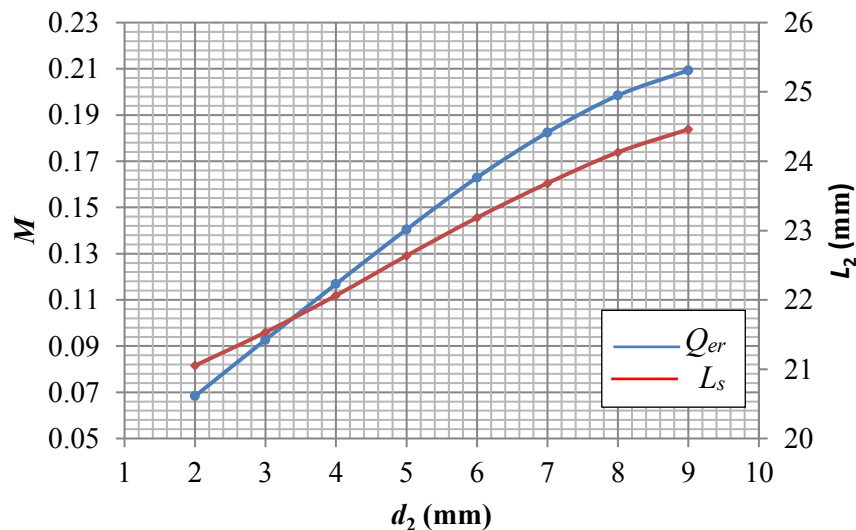


Figure 6.21: Coupling coefficient and the cavity length of X-band waveguide resonator at different iris widths

6.4.4. Filter-sensor integration

From the previous extraction of quality factors and coupling coefficients, the filter-sensor topology in Figure 6.14 is realised as shown in Figure 6.22. The initial dimensions of the structure are listed in Table 6.4.

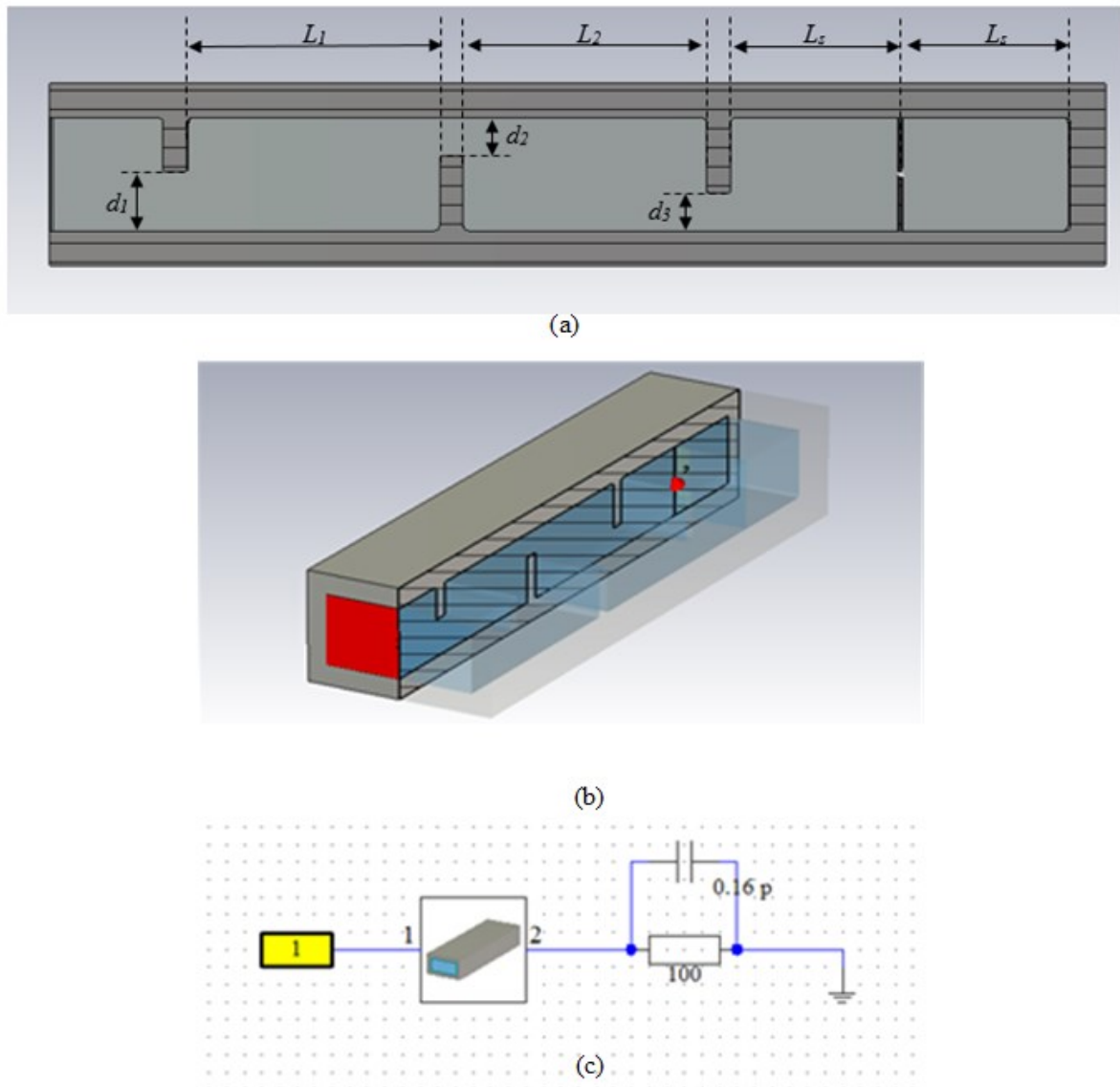


Figure 6.22: The filter-sensor integration (a) cut side view (b) cut perspective view (c) Schematic including the thermistor circuit

Parameter	value
w (mm)	4.65
d_1 (mm)	5.42
d_2 (mm)	3.5
d_3 (mm)	3.5
L_1 (mm)	22.57
L_2 (mm)	21.79
L_s (mm)	15.17

Table 6.4: Initial dimensions of the filter sensor integration

The response of the structure from the initially extracted dimensions is obtained by electromagnetic simulation as shown in Figure 6.23. It clearly is not the targeted filter response of S_{11} in Figure 6.2. An optimisation process is required to improve the response.

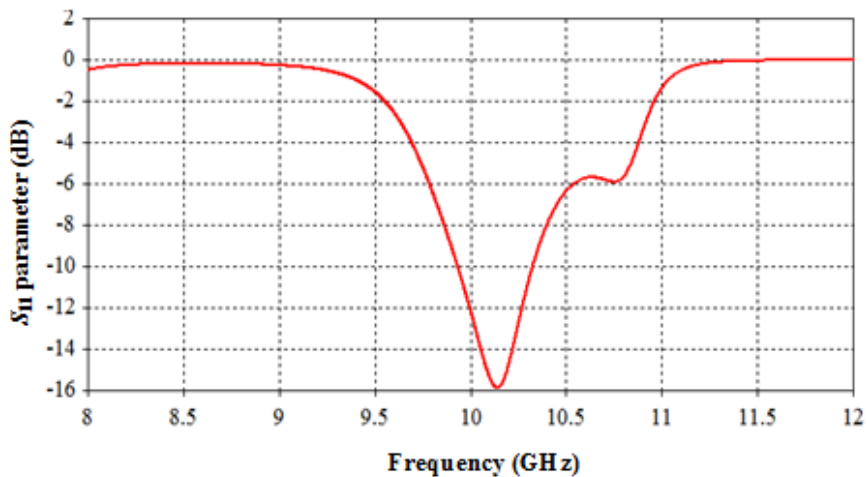


Figure 6.23: Initial response of the filter-sensor integration

The optimisation is performed by built-in algorithm in CST Microwave Studio. The goal is to obtain the filter-like response in Figure 6.2. The criteria of the optimisation are as follows:

- $S_{11} > -20$ dB from 9.5 GHz to 10.5 GHz
- $S_{11} < -20$ dB from 8 GHz to 9.5 GHz
- $S_{11} < -20$ dB from 10.5 GHz to 12 GHz

The optimisation of the filter-sensor response is divided into three stages:

- Stage 1: use the equivalent filter with the same topology to optimise the resonator lengths L_1 and L_2 .
- Stage 2: optimise the sensor-resonator related parameters including the cavity length L_s , the iris gap d_3 and the width w of the PCB accommodating the bead thermistor.
- Stage 3: final optimisation on all parameters.

The optimised result is shown in Figure 6.24, and the updated parameters are recorded in Table 6.5.

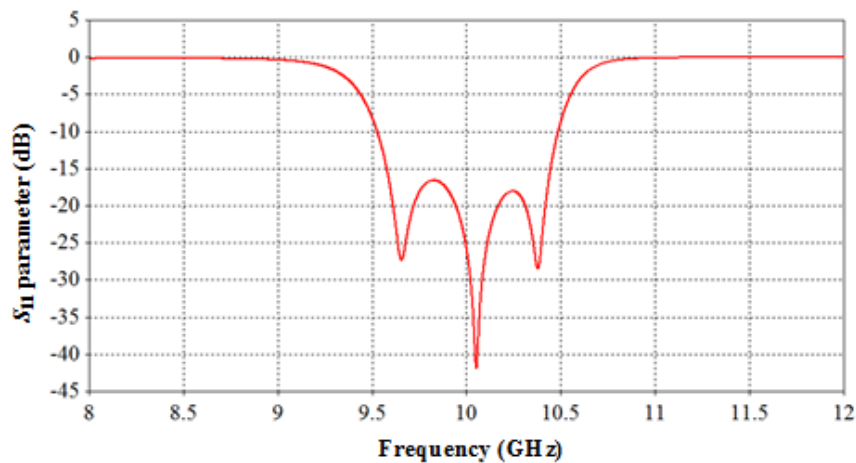


Figure 6.24: Optimised result of the integration of sensor-resonator to filter

The optimised response has the characteristic of the reflection coefficient of a third order Chebyshev filter, the insertion loss in the pass-band is lower than 15 dB. The simulation at this stage is for the inner structure of the filter-sensor. The further optimisation will be run after the design of the complete structure of the power filter-sensor discussed in the following section. The optimised parameters are recorded in Table 6.5.

Parameter	Before optimisation	After optimisation
L_1 (mm)	22.57	24.19
L_2 (mm)	21.79	23.37
d_1 (mm)	5.42	5.44
d_2 (mm)	3.5	3.12
L_s (mm)	15.17	15.10
d_3 (mm)	3.5	4.54
w (mm)	4.65	3.51

Table 6.5: The record of all parameters before and after optimisation process

6.4.5. The structure of the third order filter-sensor

The structure of the filter-sensor is shown in Figure 6.25. In fact the structure of the filter-sensor is very similar to the structure of the sensor in Chapter 4. The most noticeable difference between the two devices is that the front waveguide part of the X-band filter-sensor consists of three capacitive irises. The description of the construction of the waveguide and the PCB accommodating the bead thermistor can be found in section 4.1.3.

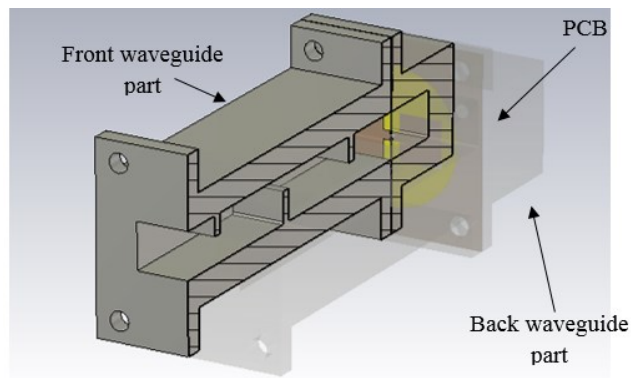


Figure 6.25: The structure of the X-band filter-sensor in 3D design environment.

By using the updated dimensions in Table 6.5, the initial reflection coefficient was obtained and shown in Figure 6.26 as the red dashed line. The response is different from the optimised

result of the integration because the PCB introduces a discontinuity between the two waveguide parts. As a result, the dimensions of the filter sensor need to be further optimised to compensate for that effect. The optimised result is also included in Figure 6.26 as the green line, the pass band is well below -20 dB. The corresponding parameters are presented in Table 6.6.

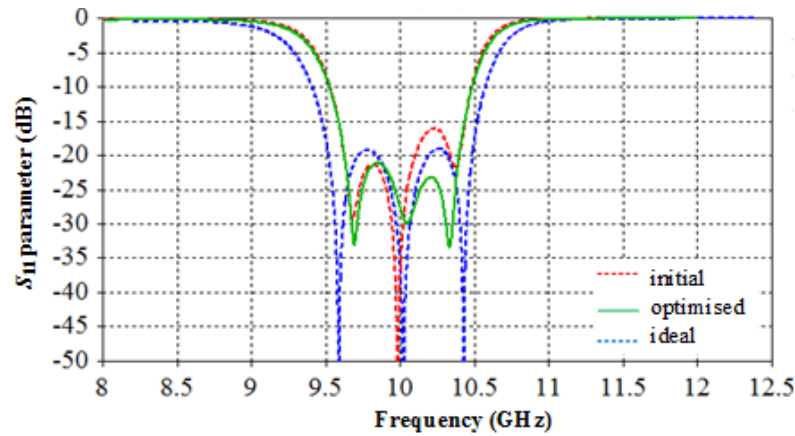


Figure 6.26: The reflection coefficient of the filter-sensor

Parameters	Initial	Optimised
L_1 (mm)	24.19	24.52
L_2 (mm)	23.37	23.59
d_1 (mm)	5.44	5.88
d_2 (mm)	3.12	3.35
L_s (mm)	15.10	14.94
d_3 (mm)	4.54	4.66
w (mm)	3.51	3.54

Table 6.6: Optimised parameter of the filter-sensor for the initial and optimised responses

Compared to the ideal response from the coupling matrix, the -20 dB bandwidth is 80% of the ideal value that could be resulted by the optimisation algorithm built-in the electromagnetic simulation software. In addition, the realisation of the filter response at 10% *FBW* could reach the limit bandwidth of the coupling matrix theory because the design theory is based on the

narrowband assumption. Nevertheless, the band width of the simulated filter-sensor is much larger than that of sensor designed in Chapter 4 as shown in Figure 6.27.

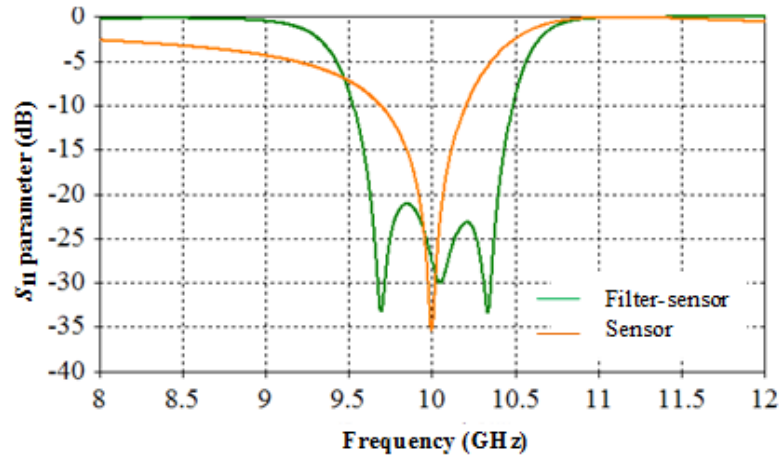
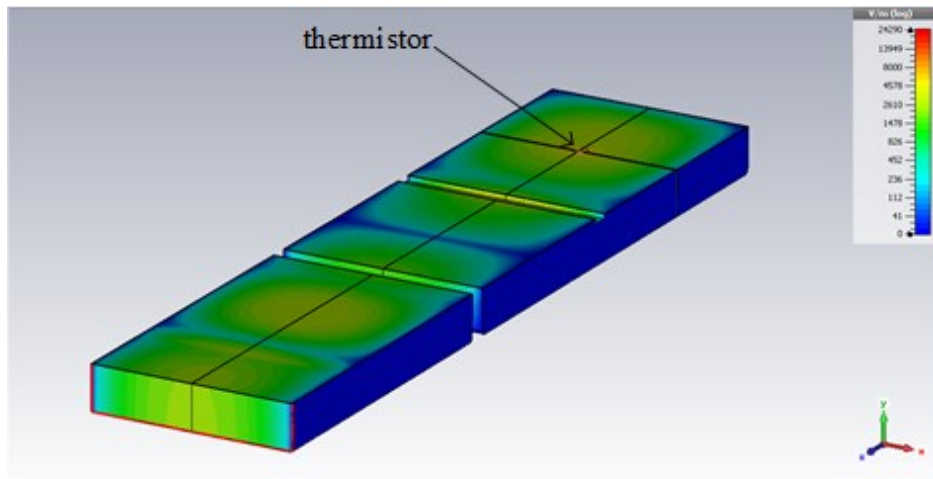


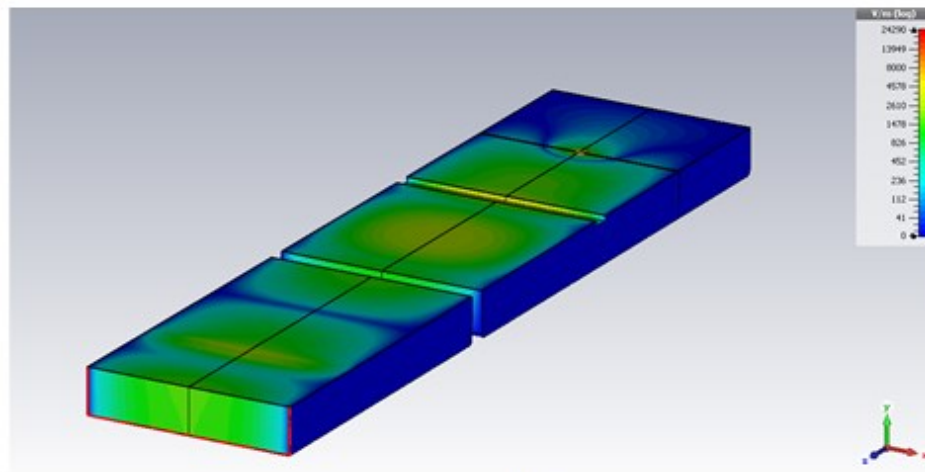
Figure 6.27: Comparison between simulated responses of the sensor in chapter 4 and the X band filter-sensor

The electric field at frequencies where minima in S_{11} of the filter-sensor was observed. The rms amplitude of the fields are shown in Figure 6.28. It can be seen that at the frequencies of 9.6 GHz, 10.05 GHz and 10.4 GHz, the maximum electric field strength is found at the thermistor mount position. That indicates the microwave power is absorbed by the thermistor across the bandwidth of the filter-sensor. In fact, the filter-sensor is one-port device, when incident power is not fully reflected, the thermistor is the lossy component that can dissipate the incident power.

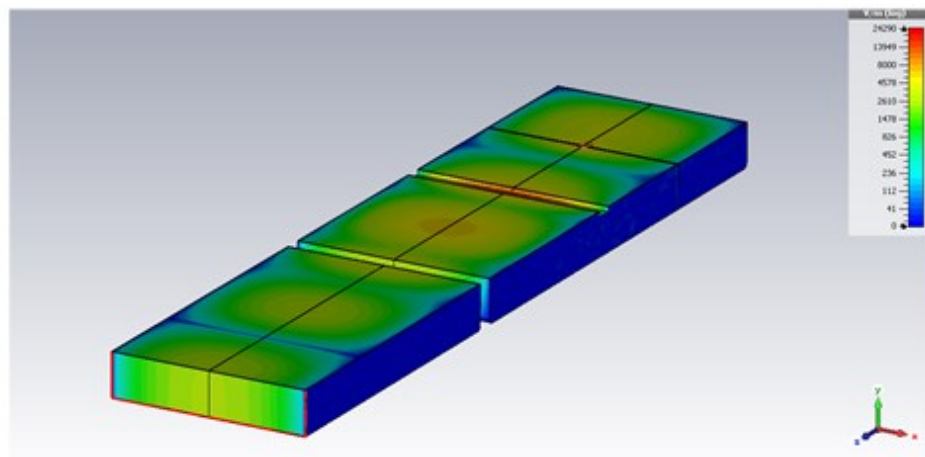
The same amplitude of the electric field at the investigated frequencies also suggest the same absorptivity. Therefore, the efficiency of the power sensor at the frequencies of minimum reflection coefficient should be equal. In practice, the effective efficiency of the sensor can vary across the operating bandwidth of the sensor. The values of calibration factor and effective efficiency can be obtained by the calibration service at each frequency of interest.



(a)



(b)



(c)

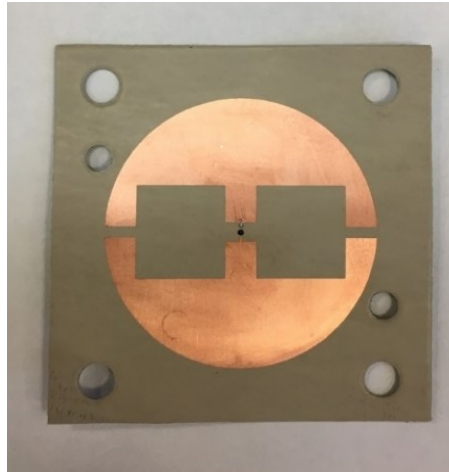
Figure 6.28: The rms amplitude of the electric field inside the filter-sensor structure at (a) 9.6 GHz, (b) 10.05 GHz and (c) 10.4 GHz.

The new design of filter-sensor has shown a huge improvement in the bandwidth of the microwave power sensor, it has the -20 dB bandwidth of 0.8 GHz at 10 GHz centre frequency. In this design, the traditional sensor is considered in term of a resonator and is integrated at the end of a series of resonators with a similar topology to microwave filter design.

6.4.6. Fabrication and measurement

The filter-sensor at X-band was fabricated at Birmingham by same technique and materials as the X-band power sensor. The PCB was fabricated with circular electrodes as shown in Figure 6.29(a). The waveguide parts are made by two halves and joined together by M3 screws. The fully assembled X-band filter-sensor is shown in Figure 6.29 (b) with the PCB being clamped between the front waveguide part and the short waveguide part. The red and blue cables are attached to the waveguide body in order to apply d-c power to the thermistor at the centre of the PCB. The detailed structure with dimensions of all parts can be found in Appendix J.

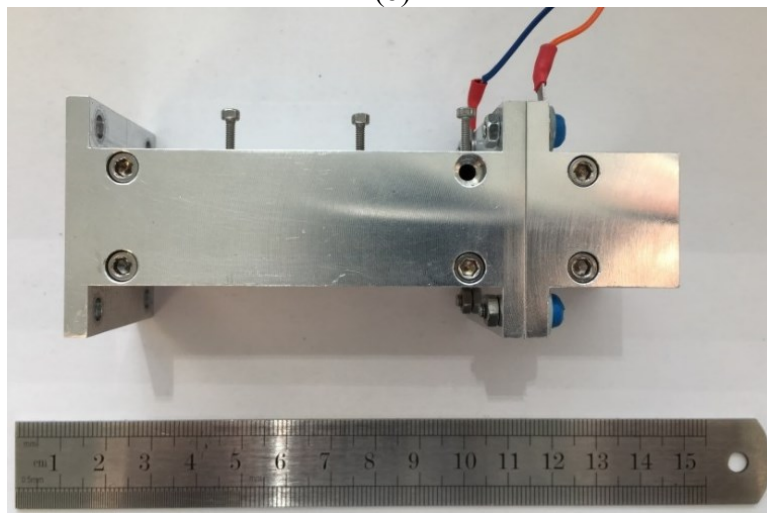
The X-band filter-sensor was measured by the same set-up used in the measurement of the X-band sensor presented in Chapter 4. By using the NPL-UK auto-balancing circuit reviewed in Chapter 2, the thermistor can be biased to any resistances for testing. The reflection coefficient, the sensor linearity, the effective efficiency and the calibration factor of the X-band filter-sensor are sequentially evaluated.



(a)



(b)



(c)

Figure 6.29: (a) The fabricated PCB for the X-band filter-sensor (b) the waveguide parts after assembling and (c) the fully assembled X-band filter-sensor.

Measurement of the reflection coefficient

The NPL balancing circuit is used to automatically maintain the bead thermistor to 100 Ω . The sensor is connected to one port of the VNA setup in order to measure the reflection coefficient. The measured response is shown in Figure 6.30, it has the characteristic of the reflection coefficient of a third order filter. However, the return loss in the band pass is about 15 dB. The differences between the measured and simulated response may be due to many factors but the approximation of the bead thermistor circuit components is the major factor as discussed in the measurement of the X-band sensor.

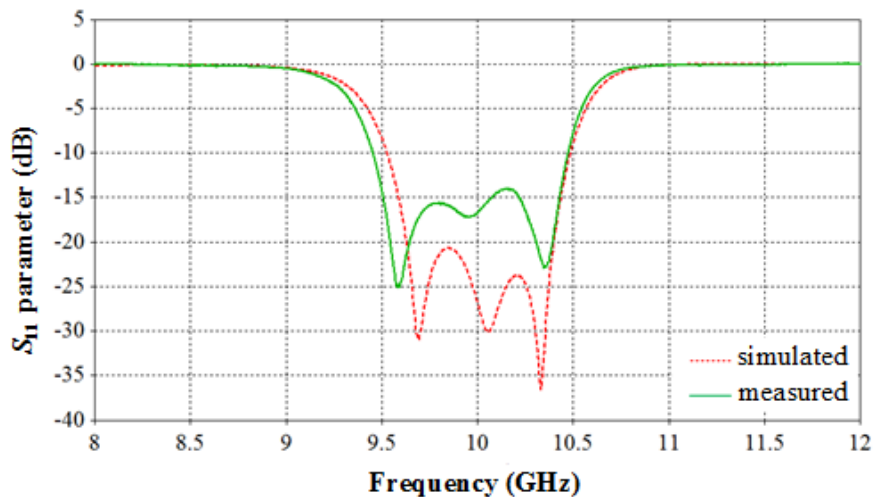


Figure 6.30: The measured and simulated reflection coefficient of the X-band filter-sensor at 100 Ω thermistor resistance.

The measured response can be tuned by introducing M2 tuning screws. The first two conventional waveguide resonators have the tuning screws at the centre of the cavity, the sensor-resonator has two screw poisoned symmetrically at the two sides of the PCB as shown in Figure 6.29(c). The tuned response of the filter-sensor at 100 Ω thermistor resistance is presented in Figure 6.34. The reflection coefficient has the maximum in the pass-band at -15 dB and the centre frequency is about 9.8 GHz

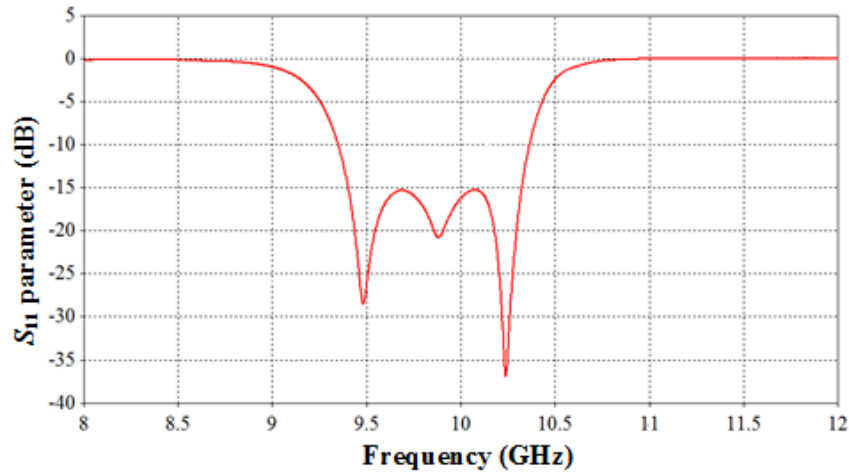


Figure 6.31: The tuned S_{11} parameter of the X-band filter-sensor by tuning screws at 100Ω thermistor resistance.

The extraction in section 6.4.1 shows that the thermistor's d-c resistance can affect the quality factor Q_{er} of the sensor-resonator. Therefore, the response of the filter-sensor can be further improved. By adjusting the thermistor resistance to 150Ω and applying tuning screws at the resonators, the pass-band of the reflection coefficient can be brought down to -20 dB and the centre frequency was moved to 9.98 GHz as indicated in green in Figure 6.32.

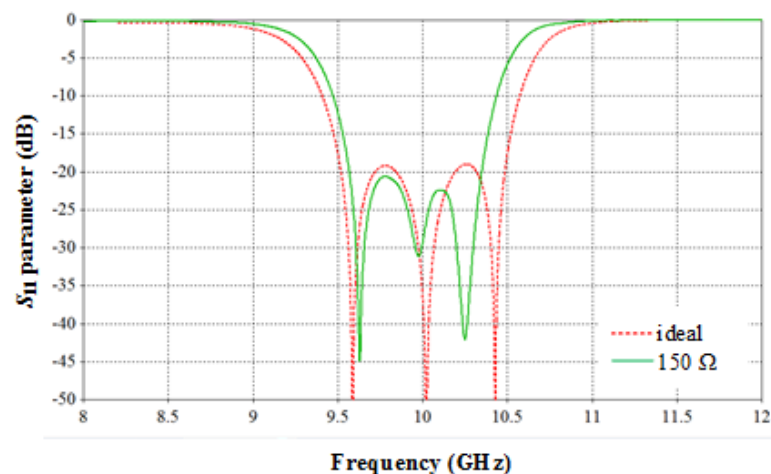


Figure 6.32: The reflection coefficient of the X-band filter-sensor at 150Ω thermistor resistance and the ideal third order Chebyshev filter response in comparison.

Compared to the ideal S_{11} of a third order Chebyshev filter, the measured response has a smaller -20 dB bandwidth of about 80 % of the ideal filter response. In the following section, the filter-sensor is measured at 150 Ω operating condition where the best insertion loss is obtained.

Measurement of the linearity with power

Similar to the measurement with microwave input powers of the X-band sensor in section 4.4.3, the filter-sensor is tested with the measurement set-up in Figure 4.22 at 10 GHz. The auto-balancing circuit is used to maintain the thermistor resistance at 150 Ω . The voltage on the thermistor is monitored before and after the input of microwave power from the signal generator. The relationship between the substitutional d-c power P_{sub} and the input microwave power P_{in} is plotted in Figure 6.33. The red dots are the measured points at different input powers up to 12 mW and the linearity can be seen by the blue fitted line

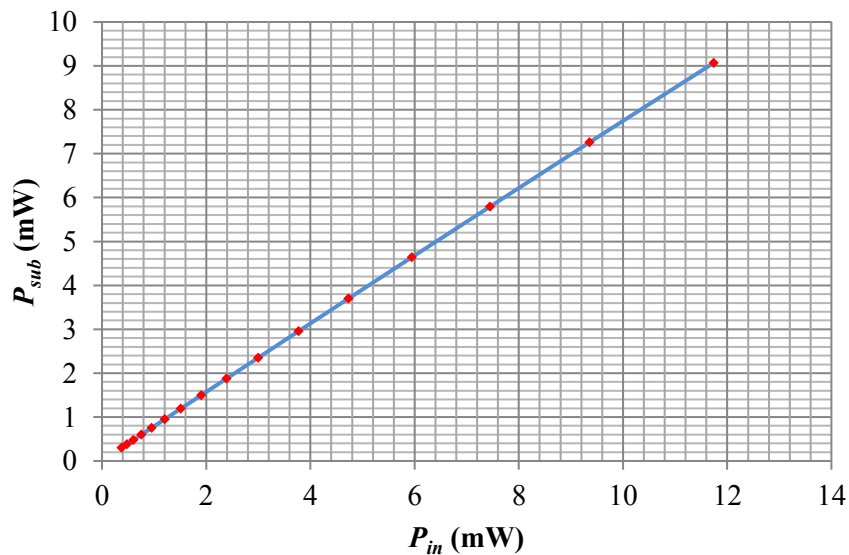


Figure 6.33: The relationship between input power and substitutional power at 150 Ω thermistor operation of the X-band filter-sensor.

The mathematical relationship can be obtained by using linear regression algorithm, which gives

$$P_{sub} = 0.9029P_{in} + 0.0307 \text{ (mW)} \quad (6.28)$$

The correlation coefficient r of 0.9999 suggests an excellent positive linear relationship. The common error variance σ of 17×10^{-3} indicates the small errors obtained. The measurement validates the usability of the sensor for the power application.

Measurement of effective efficiency and calibration factor

The calibration factor and the effective efficiency of the filter-sensor at 150 Ω operation can be obtained from the data of linearity measurement at the University of Birmingham as discussed in section 4.4.4. The parameters were also obtained at National Physical Laboratory. Table 6.7 summarises the results from both places.

Measurement lab	VRC	Calibration factor	Effective efficiency
University of Birmingham	$0.033 \angle 157.61^{\circ}$	0.9029	90.41%
National Physical Laboratory	$0.037 \angle 163.83^{\circ}$	0.8877	88.90%

Table 6.7: The calibration factor and effective efficiency from the measurement at the University of Birmingham and National Physical Laboratory.

The same discussion in the measurement of X-band sensor can be applied. The more accurate values of the calibration factor and effective efficiency can be obtained from the NPL measurement. The values obtained from Birmingham are quite close to the NPL numbers that shows confidence in the previous measurements of the X-band filter-sensor.

References

- [1] A. E. Atia and A. E. Williams, "Narrow-Bandpass Waveguide Filters," *IEEE Transactions on Microwave Theory and Techniques*, vol. 20, pp. 258-265, 1972.
- [2] A. Atia, A. Williams, and R. Newcomb, "Narrow-band multiple-coupled cavity synthesis," *IEEE Transactions on Circuits and Systems*, vol. 21, pp. 649-655, 1974.
- [3] R. M. Richard J. Cameron, Chandra M. Kudsia, *Microwave Filters for Communication Systems: Fundamentals, Design and Applications*: Wiley, 2007.
- [4] J. S. Hong, *Microstrip Filters for RF/Microwave Applications: Second Edition*, 2001.
- [5] D. M. Pozar, "Microwave engineering / by David M. Pozar," 4th ed. ed. Hoboken, N.J.: Wiley, 2012.
- [6] M. J. Lancaster, "Passive microwave device applications of high temperature superconductors / M.J. Lancaster," ed. Cambridge: Cambridge University Press, 1997.

Chapter 7

Conclusion and Future Work

7.1. Conclusion

This work presents two design techniques of the microwave power sensors which can be used as power transfer standard at National Physical Laboratory in the United Kingdom. The power sensors are of bolometric type where the dissipation of microwave power results in the change of the resistance of the sensing element. The d-c substitution power compensating for the resistance change indicates the amount of incident power to the sensor.

The first design technique is based on transmission line theory. Several applications of the technique has been reported in the literature, however, the detail of mathematical analysis and design process has not been explicitly documented. The conventional microwave power sensor is considered in terms of a transmission line consisting of a complex impedance load placed at the appropriate distance from a short at the end of the line. The relationship between the impedance of the mount and the electrical short length is obtained, in order to satisfy the matching condition of the sensor. The approach results in narrow band sensor response. In the design process, the impedance of the mount can be extracted with the aid of a full wave electromagnetic simulator.

The first application of the technique described in the thesis is the X-band power sensor operating at 10 GHz. The sensor utilises a bead thermistor as the sensing element. The

thermistor is modelled in the simulation by its equivalent circuit. At operating condition, the thermistor has the resistance of 200Ω . The dimensions of the thermistor mount in the waveguide are determined by the transmission line design process followed by optimisation in the electromagnetic simulator. The X-band sensor is fabricated and measured at the University of Birmingham. By tuning the d-c resistance of the thermistor to 400Ω , the measured reflection coefficient of the sensor has the centre frequency at 10 GHz, the -15 dB bandwidth is about 250 MHz. The sensor shows an excellent power linearity. The calibration with the multi-state reflectometer at NPL gives the effective efficiency of 85%.

The second design based on transmission line theory is the W-band power sensor at 94 GHz. The sensor uses a narrow platinum thin film placed at the transverse plane of the W-band waveguide. The thin film is modelled as an Ohmic sheet in the full-wave simulation. The simulation model is validated by two comparisons between the theoretical analysis and simulated results of (i) the transmission of the electromagnetic wave in a waveguide through a metallic thin film and (ii) the reactance of a transverse narrow thin film in waveguide. The dimensions of the sensor is determined so that the impedance matching in the waveguide is obtained at 94 GHz. The simulated sensor response has the centre frequency at 94 GHz and the -20 dB band width of 5 GHz. The W-band sensor design can be scaled to work at higher frequencies up to 300 GHz. The design and simulated response of the D-band waveguide and WR-3 waveguide power sensor are presented.

The second design technique, is entirely new, and is based on the synthesis of the coupling matrix of a two-port resonator network. The conventional power sensor designed by the first technique is integrated with the network as the last resonator. The integration results in microwave power sensor having filtering transfer function, the response is described by the

coupling matrix. The bandwidth of the device can be controlled and subsequently improved. For demonstration of the design ideas, an X-band thermistor power sensor with integrated third order Chebyshev filter function is realised by rectangular resonators with capacitive irises. The sensor is designed to have 10% fractional bandwidth at 10 GHz, when the thermistor is biased at 100 Ω . The fabricated filter-sensor, without tuning, has the response of a third order Chebyshev filter, the maximum pass-band return loss is 15 dB and the centre frequency is 9.8 GHz. By adjusting the operating resistance to 150 Ω and applying tuning screws, the response is tuned to the centre frequency of 9.98 GHz, and 8% fractional bandwidth is achieved. The excellent power linearity of the sensor is demonstrated by the measurement in Birmingham. The effective efficiency of 89% is obtained from the calibration in NPL. Compared to the power standards at NPL, the device has a better matching.

The microwave power sensors fabricated in this work are compatible with the existing calorimetric technique of calibration power sensors. While the available standards for X-band waveguide have the effective efficiency of 98%, the designed power sensors have lower efficiencies. The discrepancies can be attributed by the difference of semiconducting behaviour between the commercial bead thermistors used in this work and the bead thermistors in the power standards. Nevertheless, the design techniques here can be applied regardless of the type of bolometric sensing elements. After the calibration at NPL, they can be used as transfer power standards.

7.2. Future Work

Immediate work to complete the experimental demonstrators will be on the fabrication of platinum thin film for the W-band power sensor. At the University of Birmingham, the thin film can be deposited on SU-8 substrate by evaporation process. An alternative method of pulsed laser deposition can be performed at the Department of Materials, Imperial College, London. Thin film of the order of 10 nm can be fabricated [1, 2]. Another promising candidate for the thin film material can be vanadium oxides (VO_x). The VO_x thin film has been extensively studied at the University of Glasgow for terahertz imaging [3, 4]. The material experiences negative temperature coefficient and the thin film of vanadium oxides could potentially operate as an NTC thermistor in bolometric power sensors. The use of thin film sensing element can result in very high effective efficiency of the power sensor as the d-c resistance of the film is equal to the r-f resistance.

Further development for improving the bandwidth of the power sensor can be performed by the synthesis of coupling matrix. At the moment, the X-band filter-sensor in Chapter 6 has significantly larger -20 dB bandwidth compared to the X-band sensor in Chapter 4. However, the filter-sensor cannot cover all the X-band frequencies from 8.2 GHz to 12.4 GHz because the device is designed as single band at the centre frequency of 10 GHz. The coupling matrix optimisation can be used to design multiple band microwave filters [5, 6]. The approach can be applied for waveguide filter-sensor so that the impedance matching and suitable bandwidths can be specified at a number of frequencies of interest in the waveguide band.

References

- [1] S. T. Yu H, Liu W, Ronning C, Petrov PK, Oh S-H, Maier SA, Jin P, Oulton RF, "Influence of Silver Film Quality on the Threshold of Plasmonic Nanowire Lasers," *Advanced Optical Materials*, vol. 5, ISSN:2195-1071, 2017.
- [2] I. G. T. O. I. J. Pang a, A. Centeno ab, P. K. Petrov a, N. M. Alford a, M. P. Ryan a and F. Xie, "Gold nanodisc arrays as near infrared metal-enhanced fluorescence platforms with tuneable enhancement factors," *Journal of Materials Chemistry C*, vol. 5, ISSN:2050-7526, pp. 917-925, December 2016.
- [3] I. E. Carranza, J. Grant, J. Gough, and D. R. S. Cumming, "Metamaterial-Based Terahertz Imaging," *IEEE Transactions on Terahertz Science and Technology*, vol. 5, pp. 892-901, 2015.
- [4] I. E.-C. James Grant, Chong Li, Iain J. H. McCrindle, John Gough, David R. S. Cumming, "A monolithic resonant terahertz sensor element comprising a metamaterial absorber and micro-bolometer," *Laser and Photonics Reviews*, September, 2013.
- [5] X. Shang, Y. Wang, and M. J. Lancaster, "Coupling matrix synthesis of triple-passband filters using optimisation," in *2nd Annual Passive RF and Microwave Components Seminar*, 2011, pp. 23-28.
- [6] X. Shang, Y. Wang, G. L. Nicholson, and M. J. Lancaster, "Design of multiple-passband filters using coupling matrix optimisation," *IET Microwaves, Antennas & Propagation*, vol. 6, pp. 24-30, 2012.

Appendix A- Field analysis of Transmission lines

Consider a uniform TEM transmission line in Figure A.1 which consists of two conductors C_1 and C_2 . The electric field and magnetic field on the cross section of the line are \bar{E} and \bar{H} . The voltage and current on the transmission line are $V_0 e^{\pm j\beta z}$ and $I_0 e^{\pm j\beta z}$, respectively.

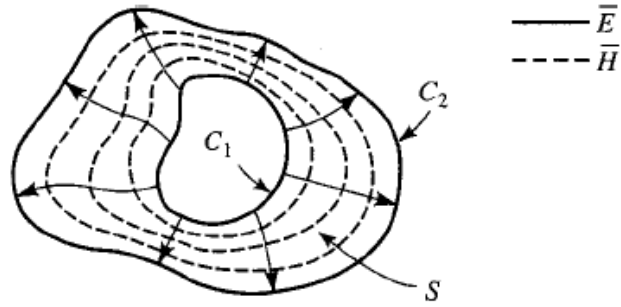


Figure A. 1: A cross section of an TEM transmission line (taken from [1])

The circuit theory gives the time average stored magnetic energy W_m is related to the self-inductance L as [1]

$$W_m = L \frac{|I_0|^2}{4} \quad (\text{A.1})$$

In field analysis, the stored magnetic energy in the crossed sectional area S can be derived from the magnetic field [1].

$$W_m = \frac{\mu}{4} \int_S \bar{H} \cdot \bar{H}^* ds \quad (\text{A.2})$$

Combining equation A.1 and A.2 gives

$$L = \frac{\mu}{|I_0|^2} \int_S \bar{H} \cdot \bar{H}^* ds \quad (\text{A.3})$$

where the magnitude of the current can be calculated by Ampere's law as

$$|I_0| = \oint \vec{H} \cdot d\vec{l} \quad (\text{A.4})$$

The integration path is any closed path within the two conductors

Hence, the expression for the self-inductance per unit length is obtained.

$$L = \frac{\mu \int \vec{H} \cdot \vec{H}^* ds}{| \circ |} \quad (\text{A.5})$$

Similarly, the time average stored electric is written as [1]

$$W_e = \frac{\epsilon}{4} \int \vec{E} \cdot \vec{E}^* ds \quad (\text{A.6})$$

The circuit theory gives [1]

$$W_e = C \frac{|V_0|^2}{4} \quad (\text{A.7})$$

where $|V_0| = \int_{C_1}^{C_2} \vec{E} \cdot d\vec{l}$ is integration from the positive conductor to the negative one. The

capacitance per unit length can be found

$$C = \frac{\epsilon \int \vec{E} \cdot \vec{E}^* ds}{\left| \int_{C_1}^{C_2} \vec{E} \cdot d\vec{l} \right|^2} \quad (\text{A.8})$$

The power loss per unit length due to the finite conductivity of the conductors is [1]

$$P_C = \frac{R_s}{2} \int_{C_1+C_2} \bar{H} \cdot \bar{H}^* dl \quad (\text{A.9})$$

where R_s is the surface resistance of the conductors, the integration path of P_C is over the conductor boundaries. The series resistance per unit length can be obtained as

$$R = \frac{2P_C}{|I_0|^2} = \frac{R_s \int_{C_1+C_2} \bar{H} \cdot \bar{H}^* dl}{\left| \oint \bar{H} \cdot d\vec{l} \right|^2} \quad (\text{A.10})$$

The time average power dissipated due to the dielectric loss is [1]

$$P_d = \frac{\omega \varepsilon''}{2} \int_s \bar{E} \cdot \bar{E}^* ds \quad (\text{A.11})$$

where ε'' is the imaginary part of the complex permittivity of the medium filled between two conductors. The shunt conductance per unit length can be found as

$$G = \frac{2P_d}{|V_0|^2} = \frac{\omega \varepsilon'' \int_s \bar{E} \cdot \bar{E}^* ds}{\left| \int_{C_1}^{C_2} \bar{E} \cdot d\vec{l} \right|^2} \quad (\text{A.12})$$

References

- [1] D. M. Pozar, "Microwave engineering / by David M. Pozar," 4th ed. ed. Hoboken, N.J.: Wiley, 2012.

Appendix B- Parasitic capacitance of bead thermistors

Consider the bead thermistor in Figure B.1. At a d-c biased condition, the bead inner structure has the relative permittivity of ϵ_r which could be a function of dc bias power on the thermistor. Assume the uniform distribution of electric charges on the two wires in the thermistor body. The capacitance between the two wires can be accounted for the non-linear behaviour of the bead thermistor.

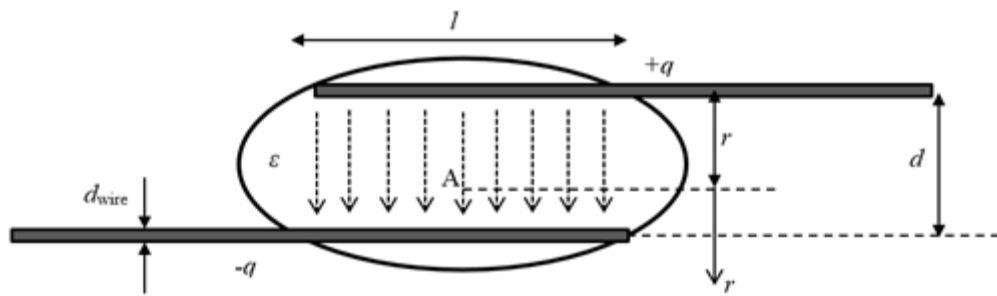


Figure B.1: The bead thermistor structure. The length of the bead is l , the lead wire of the bead has the diameter of d_{wire}

Gauss's law states that

$$\oint E dS = \frac{\sum Q}{\epsilon_r \epsilon_0} \quad (B.1)$$

The electric field caused by a single wire with uniform charge distribution q along the length l can be derived from Gauss's law as

$$E(r) = \frac{q}{2\pi\epsilon_r\epsilon_0 r} \quad (B.2)$$

The total electric field at point A can be written as

$$E_A(r) = \frac{q}{2\pi\epsilon_r\epsilon_0 r} + \frac{q}{2\pi\epsilon_r\epsilon_0 (d-r)} \quad (B.3)$$

The potential difference between the two wires is

$$V = \int_{d_{wire}/2}^{d-d_{wire}/2} E_A(r) dr = \frac{q}{\pi\epsilon_r\epsilon_0} \ln\left(\frac{d-d_{wire}/2}{d_{wire}/2}\right) \quad (\text{B.4})$$

The capacitance is thus written as

$$C_{th} = \frac{Q}{V} = \frac{\pi\epsilon_r\epsilon_0 l}{\ln\left(\frac{d-d_{wire}/2}{d_{wire}/2}\right)} \quad (\text{B.5})$$

The equivalent capacitance depends not only on the dimension of the bead, but also the relative permittivity of the material. as the capacitance changes with d-c bias on the thermistor, the permittivity is sensitive to the d-c bias power on the bead.

Figure A. 2 **Appendix C** - The detailed structure of the X-band power sensor

The appendix presents the detailed dimensions of the X-band microwave power sensor designed in Chapter 4. Figure C.1 shows the structure of the sensor consisting of a PCB and two waveguide parts, which are shown in Figure C.2, C.3 and C.4, respectively.

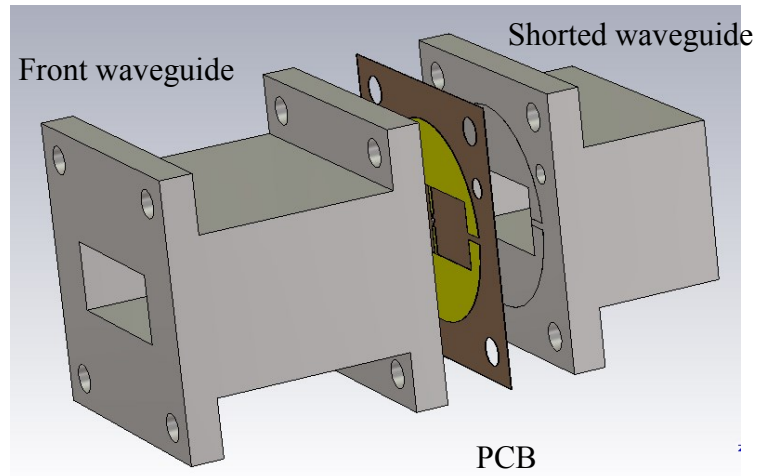


Figure C.1: The structure of the X-band power sensor.

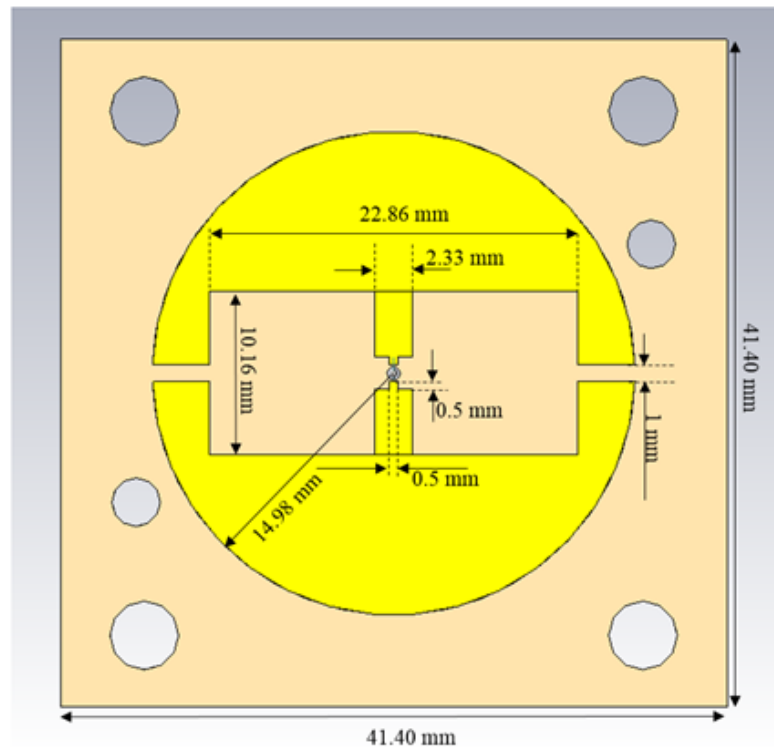


Figure C.2: The PCB of the X-band power sensor.

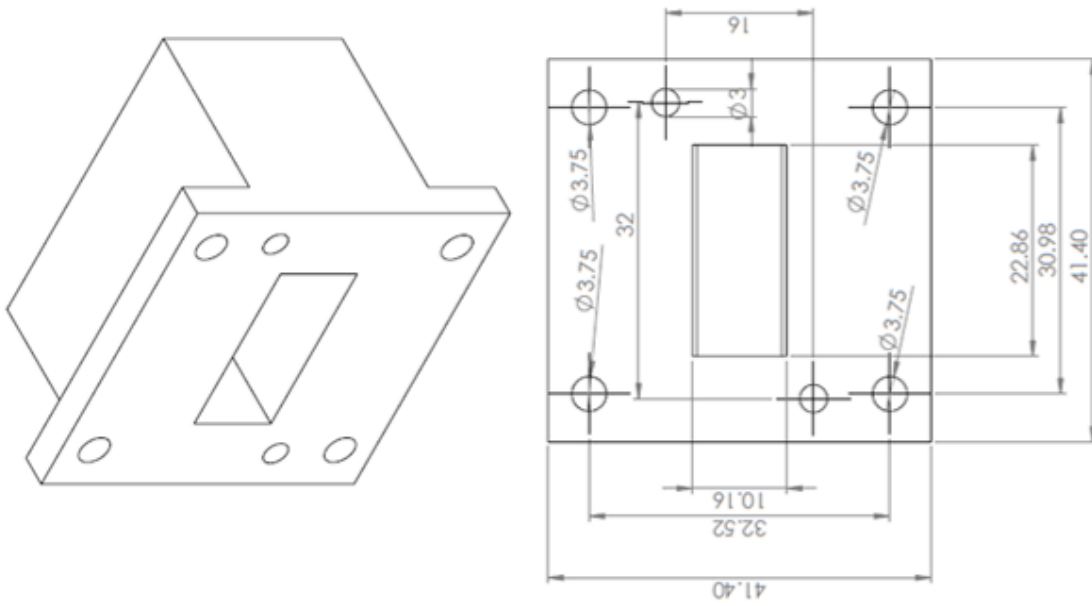
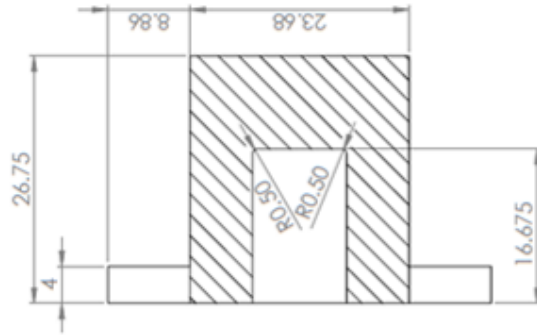


Figure C.3: The shorted waveguide part of the X-band power sensor.

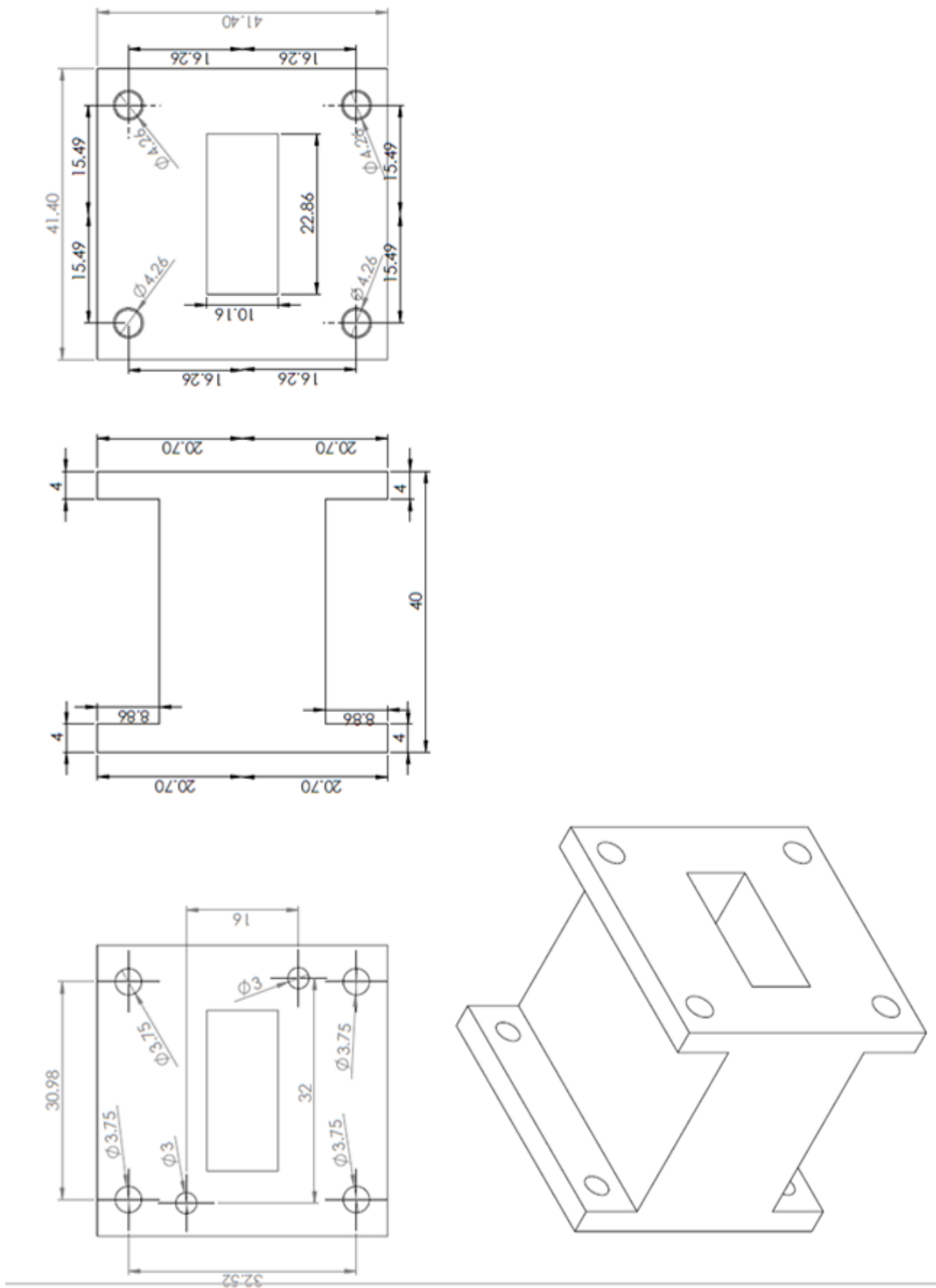


Figure C.4: The front waveguide part of the X-band power sensor.

Appendix D- Thin film nickel manganese developed at the University of Birmingham

Nickel Manganite (NiMn) thin films are being investigated by Prof Tim Button and Shaun Dorey in the School of Metallurgy and Material, University of Birmingham. The material is deposited on Alumina substrate having a size 10 mm x 10 mm by Pulsed Laser Deposition (PLD) process. The thickness of the film can be controlled to about 1-2 μm [1].

The Alumina substrates were used in the deposition at 400 $^{\circ}\text{C}$ and at different pressures (50 mTorr to 250 mTorr). The material has shown NTC thermistor characteristics from 20 $^{\circ}\text{C}$ to 90 $^{\circ}\text{C}$, the B constant is about 3000 which is similar to the commercial NTC thermistors.

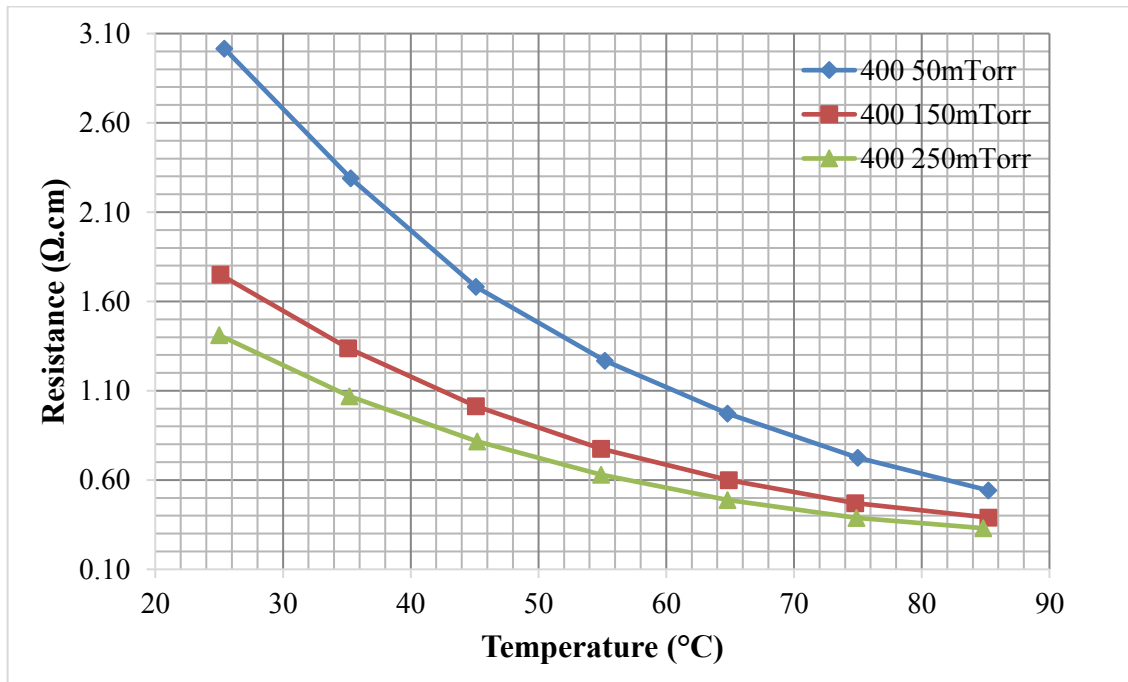


Figure D.1: Characteristic of the film thermistor at different conditions.

Figure D.1 shows that the film has negative temperature coefficient (NTC), its resistance decreases as the temperature increases. However the resistance is very high, and is at about 330 K Ω at 85 $^{\circ}\text{C}$. The resistivity of the film reduces from 7.49 Ωm at 25 $^{\circ}\text{C}$ to 1.1 Ωm at 85 $^{\circ}\text{C}$.

A number of attempts have been made to deposit the material on SU-8 substrate. However, the result shows that SU-8 is not as good as Alumina. The first attempt was to deposit the thermistor material on 10 mm x 10 mm SU-8 substrate at room temperature (the temperature rises to 31 °C during deposition) and at 50 mTorr and 150 mTorr Oxygen partial pressure. The resistance of the thin film is measured at different temperature; the result is depicted on Figure A2 and Figure A3. It can be seen that the resistance of the film is in the order of Megohms, which is very resistive compared to the samples on alumina substrate. Secondly, the substrate was damaged when the temperature rises above 60 °C in the first case and 30°C in the second deposition. It can be concluded that the SU-8 substrate is not suitable for the deposition of Nickel Manganite thin films by PLD process.

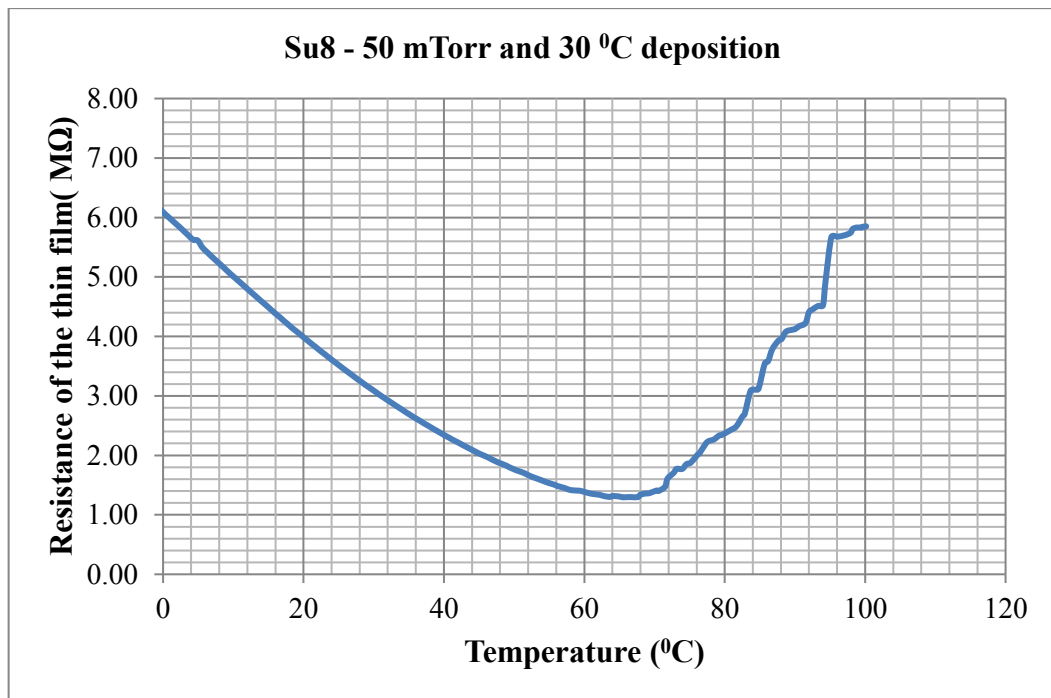


Figure D.2: The measurement of the thin thermistor film on Su8 substrate (deposition at room temperature and at 50 mTorr pressure)

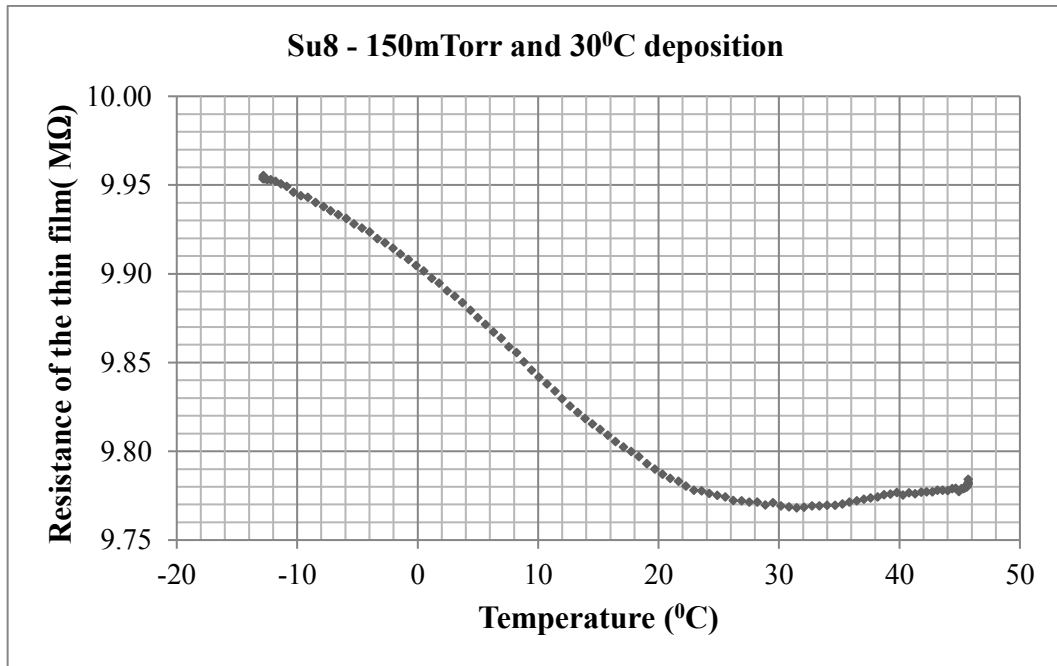


Figure D.3: The measure of the thin thermistor film on Su8 substrate (deposition at room temperature and at 50 mTorr pressure)

References

- [1] S. Dorey, "Fabrication and characterisation of nickel manganite thin films by pulsed laser deposition," ed, 2016.

Appendix E- The detailed structure of the W-band power sensor

The appendix presents the detailed dimensions of the W-band microwave power sensor designed in Chapter 5. The power sensor consists of six layers including front brass plate, waveguide layer, isolation layer, thin film layer, shorted waveguide layer and back brass plate as shown in Figure 5.13. The details of each layer is shown in the following figures.

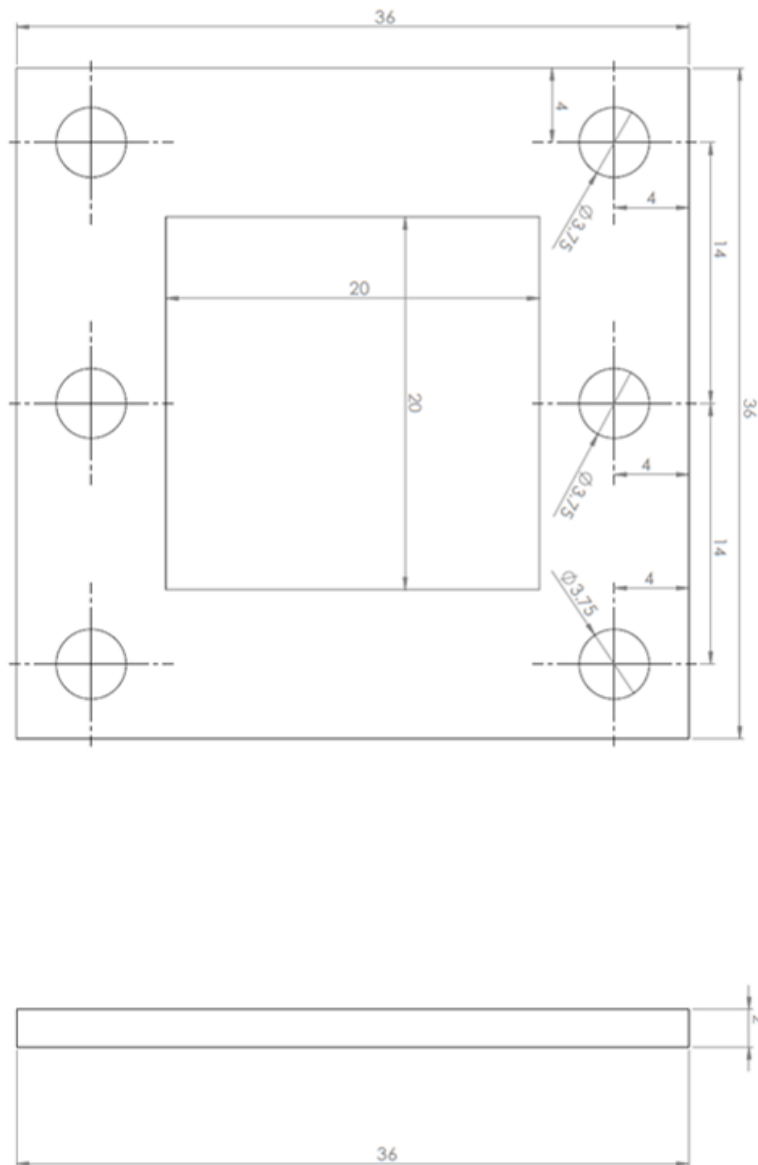


Figure E.1: The front brass plate of the X-band power sensor.

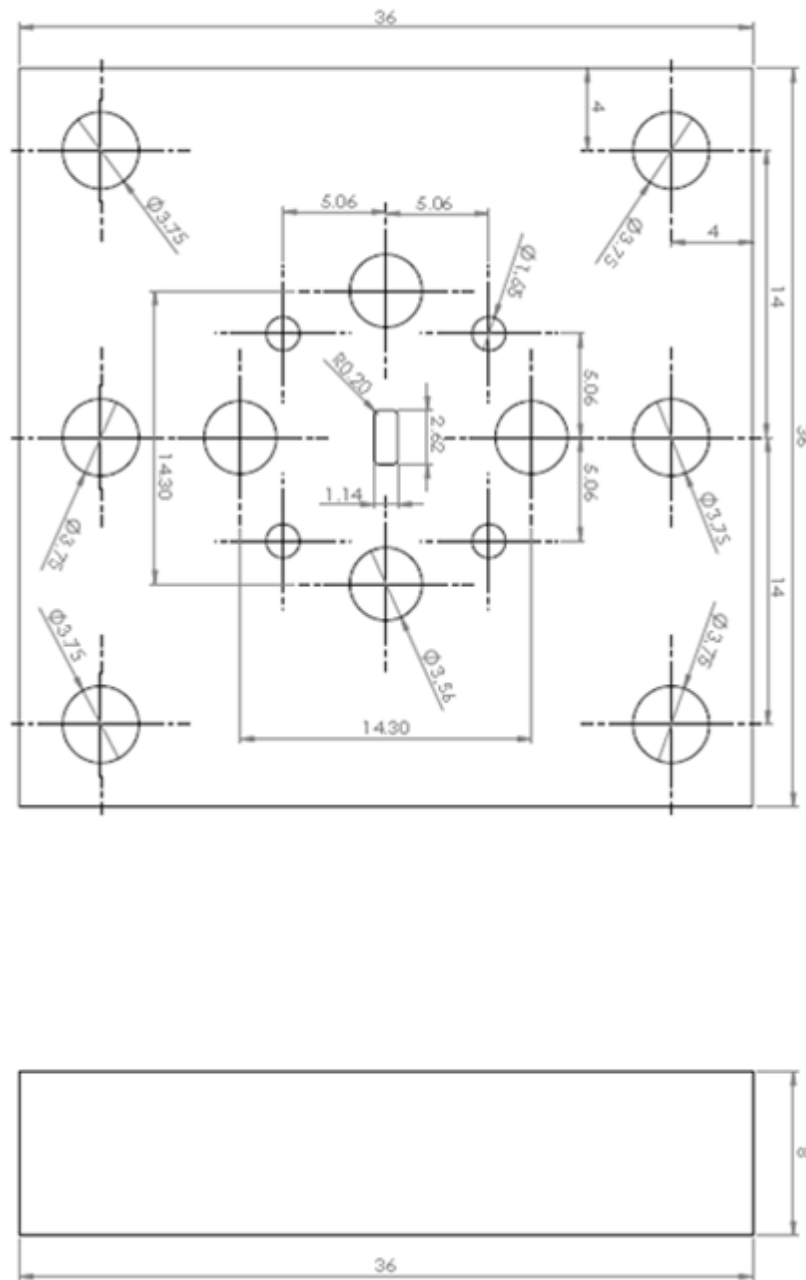


Figure E.2: The waveguide layer of the W-band power sensor

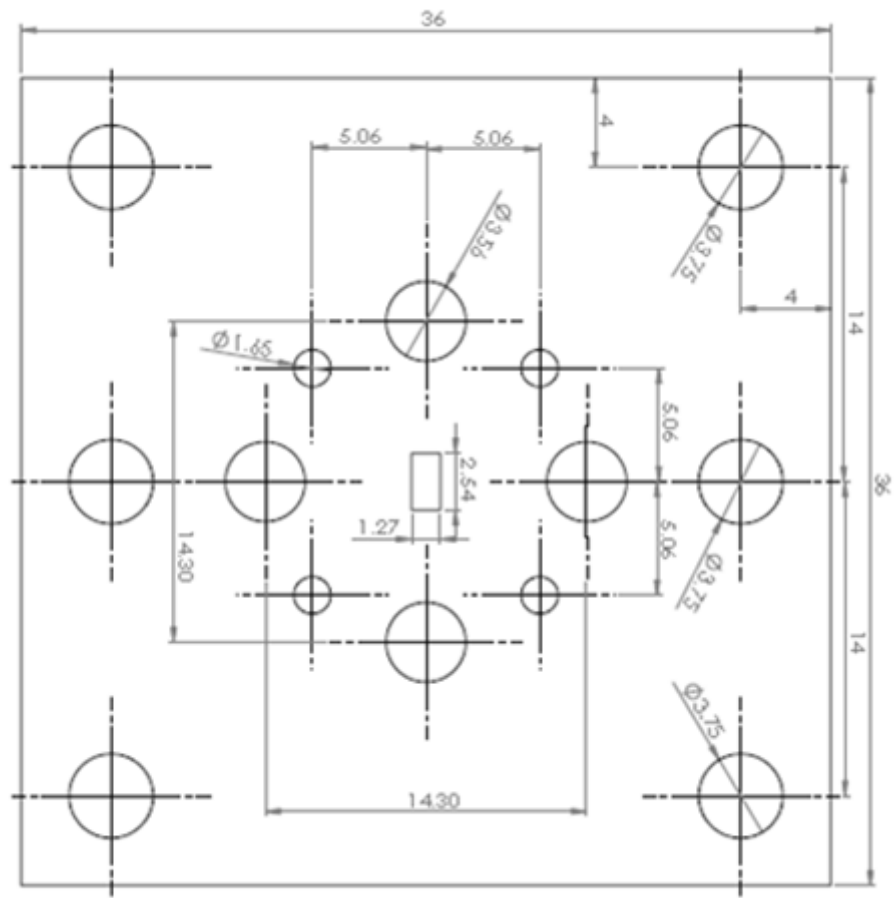


Figure E.3: The isolation layer of the W-band power sensor, the thickness is 50 μm

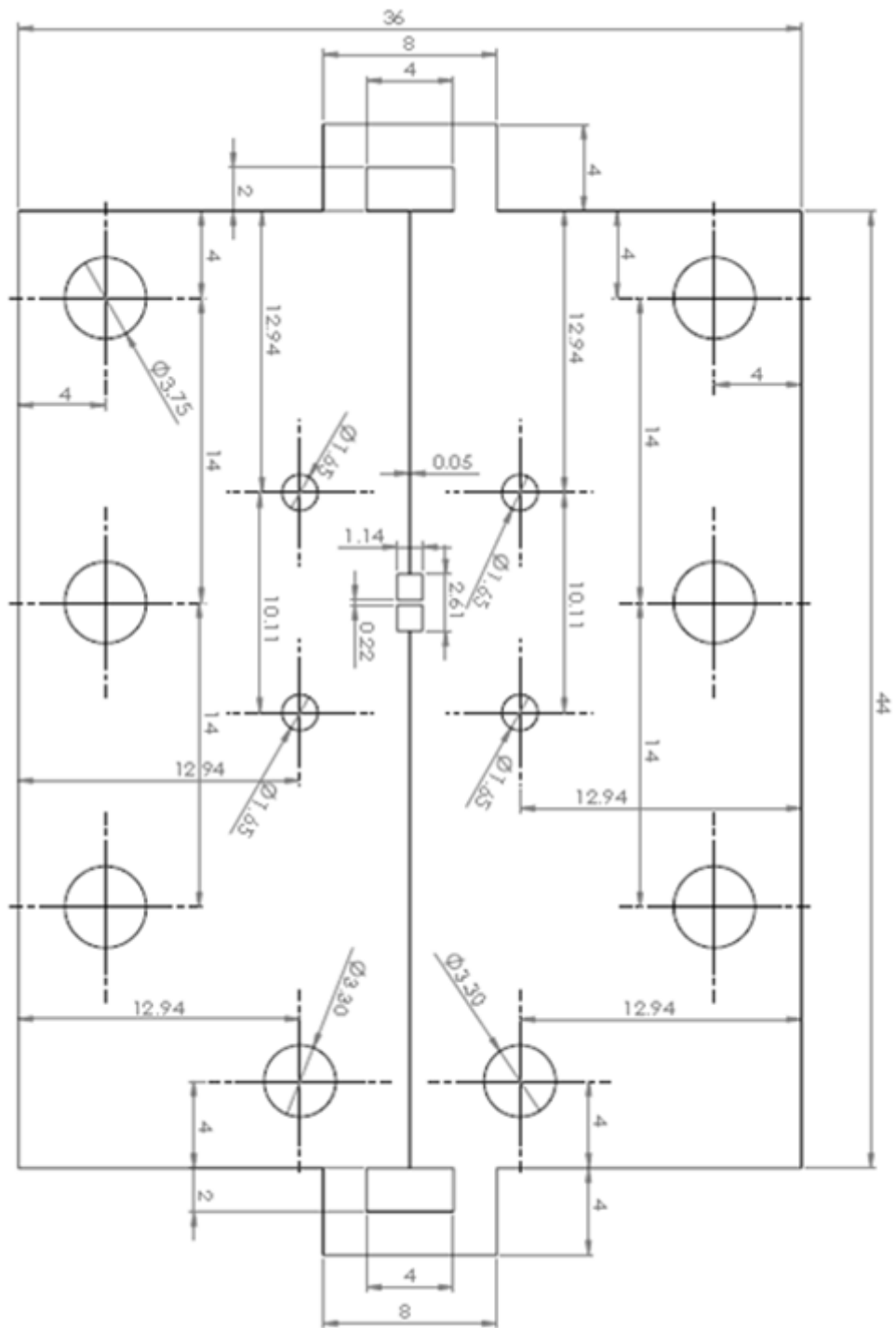


Figure E.4: The thin film layer of the W-band sensor, the thickness is 50 μm .

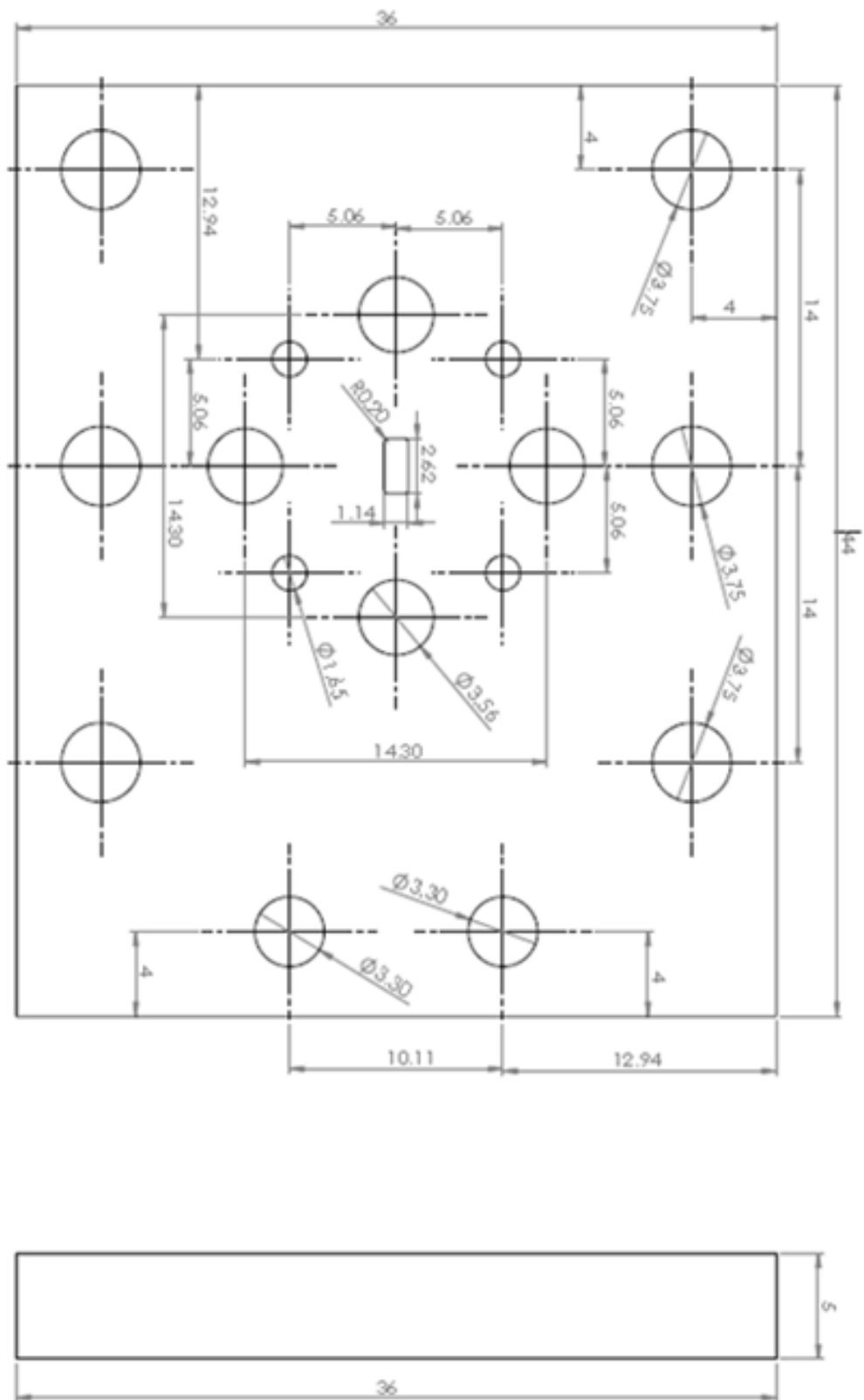


Figure E.5: The shorted waveguide layers of the W-band power sensor.

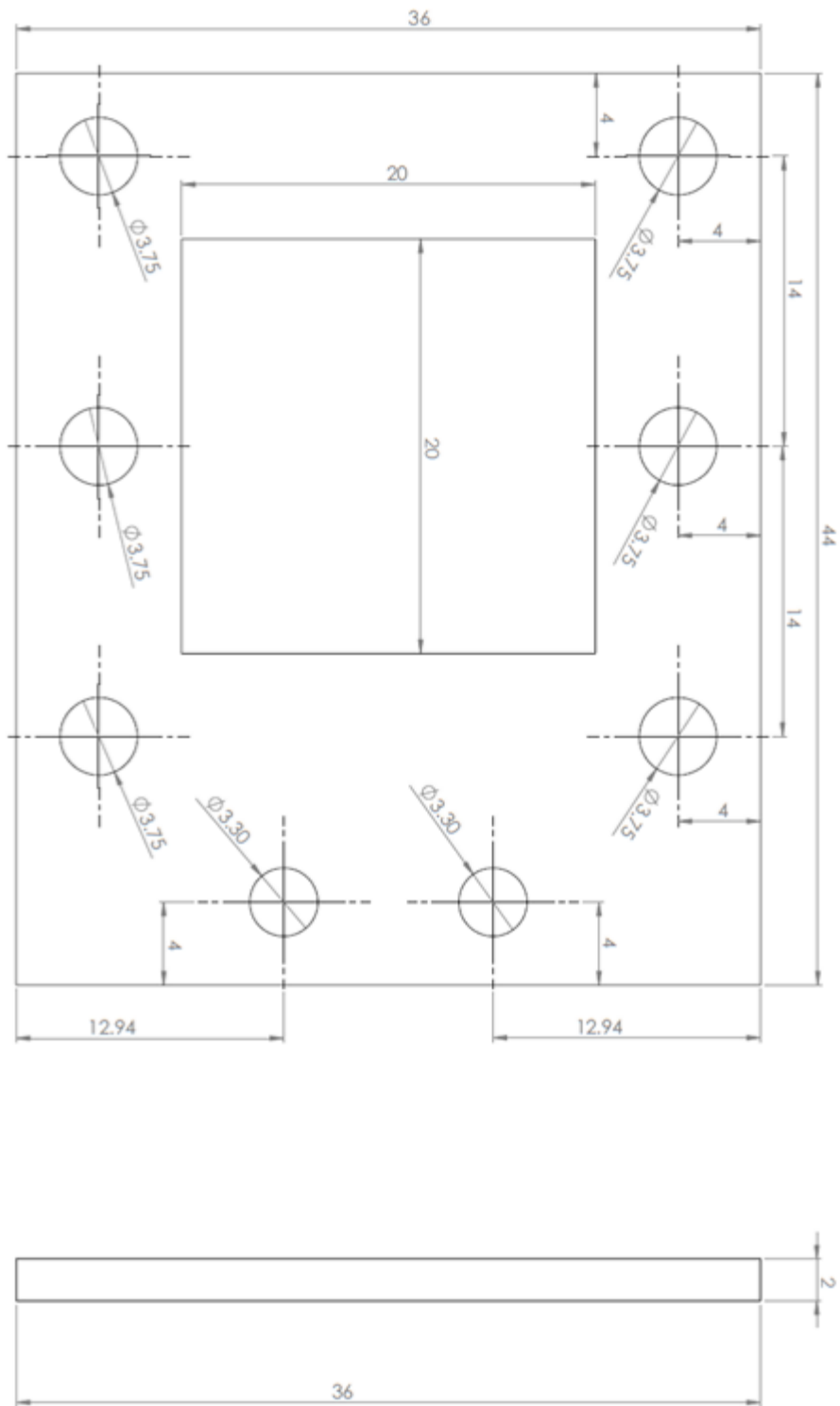


Figure E.6: the back brass plate of the W-band power sensor.

Appendix F - The structure of WR6 power sensor

The WR-6 waveguide power sensor consists of eight layers including front brass plate, front waveguide layer, front choke layer, isolation layer, thin film layer, back choke layers, short plane layer and back brass plate layer as shown in Figure 5.28. The detailed dimensions of the layers are presented in the following figures.

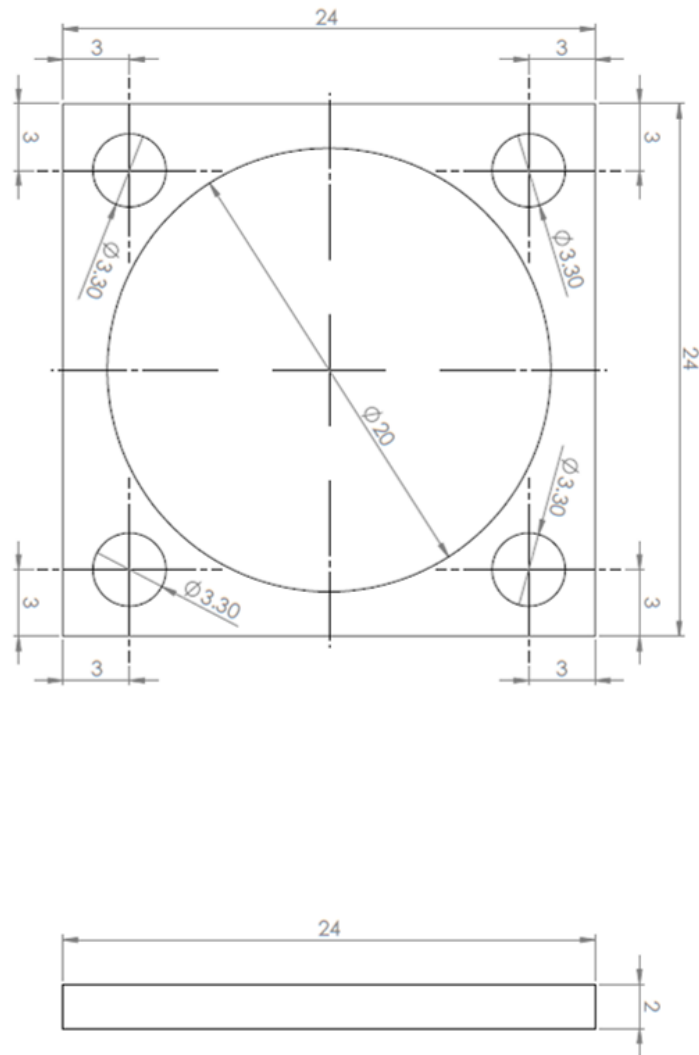


Figure F.1: The front brass plates of the WR_6 waveguide power sensor

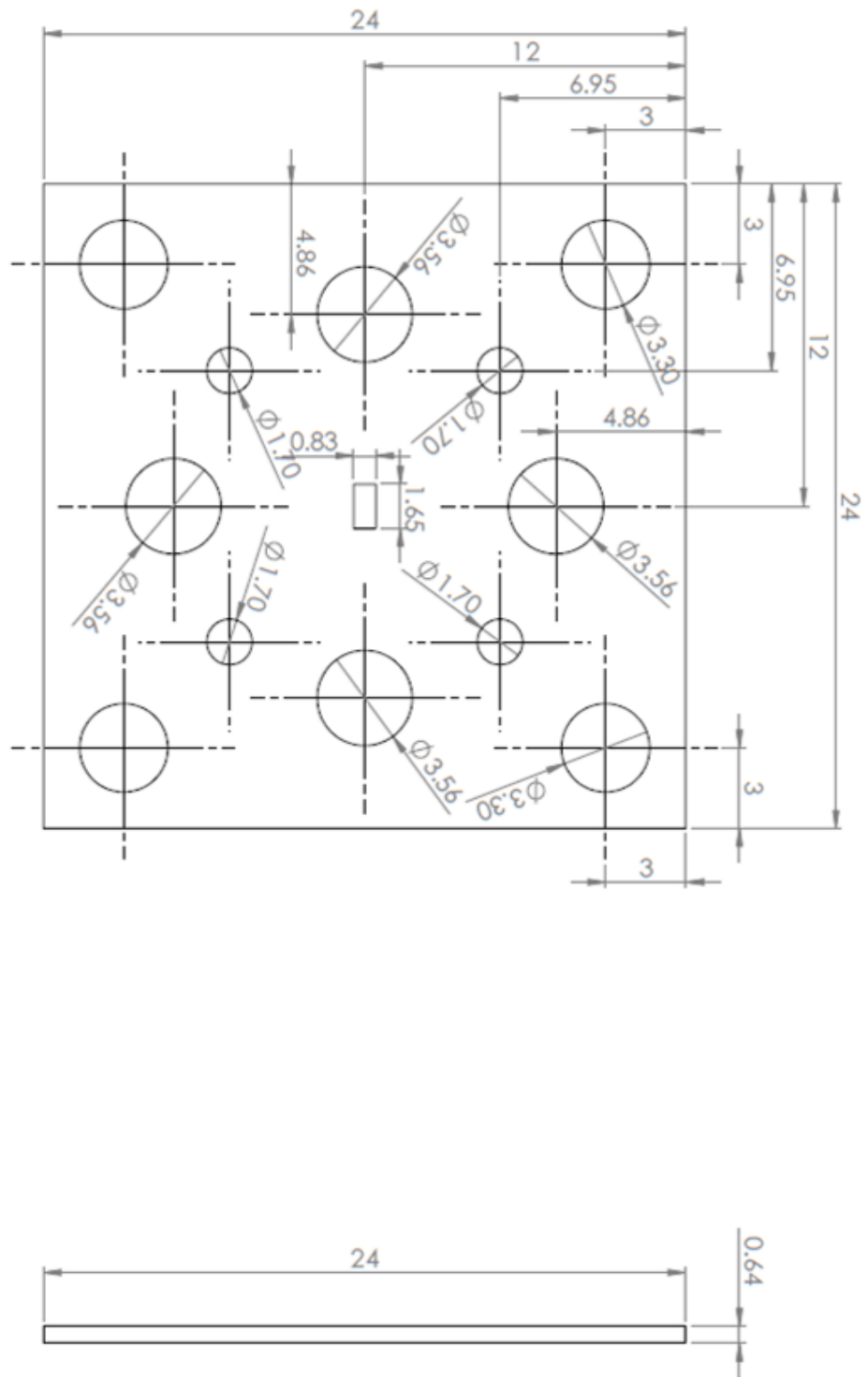


Figure F.2: The front waveguide layer of the WR-6 waveguide power sensor.

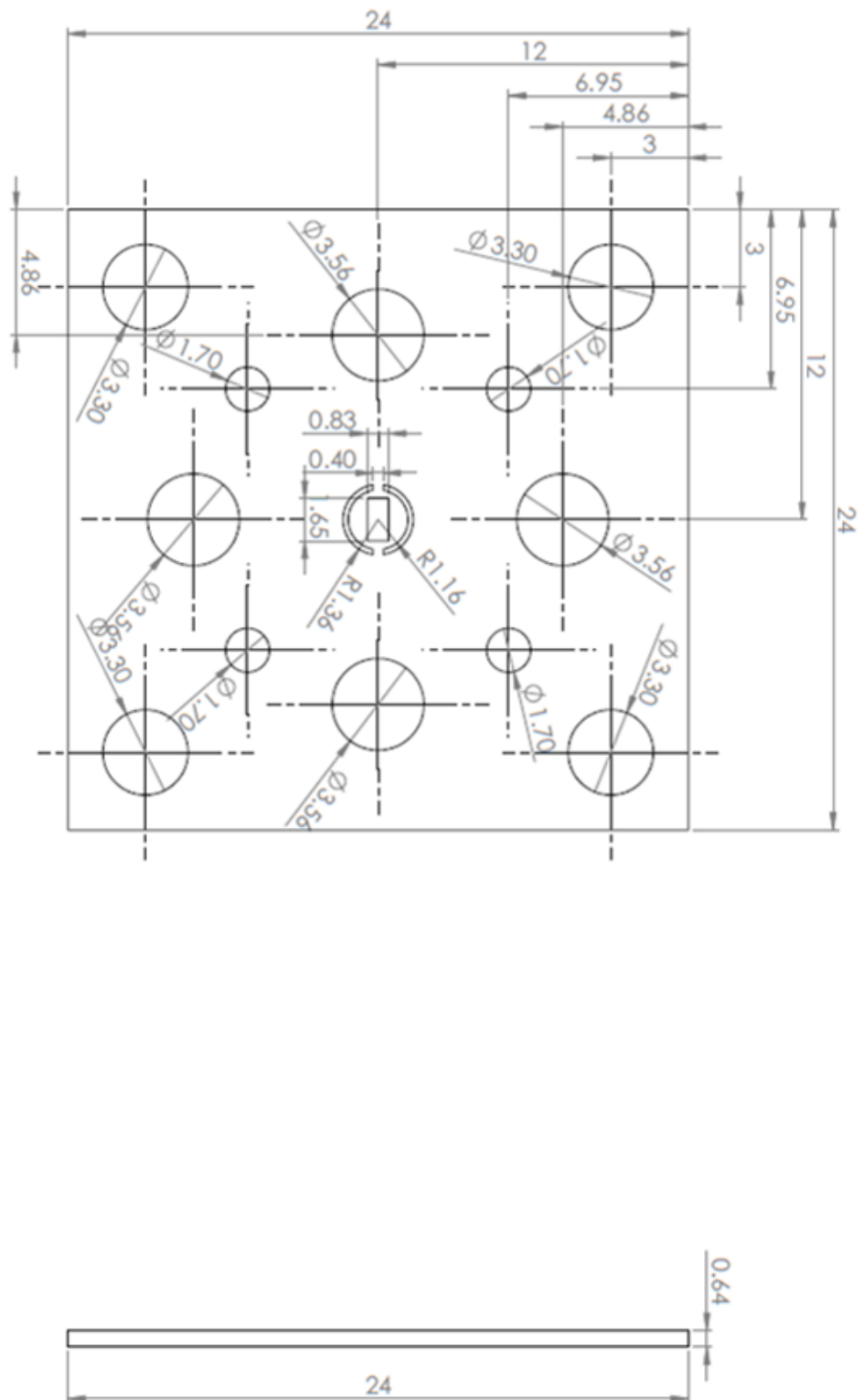


Figure F.3: The front choke layer of the WR-6 waveguide power sensor.

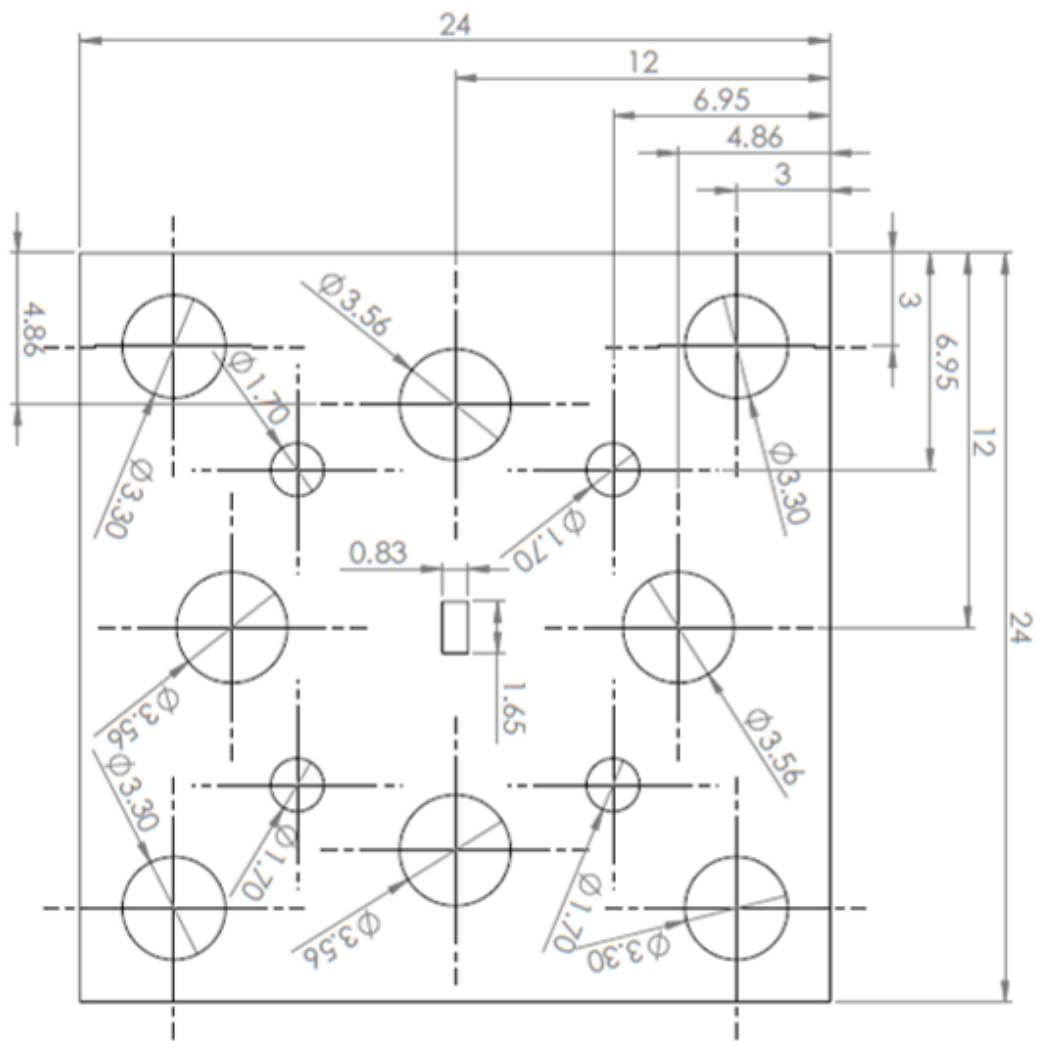


Figure F.4: The isolation layer of the WR-6 waveguide power sensor, the thickness is 50 μm .

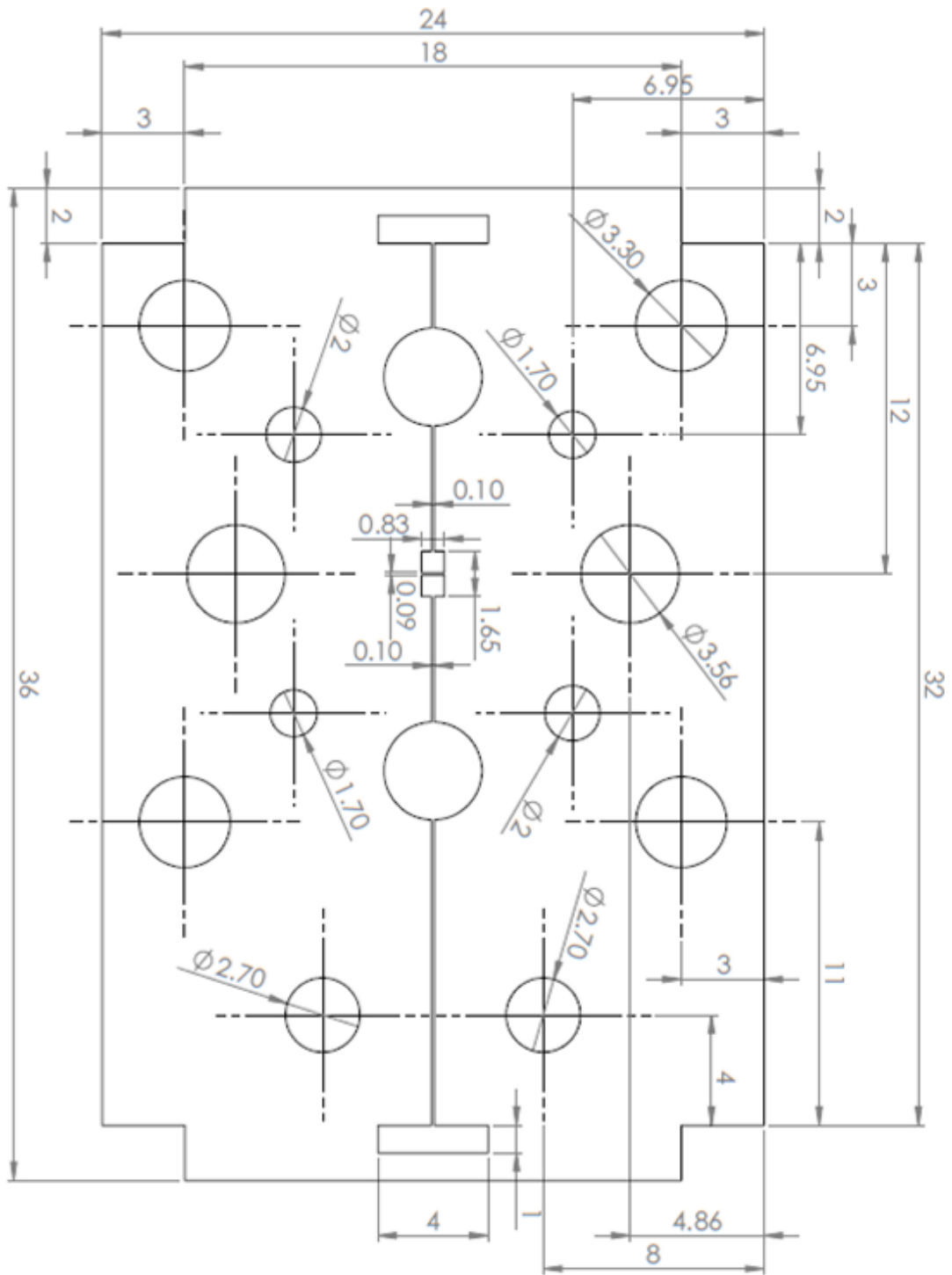


Figure F.5: The thin film layer of the WR-6 waveguide power sensor, the thickness is 50 μm .

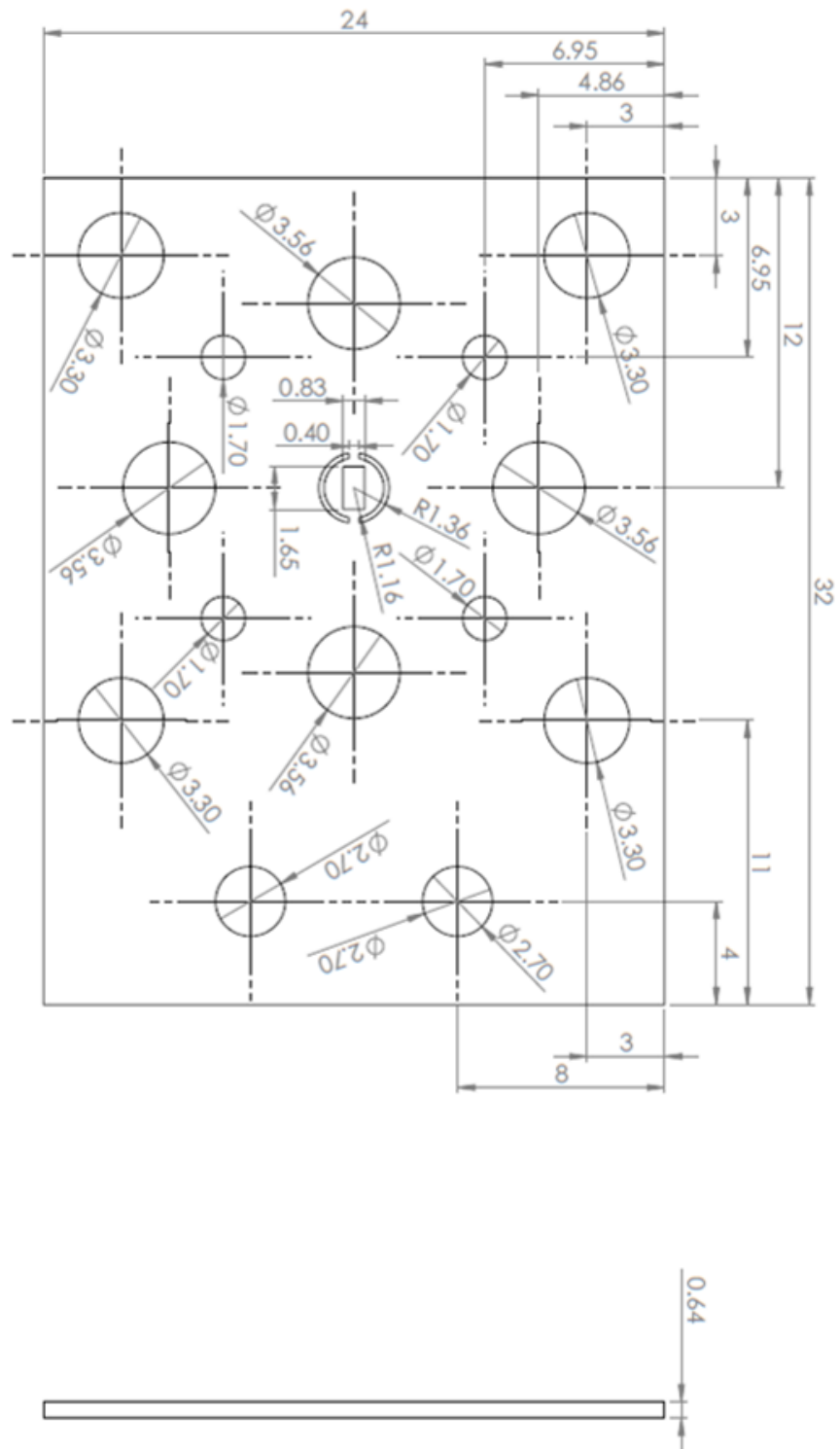


Figure F.6: The back choke layer of the WR-6 waveguide power sensor.

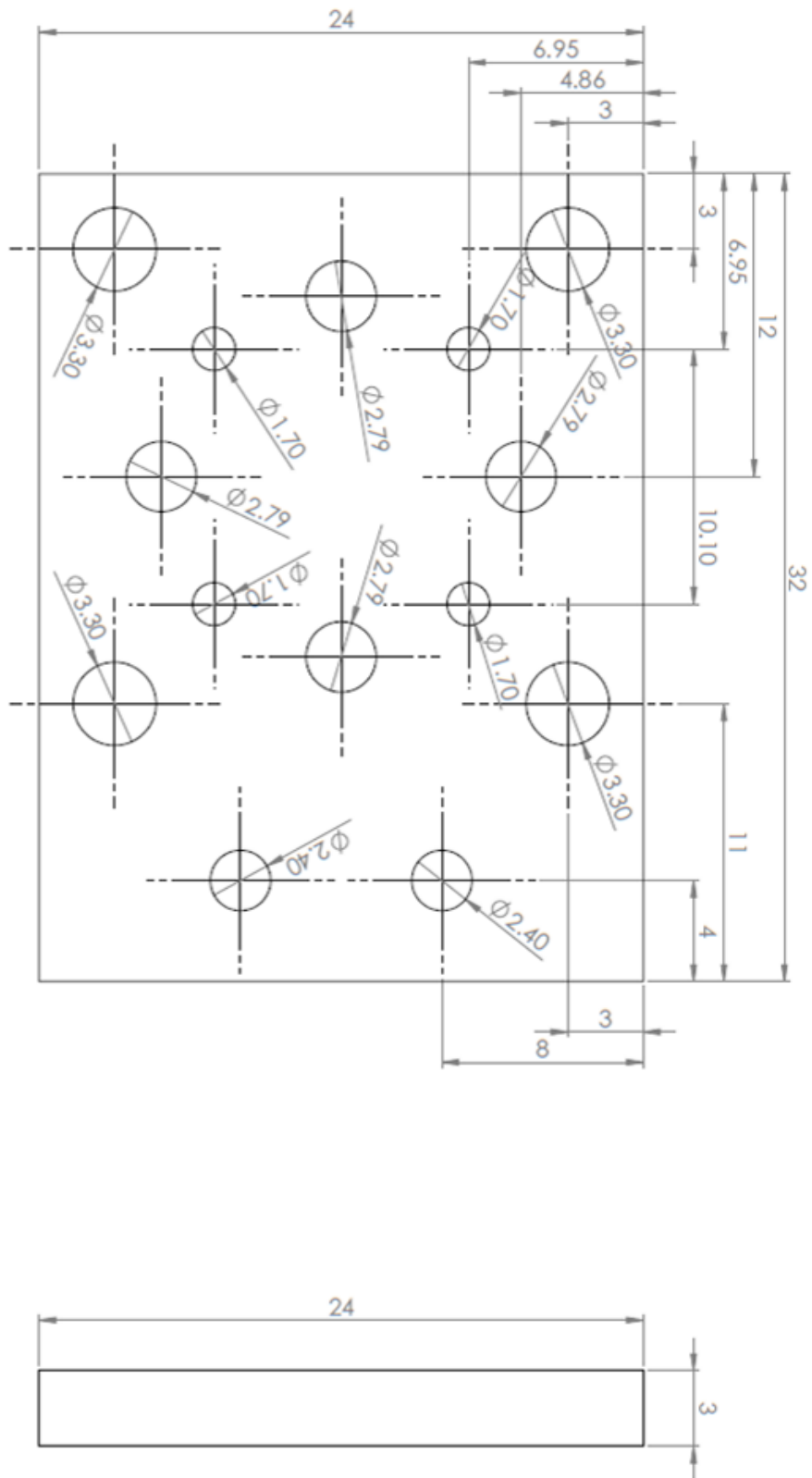


Figure F.7: The short plane layer of the WR-6 waveguide power sensor.

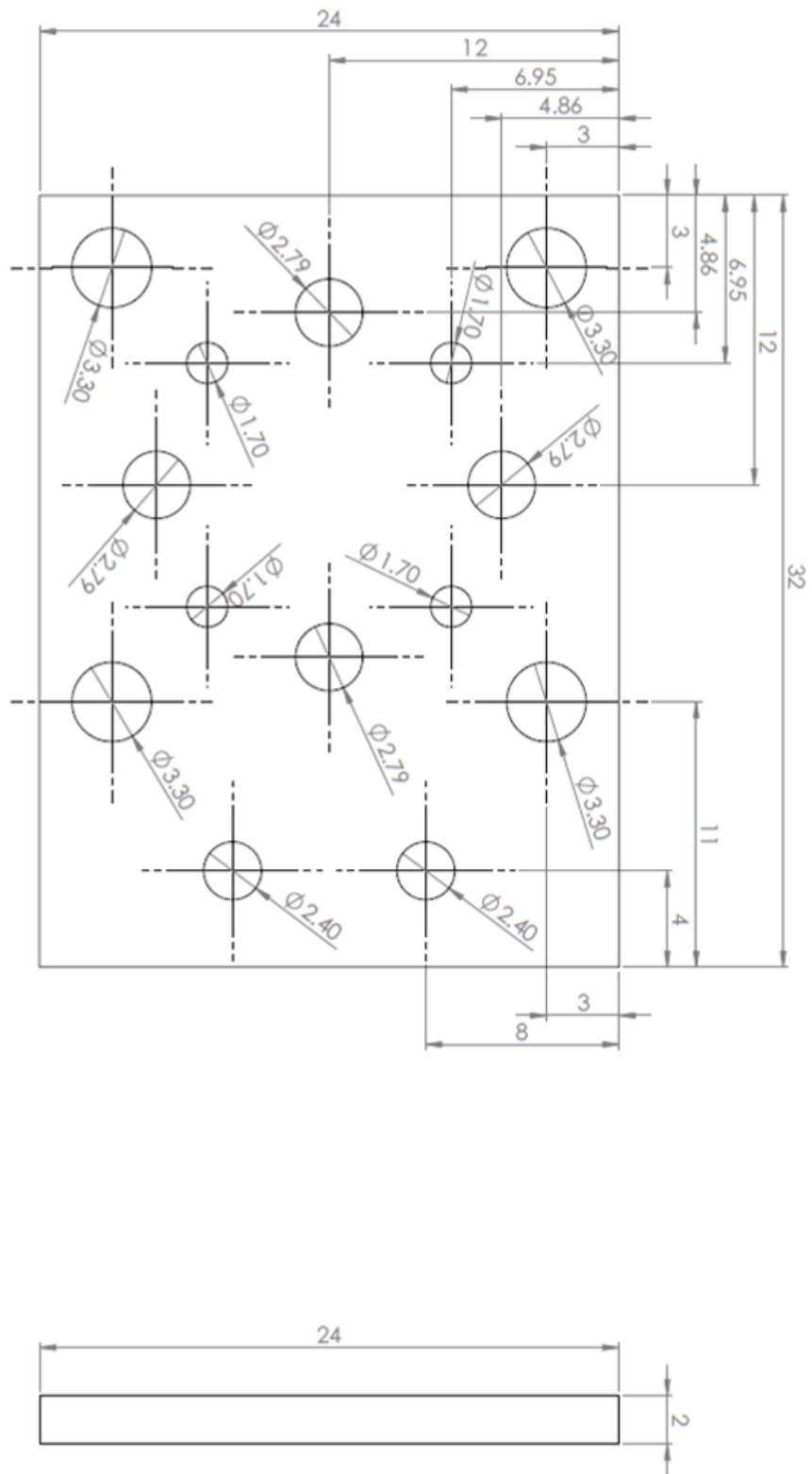


Figure F.8: The back brass plate of the WR-6 waveguide power sensor

Appendix G - The structure of WR-3 waveguide power sensor

The appendix presents the detailed dimensions of the WR-3 waveguide power sensor, which is discussed in Chapter 5. The power sensor consists of eight layers including front brass plate, front waveguide layer, front choke layer, isolation layer, thin film layer, back choke layers, short plane layer and back brass plate layer as shown in Figure 5.28. The structure of the WR-3 sensor is similar to the WR-6 design. In fact, the two design have the same front brass plate, short plane layer and back brass plate as they uses identical waveguide flanges. The dimensions of the front brass plate, short plane layer and back brass plate of the WR-3 design can be found in Figure F.1, F.7 and F.8, respectively. The details of the other layers are included in the following figures.

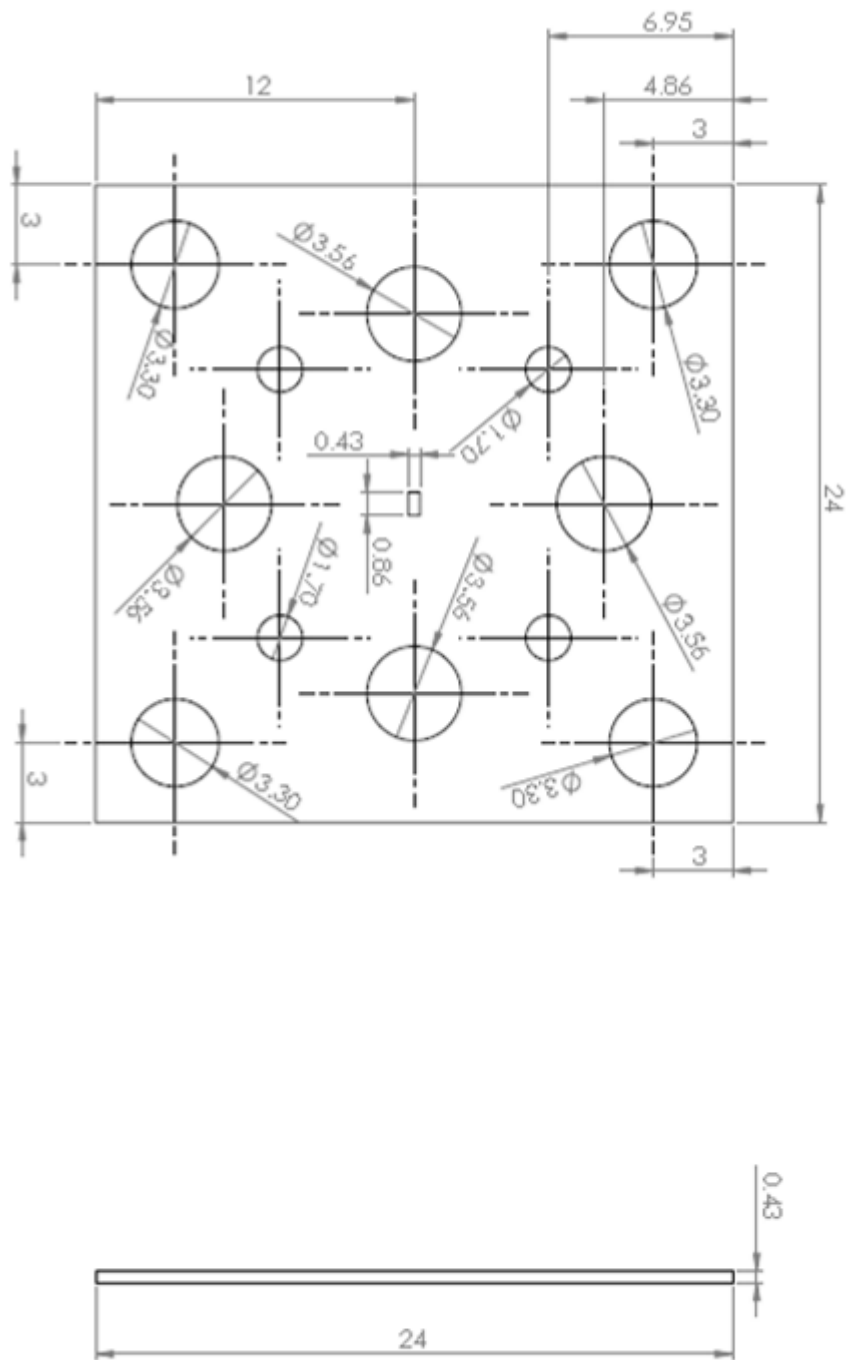


Figure G.1: The front waveguide layer of the WR-3 waveguide power sensor

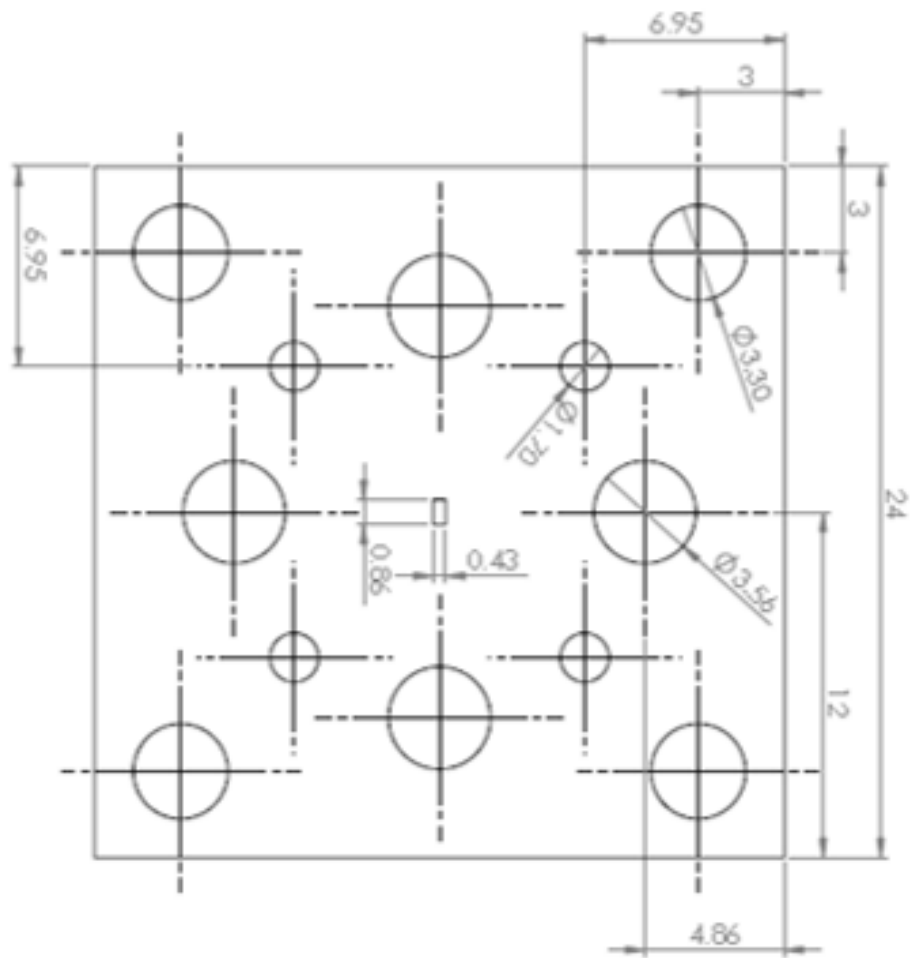


Figure G.3: The isolation layer of the WR-3 waveguide power sensor

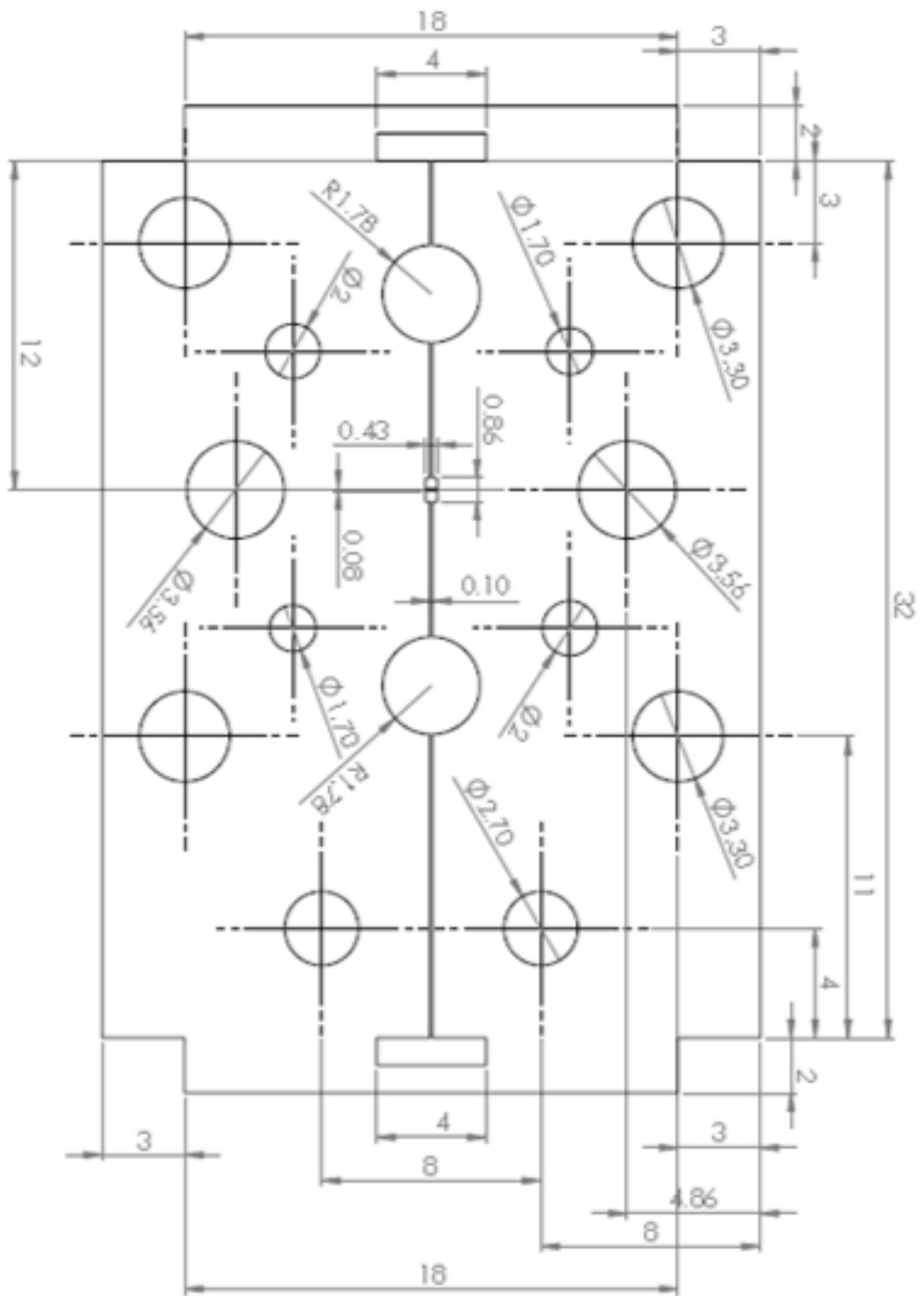


Figure G.4: The thin film layer of the WR-3 waveguide power sensor

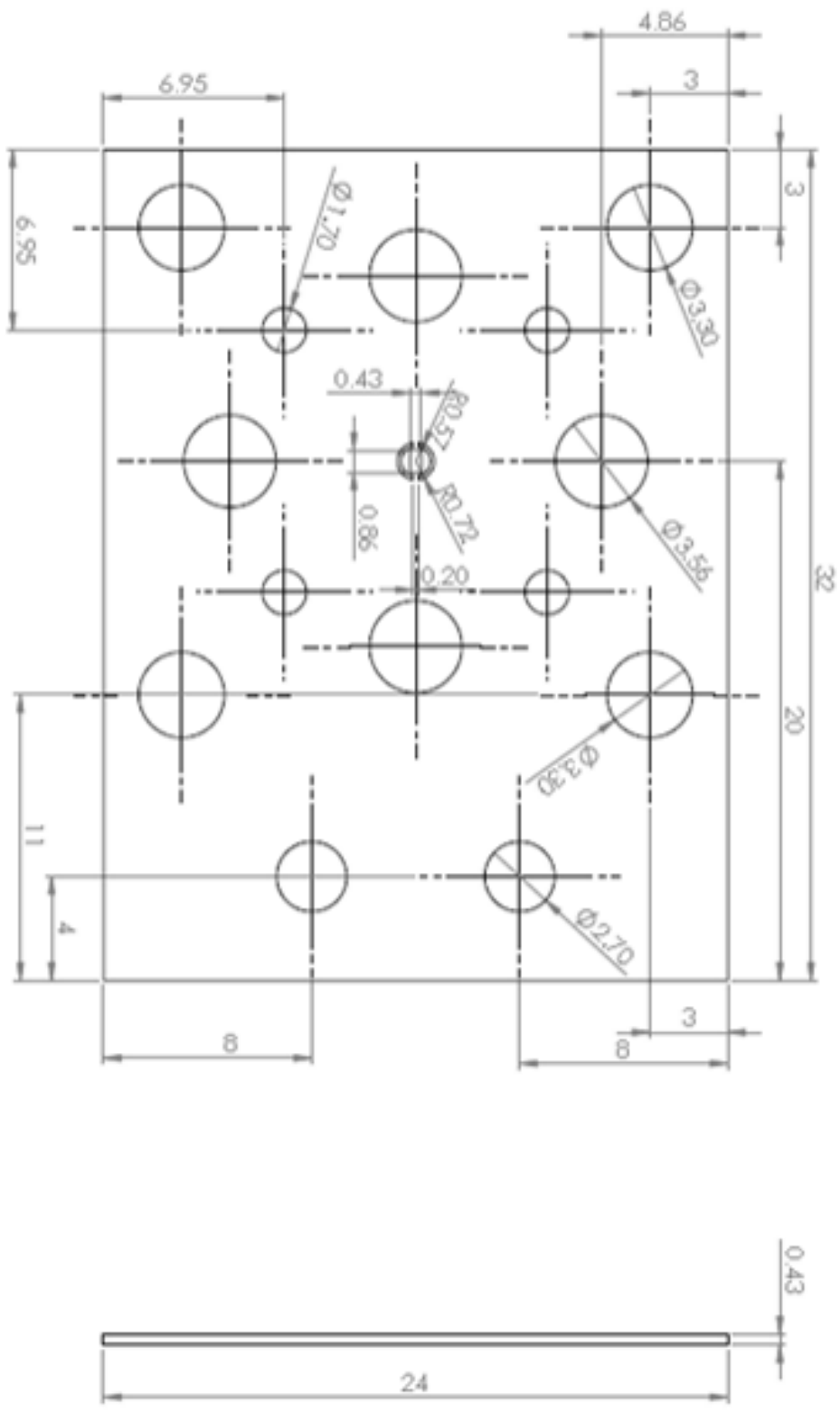


Figure G.5: The back choke layer of the WR-3 waveguide power sensor.

Appendix H - The method of extracting the external quality factor Q_e for a lossless resonator

The appendix present the method of extraction of the external quality factor based on a two-port measurement of a resonator as shown in Figure H.1. The lossless resonator is presented by the parallel LC circuit. The external ports coupled with the resonator are presented by the conductance G_1 and G_2 . In order to have a very weak coupling at the second port, the conductance G_2 should be very large compared the conductance G_1 , the inductance and capacitance of the circuit.

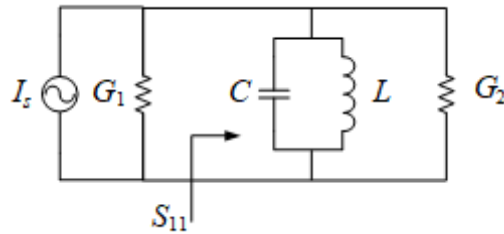


Figure H.1: The equivalent circuit of the extraction of the external quality factor Q_e , port 2 is weakly coupled to the LC circuit (i.e. $G_2 \gg G_1, L$ and C)

The input admittance of the resonator can be written as

$$Y_{in} = j\omega C + \frac{1}{j\omega L} + G_2 \quad (\text{H.29})$$

The resonant of the circuit $\omega_0 = 1/\sqrt{LC}$ and the approximation $(\omega^2 - \omega_0^2)/\omega \approx 2\Delta\omega$ are substituted in the input admittance equation, we have

$$Y_{in} = j\omega_0 C \frac{2\Delta\omega}{\omega_0} + G_2 \quad (\text{H.30})$$

The reflection coefficient S_{11} at the first port of the resonator is

$$S_{11} = \frac{G_1 - Y_{in}}{G_1 + Y_{in}} = \frac{1 - j \frac{\omega_0 C}{G_1} \frac{2\Delta\omega}{\omega_0} - \frac{G_2}{G_1}}{1 + j \frac{\omega_0 C}{G_1} \frac{2\Delta\omega}{\omega_0} + \frac{G_2}{G_1}} \quad (\text{H.31})$$

The external quality factor at the excitation port of the resonator $Q_e = \omega_0 C / G_1$, we obtain

$$S_{11} = \frac{\left(1 - \frac{G_2}{G_1}\right) - jQ_e \frac{2\Delta\omega}{\omega_0}}{\left(1 - \frac{G_2}{G_1}\right) + jQ_e \frac{2\Delta\omega}{\omega_0}} \quad (\text{H.32})$$

The transmission coefficient S_{21} can be calculated as

$$|S_{21}|^2 = 1 - |S_{11}|^2 \quad (\text{H.33})$$

The magnitude of S_{21} is then given by

$$|S_{21}| = \frac{2\sqrt{\frac{G_2}{G_1}}}{\sqrt{1 + \left(Q_e \frac{2\Delta\omega}{\omega_0}\right)^2}} \quad (\text{H.34})$$

where the assumption $G_2 \gg G_1$ has been applied

At the resonant frequency $\Delta\omega = 0$, the transmission coefficient reaches its maximum values.

Note that $S_{21}(\omega_0)$ in dB is well below 0 level due to $G_2 \gg G_1$. The magnitude of S_{21} reduces 3 dB, when the frequency shifts such that

$$Q_e \frac{2\Delta\omega}{\omega_0} = \pm 1 \quad (\text{H.35})$$

The 3 dB band width of S_{21} can be defined as

$$\Delta\omega_{3\text{dB}} = \omega_+ - \omega_- = (\omega_+ - \omega_0) + (\omega_0 - \omega_-) \quad (\text{H.36})$$

where $S_{21}(\omega_+) = S_{21}(\omega_-) = S_{21}(\omega_0) - 3$ (dB), hence

$$\Delta\omega_{3\text{dB}} = \frac{\omega_0}{Q_e} \quad (\text{H.37})$$

With a given S_{21} response of the circuit in Figure 6A.1, the external quality factor at port 1 can be calculated as

$$Q_e = \frac{\omega_0}{\Delta\omega_{3\text{dB}}} \quad (\text{H.38})$$

Appendix I – The method of extracting the quality factor Q_0 for a lossy resonator

The appendix present the method of extraction of the external quality factor based on a one-port measurement of a lossy resonator as shown in Figure I.1. The lossless resonator is presented by the parallel GLC circuit. The external ports coupled with the resonator are presented by the conductance G_e .

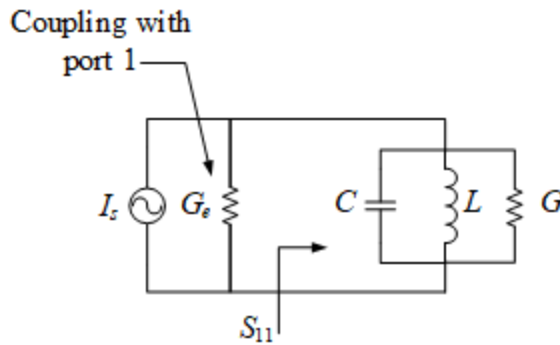


Figure I.1: The equivalent circuit of the one port measurement of the quality factor Q_0

The input admittance of the resonator can be written as

$$Y_{in} = j\omega C + \frac{1}{j\omega L} + G \quad (I.39)$$

The resonant of the circuit $\omega_0 = 1/\sqrt{LC}$ is substituted in the input admittance equation, we have

$$Y_{in} = G(1 + jQ_0\Delta(\omega)) \quad (I.40)$$

where the unloaded quality factor Q_0 is defined as

$$Q_0 = \frac{\omega C}{G} \quad (I.41)$$

$$\Delta(\omega) = 1 - \frac{\omega_0^2}{\omega^2} \quad (I.42)$$

The reflection coefficient S_{11} at the first port of the resonator is

$$S_{11} = \frac{1 - \frac{Y_{in}}{G_e}}{1 + \frac{Y_{in}}{G_e}} = \frac{1 - \frac{G}{G_e}(1 + jQ_0\Delta(\omega))}{1 + \frac{G}{G_e}(1 + jQ_0\Delta(\omega))} \quad (I.43)$$

The coupling coefficient β is defined as the ratio of the resonator conductance G to the port conductance G_e , the reflection coefficient can be rewritten as

$$S_{11} = \frac{(1 - \beta) + jQ_0\Delta(\omega)}{(1 + \beta) + jQ_0\Delta(\omega)} \quad (I.44)$$

At the resonant frequency $\Delta(\omega = \omega_0) = 0$, hence

$$S_{11}(\omega_0) = \frac{1 - \beta}{1 + \beta} \quad (I.45)$$

Note that the coupling coefficient β relates to the power dissipated externally P_e and internally P_0 to the resonator, thus it can be referred to the external quality factor and the unloaded quality factor of the resonator as follows

$$\beta = \frac{P_0}{P_e} = \frac{Q_e}{Q_0} \quad (I.46)$$

Substituting equation I.7 to equation I.6, the amplitude and phase of the reflection coefficient can be obtained as

$$|S_{11}(\omega)|^2 = \frac{|S_{11}(\omega_0)|^2 (1 + \beta)^2 + Q_0^2 \Delta^2(\omega)}{(1 + \beta)^2 + Q_0^2 \Delta^2(\omega)} \quad (I.47a)$$

$$\phi_{11}(\omega) = \tan^{-1}\left(\frac{Q_0\Delta(\omega)}{1 - \beta}\right) - \tan^{-1}\left(\frac{Q_0\Delta(\omega)}{1 + \beta}\right) \quad (I.9b)$$

In equation I.9, β can be determined from the magnitude of the reflection coefficient as

$$\beta = \frac{1 \pm |S_{11}(\omega_0)|}{1 \mp |S_{11}(\omega_0)|} \quad (I.48)$$

There are two possible values of β , one being greater than unity and the other being less than unity. The resonant circuit is called under-coupled, if $\beta < 1$. If $\beta > 1$, the resonance is referred as over-coupled [1]. The value of β can be determined by observed the gradient of the phase at the resonant frequency, differentiating equation I.9b gives

$$\left. \frac{d\phi}{d\omega} \right|_{\omega=\omega_0} = \frac{2Q_0}{\omega_0} \frac{2\beta}{1-\beta^2} \quad (I.49)$$

If the gradient is positive, then $\beta < 1$; if the gradient is negative, then $\beta > 1$ [1].

The unloaded quality factor Q_0 can be obtained from equation I.9a as

$$Q_{er} = \frac{|1+\beta|}{|\Delta(\omega)|} \sqrt{\frac{|S_{11}(\omega)|^2 - |S_{11}(\omega_0)|^2}{1-|S_{11}(\omega)|^2}} \quad (6B.50)$$

Reference

- [1] M. J. Lancaster, "Passive microwave device applications of high temperature superconductors / M.J. Lancaster," ed. Cambridge: Cambridge University Press, 1997.

Appendix J – The construction of the X-band filter-sensor

The appendix presents the detailed dimensions of the X-band microwave power sensor with integrated third order Chebyshev filter function designed in Chapter 6. Figure J.1 shows the structure of the sensor consisting of a PCB and two waveguide parts. The details dimensions of the components are shown in Figure J.2, J.3 and J.4, respectively.

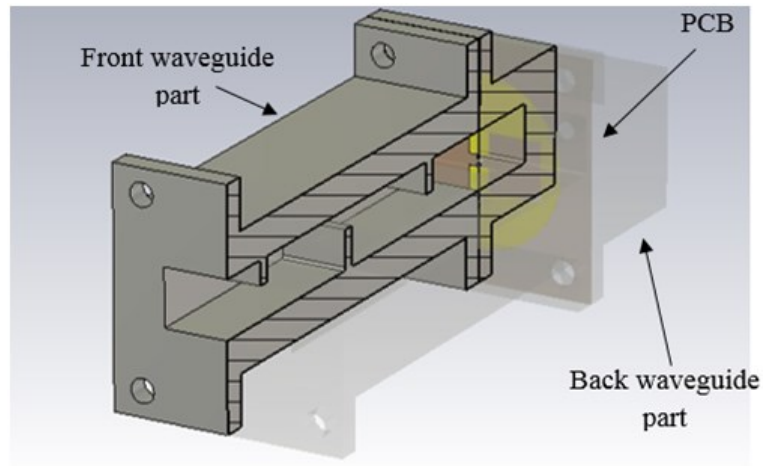


Figure J.1: The structure of the X-band filter-sensor.

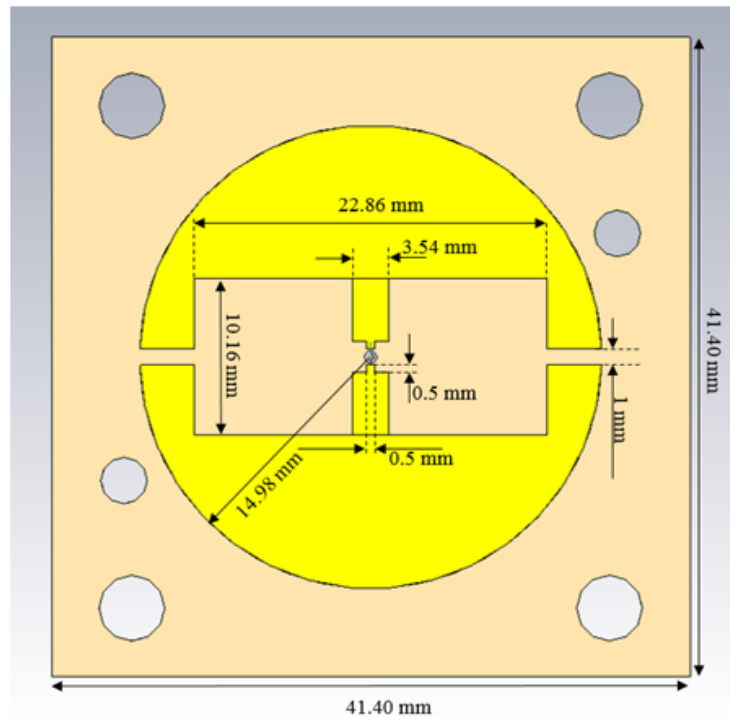


Figure J.2: The PCB of the X-band filter-sensor

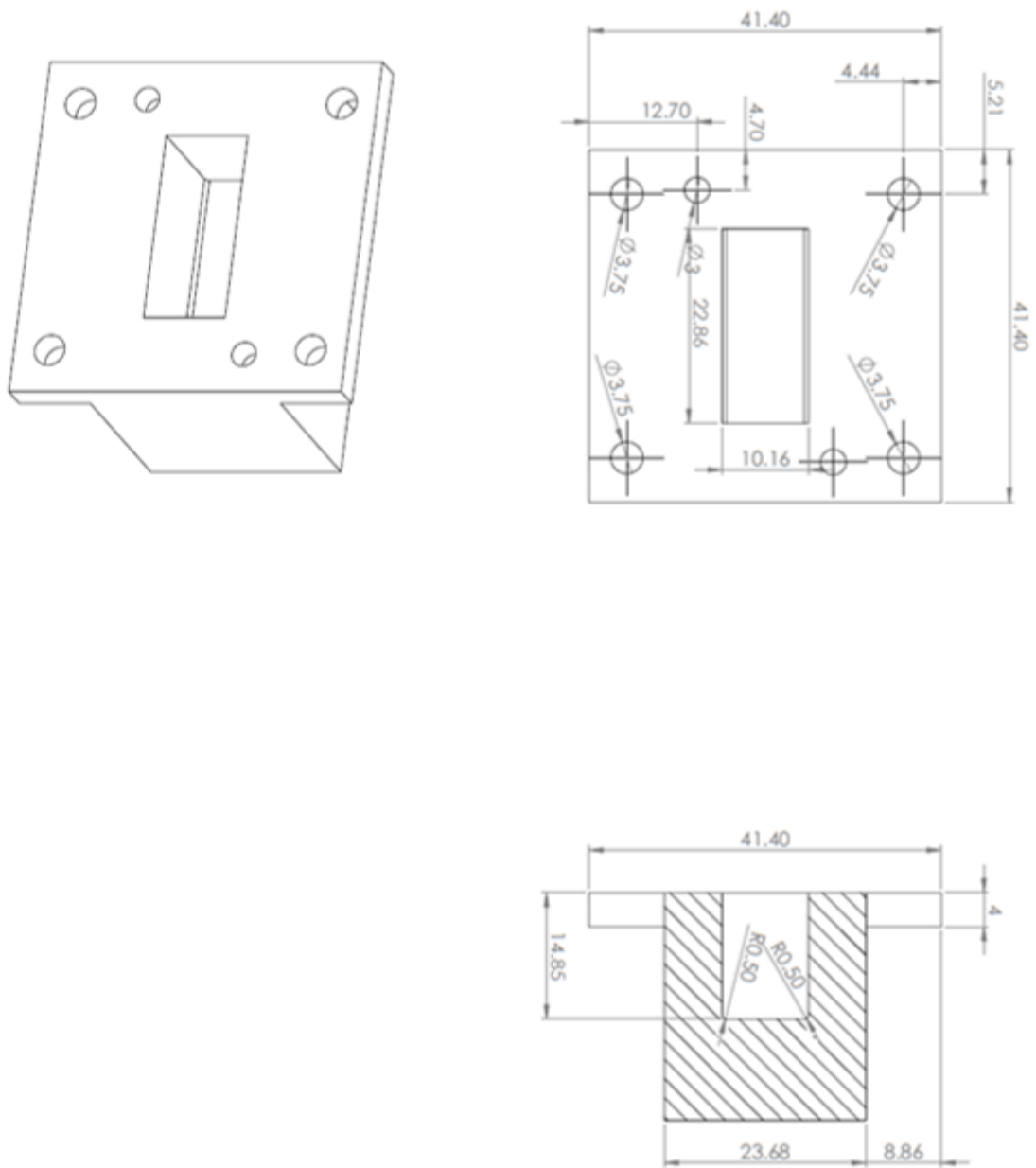


Figure J.3: The shorted waveguide part of the X-band filter-sensor

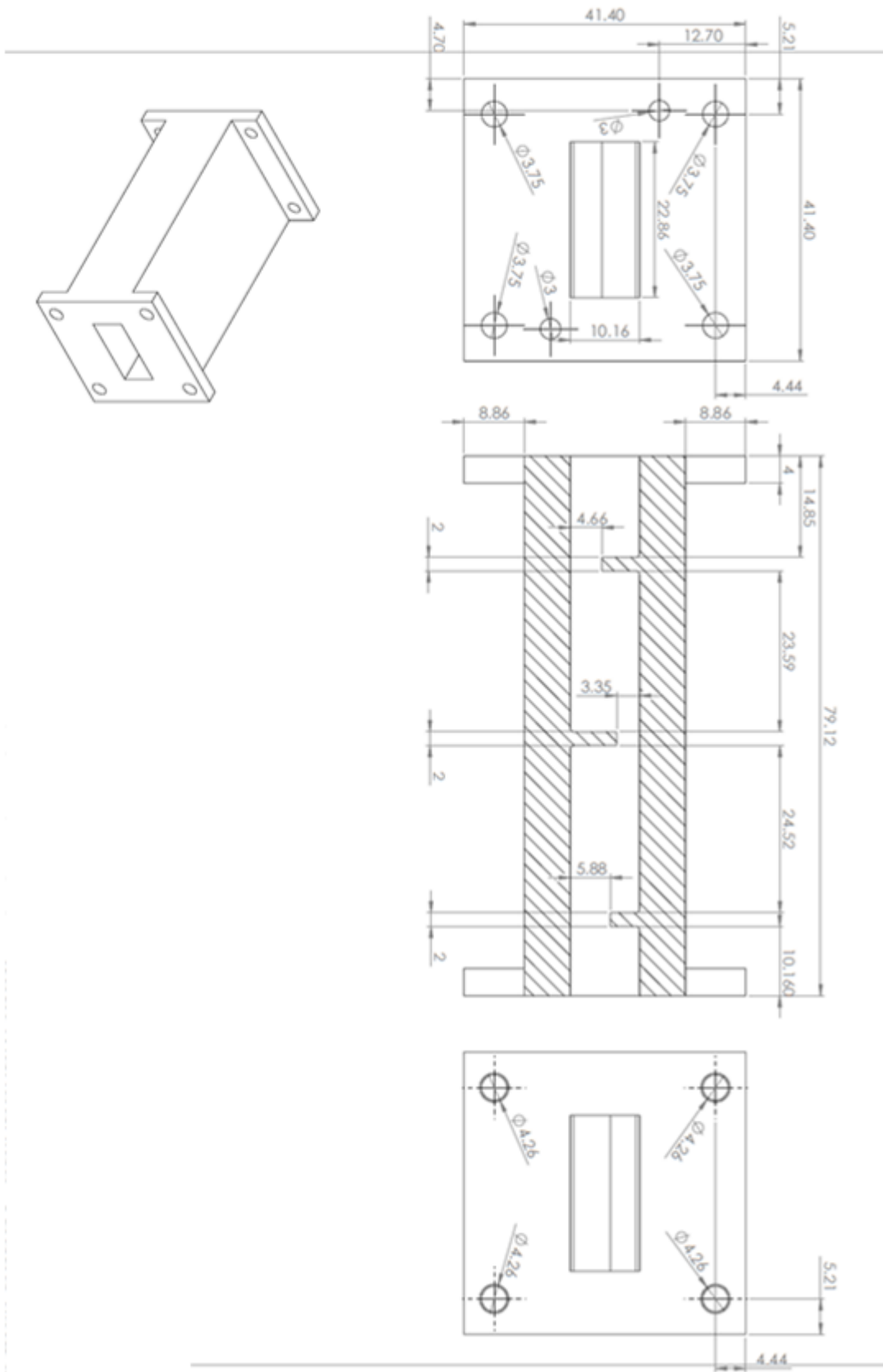


Figure J.4: The front waveguide part of the X-band filter-sensor.

List of Publications

- 1 C. Guo, J. Li, **D. D. Dinh**, X. Shang, M. J. Lancaster and J. Xu, "Ceramic filled resin based 3D printed X-band dual-mode bandpass filter with enhanced thermal handling capability," in *Electronics Letters*, vol. 52, no. 23, pp. 1929-1931, 11 10 2016.
DOI: 10.1049/el.2016.2955
- 2 **D. D. Dinh** and M. J. Lancaster, "The design techniques of microwave power sensors for transfer power standards," Submitting to *IEEE Transactions on Microwave Theory and Techniques*

Note: Paper (1) is available at IEEE Explore Digital Library, the author contributed in the measurement to observe the change in scattering parameter of the filter with respect to the temperature and discussion on the theoretical analysis of the thermal and mechanical property of the filter.

Paper (2) is attached.

The Designs of Microwave Power Sensors for Transfer Power Standards

Duc D. Dinh, and Michael J. Lancaster, *Senior Member, IEEE*

Abstract— This paper presents two techniques for the design of microwave bolometric power sensors for transfer power standards in waveguide. A conventional design technique based on transmission line theory is explained and generalized. An X-band waveguide power sensor using a small bead thermistor is designed to validate the proposed technique. The sensor was fabricated and measured, and excellent linearity and high effective efficiency of the design were obtained. In order to add more flexibility in selecting frequency and bandwidth of the conventional approach, a novel design of microwave power sensor with integrated filter function is described. An analytical power sensor synthesis technique using the coupling matrix is presented here for the first time. An X-band power sensor with integrated third order Chebyshev filter function was designed and manufactured. Measurements are in good agreement with simulation and theoretical expectation.

Index Terms— power standards, power measurements, thermistor power sensor, X-band, waveguide, resonator, filter, coupling matrix.

INTRODUCTION

RESEARCH and development of millimetre wave systems requires accurate supporting measurements and power is one of the primary standards. In power measurements, the traceability to the Watt is critical. In order to provide traceability of high frequency power, two basic building blocks are needed, one is traceable microwave power sensors and the second is calorimeters to calibrate the former [1]. The calorimeters are often developed at National Measurement Institutes (NMIs) [2]. State of the art power standards exist in the form of coaxial and waveguide sensors, where the latter tends to serve at higher frequencies than the former. The coaxial calorimeters and power standards of this type are generally available up to 50 GHz [3, 4]. In the waveguide form, micro-calorimeters up to 110 GHz have been developed [5, 6]. It is also known that several NMIs, such as in Japan [7-10] and in China [11-13], are actively developing their own micro-calorimeters up to and above 110 GHz to support domestic industrial and scientific measurement requirements.

The transfer standards of micro-calorimeter calibration are based on waveguide thermistor power sensors manufactured by Hughes and subsequently by Millitech [11,14] and the

thermistors are becoming increasingly rare as they are now out of production [6].

Modern commercial microwave power sensors are currently available up to 110 GHz (coaxial) and 1.1 THz (waveguide), but they are not suitable as direct traceable transfer standards. Their detection principle, based on rectification of low barrier Schottky diodes or direct heating effect of thermocouples, is incompatible with the existing calorimetric method. In the past, a millimetre wave power standard for the WR-6 waveguide band has been developed [15,16], but a detailed uncertainty calculation towards traceability has not been published. A traceable power sensor at 94 GHz was developed earlier [17], and the sensor is commercially available, but it is suited to free space power measurement rather than in waveguide [6].

This paper presents two design techniques of waveguide bolometric power sensors for transfer standards, they are not only suitable for use at high frequencies (> 110 GHz) but also at lower frequencies (< 75 GHz). These designs fill the gap left by the discontinued production of commercial thermistor sensors in waveguide frequency bands.

The power detector often consists of a sensing element, a mount to accommodate the element and a meter circuit to provide reading of the incident microwave power. The sensing element of the bolometer is capable of dissipating the incident microwave power and then turning the heat into a change in resistance [18, 19]. The amount of applied microwave power can be determined from the d-c substitution power to compensate the resistance change. The most popular sensing element of bolometer sensors is the Negative Temperature Coefficient (NTC) thermistor. The bolometer mount, or microwave transmission line housing, is probably the most challenging aspect in designing bolometric sensors for microwave power measurement. The essential requirement of the mount is that its impedance should be closely matched to the characteristic impedance of the transmission line [2]. The meter circuit is often an auto-balancing bridge circuit, which not only maintains the sensing element in the operating resistance range of the mount, but also extracts the changes, providing meaningful reading of absorbed microwave power.

In this paper, section II introduces the first sensor design technique based on transmission line theory. The technique is applied to design an X-band thermistor power sensor. Section

This work was supported by the University of Birmingham, The UK National Physical Laboratory and the UK Science and Engineering Research Council.

D. D. Dinh and M. J. Lancaster are with the Department of Electronic, Electrical and Systems Engineering, University of Birmingham, Birmingham B15 2TT, U.K. (email: ddd917@bham.ac.uk; m.j.lancaster@bham.ac.uk)

III presents a novel design of power sensor integrated with microwave filter. The design approach is illustrated by the design of a power sensor having third order Chebyshev filter response. Measurements of the two sensors and discussions are presented in section IV, and finally conclusions are given in section V.

MICROWAVE POWER SENSOR DESIGN BASED ON TRANSMISSION LINE THEORY

The design of waveguide bolometers can be based on transmission line theory. It believed that the technique was applied in previously published designs up to 94 GHz [20-24], but it has not been explicitly documented in the literature. The mathematics of the design principle is therefore briefly presented here. The design procedure for an X-band bolometric sensor is then introduced.

The conventional design technique

A waveguide bolometer traditionally consists of a sensing element mount which is placed at an appropriate distance from the shorted end of the waveguide. The waveguide bolometer can be presented in terms of the transmission line model shown in Fig. 1. The characteristic impedance of the line/waveguide is Z_0 and the propagation constant is β at the operating frequency f_0 . The shorted end of the line is represented by the zero load impedance $Z_L = 0$. The impedance of the mount is $R + jX$. It is important to note that the mount impedance is the total impedance of the sensing element and the structure that accommodates the element. The transmission line length l_s relates to the distance between the mount and the shorted end of the line/waveguide.

Here we will assume a lossless transmission line which is valid for most practical transmission lines/waveguides. The impedance matching results in zero reflection coefficient Γ_l at the mount as shown in Fig.1. The reflection coefficient Γ_l can be calculated as

$$\Gamma_l = \frac{Z_l - Z_0}{Z_l + Z_0} = 0 \quad (51)$$

where Z_l is the total impedance at $z = l_s$ looking toward the load. The corresponding admittance is obtained as

$$Y_l = \frac{1}{Z_l} = \frac{1}{R + jX} + \frac{1}{jZ_0 \tan(\beta l_s)} \quad (52)$$

Solving the (1) and (2) for the mount resistance R and the mount reactance X , assuming R and X cannot be zero gives

$$\frac{R}{Z_0} = \frac{1}{2}(1 - \cos(2\beta l_s)) \quad (53a)$$

$$\frac{X}{Z_0} = -\frac{1}{2}\sin(2\beta l_s) \quad (53b)$$

The expressions present the relationship of the mount resistance R and the mount reactance X to the electrical length l_s which can be used to provide the required matching i.e. no power being reflected. For this work the impedance of the mount ($R+jX$) has been found by simulation of the structure mounted centrally in a waveguide section and calculating it

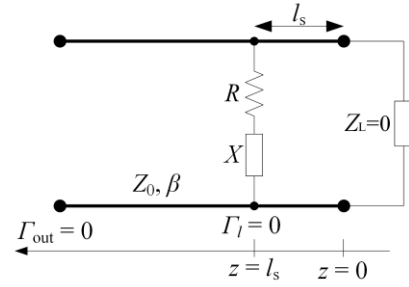


Fig. 1. Equivalent transmission line circuit of a waveguide bolometer. Impedance matching gives zero reflection coefficient at the open end and the mount of the sensor.

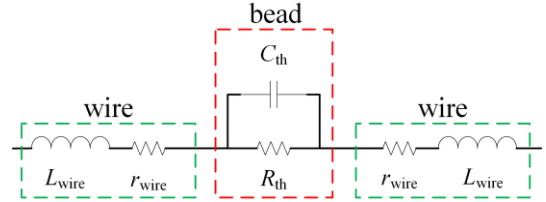


Fig. 2. Equivalent circuit of an RF thermistor [26].

from the resulting S -parameters. This technique is described in the Appendix.

In practice, the impedance of the mount depends on parameters such as the operating resistance and its physical dimensions. In order to find the appropriate parameters at matching condition, equations (2) and (3) can be used to calculate the lengths l_R and l_X which are related to the resistance and the reactance of the mount as follows

$$l_R = \frac{1}{2\beta} \arccos\left(1 - \frac{2R}{Z_0}\right) \quad (54a)$$

$$l_X = \frac{1}{2\beta} \arcsin\left(-\frac{2X}{Z_0}\right) \quad (4b)$$

When they are equal perfect matching is obtained, the convergence of the two lengths suggests the corresponding matching values of the parameters. This approach is exemplified in the following design of X-band sensor.

The design of X-band sensor

This section presents the design of a microwave power sensor in X-band waveguide, which is based on the technique described above. Microwave power sensors traditionally use NTC thermistors for frequencies up to 50 GHz [18, 23]. The centre frequency of the X-band sensor is designed at 10 GHz.

The small bead thermistor from Sensor Scientific [25] was used here. The bead has the body diameter of 0.36 mm and the nominal length of 0.5 mm, the diameter of the platinum alloy wire is 0.028 mm. The room temperature (at 25 °C) resistance of the thermistor is 1000 Ω . At the operating condition, the thermistor resistance should be biased by d-c power down to the operating resistance of 200 Ω which is a very popular value and compatible with commercial power meters. For theoretical analysis and simulation purposes, the bead behavior can be modelled over a broadband frequency range by the equivalent circuit in Fig. 2 [26]. R_{th} is the d-c resistance of the thermistor. L_{wire} and r_{wire} are parasitic elements of the thermistor wires. The

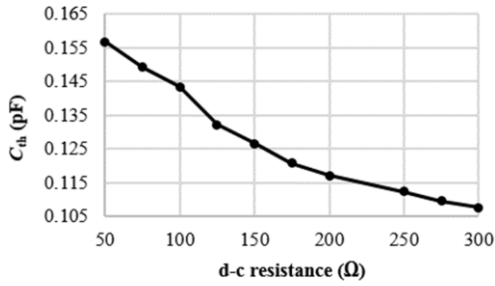


Fig. 3. Estimated capacitance C_{th} of the Sensor Scientific bead thermistor at different d-c biased thermistor resistance.

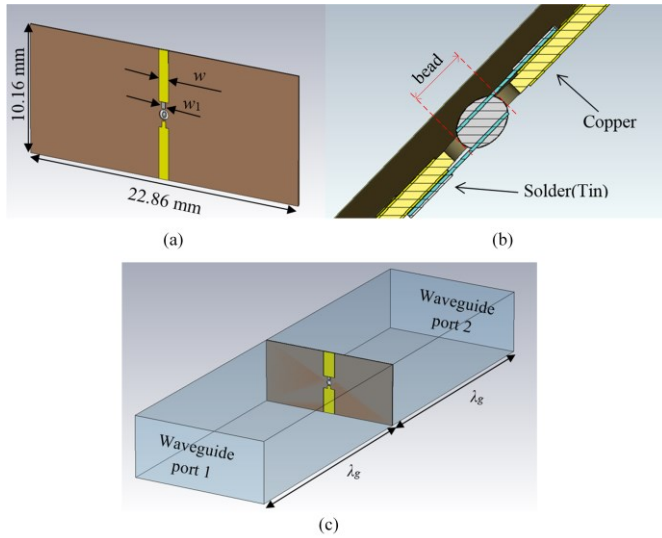


Fig. 4. (a) The section in the waveguide of the PCB accommodating the bead thermistor, the soldering area has the width $w_1 = 0.5$ mm; (b) the cut view to show how the thermistor is soldered on the PCB; (c) The two port simulation of impedance extraction for the thermistor mount.

capacitance C_{th} represents the non-linear capacitive behavior of the inner structure of the bead thermistor.

The value of C_{th} depends on the thermistor body condition such as temperature and the d-c resistance of the bead. The self-capacitance of the bead body can be calculated by

$$C_{th} = \frac{\pi \epsilon_r \epsilon_0 l}{\ln(d - d_{wire}/2) - \ln(d_{wire}/2)} \quad (55)$$

where ϵ_r is the relative permittivity of the inner body material of the bead thermistor, the permittivity is assumed to have a non-linear relationship with the bead temperature. l and d are the length and the width of the bead, respectively. d_{wire} is the diameter of the connecting wire. d_{wire} is very small compared to d , hence the capacitance is approximately equal to $\pi \epsilon_r \epsilon_0 l / \ln(d)$. The derivation of (5) is based on the calculation of the capacitance between two parallel wires in a dielectric medium [27].

For the chosen thermistor, we have no information on ϵ_r , however in the work of Kazemipour [26], the self-capacitance was estimated at different resistance values from the measured scattering parameters of the bead thermistor. Note that the thermistor used by Kazemipour and the thermistor used in this design are different in size, with $l = 0.228$ mm and $l = 0.5$ mm, respectively. However, the capacitance C_{th} of the Sensor Scientific thermistor can be estimated from the values of the

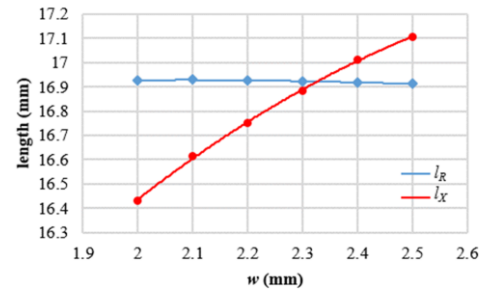


Fig. 5. The graph of the effective length l_R and l_X at different widths w .

capacitance measured by Kazemipour [26]; this of course assumes that the two thermistors are of similar construction. The factor of $\epsilon_r / \ln(d)$ can be used to scale the C_{th} of the two bead thermistors. With the assumption that the relative permittivities are equal at the same resistance of the thermistor, the equivalent capacitance of the Sensor Scientific thermistor can be estimated at different d-c resistance, the result is shown in Fig. 3. At the chosen operating resistance of 200 Ω , the self-capacitance of the thermistor is about 0.117 pF. The equivalent circuit of the bead in Fig. 2 can now be used together with a full wave simulation of its mount to determine the mount impedance $Z = R + jX$ using the technique discussed in the Appendix.

For simulation (and experiment), the bead thermistor is mounted on a double-sided PCB as shown in Fig. 4(a). The PCB is made from RT/duroid 6010.2LM from Rogers corporation [28]. The relative permittivity of the substrate is 10.2, the PCB thickness is 127 μm , and both sides are clapped with 17.5 μm copper. Fig. 4(a) shows only the section of the PCB which is inside an X-band rectangular waveguide, varying the width w of the copper track can adjust the mount impedance. In the centre of the PCB, a hole is drilled with 0.8 mm diameter for the thermistor to be accommodated. The two connecting wires of the bead thermistor are soldered on the upper and lower sides of the PCB as shown in Fig. 4(b). In simulation, the bead is modelled by the parallel circuit of R_{th} and C_{th} (shown inside the red dotted area in Fig. 2), the connecting wires of the thermistor are modelled by their physical construction (rather than the green dotted areas in Fig. 2) as the dimensions and the material of the wires can be explicitly used in the full wave simulation. The full wave simulator used is CST microwave studio [29].

The first part of the design is to determine the normalized impedance of the mount, a description of how to do this is given in the Appendix. In CST, the mount described above is placed in the middle of the X-band waveguide with a total length of two guided wavelengths ($2\lambda_g$) at 10 GHz. This is illustrated in Fig. 4(c). Only the vacuum filling of the waveguide is presented in the figure, the surrounding material is set as Perfect Electric Conductor (PEC), and the two ends of the waveguide are connected to matched waveguide ports.

The normalised impedance of the mount can be obtained from the simulated reflection coefficient and hence l_R and l_X can be found from 4(a) and 4(b). By varying the width w of the PCB, the values of the length l_R and the length l_X can be calculated at each value of w . The results are plotted on Fig. 5.

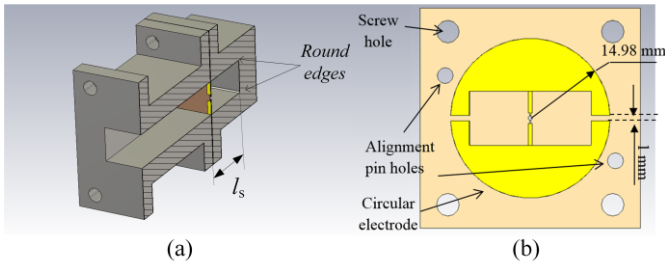


Fig. 6. The structure of (a) the X-band power sensor and (b) the PCB accommodating the bead thermistor.

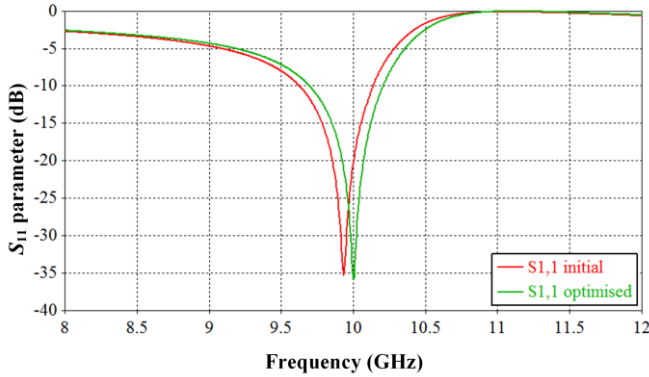


Fig. 7. The simulation result of the X-band power sensor.

The change in the width of the PCB track mostly affects the reactance of the mount. As a result, there is a noticeable rise in the reactance effective length l_X while the length l_R stays almost unchanged. The lengths are equal at the width w of 2.33 mm and the corresponding shorted electrical length l_s of 16.92 mm.

Now that the optimal mount structure is known, the entire structure can be simulated, and this is presented in Fig. 6(a). There are two separate parts of the waveguide. The front part is a conventional X-band waveguide, and the second part is a shorted waveguide with the determined short length l_s . Due to the fabrication limitation of the milling tool, there are round edges of 0.5 mm in radius at the shorted end.

The double sided PCB, shown in Fig. 6(b), is positioned between the two waveguide parts. Semi-circular electrodes are added to the PCB shown in Fig. 4(a) to enable a bias to be applied to the thermistor. The separation of 1 mm between the upper and lower electrodes is to create electrical isolation.

With the determined dimensions w and l_s , the simulated response of this sensor structure is obtained, this is shown in red in Fig. 7. The centre frequency of the response is at 9.932 GHz. The deviation in the centre frequency is attributed by the round edges in the shorted waveguide and the gap introduced by the PCB between the two waveguide flanges. Now the centre frequency is optimized in CST to 10 GHz by adjusting the short length l_s to 16.76 mm. The optimum S_{11} gives the narrow bandwidth of 145 MHz for 20 dB return loss or 200 MHz for 15 dB return loss. The comparison of the pre-optimizes or initial response and the optimised response is shown in Fig. 7.

The fabrication and measurement of the X-band sensor is presented in section IV.

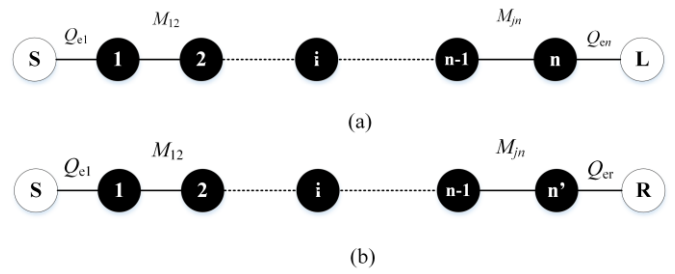


Fig. 8. (a) The topology of an n direct-coupled resonator band-pass filter network where M_{ij} is the coupling coefficient between resonators and Q_e is the external quality factor of the first and last resonators to the ports, (b) The topology of the power sensor integrated band-pass filter function.

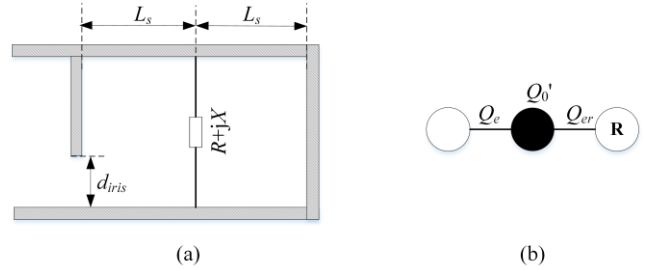


Fig. 9. (a) The sensor-resonator structure realized by adding a capacitive iris to the conventional power sensor structure discussed in section II, (b) The topology of the sensor-resonator.

MICROWAVE POWER SENSOR DESIGN BASED ON COUPLING MATRIX SYNTHESIS

This section discusses the integration of a power sensor with a filter structure, this is in order to control and consequently improve the bandwidth of the sensor in the previous design. A bandpass filter can be represented by a series of coupled resonators as shown in Fig 8(a). Here we assume there is no cross coupling between the resonators and the coupling shown can represent, for example, a Chebyshev filter. The conventional power sensor is integrated with the filter structure. Techniques based on the use of the coupling matrix can be used to design the filtering-sensor. The X-band sensor with integrated 3rd order filter function is designed by the proposed technique.

The design of bolometric sensor with integrated filter function

It should be noted that the sensor discussed in section II is indeed a resonator at the designed frequency f_0 . In order to be coupled with other waveguide resonators to make a filter, an iris should be added to the structure while preserving the existing resonance. Fig. 9(a) shows an example of the realization of the sensor-resonator by adding a capacitive iris. Note that other types of irises are also possible. The mount of the sensing element is placed at equal distance L_s to the shorted end and to the iris.

In terms of quality factors of the sensor-resonator, there is no loss in the dielectric and no radiation. The unloaded Q of an Aluminum X-band cavity with the length of about a half guided wavelength is approximately 11450 [30], hence the conductor loss is negligible. Therefore, the total unloaded quality factor Q_0 of the sensor-resonator should be equal to the quality factor Q_{er} which is the Q associated with the power loss due to the absorption of the resistive sensing element in the cavity.

The power absorbed by the sensing element can be

considered as an output with the power going to the element rather than a conventional output port. This arrangement is shown in Fig. 9(b). In this topology, the quality factor Q_{er} has the role of the external quality factor of the equivalent resonator, the unload quality Q'_0 can be taken as infinity.

As a result, the topology of the integration of the sensor-resonator with the filter topology in Fig. 8(a) can be presented in Fig 8(b), where the last resonator and the load of the filter are replaced by the sensor-resonator. The device described by the above topology is called filtering-sensor in this paper.

The topology of the filtering-sensor is similar to the n coupled resonator filter circuit, thus, it can be described by the $[A]$ matrix as [31]

$$[A] = [q] + p[U] - j[m] \quad (56)$$

where $[q]$ is $n \times n$ matrix containing the scaled external quality factor q_{e1} and q_{er}

$$[q] = \begin{bmatrix} 1/q_{e1} & 0 & \dots & \\ 0 & 0 & \dots & \\ \vdots & \vdots & \ddots & \vdots \\ 0 & 0 & \dots & \end{bmatrix} \quad (57)$$

$[U]$ is $n \times n$ identity matrix and p is the complex low-pass frequency variable. FBW is the fractional bandwidth.

$$p = j \frac{1}{FBW} \left(\frac{\omega}{\omega_0} - \frac{\omega_0}{\omega} \right) \quad (58)$$

The general coupling matrix $[m]$ denotes the normalised coupling coefficient between resonators.

$$[m] = \begin{bmatrix} m_{11} & m_{12} & \dots & \\ m_{21} & m_{22} & \dots & \\ \vdots & \vdots & \ddots & \vdots \\ m_{n1} & m_{n2} & \dots & \end{bmatrix} \quad (59)$$

The reflection coefficient S_{11} can be calculated by [31]

$$S_{11} = \pm \left(1 - \frac{2}{q_{e1}} [A]_{11}^{-1} \right) \quad (60)$$

It is worth mentioning that the filter-sensor is in fact a one port device, hence the calculation of S_{21} by coupling matrix, although possible, does not have a useful meaning.

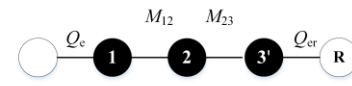
The quality factors and coupling coefficients are related to the normalised quantities in the matrix $[A]$ as follows

$$Q_{ei} = \frac{q_{ei}}{FBW} \quad M_{ij} = m_{ij} \cdot FBW \quad (61)$$

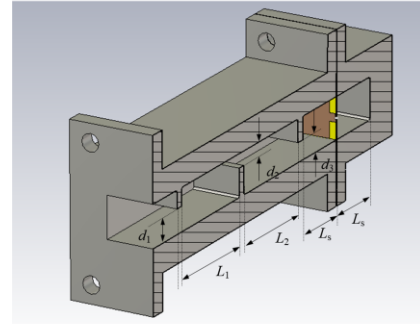
It is now possible to calculate a coupling matrix for the filtering-sensor with the usual algebraic operations [31]. The design of the sensor can now be treated in the same manner as designing microwave filter. Here we look at a simple Chebyshev filter, but more complex filters are possible.

The design of X-band sensor having 3rd order Chebyshev filter function

In this section, the design of an X-band power sensor with integrated third order Chebyshev filter function is presented. The equivalent topology of a third order filter sensor is shown in Fig. 10(a), in which the third resonator is the sensor-resonator



(a)



(b)

Fig. 10. (a) Equivalent topology of third order Chebyshev filtering-sensor; (b) the structure of the filter-sensor is very similar to the structure of the X-band sensor, the PCBs in the two sensors has similar design.

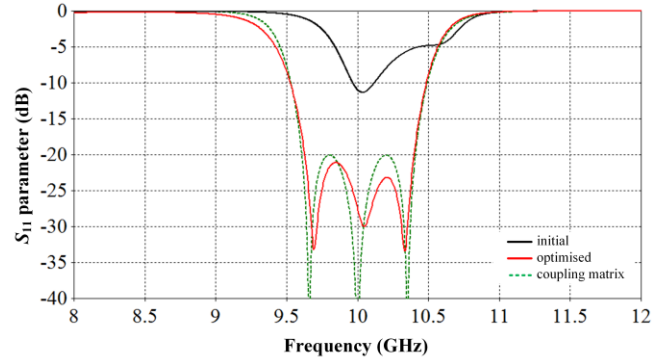


Fig. 11. The optimized response in red of the filtering-sensor from simulation compared to the response derived from the coupling matrix in dashed green, the response of the sensor before optimization is shown in black.

with the equivalent external quality factor Q_{er} as discussed previously. The coupling between the resonators is realized by capacitive irises as shown in the structure of the filtering-sensor in Fig. 10(b).

The bead thermistor used in the sensor-resonator is the same as the one used in the sensor design in section II. The filtering-sensor is designed to have 8% FBW at the centre frequency of 10 GHz, the maximum return loss in the pass-band is 20 dB. The general coupling matrix of the sensor is similar to that of a third order Chebyshev band pass filter [31] which are $Q_e = Q_{er} = 10.645$ and $M_{12} = M_{23} = 0.083$.

The external quality factor Q_e and the coupling coefficients M_{ij} are extracted from a waveguide simulation by a technique described in [30]. The equivalent quality factor Q_{er} of the sensor-resonator can be obtained by the technique of extracting quality factor by one port measurement technique discussed in [32]. This will find the sizes of coupling irises and the shape of the probe mount which corresponds to the coupling coefficients and external quality factors. The external quality factor Q_e and the coupling coefficient M_{12} and M_{23} can be calculated at different values of the iris width and the corresponding length of the rectangular waveguide resonator [30]. Using this technique the dimensions of the first two resonators in Fig. 10(b) are $d_1 = 5$ mm, $d_2 = d_3 = 2.6$ mm, $L_1 = 22.41$ mm and

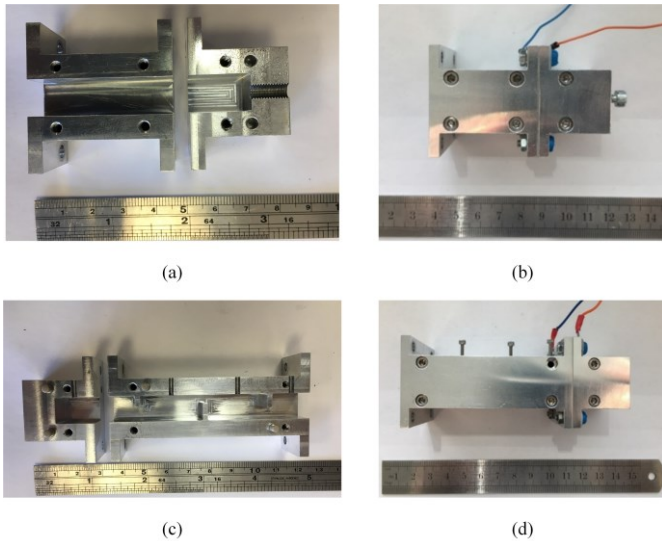


Fig. 12. (a) Half of the waveguide structure and (b) the fully assembled structure of the fabricated X-band power sensor, (c) half of the waveguide structure and (d) the fully assembled structure of the fabricated X-band sensor integrated with third order Chebyshev filter.

$L_2 = 21.36$ mm. The equivalent external quality factor Q_{er} can also be estimated at different PCB width w when the thermistor resistance is 100Ω and the corresponding self-capacitance is 0.144 pF as shown in Fig. 3. The initial dimensions of the sensor-resonator are $w = 3.5$ mm and $L_s = 15.45$ mm.

The simulated response of the filtering-sensor in Fig. 10(b) is obtained, this is shown in Fig. 11. The response is then optimized by CST as shown in Fig. 11 with the resulting dimensions $L_1 = 24.19$ mm, $L_2 = 23.37$ mm, $L_s = 15.10$ mm, $d_1 = 5.44$ mm, $d_2 = 3.12$ mm, $d_3 = 4.54$ mm and $w = 3.51$ mm.

The optimized response of the filtering-sensor is in excellent agreement with the computed response obtained from the coupling matrix analysis. The fabrication and measurement of the device is presented in the next section.

MEASUREMENTS & DISCUSSIONS

The waveguide parts are made from two halves with the cut on E-plane as shown in Fig. 12(a) and 12(c). The PCB is clamped in the middle of the two aluminum waveguide parts by four bolts. At the back of the shorted waveguide part of the X-band sensor, there is an M4 screw for tuning. The X-band filtering-sensor has four M2 tuning screws, one each at the two conventional resonators and two at the sensor-resonator. The red cable is connected to the shorted waveguide part and the blue cable is connected to the front, input waveguide of the sensor. The d-c bias can be applied to the thermistor through these wires.

Measurement of reflection coefficients

Without using tuning screws and with the holes for them absent, the measured reflection coefficient, when the thermistor is biased to 200Ω , has the minimum of -21.53 dB at 9.88 GHz as presented in Fig. 13. The measured response has the similar shape to the simulated response, but the centre frequency is slightly lower than the designed 10 GHz. The difference between the simulation and the measurement can be attributed

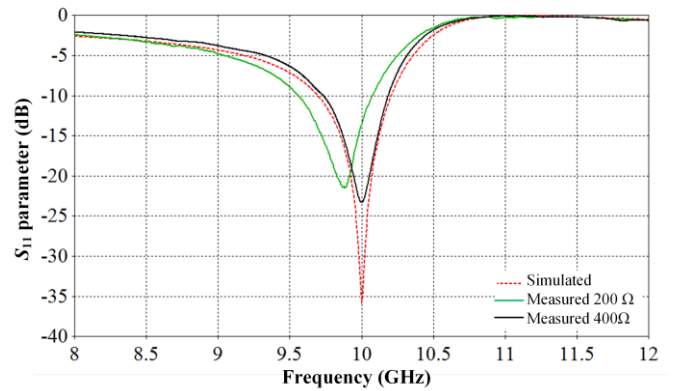


Fig. 13. The measured reflection coefficient of the X-band sensor designed in section II at 200Ω and 400Ω operation, the simulated response at 200Ω resistance is also shown.

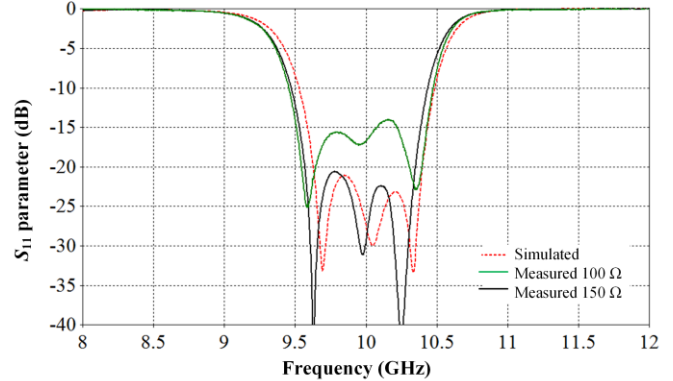


Fig. 14. The measured response of the X-band filter-sensor design in section III at 100Ω and 150Ω operation. The simulated response of the third order filter-sensor is shown in black for comparison.

to a number of factors such as (i) the errors in the dimensions of the fabricated PCB and waveguide and (ii) the approximation of the bead thermistor model in the simulation. The simulation with measured dimensions of the fabricated sensor shows a negligible difference from the simulated sensor response. Therefore, the estimation of the non-linear behavior of the bead thermistor is the main contribution to the discrepancy between simulation and measurement results. As shown in Fig. 13 the centre frequency of the sensor can be tuned to 10 GHz by biasing the operating resistance of the thermistor to 400Ω and applying tuning screws giving a minimum of S_{11} of -23.5 dB.

The measured reflection coefficient of the X-band filtering-sensor response at 100Ω operation is shown in Fig. 14. This response is with a structure with no tuning screws. The filtering-sensor has the characteristic response of a third order filter. However, the return loss in the pass band is about 15 dB. Similar to the measurement of the X-band sensor, the discrepancy can also be attributed by the approximation of the equivalent bead thermistor circuit components. By adjusting the thermistor resistance to 150Ω and adding tuning screws, the pass-band of the reflection coefficient can be brought down below -20 dB and the centre frequency tuned response to 9.98 GHz. Here the -20 dB bandwidth is about 800 MHz.

Measurement of power linearity

A perfectly linear RF power sensor is one whose output varies in direct proportion to a change in input power. The

relationship between the d-c substitution power (output) and the incident microwave power (input) is investigated here for the case of the bolometric sensors.

The d-c power needs to be reduced by enough to maintain the operating resistance at R_0 when the microwave power is dissipating on the thermistor. The d-c substitution power can be calculated as

$$P_{\text{sub}} = \frac{V_{\text{off}}^2 - V_{\text{on}}^2}{R_0} \quad (62)$$

where V_{off} and V_{on} are the voltage across the thermistor before and after being exposed to microwave power.

A measurement setup was built to observe the d-c substitution power on the bead thermistor at different microwave input powers. A 3 dB coupler is used to split the input power from a signal generator at 10 GHz so signals go to both its through port and coupled port. The coupled port is connected to a coaxial power meter by a coax to waveguide adapter. The sensor is connected to the through port of the coupler. By monitoring the power meter at the coupled port, the incident power to the sensor is known.

The X-band sensor and the X-band filtering-sensor are measured at different input power levels up to 10 mW. At each level, the substitution d-c power is recorded. The X-band sensor operates at 400 Ω and the X-band filtering-sensor operates at 150 Ω . The linearity of the substitution power to the incident power can be mathematically evaluated by the linear regression algorithm. In both cases, the correlation coefficient r of the regression is 0.9999 and the common error variance σ are very small, 4.85×10^{-3} and 17×10^{-3} for the X-band sensor and the X-band filter sensor, respectively. As a result, both designed sensors are designated linear with respect to the incident microwave power.

Sensor calibration

The calibration factor and effective efficiency at 10 GHz of the sensors were determined by the measurement with the X-band multistate reflectometer[33]. The results are shown in Table I.

The effective efficiency of thermistor power sensor is often less than 100 % because of (i) microwave leakage and/or (ii) a fraction of absorbed power dissipating outside the thermistor bead. The potential microwave leakage is at the gap introduced by the PCB between the two waveguide sections and the contacts between the PCB and waveguide flanges and there are also possibilities of power being absorbed in the waveguide section, the PCB track and the soldered contacts. In this particular case, the leakage is very small because the air gap (about 20 μm) and the PCB thickness (127 μm) are small as compared to the waveguide size of 22.86 mm \times 10.16 mm. The microwave leakage is estimated at about 1% of the incident power by CST simulation. The power absorbed in the aluminum waveguide and copper PCB is negligible compared to the dissipated power at the thermistor, as their resistances are small compared to the thermistor resistance. Therefore, the main reason here is believed to be at the thermistor. The thermistor resistance consists of the contact resistances and the

TABLE I
THE RESULTS OF THE CALIBRATION

Device	X-band sensor (400 Ω)	X-band filter-sensor (150 Ω)
VRC	0.073 ± 24.145^0	0.037 ± 163.83^0
Calibration factor	0.8494	0.8877
Effective efficiency	85.4%	88.90%

semiconductor resistance which is sensitive to temperature. At d-c and low frequency operation, the semiconductor resistance is dominant. At high frequency, the effective capacitance C_{th} (see Fig. 3) tends to shunt the semiconductor resistance, so that the effective resistance of the bead gets smaller and the contact resistance including the inner wires inside the bead and the protective glass layer of the bead becomes comparable to it. For instance, the effective resistance of 200 Ω thermistor in Fig. 2 at 10 GHz is 63.26 Ω , note that the self-capacitance value in this example is 0.117 pF, while the wire resistance of the bead alone at 10 GHz is about 2 Ω with the effect of the skin depth accounted for. Thus, the absorbed microwave power is not entirely dissipated in the semiconductor part of the thermistor. The phenomenon was discussed in Collard's work [34]. In order to achieve high effective efficiency, the sensing elements such as thermistors need to be carefully design so that the parasitic parameters can be minimized at high frequency operation.

CONCLUSION

Two design techniques of the microwave power sensors are presented. The techniques are realized by the designs of a conventional X-band power sensor and an X-band filtering-sensor. Both sensors are compatible with the current calorimetric technique of calibration for power standards. The first design provides a narrow band response at one centre frequency. The second design, based on coupling matrix synthesis, utilizes the advantage of a controlled bandwidth through an implicit filter design. The two sensors designed in this paper have the same centre frequency in order to provide a comprehensive comparison between the two approaches. The measurements of the sensors agree with theoretical expectation. The power linearity of the sensors is proven. High effective efficiencies are obtained. Both design approaches are validated. The presented design techniques are promising for designing transfer power standards at much high frequencies, as they can be applied regardless of the type of the sensing element.

APPENDIX

In the design we are required to find the impedance of the thermistor and mount by simulation so that the impedance can be used in the transmission line calculations outlined in section II. In order to do this we simulate the mount placed in the centre of a waveguide section. In this work, we take the length of the line to be two wavelengths (2λ), and the characteristic impedance of the line Z_0 . At each end of the transmission line, there is a matched port to measure the complex reflection coefficient Γ . The reflection coefficient at the load is equal to that at the measurement port, i.e. Γ .

The reflection coefficient at the load can be calculated in terms of impedances as

$$\Gamma = \frac{Z_p - Z_0}{Z_p + Z_0} \quad (63)$$

where Z_p is the total impedance at the centrally located mount i.e. $Z_p = ZZ_0/(Z+Z_0)$. Solving (13) for the normalized impedance Z/Z_0 gives

$$\frac{Z}{Z_0} = -\frac{1+\Gamma}{2\Gamma} \quad (64)$$

So once Γ is known from the simulation then the complex impedance of the mount Z can be ascertained.

ACKNOWLEDGMENT

The authors wish to express their gratitude to John Howes and other colleagues at the National Physical Laboratory for the collaboration during this work and for their many helpful comments, discussions and measurement assistance.

REFERENCES

- [1] R. A. Ginley, "Traceability for microwave power measurements: Past, present, and future," in *Wireless and Microwave Technology Conference (WAMICON), 2015 IEEE 16th Annual*, 2015, pp. 1-5.
- [2] "Fundamentals of RF and Microwave Power Measurements (Part3) Power Measurement Uncertainty per International Guides," *Agilent Technologies, Application note 64-32, 5988-9215EN*, April 2011.
- [3] J. T. Ascroft, "Developments in coaxial power standards at NPL," in *1998 Conference on Precision Electromagnetic Measurements Digest (Cat. No.98CH36254)*, 1998, pp. 619-620.
- [4] M. Bourghes, D. Allal, D. Béliers, A. Kazemipour, and A. Litwin, "Development of a 2.4 mm coaxial microcalorimeter for power measurements up to 50 GHz," in *CPEM 2010*, 2010, pp. 324-325.
- [5] D. Adamson, J. Miall, J. Howes, M. Harper, and R. Thompson, "A new 75-110 GHz primary power standard with reduced thermal mass," in *75th ARFTG Microwave Measurement Conference*, 2010, pp. 1-4.
- [6] D. B. Adamson, Howes, J, Ridler, N M, "Recent and future developments in millimetre and sub-millimetre wavelength measurement standards at NPL," *Proceedings of the Joint 5th ESA Workshop on Millimetre Wave Technology and Applications and 31st ESA Antenna Workshop*, pp. Noordwijk, The Netherlands, 463-467, 18-20 May 2009.
- [7] K. Shimaoka, M. Kinoshita, K. Fujii, and T. Tosaka, "Design of a broadband calorimeter for mm-wave power standard in the frequency range from 110 GHz to 170 GHz," in *2012 37th International Conference on Infrared, Millimeter, and Terahertz Waves*, 2012, pp. 1-2.
- [8] K. Shimaoka, M. Kinoshita, and T. Inoue, "A broadband waveguide calorimeter for mm-wave power meter calibration in the frequency range from 50 GHz to 110 GHz," in *2012 Conference on Precision electromagnetic Measurements*, 2012, pp. 88-89.
- [9] K. Shimaoka, M. Kinoshita, K. Fujii, and T. Tosaka, "Calibration of mm-wave power meters using a broadband calorimeter in the frequency range from 110 GHz to 170 GHz," in *2013 38th International Conference on Infrared, Millimeter, and Terahertz Waves (IRMMW-THz)*, 2013, pp. 1-2.
- [10] K. Shimaoka, M. Kinoshita, and T. Inoue, "A Broadband Waveguide Calorimeter in the Frequency Range From 50 to 110 GHz," *IEEE Transactions on Instrumentation and Measurement*, vol. 62, pp. 1828-1833, 2013.
- [11] X. Cui, Y. S. Meng, R. Judaschke, J. Rūhaak, T. P. Crowley, and R. A. Ginley, "International comparison of WR15 (50 to 75 GHz) power measurements among NIST, NIM, PTB and NMC, ASTAR," in *2016 Conference on Precision Electromagnetic Measurements (CPEM 2016)*, 2016, pp. 1-2.
- [12] X. Cui, W. Yuan, Y. Li, C. Jia, and Y. S. Meng, "Development of a national WR-10 (75 to 110 GHz) microcalorimeter," in *2016 URSI Asia-Pacific Radio Science Conference (URSI AP-RASC)*, 2016, pp. 478-480.
- [13] C. Ma, X. Cui, W. Yuan, and Y. Li, "Design of a WR-6 thermoelectric conversion power sensor," in *2015 40th International Conference on Infrared, Millimeter, and Terahertz waves (IRMMW-THz)*, 2015, pp. 1-2.
- [14] R. H. Judaschke and J. Rūhaak, "Leakage effects in millimeter-wave power transfer standards," in *2016 Conference on Precision Electromagnetic Measurements (CPEM 2016)*, 2016, pp. 1-2.
- [15] J. A. Mallat, S. N. Dudorov, D. V. Lioubtchenko, and A. V. Raisanen, "110-170 GHz Millimetre Wave Power Standard," in *2006 European Microwave Conference*, 2006, pp. 482-485.
- [16] A. N. Akhiezer, A. P. Senko, and V. P. Seredniy, "Millimeter wave power standards," *IEEE Transactions on Instrumentation and Measurement*, vol. 46, pp. 495-498, 1997.
- [17] D. G. Moss, J. R. Birch, D. B. Adamson, B. Lunt, T. Hodgetts, and A. Wallace, "Comparison between free space and in-waveguide power measurement standards at 94 GHz," *Electronics Letters*, vol. 27, pp. 1134-1137, 1991.
- [18] "Technique of microwave measurements / edited by Carol G. Montgomery. Vol.1," C. G. Montgomery, Ed., ed. New York: Dover : Constable, 1966, pp. 89-156.
- [19] E. L. Ginzton, *Microwave measurements*: McGraw-Hill, 1957, pp. 145-172.
- [20] J. A. Lane, "Transverse film bolometers for the measurement of power in rectangular waveguides," *Proceedings of the IEE - Part B: Radio and Electronic Engineering*, vol. 105, pp. 77-80, 1958.
- [21] I. Lemco and B. Rogal, "Resistive-film milliwattmeters for the frequency bands: 8.2-12.4 Gc/s, 12.4-18 Gc/s and 26.5-40 Gc/s," *Proceedings of the IEE - Part B: Electronic and Communication Engineering*, vol. 107, pp. 427-430, 1960.
- [22] J. A. Lane and D. M. Evans, "The design and performance of transverse-film bolometers in rectangular waveguides," *Proceedings of the IEE - Part B: Electronic and Communication Engineering*, vol. 108, pp. 133-135, 1961.
- [23] K. Sakurai and T. Nemoto, "A Thin-Film Bolometer Unit," *Instrumentation and Measurement, IEEE Transactions on*, vol. 16, pp. 206-211, 1967.
- [24] T. Inoue, I. Yokoshima, and M. Sasaki, "High-performance thin-film barretter mount for power measurement in W-band," *Electronics Letters*, vol. 21, pp. 170-172, 1985.
- [25] SensorScientific. *Small Bead hermistor*. Available: http://www.sensorsci.com/literature_122766/Glass_Bead_Thermistors
- [26] A. Kazemipour, F. Ziade, D. Allal, M. Z. M. Jenu, and E. Bergeault, "Nonlinear Modeling of RF Thermistor: Application to Bolometer Mount Calibration," *Instrumentation and Measurement, IEEE Transactions on*, vol. 60, pp. 2445-2448, 2011.
- [27] D. Halliday, "Fundamentals of physics / David Halliday, Robert Resnick, Jearl Walker. Vol.2," R. Resnick and J. Walker, Eds., 6th ed., extended. ed. New York: Wiley, 2001, pp. 717-723.
- [28] Rogercorp. (2015). *RT/duroid® 6006/6010LM High Frequency Laminates*. Available: <https://www.rogerscorp.com/documents/612/acs/RT-duroid-6006-6010LM-Laminate-Data-Sheet.pdf>
- [29] *CST-Computer Simulation Technology- Microwave Studio* Available: <https://www.cst.com/>
- [30] D. M. Pozar, "Microwave engineering / by David M. Pozar," 4th ed. ed. Hoboken, N.J.: Wiley, 2012, pp. 120-121.
- [31] R. M. Richard J. Cameron, Chandra M. Kudsia, *Microwave Filters for Communication Systems: Fundamentals, Design and Applications*: Wiley, 2007, pp. 46-59.
- [32] M. J. Lancaster, "Passive microwave device applications of high temperature superconductors / M.J. Lancaster," ed. Cambridge: Cambridge University Press, 1997, pp. 129-141.
- [33] L. C. Oldfield, J. P. Ide, and E. J. Griffin, "A Multistate Reflectometer," *IEEE Transactions on Instrumentation and Measurement*, vol. IM-34, pp. 198-201, 1985.
- [34] J. Collard, G. R. Nicoll, and A. W. Lines, "Discrepancies in the Measurement of Microwave Power at Wavelengths below 3 cm," *Proceedings of the Physical Society. Section B*, vol. 63, p. 215, 1950.

